Evaluation and Design of a Flywheel Energy Storage System

Dem Fachbereich Elektrotechnik und Informationstechnik
der Technischen Universität Darmstadt
zur Erlangung des akademischen Grades einer
Doktor-Ingenieurin (Dr.-Ing.)
genehmigte Dissertation

von

M.Sc. Xing Li

geboren am 03.02.1989
in Heilongjiang, China

Referent:	Prof. Dr.-Ing. habil. Dr. h.c. Andreas Binder
Korreferent:	Prof. Dr.-Ing. habil. Christian Mittelstedt
Tag der Einreichung:	06. 12. 2018
Tag der mündlichen Prüfung:	03. 05. 2019

D17

Darmstadt 2019

Li, Xing: Evaluation and Design of a Flywheel Energy Storage System
Darmstadt, Technische Universität Darmstadt,
Jahr der Veröffentlichung der Dissertation auf TUprints: 2019
URN: urn:nbn:de:tuda-tuprints-94619
Tag der mündlichen Prüfung: 03.05.2019

Erklärungen laut Promotionsordnung

§ 8 Abs. 1 lit. c PromO

Ich versichere hiermit, dass die elektronische Version meiner Dissertation mit der schriftlichen Version übereinstimmt.

§ 8 Abs. 1 lit. d PromO

Ich versichere hiermit, dass zu einem vorherigen Zeitpunkt noch keine Promotion versucht wurde. In diesem Fall sind nähere Angaben über Zeitpunkt, Hochschule, Dissertationsthema und Ergebnis dieses Versuchs mitzuteilen.

§ 9 Abs. 1 PromO

Ich versichere hiermit, dass die vorliegende Dissertation selbstständig und nur unter Verwendung der angegebenen Quellen verfasst wurde.

§ 9 Abs. 2 PromO

Die Arbeit hat bisher noch nicht zu Prüfungszwecken gedient.

06.12.2018, Darmstadt

Li, Xing

Motivation

With the increased energy demand and increasing energy costs in recent years, energy storage devices are becoming an important role in the industry in aim to use the energy more efficiently by compensating the mismatch of the generation side and the consumption side. Flywheels are kinetic energy storage devices, which store energy in a rotating mass. To decide whether it is profitable to apply flywheel in a system, it is necessary to give a comprehensive evaluation of the benefits and the investments. In most systems, the energetic and economic saving potentials are the main benefits and usually also the first considerations for a customer to determine the proper storage devices and their optimum specifications. Therefore, the first aim of this thesis is to provide an energetic performance evaluation methodology of the systems equipped with flywheels, in order to provide a basis for next step evaluations (e.g. costs) and designs. For this purpose, two systems are selected as the investigated applications: a household photovoltaic (PV) system and a tramway power system.

The second aim of this work is to provide a flywheel system design approach by prototyping a flywheel demonstrator, highlighting the important aspects in the essential components during the design stage. This demonstrator is designed to verify the energetic performance analysis and the implementation of key technologies, such as steel rotor construction, high speed machine, magnetic levitation and system construction.

Motivation

Durch den erhöhten Energiebedarf und die steigenden Energiekosten in den letzten Jahren kommt dem Energiespeicher in der Industrie eine wichtige Rolle zu, indem er die Fehlanpassung zwischen Erzeugungs- und Verbrauchsseite reduziert. Schwungräder sind kinetische Energiespeicher, die Energie in einer rotierenden Masse speichern können. Um die Frage zu beantworten, ob es sich lohnt, ein Schwungrad in einem System einzusetzen, ist es notwendig, eine umfassende Abschätzung der Nutzungsart und der Investitionen vorzunehmen. In den meisten Systemen sind die energetischen und wirtschaftlichen Einsparungspotentiale der Hauptgrund und normalerweise auch die erste Überlegung für einen Kunden, die richtige Speichervorrichtung und ihre optimalen Spezifikationen zu bestimmen. Zu Beginn dieser Arbeit wird eine Methodik für die Bewertung der energetischen Performance der mit Schwungrädern ausgerüsteten Systeme vorgestellt. Diese bildet die Basis für die weiteren Bewertungen (z. B. Kosten) und das

Design. Zu diesem Zweck wurden zwei Energiesysteme zur Untersuchung ausgewählt: Eine Haushalts-Photovoltaik (PV)-Anlage und ein Straßenbahn-Stromnetz.

Das zweite Ziel dieser Arbeit ist es, einen Designansatz für ein Schwungrad-System mit Hilfe eines Schwungrad-Prototyps zu zeigen, der die wichtigen Aspekte der Komponenten während der Entwurfsphase hervorhebt. Dieser Prototyp dient zur Validierung der energetischen Performanceanalyse und der Implementierung von Schlüsseltechnologien wie Stahlrotorkonstruktionen, Hochgeschwindigkeitsmaschine, Magnetlager und Systemkonstruktion.

Abstract

This thesis deals with the energetic evaluation and design of a flywheel energy storage system (FESS). The first purpose is to give a quantitative evaluation of the energetic performance of the systems equipped with flywheels. Two systems are chosen: one 5 kWp (kWp: peak power) household PV system equipped with a 3 kWh flywheel to accumulate the excessive energy generation in daytime, and one tramway power system equipped with a 1.5 kWh onboard flywheel to accumulate the recovered braking energy. The energy saving potential of each system is analyzed based on the given profiles and the modeled FESS, in which various losses are taken into account. The results show that, energy savings can be achieved for both systems by using flywheels: 15.1 % for the PV system and 20.9 % for the tramway system. But the overcall energy efficiency of the flywheel in the PV system is only 40 %, much lower than 75.5 % in the tram. The main reason is that the high self-discharge due to internal losses (7.7 % of the maximum stored energy per hour) causes considerable energy loss for the long term idling operating cycle (for hours) of the flywheel in PV system. As a comparison, in the tramway system, charge/discharge cycle is much shorter (approx. 1 min) so that the self-discharge is less critical, leading to a higher efficiency of the flywheel.

The second part of this work is design and prototyping of a flywheel demonstrator in order to verify the energetic evaluation and the implementations of high-speed technologies. The demonstrator has an energy capacity of 0.5 kWh at the maximum operating speed of 24000 min^{-1} and the power rating is 35 kVA.

This thesis introduces the design methodology of the key components. For the flywheel rotor, a constant thickness rotor body with the inertia of 0.57 kg·m^2 is designed. The mechanical issues regarding the stress caused by the centrifugal force are analyzed. The construction issues, such as balancing solutions and rotor hardening process are discussed. As an energy conversion component, a 4-pole PMSM is designed. Low loss in the rotor is required due to the inefficient rotor cooling in vacuum. Therefore, the surface mounted magnets are segmented so that the losses can be reduced to 28.4 W (approx. 0.1 % of the rated power). The calculated power efficiencies at two defined operating points are both above 96 %.

Based on the designed rotor and PMSM, magnetic bearings are selected and the housing is designed. The components are assembled and a complete system is built up, which is validated both by a 3D CAD program and by prototyping. The main issues concerning the component processing and the assemble work are presented. Due to the safety consideration, two outer housings are designed as vacuum and also burst containments in case of the rotor structural failure.

The loss analysis is carried out for the PMSM, magnetic bearings, and also the rotor due to air friction. A lumped parameter network of the system is built up for the thermal analysis. The rotor is painted black in order to improve the radiative heat dissipation. The calculated temperature rise on the black-painted rotor and stator is approx. 87.4 K for continuous operation and 73.0 K for operation with the fully-utilized duty cycle. Compared to the temperature limit of 141 °C for the E-machine carbon fiber bandage, the system can operate with the designed duty cycle with a 28 K thermal margin and is sustainable for continuous operation.

The flywheel demonstrator design is validated by FEM calculation and the prototype construction so far. Relevant testing of the prototype has been performed in order to verify the performance, including spin testing of the rotor and levitation testing. In the end of the thesis, a conceptual design of high power (150 kW) machine is presented, as an outlook for the application of the flywheel in the railway systems. Additionally, the design criterions of light weight rotor constructed with composite materials, aiming to achieve higher energy density, are presented. The critical considerations are pointed out, as an outlook for further structural optimization in the future.

Kurzfassung

Diese Arbeit beschäftigt sich mit der energetischen Bewertung und Auslegung eines Schwungradspeichersystems (FESS). Zuerst wird eine quantitative Bewertung der energetischen Performance der mit Schwungrädern ausgerüsteten Systeme gegeben. Zwei Systeme wurden hierfür ausgewählt: Eine 5 kWp (kWp: Spitzenleistung) Haushalts-PV-Anlage mit einem 3 kWh-Schwungrad zur Speicherung der am Tag überschüssigen erzeugten Energie und ein Straßenbahnsystem mit einem 1,5 kWh-Onboard-Schwungrad, welches zurückgewonnene Bremsenergie speichert. Das Energiesparpotential der Systeme wird auf Grundlage der vorhandenen Profilkurven und des modellierten FESS unter Berücksichtigung verschiedener Verlustgruppen berechnet. Die Ergebnisse zeigen eine Energieeinsparung durch den Einsatz von Schwungrädern für beide Systeme: 15,1 % für die PV-Anlage und 20,9 % für das Straßenbahnsystem. Jedoch ist die Energieeffizienz durch den Einsatz des Schwungrads in der PV-Anlage nur 40 % und damit deutlich geringer als 75,5 % bei der Straßenbahn. Der Hauptgrund ist, dass die hohe

Selbstentladung aufgrund von internen Verlusten in FESS (7,7 % der maximalen gespeicherten Energie pro Stunde) einen beträchtlichen Energieverlust für den Langzeit-Leerlaufbetrieb (für einige Stunden) des Schwungrads zwischen Laden und Entladen in der PV-Anlage verursacht. Der Lade-/Entladezyklus im Straßenbahnsystem ist zum Vergleich viel kürzer (ca. 1 min), so dass die Selbstentladung weniger in das Gewicht fällt. Dies führt zu einer höheren Energie-Effizienz des Schwungrads von 75,5 %.

Der zweite Teil dieser Arbeit befasst sich mit dem Entwurf und Bau eines Prototyps eines Schwungrads, um die energetische Bewertung und die Implementierung von Hochgeschwindigkeitstechnologien zu verifizieren. Der Demonstrator hat ein Energiespeichervermögen von 0,5 kWh bei maximaler Betriebsdrehzahl von 24000 min^{-1}; die Nennleistung beträgt 35 kVA.

Diese Arbeit stellt die Entwurfsmethodik für die Schlüsselkomponenten des Schwungrads vor. Für den Schwungradrotor ist ein Rotorkörper mit konstanter Dicke mit einem Trägheitsmoment von 0,57 kg·m^2 entworfen worden. Die mechanischen Probleme bezüglich der Belastung durch die Zentrifugalkraft werden analysiert und die mechanischen Spannungen berechnet. Konstruktionsthemen wie Auswuchtung und die Rotorhärtung werden ebenfalls diskutiert. Als Energiewandlungskomponente wird eine 4-polige permanentmagneterregte Synchronmaschine entworfen. Geringste Verluste im Rotor sind aufgrund der geringen Rotorkühlung im Vakuum erforderlich. Daher sind die oberflächenmontierten Magnete segmentiert, so dass die Wirbelstromverluste auf 28,4 W (ca. 0,1 % der Nennleistung) reduziert werden können. Die berechneten Wirkungsgrade bei zwei definierten Betriebspunkten liegen beide über 96 %.

Basierend auf dem konstruierten Rotor und der PM-Maschine werden Magnetlager ausgewählt und das Gehäuse mit Kühlmantel ausgelegt. Die Komponenten werden zusammengesetzt und ein komplettes System wird aufgebaut, das sowohl durch ein 3D-CAD Programm als auch durch einen Prototyp validiert wird. Die Hauptprobleme bezüglich der Komponentenbearbeitung und der Montagearbeit werden vorgestellt. Aus Sicherheitsgründen wurden zwei Außengehäuse als Vakuum- und auch als Berstschutz-Gehäuse im Fall eines Rotorbruchs ausgelegt.

Die Verlustanalyse wird für die PM-Maschine, die Magnetlager und auch die Luftreibung des Rotors durchgeführt. Ein Parameter-Netzwerk des Systems wird für die thermische Analyse entworfen. Um die Wärmeabstrahlung des Rotors zu verbessern, ist dieser schwarz lackiert. Der berechnete Temperaturanstieg am schwarz lackierten Rotor beträgt ca. 87.4 K für den Dauerbetrieb und 73.0 K für den Betrieb mit der angenommenen Einschaltdauer für einen Zyklus. In Bezug zur Temperaturgrenze von 141 °C für die

C-Faser-Bandage des E-Maschinenrotors kann das System durch den geplanten Arbeitszyklus mit einer thermischen Toleranz von 28 K betrieben werden und ist somit für einen Dauerbetrieb geeignet.

Das Design des Schwungrad-Prototyps wird durch FEM-Berechnungen und den Prototypenbau validiert. Es wurden Messungen am Prototyp durchgeführt, um die Performance zu überprüfen, einschließlich Schleudertest des Rotors und Schwebetest. Am Ende der Arbeit wird eine konzeptionelle Konstruktion einer Hochleistungsmaschine für 150 kW als ein Ausblick für die Anwendung des Schwungrades in Straßenbahnsystemen vorgestellt. Darüber hinaus wird ein Rotordesignbeispiel mit kohlenstofffaserverstärktem Kunststoff vorgeschlagen, mit dem eine höhere Energiedichte erreicht werden soll. Ebenfalls erfolgt ein Ausblick für weitere zukünftige strukturelle Optimierungen.

Table of Content

Symbols in Formulas and Abbreviations

Symbols in formulas

Symbol	*Unit*	*Description*
A	A/cm	Current loading of E-machine
A	m^2	Contact area of impact
A_{c3}	°C	Austenitic transform temperature
A_k	mm^2	Cross section of the cooling channel
A_r	mm^2	Surface area of rotor outer surface
A_s	mm^2	Surface area of stator inner surface
A_s	mm^2	Surface area of the stator housing without cooling channel
A_{slot}	mm^2	Slot area
A_5	%	Material elongation at fracture
a	-	Parallel branches
a_i	-	Number of strands per turn
a_T	-	Number of horizontally placed wires in one slot
B	T	Flux density
$(BH)_{max}$	kJ/m^3	Magnet energy density
B_r	T	Remanence
B'_r	T	Remanence for demagnetizing
$B_{\delta,1}$	T	Air gap flux density
b	mm	Distance of the center of the gravity
b_m	mm	Magnet segment width
b_{Qm}	mm	Average slot width
b_T	mm	Width of equivalent square wire
C_{cap}	F	Capacitance of EDLC
C_{FW}	kWh	Flywheel energy storage capacity
c	J/(kg·K)	Specific heat capacity
c_{H_2O}	J/(kg·K)	Specific heat capacity of coolant
c_m	-	Number of magnet circumferential segmentation per pole
D	mm	Flywheel body diameter

D_{c}	mm	Diameter of the containment shell
$D_{\mathrm{c,i}}$	mm	Inner diameter of the containment shell
d	mm	Diameter
d_{Cu}	mm	Diameter of copper wires
d_{E}	mm	Skin depth
d_{k}	mm	Hydraulic diameter of the cooling channel
$d_{\mathrm{o,mag}}$	mm	Outer diameter of magnet
$d_{\mathrm{ri,disk}}$	mm	Inner diameter of rotor disk
d_{ro}	mm	Rotor outer diameter
$d_{\mathrm{ro,disk}}$	mm	Outer diameter of rotor disk
d_{sh}	mm	Shaft diameter
d_{si}	mm	Stator inner diameter
d_{so}	mm	Stator outer diameter
E	kWh	Energy
E	GPa	E-modulus
E_{c}	J	Energy for compressive deformation
$E_{\mathrm{feed\text{-}in}}$	kWh	Energy fed into the grid
E_{s}	J	Energy for shear deformation
E_{save}	kWh	Energy saving from the grid
E_{t}	J	Energy for tensile deformation
E_1	J	Energy stored in one rotor segment after fracture
E_2	J	Energy of the rotor fragment and the housing after impact
e	m	Eccentricity
F	N	Force
F_{sr}	-	Facing factor of stator inner surface and rotor outer surface
f	Hz	Frequency
f_{k}	kHz	Switching frequency
f_{s}	kHz	Fundamental frequency
f_{T}	kHz	Inverter switching frequency
G	GPa	Shear modulus
G	mm/s	Balance quality
H	kA/m	Magnetic field strength
H_{c}	kA/m	Coercivity
H_{cB}	kA/m	Coercivity

H_{cJ}	kA/m	Magnetic polarization
$H_{\mathrm{sc,max}}$	kA/m	Demagnetizing field due to short circuit
h	mm	The axial length of the flywheel body
h_{B}	mm	Bandage thickness
h_{L}	mm	Height of vertically placed wires of the parallels strands
h_{m}	mm	Magnet height
h_{sr}	mm	The distance between the balancing hole bottom and the flywheel body
I	A	Current(r.m.s.)
I_{d}	A	Current in *d*-axis (r.m.s.)
I_{max}	A	Maximum current (r.m.s.)
I_{N}	A	Nominal current (r.m.s.)
I_{q}	A	Current in *q*-axis (r.m.s.)
I_{s}	A	Stator current (r.m.s.)
I_{sc}	A	Stator current at short circuit (r.m.s.)
$\hat{I}_{\mathrm{d}}$	A	Current amplitude in *d*-axis
$\hat{I}_{\mathrm{q}}$	A	Current amplitude in *q*-axis
$\hat{I}_{\mathrm{q1}}$	A	Current amplitude in *q*-axis at OP_1
$\hat{I}_{\mathrm{q2}}$	A	Current amplitude in *q*-axis at OP_2
$\hat{I}_{\mathrm{s}}$	A	Stator current amplitude
$\hat{I}_{\mathrm{s1}}$	A	Stator current amplitude at OP_1
$\hat{I}_{\mathrm{s2}}$	A	Stator current amplitude at OP_2
$\hat{I}_{\mathrm{s,max}}$	A	Maximum stator current amplitude
$\hat{I}_{\mathrm{sc,\ pk}}$	A	Maximum sudden short circuit current
J	$\mathrm{kg{\cdot}m^2}$	Moment of inertia
J	$\mathrm{A/mm^2}$	Current density of E-machine
J	T	Polarization
J_1	$\mathrm{kg{\cdot}m^2}$	Mass moment of inertia of the rotor fragment
J_2	$\mathrm{kg{\cdot}m^2}$	Mass moment of inertia of the housing
K	-	Empirical constant
K_{n}	-	*Knudsen* number
$K_{\mathrm{n,r}}$	-	*Knudsen* number in radial direction
$K_{\mathrm{n,z}}$	-	*Knudsen* number in axial direction

k_{cv}	-	The coefficient considering curvature
k_{f}	-	A reductive coefficient of magnet flux density
k_{fill}	-	Slot filling factor
k_{gap}	-	The coefficient due to the gap between each segment
k_{sf}	-	Safety factor (reference to material yield strength)
k_{str}	-	The coefficient due to inter-pole flux leakage
k_{Vd}	-	Loss increase factor of teeth
k_{Vy}	-	Loss increase factor of yoke
k_{w1}	-	Winding factor
k_0	m	Radius of gyration of the mass about the center of gravity
k_{2D}	-	The factor to consider only radial component of the flux density
L_{c}	mm	Length of the containment shell
L_{d}	mH	Inductance in d-axis
L_{Fe}	mm	Iron stack length
L_{h}	mH	Main inductance
L_{mag}	mm	Axial length of magnet
L_{p}	m	Perimeter of the sheared area
L_{q}	mH	Inductance in q-axis
$L_{\mathrm{s}\sigma}$	mH	Stator leakage inductance
l_{b}	mm	Length of the overhang winding
l_{k}	mm	Total length of the spiral cooling jacket
l_{m}	mm	Magnet segment axial length
M	kg	Rotor mass
M	Nm	E-machine torque
M_{e}	Nm	E-machine electromagnetic torque
M_{max}	Nm	E-machine maximum torque
M_{N}	Nm	E-machine rated torque (OP_1)
$M_{\mathrm{sc,max}}$	Nm	Maximum torque at sudden short circuit
M_1	kg	Mass of the rotor fragment
M_2	kg	Effective mass of the housing
m	-	E-machine phase number or modulation index
m_{FW}	kg	Flywheel body mass
m_{T}	-	Number of vertically placed wires in one slot

m_{21}	kg	Mass of the housing in line with the rotor fragment
m_{22}	kg	Housing mass adjacent to the impact area
N_c	-	Number of turns per coil
N_s	-	Number of turns per phase
n	min^{-1}	Rotating speed
n_f	-	Fragment number
n_max	min^{-1}	Maximum rotational speed
n_min	min^{-1}	Minimum rotational speed
P	Pa	Air pressure
$P_\mathrm{Cu,AC}$	W	Copper losses considering the effect of current displacement
$P_\mathrm{Cu,add}$	W	Additional eddy current losses
$P_\mathrm{Cu,DC}$	W	DC resistive losses
$P_\mathrm{Cu,end}$	W	Copper losses in the PM machine winding overhang
$P_\mathrm{Cu,s}$	W	Copper losses in the PM machine winding in slots
P_d	W	Total losses of the system
$P_\mathrm{d,m}$	W	Total losses
P_e	kW	Electromagnetic power
$P_\mathrm{Fe,r}$	W	Losses in rotor iron
$P_\mathrm{Fe,st}$	W	Iron losses in stator teeth
$P_\mathrm{Fe,sy}$	W	Iron losses in stator yoke
P_fr	W	Air friction losses
$P_\mathrm{fr,C}$	W	Friction losses on cylinder surface
$P_\mathrm{fr,D}$	W	Friction losses on two end surface
$P_\mathrm{fr,free}$	W	Friction loss for a free molecule flow
$P_\mathrm{fr,free,C}$	W	Friction losses on cylinder surface for a free molecule flow
$P_\mathrm{fr,free,D}$	W	Friction losses on two end surface for a free molecule flow
$P_\mathrm{fr,mach}$	W	Air friction losses of the machine
$P_\mathrm{fr,slip}$	W	Total friction loss on a rotating disk for a slip flow
$P_\mathrm{fr,sum}$	W	Total friction losses on a rotating disk
P_FW	W	Output power of the FESS /electric power of the flywheel
P_g	W	Power consumption from the grid
P_L	W	Load power
P_LB	W	Biased load power
$P_\mathrm{MB,r}$	W	Losses in the magnetic bearings rotor

$P_{\mathrm{MB,s}}$	W	Losses in the magnetic bearings stator
P_{N}	kW	Rated output power (motor)
P_{PM}	W	Losses in magnets
P_{PV}	W	PV generation power
P_{rad}	W	Radiative heat transfer between the rotor and stator
P_{res}	W	Power consumed by the braking resistor
$P_{\mathrm{Tram,B}}$	W	Biased power of the tram
p	-	E-machine pole count
p_{c}	MPa	Contact pressure
$p_{\mathrm{c,\,min}}$	MPa	Minimum contact pressure
$p_{\mathrm{c,\,m\text{-}B}}$	MPa	Contact pressure between magnets and bandage
$p_{\mathrm{c,\,sh\text{-}m}}$	MPa	Contact pressure between shaft and magnets
$p_{\mathrm{c},\,\Delta u}$	MPa	Contact pressure caused by press-fit
$p_{\mathrm{c},\,\vartheta}$	MPa	Contact pressure caused by thermal expansion
$p_{\mathrm{c},\,\omega}$	MPa	Contact pressure caused by rotation
p_{Fe}	W/kg	Specific iron loss
Q	m^3	Material volume of containment
Q_{s}	-	Slot number
q	-	Number of slot per pole per phase
R	$\mathrm{J{\cdot}mol^{-1}{\cdot}K^{-1}}$	Gas constant
R^{+}	MPa	Yield tensile strength
R^{-}	MPa	Yield compressive strength
R_{ad}	mΩ	Braking resistor
R_{m}	MPa	Material ultimate tensile strength
$R_{\mathrm{p0.2}}$	MPa	Material yield strength
R_{s}	mΩ	Stator winding resistance
r	mm	Radius
r_{o}	mm	Flywheel body outer radius
S	MPa	Shear strength
S_{N}	kVA	Rated apparent power
T	°C	Temperature
T	mm	Thickness of the containment shell
T_{max}	°C	Max. continuous temperature of magnet

TK_{B_r}	%/K	Temperature coefficient of remanence
$TK_{H_{cJ}}$	%/K	Temperature coefficient of coercivity
t	s	Time
t_{ch}	s	Charging time
t_{dch}	s	Discharging time
t_0	s	Time for idling at minimum speed
t_1	s	Time for idling at maximum speed
U_{AC}	V	Inverter nominal output voltage (r.m.s.)
U_{cap}	V	Voltage of the capacitor
U_{DC}	V	Inverter DC-link voltage
U_k	mm	Circumference of the cooling channel
U_p	V	Induced voltage (r.m.s.)
$\hat{U}_p$	V	Induced voltage (amplitude)
$U_{s,max}$	V	Max. phase voltage (r.m.s., Y connection)
$U_{s,ph}$	V	Phase voltage (r.m.s.)
u_s	V	Voltage
$u_{s,max}$	V	Voltage limit
$\dot{V}$	l/min	Coolant flow rate
V_1	m/s	Translational velocity of one fragment
V_2	m/s	Translational velocity of the two bodies after impact
w	m	Slot pitch
Z	%	Material section area shrinking at fracture
z_m	-	Number of magnet axial segmentation per pole
α	1/°C	Coefficient of thermal expansion
α_e	-	Pole arc ratio
α_{eq}	$W/(m^2 \cdot K)$	Equivalent heat transfer coefficient on cylindrical surface
α_k	$W/(m^2 \cdot K)$	Heat transfer coefficient at cooling channel surface
α_p	°	Pole coverage angle
$\alpha_{rad,eq}$	$W/(m^2 \cdot K)$	Equivalent heat transfer coefficient of radiation
β	°	Current angle respect to q-axis
ΔE_1	J	Energy dissipated in the momentum transfer for an impact
ΔE_2	J	Residual energy after impact stage 1
Δu	mm	Undersize

Δu_{max}	mm	Maximum undersize
Δu_{min}	mm	Minimum undersize
$\Delta\vartheta_{\mathrm{H_2O}}$	°C	Temperature rise of the coolant
δ	mm	Mechanical air gap length
$\delta_{\mathrm{c,gap}}$	mm	Space between 2 housings
δ_{e}	mm	Electromagnetic air gap length
δ_{r}	mm	Radial clearance
δ_{z}	mm	Axial clearance
ε	-	Emissivity
ε_{c}	-	Compressive plastic strain
ε_{r}	-	Emissivity on rotor outer surface
ε_{s}	-	Emissivity on stator inner surface
ε_{t}	-	Tensile strain
φ	rad	Phase angle
γ	-	Self-consumption
η	%	Efficiency
κ_{m}	S/m	Magnet conductivity
$\kappa_{\mathrm{m,eff}}$	S/m	Modified magnet conductivity
λ	m	Molecular mean free path or wave length
$\lambda_{\mathrm{H_2O}}$	W/(m·K)	Thermal conductivity of coolant
μ	-	Harmonic order
μ_{M}	-	Relative permeability of the magnet
μ_0	-	Permeability in vacuum
ν	-	Harmonic order
ν	-	*Poisson*’s ratio
$\nu_{\mathrm{H_2O}}$	$\mathrm{m^2/s}$	Kinematic viscosity of coolant
ϑ	°C	Temperature
ϑ_{amb}	°C	Ambient temperature
ϑ_{i}	°C	Temperature of the coolant inlet
ϑ_{o}	°C	Temperature of the coolant outlet
ϑ_{r}	°C	Temperature of rotor outer surface
ϑ_{s}	°C	Temperature of stator inner surface

ρ	$\mathrm{kg/m^3}$	Material density
σ	$\mathrm{W/(m^2 \cdot K^4)}$	*Stefan-Boltzmann* constant
σ	S/M	conductivity of the material
σ_d	MPa	Average dynamic plastic flow stress of the material in compression
σ_Mises	Mpa	*von Mises* stress
σ_r	Mpa	Normal stress in radial direction
$\sigma_\mathrm{t,B}$	Mpa	Tangential stress in bandage
$\sigma_\mathrm{t,B,max}$	Mpa	Maximum tangential stress in bandage
$\sigma_\mathrm{t,limit,B}$	Mpa	Strength limit in bandage
$\sigma_\mathrm{t,p,B}$	Mpa	Tangential stress in bandage due to pressure
$\sigma_{\mathrm{t},\vartheta,\mathrm{B}}$	Mpa	Tangential stress in bandage due to thermal expansion
$\sigma_{\mathrm{t},\omega,\mathrm{B}}$	Mpa	Tangential stress in bandage due to rotation
σ_u	Mpa	Ultimate strength of the material
σ_z	Mpa	Normal stress in axial direction
σ_θ	Mpa	Normal stress in tangential (circumferential) direction
τ	Mpa	Shear stress
τ_d	Mpa	Dynamic shear strength of the material
τ_p	-	Rotor pole pitch
τ_s	-	Stator pole pitch
$\upsilon_\mathrm{H_2O}$	m/s	Coolant flow speed
Ω	rad/s	Rotational angular speed
Ω_max	rad/s	Maximum speed of the flywheel
Ω_1	rad/s	Rotational angular speed of the flywheel
Ω_2	rad/s	Rotational angular speed of the two objects after impact
ω	rad/s	Electric frequency
ω_max	rad/s	Maximum operating frequency
$\omega_\mathrm{m,max}$	rad/s	Maximum mechanical angular speed
ω_s	rad/s	Electric frequency of the machine
ω_1	rad/s	Electric frequency at OP_1
ω_2	rad/s	Electric frequency at OP_2
ξ	-	Self-sufficiency
Ψ_p	Vs	Magnet flux linkage

Abbreviations

A	Austenite
AMB	Active magnetic bearing
B	Bainite
BCC	body-centered cubic
CTE	Coefficient of thermal expansion
DoD	Degree of discharge
EDLC	Electric double layer capacitors
F	Ferrite
FCC	Face-centered cubic
FESS	Flywheel energy storage system
FEM	Finite element method
HTS	High temperature superconducting
IM	Induction machine
LA	lead-acid
Li-ion	lithium-ion
M	Martensite
M_s	Martensite start temperature
MB	Magnetic bearing
m.m.f.	Magnetomotive force
MPPA	Maximum power point tracking
OP	Operating point
P	Pearlite
PM	Permanent magnet
PV	Photovoltaic
PMB	Passive magnetic bearing
PWM	Pulse width modulation
RMSE	Root mean squared error
SOC	State of charge
SRM	Switching reluctance machine
SynRM	Synchronous reluctance machine
TTT	Time-temperature-transformation
UPS	Uninterruptible power supply
VPI	Vacuum pressure impregnation

1. Introduction

Flywheels are one of the most ancient mechanical devices. In ancient times, people stated to make use of the rotary inertia by devices such as spindle whorl, potter's wheel, windmills, water wheel, etc. After the industrial revolution, big wheels were used in steam machines to smooth the rotation. Even though there were some attempts to use flywheels as energy accumulators before 1960s, the low costs of energy limited their applications. Only small amount of energy can be stored in these devices. After 1970s, as the costs of energy increased, the interest of energy accumulators started to grow [1]. Many attempts to use flywheels to store significant quantities of energy were successful, such as in connection with railways (*Gyrocar* in mine locomotives) or vehicles (*Gyrobus*), or as backup power supplier for devices which should maintain uninterrupted operating in case of power failure. The flywheels in earlier times were usually constructed with steel, which had large dimensions and big masses. In recent years, with the help of modern power electronics and high strength materials, high performance flywheels are further developed, characterized by higher energy and power density, which attract more attentions. However, the discussion about the application of this technology is still ongoing concerning their costs, energy density and complexity.

1.1 Basics of Flywheel Storage System

A flywheel stores kinetic energy in a rotating mass. The energy is proportional to the inertia J of the body and in square to the rotating angular speed Ω^2,

$$E = \frac{1}{2} \cdot J \cdot \Omega^2 . \tag{1-1}$$

The basic components of a flywheel energy storage system (FESS) can be seen in Fig. 1-1. An electric machine (E-machine) is essential for the energy conversion. It speeds up the rotor when the flywheel is charged, transforming the electrical energy into mechanical form. For discharge, the machine operates as a generator, decelerating the rotor, and feeds the energy back to the network. The power supply and energy feed-back is realized by a power inverter which allows bi-directional power flow. The supporting of the flywheel rotor can be realized by either mechanical bearings or magnetic bearings, depending on the operating speed. The flywheels can be classified into high speed

(10000 … 100000 min^{-1}) and low speed (less than 6000 min^{-1})[2]. High speed flywheels are usually magnetically levitated and operates in vacuum or partial vacuum in order to reduce friction losses. Therefore, a vacuum pump and magnetic bearing control system are required. The characteristics of low speed and high speed flywheels are compared in Table 1-1.

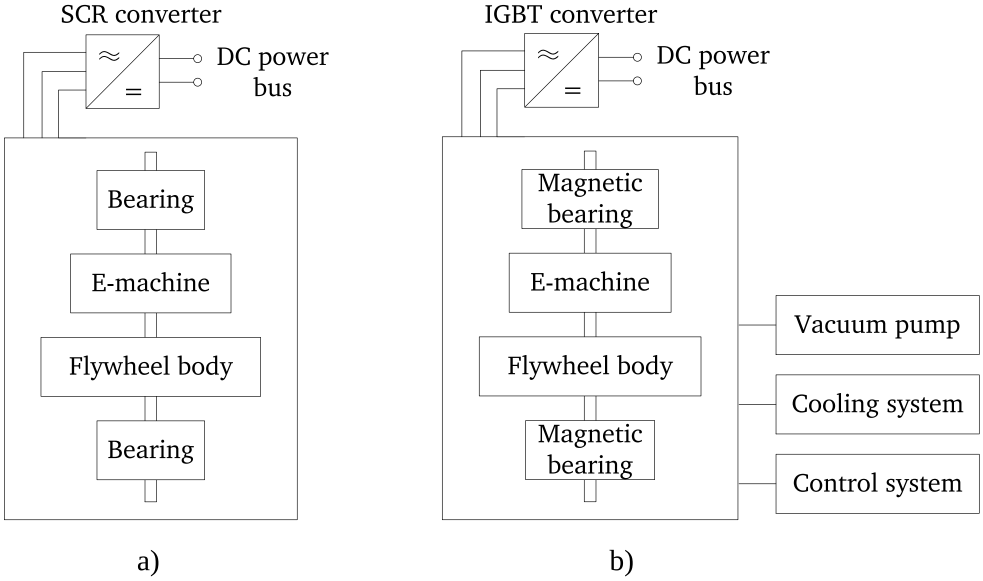

Fig. 1-1 Components of a flywheel system: a) low speed flywheel, b) high speed flywheel (SCR: Silicon Controlled Rectifier, IGBT: Insulated Gate Bipolar Transistor)

Table 1-1 Characteristics of low speed and high speed flywheels, according to [6]

	Low speed flywheels	High speed flywheels
Rotor material	Steel	Composite materials
Electric machine	Induction machine, coil excited machine, PM machine, reluctance machine	PM machine, reluctance machine
Integration of E-machine and flywheel	No integration or partial integration	Full or partial integration
Bearings	Mechanical or mixed (mechanical and magnetic)	Magnetic
Confinement atmosphere	Low vacuum or light gas	High or medium vacuum
Main application	Power quality	Traction and aerospace

1) Low speed flywheels usually have high energy capacity (1 … tens of kWh) and high power ratings (in MW). One typical application is in the power network for frequency and voltage stabilization [3]. The rotor is made of steel, thus reducing the manufacturing costs compared to the fiber reinforced composite materials. Due to the low speed, big inertia of the rotor mass is required, therefore resulting in increased weight and size of the system. But they are not crucial issues for the stationary applications. Low speed also allows the use of mechanical bearings. For an increased bearing life, auxiliary magnetic support is also advisable [4]. Low speed flywheels can operate in normal air, or in partial vacuum or lighter gas in order to reduce the air friction. Due to the cooling effect of the air or gas on the rotor, the coil excited machines or induction machines can be used instead of permanent magnet (PM) machines. Overall, despite of the low specific energy (1 Wh/kg), low speed flywheels can achieve a low-cost, robust and reliable construction with simple components [4].

2) High speed flywheels are usually developed for the purpose of high specific energy and specific power (tens of kW/kg). The energy capacity is usually small (0.01 … a few kWh). They are used, typically, for the applications of transportation and aerospace, where extreme constraints of the system weight and volume are required [5]. As the specific energy E/m (Wh/kg) of the flywheel body is in proportion to the material specific strength (the ratio of material strength σ_u to the mass density ρ) as described by (1-2) [1], high strength and lighter materials i.e. fiber reinforced composite materials (specific strength: 180 … 240 Wh/kg) are preferred rather than metals (specific strength: 12 … 66 Wh/kg) [1].

$$\frac{E}{m} \propto K \cdot \frac{\sigma_\mathrm{u}}{\rho} \tag{1-2}$$

In (1-2), m is the mass in kg, σ_u is the ultimate strength of the material, ρ is the mass density. K is called shape factor (Table 1-4), depending on the geometrical configuration of the rotor and the used failure criterion, typical values are 0.3 … 1.

High rotational speed makes it impossible to use conventional mechanical bearings due to the high friction losses. The rotor is usually levitated by magnetic bearings, which are usually more sophisticated and costly. To reduce the huge aerodynamic dragging losses, the rotor is located in vacuum or partial vacuum. This causes the difficulty of rotor heat dissipation. Therefore, PM machines, which have rather low rotor losses, are adopted in high speed flywheels. All these "high-tech" components (magnetic levitation, vacuum, high speed machine, bi-directional power flow inverter) and special materials (composite materials, rare-earth magnets) push high speed flywheels to a high price level (approx. 5 times higher than low speed flywheels [6]) and high degree of system complexity. Therefore, they are not widely used compared to the existing energy storage technologies (batteries, super capacitors …), especially concerning the hazard of high speed system failure. Potential failures may occur due to the crack in the rotor mass, in the magnetic bearing controls or in power electronic systems. A safety proved containment also increases the system complexity and costs. However, high speed flywheels are still attractive in the energy storage market due to their extraordinary advantages of high specific power and power density, nearly no degradation and suitable for extremely high cycling with very little maintenance.

1.1.1 Flywheel Characteristics

According to [7], the characteristics of the main energy storage technologies are summarized and compared in Table 1-2. The flywheels are characterized by high specific power (W/kg) and power density (kW/m^3), high cycling without degradation, low maintenance requirements and low environmental impacts. The downsides are high self-discharge due to the internal losses and higher safety risk than other storages [8].

Table 1-2 Characteristics of electrical energy storage technologies, according to [7]

	Super-caps	Flywheels	Lead-acid battery	Li-ion battery
Specific power (W/kg)	5.44 … 100000	400 … 30000	25 … 415	8 … 2000
Specific energy (Wh/kg)	0.07 … 85.6	5 … 200	10 … 50	30 … 300
Power density (kW/m^3)	15 … 4500	40 … 2000	10 … 400	56.8 … 800
Energy density (kWh/m^3)	1 … 35	0.25 … 424	25 … 90	94 … 500
Round trip efficiency (%)	65 … 99	70 … 96	63 … 90	70 … 100
Lifetime (years)	5 … 20	15 … 20	3 … 20	2 … 20
Lifetime (cycles)	10^4 … 10^6	10^4 … 10^5 or 10^5 … 10^7 [9]	100 … 2000	250 … 10^5
Self-discharge (%/day)	0.46 … 40	24 … 100	0.033 … 1.10	0.03 … 0.33
Recharge time [9]	s … min	< 15 min	8 h … 16 h	min … h
Scale [MW]	0 … 5	0.001 … 10	0 … 50	0 … 3
Power investment cost ($/kW)	100 … 800	30.28 … 700	175 … 900	175 … 4000
Energy investment cost ($/kWh)	100 … 94000	200 … 150000	50 … 1100	200 … 4000
Technical maturity	Proven, commercializing	Mature, commercializing	Very mature, fully commercialized	Mature, commercialized
Environmental impact	Very low	Very low	High	High/ medium

The flywheels can be charged and discharged rapidly, transferring large amount of power in seconds with a high efficiency of 85 … 95 % for high speed flywheels [7]. The charge and discharge power of flywheels are not influenced by the degree of discharge (DoD), unlike super-caps and batteries. And the discharge rate is easily known by measuring the rotational speed. High numbers of cycling will not cause degradation problems for flywheels, for which super-caps and batteries are not comparable, as they usually have to be replaced after 10 … 15 years due to degradation. Therefore, the benefit of flywheels can be seen for a long service time scale. However, high self-discharge is a critical disadvantage of flywheels, which determines that they are not suitable for a long term energy storage like batteries. But this disadvantage has little influence when the storage time decreases to seconds, as the losses are negligible compared to the total converted energy. The potential safety risk of a high speed rotating mass is also a critical drawback of flywheels. This drags flywheels down considering the application in mobility, e.g. vehicles and trains.

1.1.2 Flywheel Applications

Due to the high specific power and high self-discharge, flywheels are suitable for short term storage applications, where highly frequent charge/discharge with a high power level are required, thus the energetic losses are negligible compared to the converted energy. In Table 1-3 the typical industrial applications are summarized for flywheels which are commercially available. These applications include both the large scale in the grid and small scale at the customer side. Normally, high power and capacity are achieved by arranging flywheels in banks, rather than using large machines in one single module [8].

Table 1-3 Typical industrial applications for commercially available flywheels

Application	Functionality	References
Power systems	Integration of renewable energy sources	[8, 10]
	Frequency and voltage stabilization	
	Power quality and regulation	
	Voltage and power smoothing	
	Uninterruptible power supply (UPS)	
Mobility (vehicles, railways)	Braking energy recovery	[11, 12]
Aircraft launch system, ships, crane, plasma physics laboratory …	Pulsed power supply	[13]
Aerospace	Satellite attitude control, back up energy storage	[14]

1.2 A Short Review of Flywheel Technologies

1.2.1 Flywheel System Configurations

Most of the existing flywheel systems have the configurations shown in Fig. 1-2. They can be grouped into conventional type and integrated type.

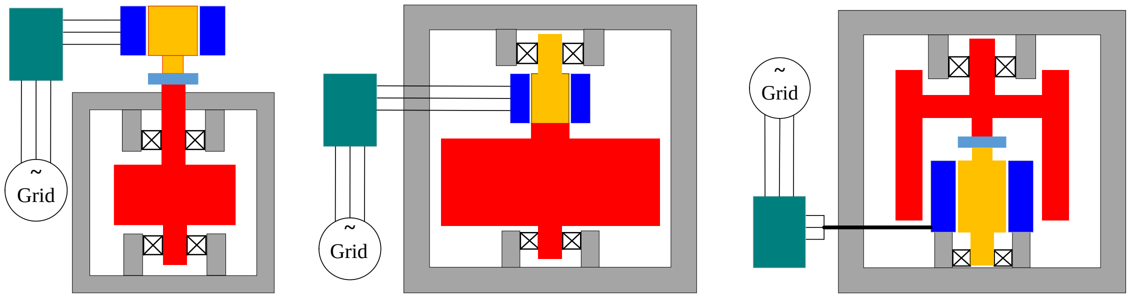

Outside E-machine Inner rotor (solid) Inner rotor outer mass

a) Conventional type

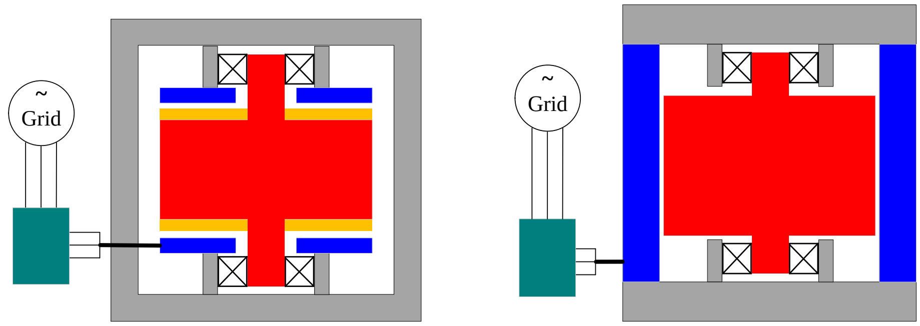

Inner rotor (axial flux) [15] Inner rotor (radial flux) [16]

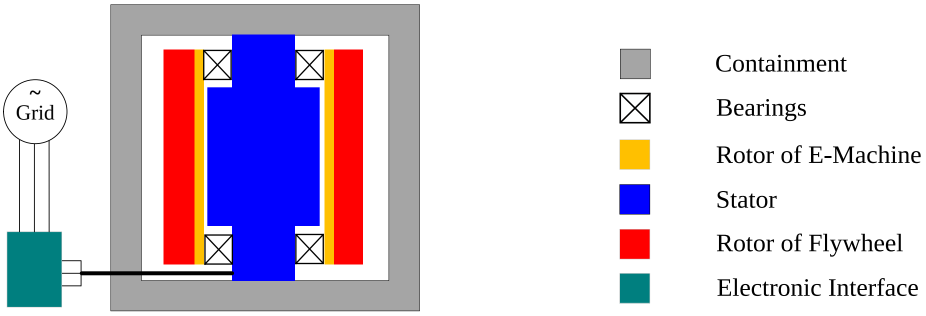

Outer rotor [17]

b) Integrated type

Fig. 1-2 Typical configurations of flywheel systems [18]

For conventional type Fig. 1-2 a), the flywheel rotor and the E-machine are separated units and coupled by mechanical coupling or sharing one shaft. The machine can be placed inside or outside of the housing. The outside machine has a well cooling condition, so that high power and low-cost induction machine can be used. But the speed is usually low due to the mechanical issues of the coupling components and the sealing issues. The flywheel rotor can be either a solid body or a cylindrical one (so called inner rotor outer mass type). The latter type is the typically used topology for a composite rotor rim connecting by a lightweight hub to the shaft, where the space inside the rim can be effectively used, leading to a compact design. But for steel rotor, this type is not suitable due to the high density and relatively low strength of the material. Steels are more suitable to build a solid rotor.

For the integrated type Fig. 1-2 b), the flywheel rotor is also acting as part of the flux path of the E-machine, thus the energy storage component and the power unit are integrated. The machine can be a conventional radial flux type or a novel axial flux type [15]. The axial flux type can take advantage of the substantial axial force, which is controlled by the additional coil in the stator winding, to counteract the rotor gravity, reducing the load and friction on the bearings. But this requires a complicated control strategy for both force and torque control. In the radial flux type, PM machine is not applicable due to the low mechanical strength of magnets. The machine is either a reluctance machine or homo-polar machine, which has lower power density than PM machine. Compared to the inner rotor configuration, outer rotor type has a higher degree of integration. The composite rotor rim can be completely levitated by outer rotor magnetic bearings without any hub connection, obtaining an even higher specific energy and energy density. The integrated configuration increases the dependency between each component. Independent component design is no more valid, therefore high development costs are required, which can be regarded as a drawback. A series of outer rotor prototypes have been developed in [17, 19].

1.2.2 Critical Technologies

1.2.2.1 High Speed Rotor Mass

Flywheels are classified by their specific energy E/m_{tot} (m_{tot}: mass of the total system) into [1]:

- Low specific energy: < 10 Wh/kg
- Medium specific energy: 10 … 25 Wh/kg
- High specific energy: > 25 Wh/kg

A high specific energy (W/kg) usually leads to the requirement of high speed. According to (1-2), one approach is to increase the shape factor of the flywheel body by changing the rotor geometries as shown in Table 1-4. The other approach is to use high strength but low density materials, such as carbon fiber composite materials. Table 1-5 shows the mechanical properties of some actual and future materials. The carbon fiber flywheels are usually manufactured into a thin rim shape, avoiding high radial stress due to centrifugal force and low manufacturing quality in a thick rim. These thin rims can be assembled into a multi-ring configuration which has shown significant improvements in strength and safety [7], thus can further increase the speed of the flywheel. However, increasing speed also requires high performance containment vessels due to safety reason [7]. For safety, most system components should be designed two times as strong as the flywheel rotor [20].

Table 1-4 Shape factor of various rotor geometries [1]

Rotor shape	Geometry	Shape factor *K*
Constant stress disk (theoretical)	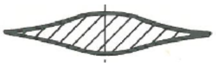	1
Constant stress disk (real)	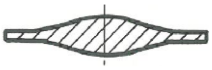	0.7 … 0.98
Conical disk	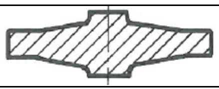	0.7 … 0.95
Constant thickness disk	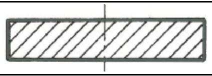	0.606
Thin rim	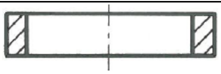	0.5
Rim with disk	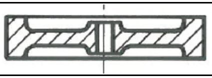	0.4 … 0.5
Pierced constant thickness disk		0.303

Table 1-5 Ultimate strength σ_u, density ρ and specific strength σ_u/ρ of some materials [1, 18]

Material	σ_u [MPa]	ρ [kg/m^3]	σ_u/ρ [Wh/kg]
Alloy steel 30CrNiMo8	1000	7760	36
Maraging steel 18Ni250	1860	8000	65
Aluminum 7075	572	2810	57
Titanium TiAl6Zr	1200	4500	74
Glass fiber reinforced composite material	1300	2000	181
Carbon fiber reinforced composite material T700+epoxy resin	2450	1550	439
Multi-walled carbon nanotubes low end	10000	1750	1587
Multi-walled carbon nanotubes high end	60000	1750	9524

1.2.2.2 E-machine

E-machine is responsible for the kinetic and electric energy conversion in a flywheel system. So far induction machines (IM), permanent magnet (PM) machines and reluctance machines are most commonly used machines. Their characteristics are compared in Table 1-6.

Table 1-6 Comparison of commonly used machines in flywheel systems [8]
(PM: permanent magnet, SynRM: synchronous reluctance machine, SRM: switching reluctance machine)

	Induction machine (IM)	PM machine	Reluctance machine	
			SynRM	SRM
Power	High	Medium and low	Medium and low	
Power density	Medium (approx. 0.7 kW/kg)	High (approx. 1.2 kW/kg)	Medium (approx. 0.7 kW/kg)	
Efficiency	High (93.4 %)	Very high (95.5 %)	High (93.0 %)	
Spinning losses	Removable by annulling flux	Non-removable due to PM	Removable by annulling flux	
Rotor losses	High	Very low	Very low	Medium
Rotor strength	Medium	Low	Medium	
Pros	High robustness, low cost, no idling losses, simple construction.	High efficiency, high power density, simple control.	Low rotor losses (SynRM), robustness of rotor overheat.	
Cons	High rotor losses, complicated control.	Demagnetization, inevitable idling losses, low robustness, high cost.	Complex structure (SynRM), low power factor (SynRM), high torque ripple (SRM), noise and vibration (SRM).	

The induction machine has high robustness with high efficiency and low costs. The drawback is high rotor losses. Therefore, it is usually used in “big” flywheels with high energy and power ratings, e.g. associated with wind generators. These flywheels have low speed and operate in air. Therefore, the rotor can be well cooled.

PM machines are more attractive and traditionally used in high speed flywheels due to their high power density, high efficiency and low rotor heat dissipation problems. However, their costs are relatively higher and have drawbacks of demagnetization risks and inevitable idling losses.

Switching reluctance machines (SRM) have simple rotor construction and therefore rotor overheating problems are less critical. But they still have complex controls and lower power density than PM machines. The torque ripple and acoustic noise are typically drawbacks of SRMs, but fortunately remain less of a problem for flywheel systems than for other applications [7]. Synchronous reluctance machine (SynRM) is also attractive due to their low rotor losses. However, the rotor structure is usually complicated and the power factor is lower compared to PM machines.

Apart from the conventional machines above, various machine topologies are proposed, such as homo-polar machines [21] [22], bearingless machines [23] and axial flux machines [24]. However, they are normally under research and not used in the industry due to different reasons. For example, homo-polar machines have a simple constructed and robust rotor, but suffer from low power factor and power density. The bearingless machines usually need complicated controls and the levitation still remains a challenge for heavy rotors.

1.2.2.3 Bearings

Traditional mechanical bearings are still the simplest and the most widely used solutions for low speed flywheels. But they suffer from severe wear and tear for high speed and require good lubrication and periodic maintenance. Ceramic bearings and hybrid bearings can be used to achieve an extended bearing life due to their low coefficients of friction and high endurance for wear. For the high speed flywheel systems where wear or maintenance is a critical issue, contact-free magnetic bearings (MBs) are required. They are classified into passive magnetic bearings (PMBs) and active magnetic bearings (AMBs). PMBs use the force produced by permanent magnets, which is not controllable, to support all or part of the rotor weight. In terms of AMB, the force is controllable depending on the position and movement of the rotor. Nevertheless, magnetic bearings also produce losses which are sometimes comparable to mechanical bearings. The parasitic losses of mechanical and magnetic bearings account for typically 1 … 5 % of the stored energy per hour [20]. The bearing losses cause self-discharge of the flywheel. Low bearing losses are achievable by using high temperature superconducting (HTS) bearings. The losses can be reduced as low as 0.1 % of the stored energy per hour including the losses of the cooling system. However, the costs of HTS bearings are so far not considerable for industrial application.

1.2.2.4 Vacuum & Burst Containment

High speed flywheel systems usually locate in vacuum container in which the vacuum level ranges from hundreds of pascal to 10^{-4} Pa. Another function of the containment is to produce safety protection in case of rotor failure. When the rotor falls apart, the containment should prevent the projectiles from flying out and dissipate the kinetic energy by deformation. However, unfortunately, the mechanism of the impact and the behavior of the involved bodies are rather complicated to predict. Experimental study must be performed for the flywheels intended for production [1]. An experiment to observe the impact behavior was carried out in [25], in order to verify and improve the containment design. Some practical recommendations for a safe design of flywheels are proposed in [26].

1.3 Motivation and Outline of This Work

To decide whether it is profitable to apply flywheel storage in a system, it is necessary to give a comprehensive evaluation of the benefits and the investments. The benefits differ for different applications. In this thesis, two systems are selected as the investigated applications: a household photovoltaic (PV) system and a tramway power system. In the former one, a flywheel can accumulate the excessive PV generation and save it for the use at night. In a tramway system, a flywheel can accumulate the regenerative energy when the tram brakes. In both systems, the energetic and economic saving potentials are the main benefits and usually also the first considerations for a customer to determine the proper storage devices and their optimum specifications. Therefore, the first aim of this thesis is to provide an energetic performance evaluation methodology of such systems, which equipped with flywheels, in order to provide a basis for next step evaluations (e.g. costs) and designs.

The second aim of this work is to provide a flywheel system design approach by prototyping a flywheel demonstrator, highlighting the important aspects in the essential components during the design stage. This demonstrator is designed to verify the energetic performance analysis and the implementation of key technologies, such as steel rotor construction, high speed machines, magnetic levitations and system constructions, and so on.

This thesis is organized as follows:

Chapter 2 and **Chapter 3** present the energetic performance evaluation of two systems equipped with flywheel storages: a household PV system and a tramway power system. A power flow model of both systems has been developed, including the loss model of the flywheel. A case study is carried out for both systems with a measured load profile. The energetic efficiency of the flywheel is evaluated regarding variable flywheel specifications.

Chapter 4 … 9 introduces the component design and construction of the flywheel demonstrator.

In **Chapter 4**, the design specifications are given. An overview of the designed system is presented. Several critical considerations are pointed out.

Chapter 5 starts with the mechanical design of the flywheel rotor. The dimensioning of the flywheel body for energy storage is carried out based on the material properties. The rotor dynamic behavior is analyzed. The rotor construction issues, such as balancing solutions and rotor hardening process are discussed.

Chapter 6 introduces the E-machine design. A 4-pole permanent magnet machine is designed according to the given design specifications and limits. The basic design parameters of the machine are presented, followed by the loss calculation. After that, three important electromagnetic performances are analyzed: the harmonics analysis due to inverter feeding, the flux weakening performance and the demagnetization at three phase short circuit. In the end, the mechanical design of the rotor components is introduced to determine the bandage thickness and the fitting.

Chapter 7 presents the magnetic bearing system. The configuration of the magnetic bearings are introduced, including one radial magnetic bearing and one combined type which produces forces in both radial and axial direction. The force and losses in the magnetic bearings are analyzed.

In **Chapter 8**, the system set-up is presented. The designed rotor, the E-machine and magnetic bearings are assembled together. An inner housing is designed as a supporting frame of all the components. The main issues concerning the component processing and the assemble work are presented. Due to the safety consideration, two outer housings are designed as burst containments in case of the rotor structural failure. In addition, the air friction losses of the rotor are calculated for the low pressure in vacuum.

Chapter 9 presents the thermal calculation of the flywheel system. The loss components of the system are summarized. A lumped parameter thermal network is modeled and used to calculate the temperatures and heat flows. The calculation is carried out for two operating conditions: continuous operation and the operation with a fully-utilized duty cycle. In the end, the design of the stator water cooling system is presented.

Chapter 10 … 11 presents the discussions concerning the critical issues for a high power (150 kW) machine and light-weight rotors made of fiber reinforced materials, as an outlook for the future work.

As the flywheel system designed in Chapter 4 … 9 is a preliminary demonstrative prototype, in which the power rating is downsized from 150 kW to 35 kVA due to power limit in the *EW* lab. In order to fulfill the power requirement for the application in the aimed tram system as discussed in Chapter 3, a theoretical design of a PM machine with a full power of 150 kW is proposed in **Chapter 10** as a conception for the follow-up design for the onboard application.

As high specific energy and energy density are usually required for onboard application, for which light-weight rotors made of fiber reinforced materials are preferred. Therefore, in **Chapter 11** some critical considerations are discussed concerning the design of such rotors as an outlook for the future work. The velocity limitations regarding the stress due to rotation are given, based on which the criteria for the dimensioning of the composite rims are introduced. Critical problems regarding the rim-shaft connection are also discussed.

The author would like to express her deeply thanks to her colleague *M.Sc. Nicolas Erd* for his contribution in Chapter 2 and Chapter 3. *Mr. Erd* proposed most of the innovative ideas for building-up the model in the power flow analysis, and was responsible for all the programing work. Thanks to his work, the worthful results in these two chapters can be obtained. Also many thanks attribute to the author's ex-colleague *M.Sc. Jeongki An*, who proposed the design of the E-machine in Chapter 6, including the dimensioning of the geometries and the loss calculation (iron losses and eddy current losses in magnets) in FEM model, as well as the stress calculation in the bandage. Based on his work, the author developed further performance analysis (copper losses calculation and field weakening performance analysis).

For building-up the prototype, the author would like to thank *Mr. Andreas Fehringer* and *Mr. Markus Lohnes* in the workshop of the *Institute for Electrical Energy Conversion, TU Darmstadt*, for their efforts in the manufacturing process. With their creative ideas and experienced work, a feasible construction layout of the prototype was proposed and the prototype was successfully built-up. Sincere thanks should also be given to *Dr. Yves Gemeinder* and *M.Sc. Nicolas Erd*, who were responsible for organizing the project, and *Dr. Gael Messager* and *M.Sc. Daniel Dietz*, who are working on the control of the magnetic bearings to realize the levitation of the rotor, as well as *Mr. Klaus Gütlich*, who sets up all the electrical systems for the testing of the prototype.

2. Power Flow Analysis of Residential PV Systems with Flywheels

The energy storage devices in residential PV systems can solve the time based mismatch of the power generation and consumption by accumulating the excessive energy and save it for later use when necessary. In this way, the electricity consumption from the grid can be reduced by increasing the self-consumption of the PV generation. Nowadays, the market of energy storage systems for residential PV installations is solely dominated by batteries with a significant trend changing from lead-acid (LA) batteries to lithium-ion (Li-ion) batteries. Compared to batteries, flywheels have longer lifetime (cycles) with no degradation problems and little environmental impacts. In 1970s, the idea of using flywheels in residential PV systems was already proposed [27], even though before that *it has been established that conventional flywheels are neither technically nor economically competitive with batteries* [28]. But, according to [28], if a flywheel is designed with an integrated functions of DC-AC power conversion and maximum power point tracking (MPPT), the flywheel will be technically and economically competitive with the battery based system: battery plus inverter and MPPT. Based on this idea, a flywheel prototype was built in [29], which has a storage capacity of 4 kWh and power of 500 W. The rotor, which is magnetically levitated, has a maximum rotational speed of 15000 min^{-1} and operates in vacuum. Experimental measurements show an overall power efficiency of 68 % of the flywheel based system including power electronics (with approx. 1.5 % loss of stored energy per hour), slightly higher than the battery based system with the value of 65 % (considering 80 % for battery, 85 % for inverter, 96 % for MPPT). This comparison is not valid for nowadays as the efficiency and performance of batteries are considerably increased, e.g. to 85 … 95 % for Li-ion battery [30]. Secondly, the measured efficiency focuses on power conversion efficiency of the prototype unit, instead of considering the cycling operation in the PV system, where the idling losses in the flywheel become critical rather than the power conversion losses for a cycling period of hours.

Therefore, in this chapter, a performance evaluation of a flywheel in the residential PV system will be presented, summarized based on the published paper [77]. The emphasis stays on the overall energy efficiency of the flywheel taking the operating cycle into account, and the energy saving potential of the PV system in a time scale of one year. The aim is to give a quantitative evaluation in order to point out the challenges that restrain the usage of flywheels and the technical improvement hints of the flywheels for the use of long term storage in the future.

2.1 System Description and Modeling

The investigated residential PV system is designed to maximize the self-consumption of the PV generation instead of maximizing the feeding into the grid, as this is more profitable due to the significantly falling grid feed-in tariffs in recent years in *Germany* [32].

2.1.1 System Operating Strategy

The main components of the residential PV system with FESS are shown in Fig. 2-1: the PV generation system ("PV"), the household consumption ("Load"), the storage system ("FESS") and the "Grid" which can supply the household with electrical energy as well as receive the excessive energy from the PV system. Based on varying generation and consumption, there are different power flow conditions among the components in the system. They can be divided into two operating modes: a generation dominant mode (mode A) and a consumption dominant mode (mode B), as shown in Fig. 2-1. The notations 1, 2, 3 denote the priorities (in decreasing orders) of the power flow paths.

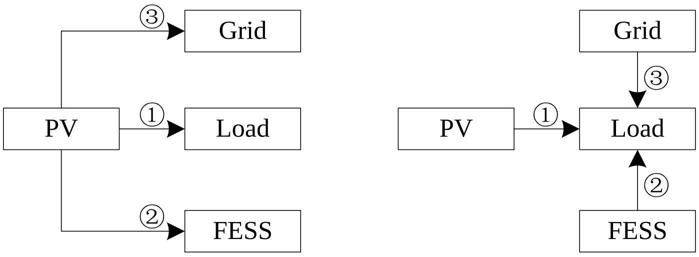

a) b)

Fig. 2-1 PV system operating modes: a) Mode A: generation dominant, b) Mode B: consumption dominant. (Numbers show the priority of the power flow from 1 to 3 in decreasing order.)

Mode A occurs when the PV generation is higher than the consumption: $P_{PV} \geq P_L$ (P_{PV}: PV generation power, $P_{PV} \geq 0$; P_L: load power, $P_L \geq 0$). The PV generation fulfills the load in the first place and stores the excess energy in the FESS. After the FESS is fully charged or the charging power limit is reached, the residual generation will be fed into the grid.

If $P_{PV} < P_L$, the system operates in mode B. The consumption is fulfilled by different sources according to the priority. Firstly all the PV generation is used to fulfill the load. Then the FESS is discharged to cover the remaining load. If the FESS is empty or the residual power demand exceeds the FESS power rating, additional energy is bought from the grid.

By defining the output power of the FESS as P_{FW} ($P_{FW} > 0$ for discharge; $P_{FW} < 0$ for charge) and the power consumption from the grid as P_g ($P_g > 0$ for consumption; $P_g < 0$ for grid feed-in), the system energy balance can be represented by

$$P_{PV} + P_{FW} + P_g = P_L . \tag{2-1}$$

In the simulation, the input data are P_{PV} and P_L. P_{FW} can be determined according to the constraints introduced in the following section (refer to [77] for detailed descriptions). P_g can be obtained according to (2-1). Thus the power flow of the system is determined for next step evaluation.

2.1.2 Flywheel Modeling

The flywheel system consists of a rotor mass and an E-machine, which are coupled with one common shaft. The rotor is levitated by active magnetic bearings and located in a low pressure containment to reduce friction losses.

1) *SOC* Constraint

The energy E stored in the flywheel is proportional to the inertia J of the body and in square to the rotating angular speed Ω^2 as described in (1-1). The energy capacity is defined to be maximum kinetic energy $C = E_{max}$ stored in the body when the maximum speed is reached. The state of charge (*SOC*) is defined by

$$SOC = E/E_{max} . \tag{2-2}$$

The *SOC* constraint is

$$0 \le SOC \le 1 . \tag{2-3}$$

In order to make a full use of the stored energy, the flywheel is assumed to be discharged to a minimum speed of 0, i.e. $SOC_{min} = 0$. After that the magnetic bearings and all the auxiliary components (vacuum pump, control system …) will be shut off in order to reduce the standby losses. This is a special case compared to normal flywheels, which are usually discharged to a minimum speed (e.g. half of the maximum speed) instead of zero. Because the energy demand to maintain even the low speed rotation of the flywheel, which can be regarded as additional energy consumption of the household, is unaffordable for a standby duration of hours, especially for the system aiming at energy saving.

2) Power Constraint

The power of the flywheel follows the constraints in Fig. 2-2, determined by the power limit of the E-machine. The power limit increases linearly as the speed increases and reaches the maximum value at half of the maximum speed and is constant for higher speed. If the flywheel is charged, $P_{\mathrm{FW}} < 0$, and if discharged $P_{\mathrm{FW}} > 0$.

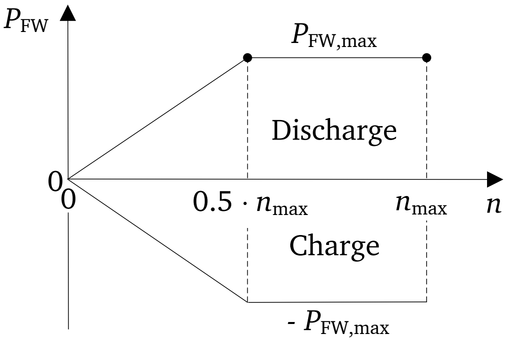

Fig. 2-2 Power constraints of the modeled flywheel system
(P_{FW}: electric power of the flywheel, n: rotational speed)

3) Loss Components

The loss components of the flywheel system include the following:

1) The windage loss in vacuum is calculated by an analytical model following (8-19) … (8-22) in Chapter 8.
2) The losses in the E-machine and inverter are modelled by constant power efficiency: η_{ch} for charge and η_{dch} for discharge.
3) The power demand of the magnetic bearings and all other auxiliary components (vacuum pump, control system …) is modeled as an additional electrical load P_{e} by (2-4), acting when the flywheel is turning. The additional electrical load P_{e} increases the total power demand of the household from P_{L} to P_{LB}, as shown in (2-5).

$$P_{\mathrm{e}} = \begin{cases} \text{const.} & SOC > 0 \\ 0 & SOC = 0 \end{cases} \tag{2-4}$$

$$P_{\mathrm{LB}} = P_{\mathrm{L}} + P_{\mathrm{e}} \tag{2-5}$$

2.1.3 Quantitative Indicators for Evaluation

For the quantitative evaluation of the simulation results, two absolute indicators are introduced. The first one, calculated by (2-6), is the energy saving from the grid E_{save} compared to a bare household with the same load profile but without any PV system or storages. The other one is the energy fed into the grid $E_{\mathrm{feed\text{-}in}}$, given by (2-7). The superscript "+" denotes the positive value and "–" the negative value.

$$E_{\mathrm{save}} = \sum \left(P_{\mathrm{L}} - P_{\mathrm{g}}^{+} \right) \cdot \Delta t \tag{2-6}$$

$$E_{\mathrm{feed\text{-}in}} = \sum \left| P_{\mathrm{g}}^{-} \right| \cdot \Delta t \tag{2-7}$$

Apart from these two absolute indicators, three commonly used relative indicators are introduced: the self-sufficiency ξ, the self-consumption γ and the flywheel energy efficiency η, calculated by (2-8) … (2-10). One should note that, the energy efficiency η here is defined by the sum of the energy (in kWh) discharged from the flywheel to the one charged into the flywheel. This is different with the normal defined efficiency regarding the power and losses in watts. To clarify this, they are named by *energy efficiency* and *power efficiency* respectively in this thesis.

$$\xi = 1 - \frac{\sum P_{\mathrm{g}}^{+} \cdot \Delta t}{\sum P_{\mathrm{L}} \cdot \Delta t} \tag{2-8}$$

$$\gamma = 1 - \frac{\sum \left| P_{\mathrm{g}}^{-} \right| \cdot \Delta t}{\sum P_{\mathrm{PV}} \cdot \Delta t} \tag{2-9}$$

$$\eta = \frac{\sum P_{\mathrm{FW}}^{+} \cdot \Delta t}{\sum \left| P_{\mathrm{FW}}^{-} \right| \cdot \Delta t} \tag{2-10}$$

2.2 Simulation Results: Case Study

By using the established model, the case of a one-family house with a roof mounted PV system will be studied for the time scale of one year.

2.2.1 PV Generation and Load Profile

The load profile is synthetically generated by a load generator [33] for a household with a couple and two kids. The annual consumption is 4135 kWh. A time resolution of 30 seconds is chosen in order to preserve the typical domestic short term demand peaks. The PV generation profile is taken from empirical data of a roof mounted PV system located in *Eschwege, Germany* from 2014, and linearly scaled to 5 kWp with an annual generation of 5030 kWh [34]. The time interval of PV generation power is 15 min.

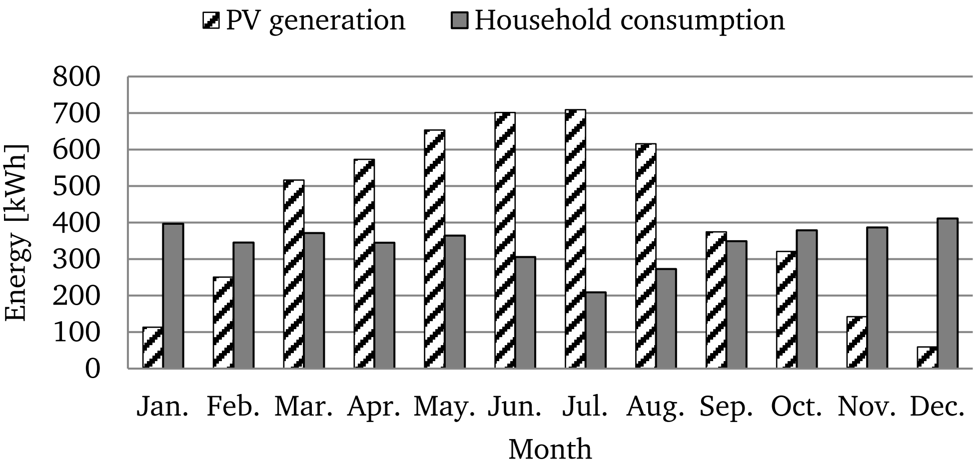

Fig. 2-3 Monthly consumption (synthetically generated by [33]) and PV generation (measured by [34]) of the investigated household with 5 kWp PV system in *Eschwege, Germany*

Fig. 2-3 shows the monthly generation and consumption data of the studied case, in which an obvious seasonal change can be seen. In summer time, abundant solar energy is obtained due to the long sunshine duration. It is possible to achieve complete self-sufficiency if the daily mismatch of the generation and consumption can be solved by using storage devices. However, the generation in winter time is rather low due to the cloudy weather that the electricity must be provided from the grid. The diurnal energy storage device cannot cope with this seasonal change.

The one-year time based load and PV generation profiles are presented by statistical diagrams shown in Fig. 2-4. The probability density diagrams (top graphs), in which the area denotes probability, reflects how often that a specific demand or generation power occurs. For example, in the top graph of Fig. 2-4 a), the most often occurred power demand is 117.5 W, however, from the energy demand point of view in the bottom graph, the biggest energy demand is for the power of 317.5 W. In Fig. 2-4 b), the top graph shows the probability density $f(P)$ of different PV generation power. The total area is

0.47, saying that 53 % of the time there is no PV generation. The energy contributions E (P) for each power level are of similar importance, except the very low and very high power which have smaller energy contribution.

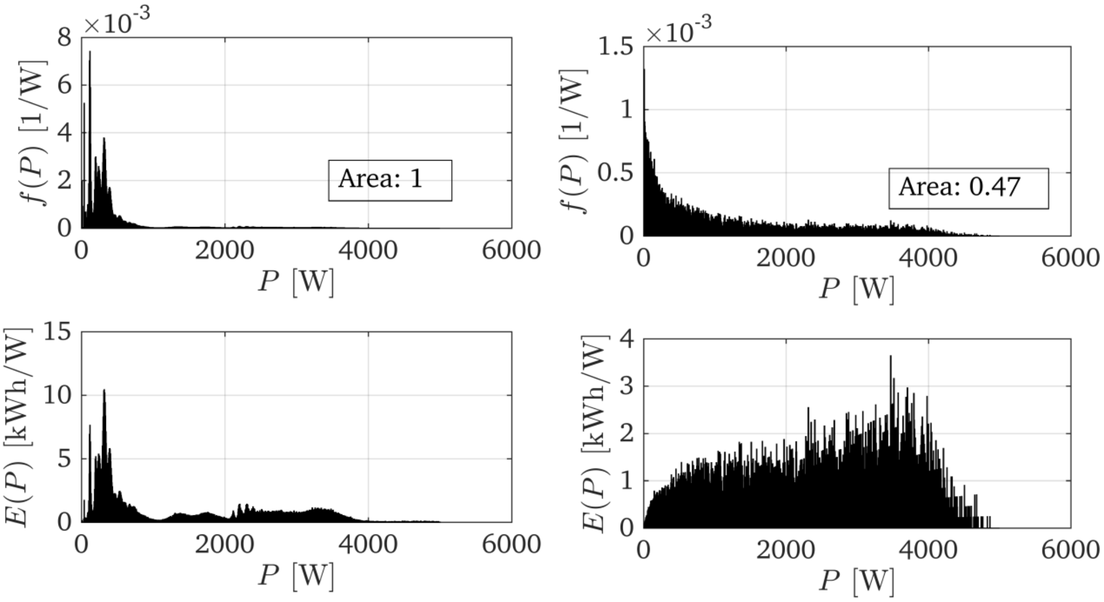

a) b)

Fig. 2-4 Calculated statistical data of the load and generation profiles: probability density $f(P)$ (top graphs) and energy distribution $E(P)$ (bottom graphs) versus power P: a) household consumption (synthetically generated by [33]), b) PV generation (measured by [34])

2.2.2 Parameters of Flywheel

The investigated flywheel has the parameters shown in Table 2-1. The storage capacity is chosen to be 3 kWh here, and a further analysis for varying capacity will be carried out in Chapter 2.2.4. The maximum power is determined to be 4 kW, which covers almost all the power demand in the household as shown in Fig. 2-4 a). The pressure P in the flywheel is chosen to be 0.3 Pa. This value is the typical lower limit of rotary vane pumps. Higher vacuum can be obtained if turbo-molecular pumps are used, which are significantly more expensive. The flywheel rotor body is dimensioned for a construction with carbon fiber reinforced composite material. The power efficiency considers an inverter and an induction machine, for the reason of lower idling losses at no load compared to permanent magnet machines [79]. The auxiliary power demand for the magnetic bearings, vacuum pump and control and cooling systems is difficult to estimate here. A constant value is assumed for the preliminary simulation and the influence will be discussed afterwards with a parametric study.

Table 2-1 Parameters of the flywheel used in the investigated PV system

Parameter	Symbol	Value	Parameter	Symbol	Value
Storage capacity	C	3 kWh	Rotor outer radius	R_o	260 mm
Maximum speed	n_{max}	24000 min^{-1}	Rotor height	h	294 mm
Maximum power	$P_{FW,max}$	4 kW	Power efficiency	η_{ch}/ η_{dch}	0.87/0.87
State of charge	SOC_{min}/ SOC_{max}	0/1	Auxiliary power demand	P_e	100 W
Air pressure	P	0.3 Pa	Air friction losses	$P_{fr}(n_{max})$	115 W @ 60 °C

2.2.3 Simulation Results

Based on the established model and the load and PV generation profiles as input data, the simulation was carried out in *Matlab*. The results are shown as follows:

1) Single day operation

Fig. 2-5 shows the simulated power flow of the PV system and *SOC* of the flywheel for a single sunny day (September 5th, 2014). In the top graph the load P_{LB} is the biased load compared to P_L according to (2-5), considering auxiliary power demand of the flywheel. The given power flow graphs show the typical operating sequences during a single day. At approx. 1 a.m. the stored energy from the previous day is used up. For the rest of the night until 10 a.m. the flywheel stands still for approx. 9 hours. The charging starts at 10 a.m. and lasts about 3 hours. After that the flywheel is fully charged and has a sequence of over 5 hours high speed idling. It consumes the energy of the PV generation to overcome the idling losses, which can be calculated by $P_e + P_{fr}/\eta_{ch} = 232$ W, shown in the middle graph in Fig. 2-5. In this case the flywheel can be regarded as an energy consumer instead of energy converter, which will lead to a significantly dropped energy efficiency. The discharging sequence for the particular day only covers around 2 hours and provides energy for the increased demand between 6 p.m. … 8 p.m.. At 8 p.m. the flywheel is completely discharged and stays at standstill for the whole night.

The example day reveals that even on a sunny day, the flywheel is empty and at standstill for most of the total time (13.5 hours). The active charging and discharging time is only 5.5 hours, while the energy dissipating high speed idling takes approx. 5 hours.

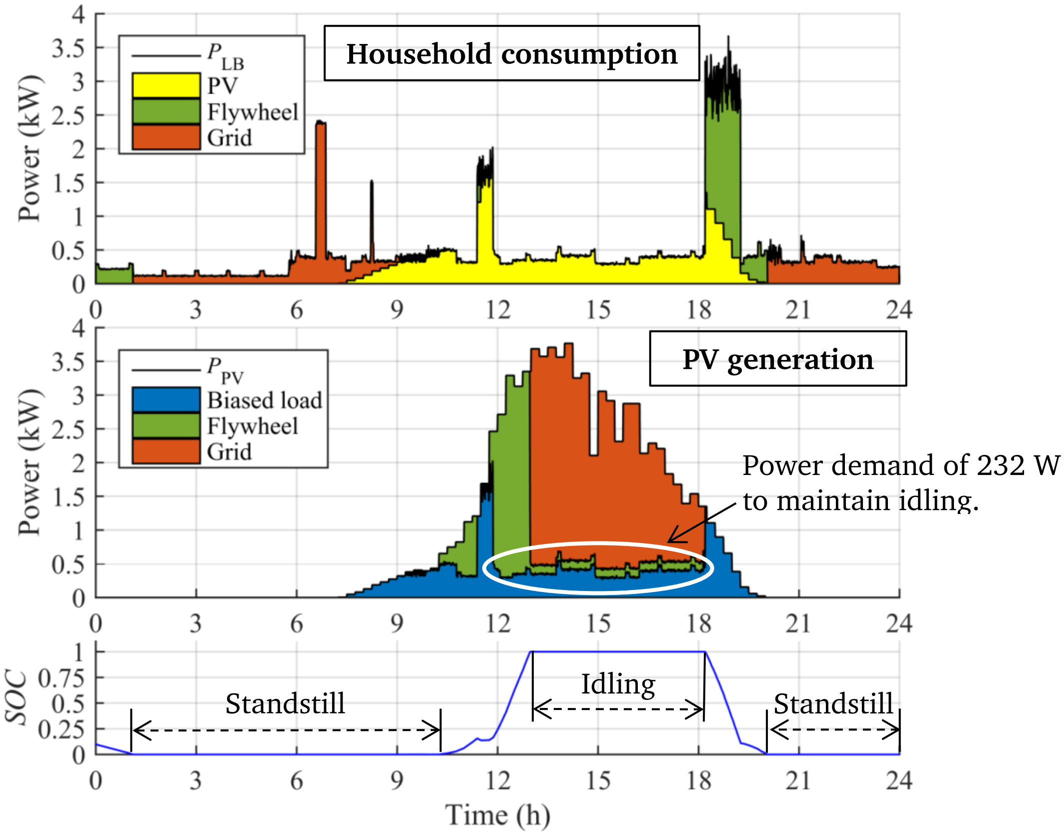

Fig. 2-5 Simulated power flow for a household with 5 kWp PV system and 3 kWh FESS on September 5th, 2014.

(Top: biased household consumption; middle: PV generation; bottom: *SOC* of flywheel.)

2) One year operation

Fig. 2-6 shows the proportion of the flywheel operating points in a histogram on a logarithmic scale, representing the percentage for the flywheel operating at different power level and *SOC* in the simulated case. The power limits are represented by dashed lines. One can see that, 55 % of the operating time (one year) the flywheel is at standstill, which means empty. And 12 % of the year the flywheel is at high-speed idling after fully charged. These two operating points cover most of the time. The power conversion only accounts for 33 % of the time in this operating cycle. The discharging power ($P_{FW} > 0$) is mainly below 500 W, which can be observed by a concentrated power range from the graph. Operating points with powers above 500 W scattered in a broad range, indicating smaller probability of occurrence. The charging power varies between 0 and 4 kW, depending on the generative power of the PV system.

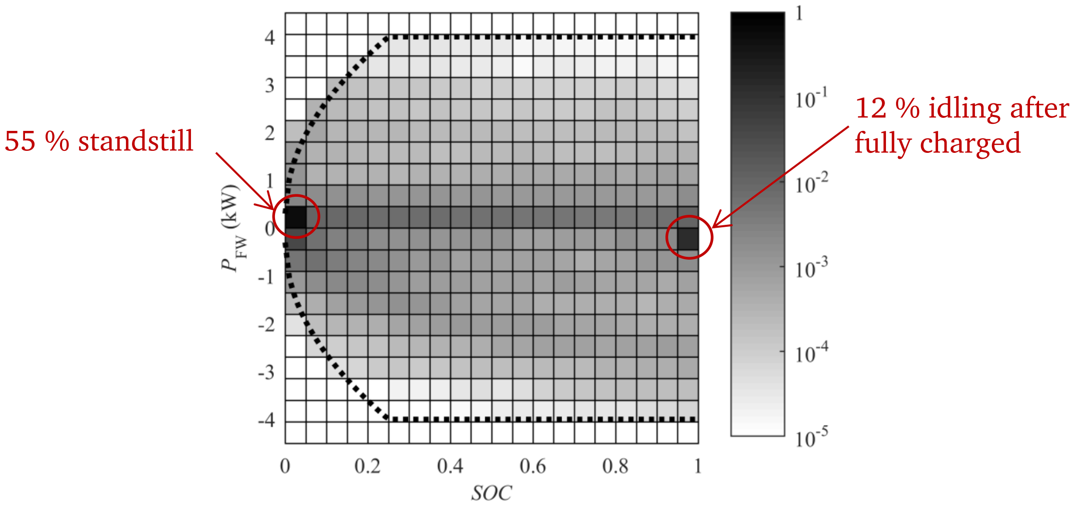

Fig. 2-6 2D histogram: calculated flywheel operating points for the simulated cycle in the case study. Dashed lines: power limits of the flywheel for charge ($P_{FW} < 0$) and discharge ($P_{FW} > 0$)

The energy saving and grid feed-in are shown in Fig. 2-7 compared to a household without PV system or energy storage devices. By using the energy directly consumed from the PV generation without an energy storage device, 1521 kWh grid energy can be saved. If using an ideal 3 kWh flywheel with 100 % power efficiency, no windage losses and zero auxiliary power demand, the energy saving increases by 943 kWh and reach 2464 kWh. Meanwhile, 943 kWh energy is reduced from the grid feed in and is self-consumed. Taking the losses of the flywheel into account, the saved grid consumption is 2146 kWh, 625 kWh higher than the system without an energy storage device. However, it reduces the grid feed-in energy by 1564 kWh, 2.5 times more than the extra energy saving after using flywheel. This value indicates that the benefit of a flywheel can be only achieved if the feed-in price is 2.5 times lower than the consumption price, regardless of the capital costs of the flywheel.

The self-sufficiency, self-consumption and the energy efficiency of the flywheel are evaluated by the relative index ξ, γ and η respectively, which are introduced in Chapter 2.1.3. For a PV system without a flywheel, the self-sufficiency ξ reaches 36.8% by direct consumption of PV generation. With a flywheel, ξ increases to 59.6 % for an ideal one and 51.9 % considering the losses and auxiliary power demand. This is an absolute increase of 15.1 % from no flywheel to a flywheel with losses. Compared to the self-consumption of 30.2 % for the PV system without the flywheel, 61.4 % is reached with the use of a flywheel with losses, indicating more PV generation is consumed to cope with the losses of the flywheel. The energy efficiency of the flywheel is only 40 % for this cycling operation of one year due to the losses especially during long term high speed idling.

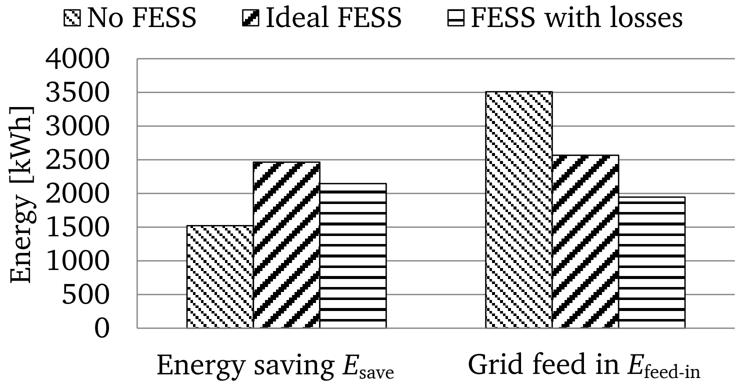

Fig. 2-7 Calculated energy saving E_{save} and grid feed-in $E_{feed\text{-}in}$ for one year operation of the residential 5 kWp PV system with annual generation of 5030 kWh and annual electricity consumption demand of 4135 kWh (reference: household without PV system or storage devices)

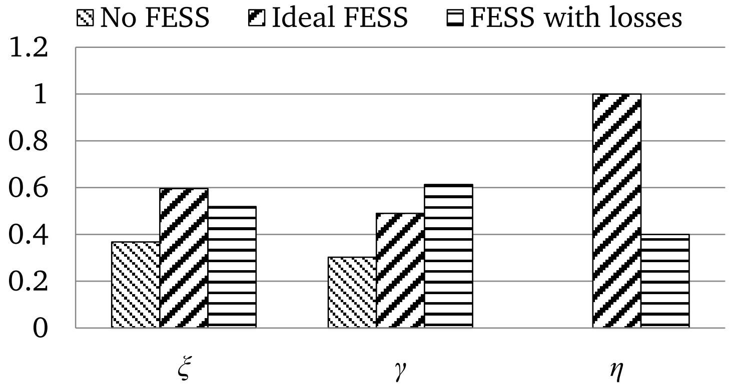

Fig. 2-8 Calculated self-sufficiency ξ, self-consumption γ and the energy efficiency η of the flywheel for one year operation of the residential 5 kWp PV system with annual generation of 5030 kWh and annual electricity consumption demand of 4135 kWh (reference: household without PV system or storage devices)

2.2.4 FESS Parametric Study

The parametric analysis of the flywheel storage capacity C and auxiliary power demand P_e will be presented here. The purpose is to discuss the influence of these two parameters on the system performance and also to obtain the optimum sizing of the flywheel. The capacity C is varied by changing the height h of the flywheel rotor. The windage losses will change with h as well. P_e varies independently.

Fig. 2-9 depicts the self-sufficiency ξ of the PV system. For a fixed P_e, with the increasing C, ξ increases at first and then saturates to a certain value due to the poor PV generation in the winter. Even for the hypothetic case of the FESS without any auxiliary power demand ($P_e = 0$) and a very large capacity C, the self-sufficiency is limited to approx. 65 %. With increasing P_e, ξ drops, as P_e has to be satisfied by discharge of the FESS when operating in consumption dominant mode, thereby the usable amount of energy is reduced. Actually, P_e increases with higher capacities depending on the technology applied. Therefore, an oversized capacity of the FESS is not reasonable.

The self-consumption increases with higher capacity and P_e, as shown in Fig. 2-10. This graph also provides an idea how the FESS consumes the energy from PV generation. For example, with $C = 8$ kWh and $P_e = 400$ W, 50 % self-sufficiency can be obtained from Fig. 2-9. But nearly 90 % of the PV generation is consumed from Fig. 2-10. The high self-consumption cannot be treated as a benefit here, as the generated energy is consumed by the losses of the flywheel.

Concerning the energy efficiency of the FESS, Fig. 2-11 illustrates that η is never higher than 60 % even for the case of $P_e = 0$, which considers solely air friction losses and energy conversion losses in the E-machine. Only for low capacities η increases with C. With higher capacities, the windage losses also increases, η declines gradually due to the long term high speed idling. It should be mentioned that the efficiency can be improved by changing the technology applied, especially by reducing the pressure level in the containment or reducing the auxiliary power P_e (e.g. by using superconducting magnetic bearings). However, both technologies will increase the costs.

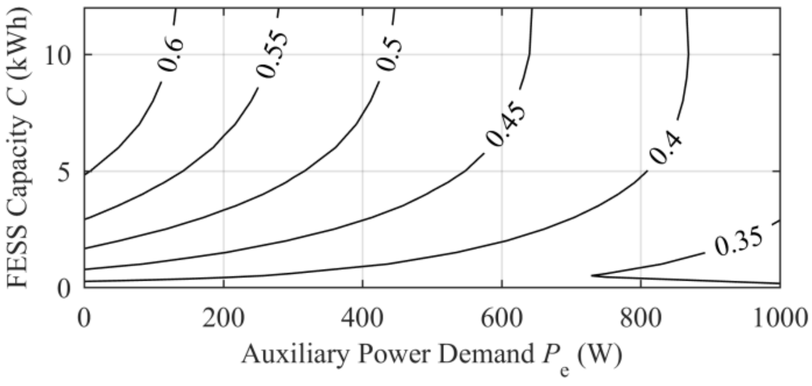

Fig. 2-9 Calculated self-sufficiency ξ of 5 kWp PV system with a FESS for varying capacity and auxiliary power demand

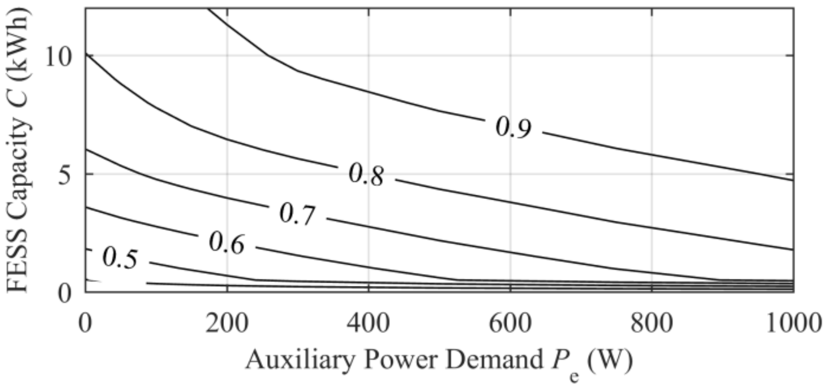

Fig. 2-10 Calculated self-consumption γ of 5 kWp PV system with a FESS for varying capacity and auxiliary power demand

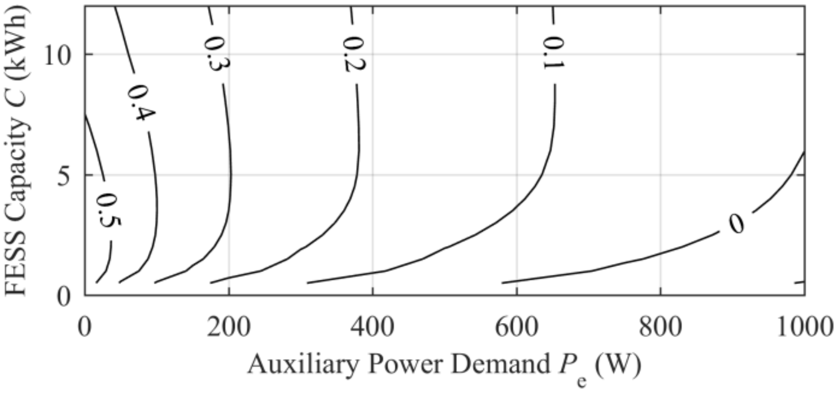

Fig. 2-11 Calculated energy efficiency η of the FESS used in 5 kWp PV system for varying FESS capacity and auxiliary power demand

2.3 Discussion of Flywheel vs. Batteries

Based on the simulated case of a 5 kWp PV system with 3 kWh FESS in a one-family house, we can summarize:

The self-sufficiency (indicating also a percentage of energy saving) of the studied PV system can be improved from 36.8 % to 51.9 % by a FESS, meaning also an extra energy saving of 15.1 % compared to a household without PV system or storage devices. But this extra benefit is achieved by sacrificing the grid feed-in energy, which is 2.5 times the amount of the extra saving. Therefore, the benefit of using a flywheel can be only achieved if the feed-in price is 2.5 times lower than the electricity price, regardless of the capital costs of the flywheel.

Furthermore, the flywheel is 12 % of the time fully charged and 55 % at standstill. The utilization for energy conversion and transfer is rather low. The overall energy efficiency is 40 % for the investigated one-year operating cycle. The main reason is the high self-discharge due to internal losses (approx. 232 W, which is 7.7 % of the maximum stored energy per hour) and the long term idling operating cycle.

As a comparison, the efficiency of commercial Li-ion battery systems (including inverter and charge regulator) can reach 70 … 85 % [30] with the self-discharge in the range of 0.03 … 0.33 % per day [7]. Concerning the costs, the retail price for a complete battery storage system including an inverter is approx. 2500 €/kWh [36]. The flywheels are not commercialized, a cost range of 200 … 150000 €/kWh is given in [7]. Even though the Li-ion batteries have a lower cycle life (5000 cycles [36]) than flywheels (10^5 … 10^7 cycles [9]), the diurnal cycle requirement in the residential PV system can still assure a 10 … 15-year service life of the batteries. Therefore, high cycle endurance of flywheels cannot achieve significant benefits here.

Based on the analysis above, the author concludes that conventional flywheels are neither technically nor economically competitive with commercial batteries as long term storage devices in household PV systems. The high self-discharge is the critical disadvantage of flywheels. This shortage must be overcome if using flywheels for long term storage. One possibility is to develop low loss flywheels, which relies on low loss levitation technology (e.g. superconducting magnetic bearings) and high level vacuum technology (e.g. turbo-molecular pumps). Another solution regarding the high self-discharge is to reduce the idling time of the operating cycle, using a highly frequent charge/discharge cycle. In this way, the energy losses in a short time can be neglected compared to the energy converted during the frequent charge/discharge. That is also the reason why flywheels are suitable for short term storage with high cyclic and high power demands.

3. Power Flow Analysis of a Tramway System with an Onboard Flywheel

Flywheels can be used in the city railway systems (Tram, subway, E-bus, etc), where a highly fluctuating power demand is usually observed due to the frequent starting and braking periods of the vehicles. These fluctuated power peaks cause two main problems. Firstly, they evoke high current in the transmission lines, leading to high losses. Secondly, the regenerative energy during braking, if they are not able to be fed back into the grid nor shared with the vehicles in vicinity, have to be converted into heat by the resistor and wasted. By using storage devices, the power demand can be smoothened, as they can accumulate the recovered energy and save it for the use in the next traction period, avoiding the energy wasting in the braking resistor and reducing the power demand from the transmission lines for the traction. As a result, the total energy consumption of the vehicles can be reduced.

Storages can be installed onboard or off-board in substations. If installed in substations, one single storage device can supply all the pass-by trains. However, the losses in the transmission lines are inevitable. The onboard storages can minimize the transmission losses and more flexible. It also offers the possibility of centenary-free operation to reduce the visual impact. The discussion in this chapter will focus on the onboard flywheel instead of the stationary ones in the substations.

Various storage devices are developed for onboard storage purpose: batteries, electric double layer capacitors (EDLC), as well as flywheels. Batteries and EDLCs are more widely used than flywheels so far. Batteries have high specific energy (at least 10 times higher than EDLCs [37]), but present two disadvantages: lower specific power (0.5 kW/kg [37]) and shorter cycle life (approx. 2000 cycles [38]). Therefore, batteries are more suitable for centenary-free operation as an energy container rather than an energy accumulator for the braking energy recovery. EDLCs are suitable for energy recovery due to the high specific power (approx. 5 … 10 kW/kg [37]) and long cycle life (10^6 cycles [38]). Therefore, the trend now is to combine both technologies.

Flywheels have comparable performance as EDLCs. But EDLCs have degradation problems. According to [37], accepted levels of performance degradation for EDLCs are 100 % resistance growth and 20 … 30 % capacity loss over 10 years and half million cycles, whereas, flywheels usually have a lifetime of 20 years without degradation problems. However, flywheel systems are more complicated and have higher safety risk. Both technologies have pros and cons. As an important aspect for the comparison between these two technologies, an energetic performance evaluation based on the measured driving cycle of a tram is presented in this chapter, which is summarized from the published paper [75]. The evaluation modeling is similar to the system in Chapter 2.

3.1 System Description and Modeling

3.1.1 System Operating Strategy

According to the accelerating and decelerating demand, two operating modes with power flows between each power source and load are defined, as shown in Fig. 3-1. For the consumption mode, the power supplied by FESS has the highest order of priority. If the FESS is fully discharged or the power demand exceeds the maximum power of FESS, the power is provided by the grid. When the tram decelerates, the regenerated energy feeds the FESS in the first priority. When the FESS is fully charged or the generated power exceeds the power limit of the FESS, the excessive energy is fed back to the grid. Here, a feed-in power limit of the grid is defined in order to incorporate the feedback energy of other sources. Therefore, the power above this limit should be consumed by the braking resistor.

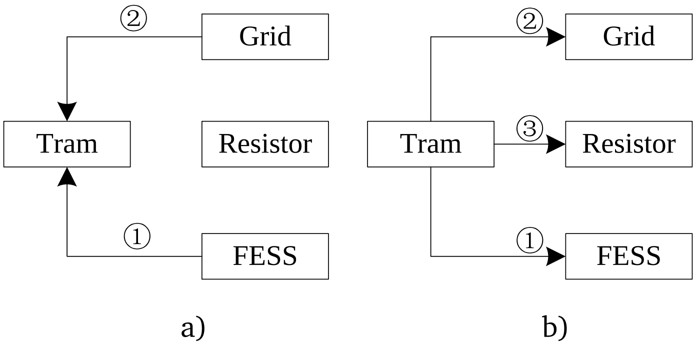

Fig. 3-1 Tram system operating modes: a) consumption mode, b) generation mode. (Numbers show the priority of the power flow from 1 to 3 in decreasing order.)

By defining the output power of the FESS as P_{FW} ($P_{\mathrm{FW}} > 0$ for discharge; $P_{\mathrm{FW}} < 0$ for charge) and the power consumption from the grid as P_{g} ($P_{\mathrm{g}} > 0$ for consumption; $P_{\mathrm{g}} < 0$ for grid feed-in), the system energy balance can be represented by

$$P_{\mathrm{Tram,B}} + P_{\mathrm{res}} = P_{\mathrm{FW}} + P_{\mathrm{g}}, \tag{3-1}$$

where P_{res} is the power consumed by the braking resistor, which is only active ($P_{\mathrm{res}} > 0$) when the power limit of P_{g} is exceeded in generation mode: $P_{\mathrm{g}} < P_{\mathrm{g,max}} < 0$. For other cases, $P_{\mathrm{res}} = 0$. The $P_{\mathrm{Tram,B}}$ is the biased power of the tram, which is the sum of the power of the tram P_{Tram} and the additional power demand P_{e} in FESS (explained in Chapter 3.1.2).

In the simulation, the input data is P_{Tram}. P_{FW} and P_{e} can be determined according to the constraints and the loss calculation introduced in the following section (refer to [77] for detailed descriptions). P_{g} can be calculated by

$$P_{\mathrm{g}} = \max\{P_{\mathrm{Tram,B}} - P_{\mathrm{FW}}, P_{\mathrm{g,max}}\}. \tag{3-2}$$

Then the losses in the resistor can be determined by (3-1).

3.1.2 Flywheel Modeling

1) *SOC* Constraint

We still use the definition of *SOC* in (2-2). But differently, the *SOC* constraint in the tram is

$$SOC_{\mathrm{min}} \le SOC \le 1, \tag{3-3}$$

where

$$SOC_{\mathrm{min}} = E_{\mathrm{min}} / E_{\mathrm{max}}, \tag{3-4}$$

corresponding to the minimum speed of the flywheel, which is half of the maximum speed here. Therefore, $SOC_{\mathrm{min}} = 0.25$.

2) Power Constraint

The same as in Chapter 2, the power of the flywheel follows the constraints in Fig. 3-2, determined by the power limit of the E-machine. The power limit increases linearly as the speed increases and reaches the maximum value at $0.5 \cdot n_{\mathrm{max}}$. During the cycling, an operating speed range of $0.5 \cdot n_{\mathrm{max}} \dots n_{\mathrm{max}}$ is defined, in which the flywheel has a constant power limit.

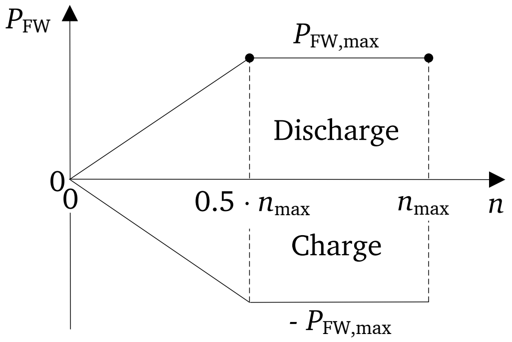

Fig. 3-2 Power constraints of the modeled flywheel system
(P_{FW}: electric power of the flywheel, n: rotational speed)

3) Loss Components

The same as in Chapter 2, the loss components of the flywheel system include the following:

i): The windage loss in vacuum is calculated by an analytical model following (8-19) … (8-22) in Chapter 8.
ii): The losses in the E-machine and inverter are modelled by constant power efficiency: η_{ch} for charge and η_{dch} for discharge.
iii): The power demand of the magnetic bearings and all other auxiliary components (vacuum pump, control system …) is modeled as an additional electrical load P_{e} by (3-5), acting when the flywheel is turning. The additional electrical load P_{e} increases the total power demand of the tram from P_{Tram} to $P_{\mathrm{Tram,B}}$, as shown in (3-6).

$$P_{\mathrm{e}} = \begin{cases} \text{const.} & SOC > 0 \\ 0 & SOC = 0 \end{cases} \tag{3-5}$$

$$P_{\mathrm{Tram,B}} = P_{\mathrm{Tram}} + P_{\mathrm{e}} \tag{3-6}$$

3.1.3 Quantitative Indicators for Evaluation

The main purpose of using an onboard flywheel is to reduce the energy consumption from the grid by accumulating the recovered energy. The overall energy consumption of the tram is defined by

$$E_{\mathrm{Tram}} = \sum \left(P_{\mathrm{g}}^{+} + \eta_{\mathrm{g}} \cdot P_{\mathrm{g}}^{-} \right) \cdot \Delta t \, , \tag{3-7}$$

in which η_{g} denotes the efficiency of grid feed in considering the losses in the overhead lines. The superscript “+” denotes the positive value and “–” the negative value.

The indicator to evaluate the overall energy efficiency of the FESS is

$$\eta = \frac{\sum P_{\mathrm{FW}}^{+} \cdot \Delta t}{\sum \left| P_{\mathrm{FW}}^{-} \right| \cdot \Delta t} . \tag{3-8}$$

3.2 Simulation Results: Case Study

The case study is based on a tramway *Bombardier Variobahn*, operating in the German city *Heidelberg*. The tram consists of 3 traction axis and 1 rolling axis. Each traction axis is driven by 2 induction motors with a rated power of 95 kW for each. Also an EDLC with a capacity of 1 kWh is equipped on each traction axis [40]. The tram has a total length of approx. 40 m and weight of 275 kg. Detailed technical data of the tram can be found in [31].

3.2.1 Tramway Driving Cycle

The driving cycle used for this simulation was measured by the company *Bombardier*, shown in Fig. 3-3. This urban driving lasts for 60 min, in which the tram travels a distance of 17.6 km with a total energy consumption of 50.8 kWh. The instantaneous power consumption is measured with a time resolution of 32 ms. A negative value indicates that the regenerated power is higher than the power demand of the tram.

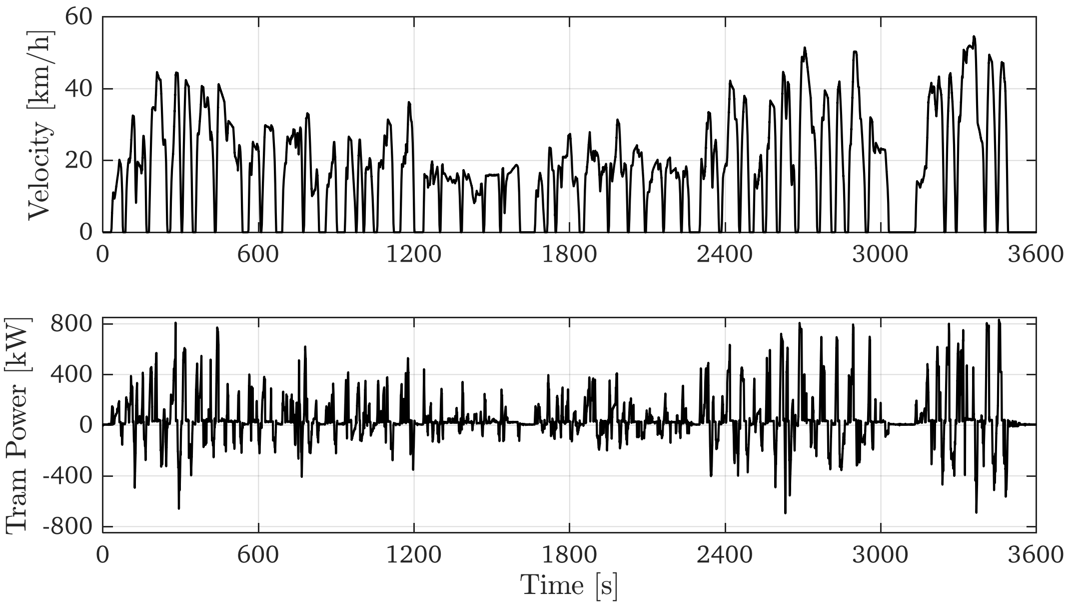

Fig. 3-3 Measured urban driving cycle and power consumption of the tram *Bombardier Variobahn* in *Heidelberg, Germany* [40]

A statistical diagram in Fig. 3-4 shows the energy distribution (kWh/kW) for both consumption and generation at each power level, the integration of which indicates the energy. A dense energy consumption occurs at the power around 30 kW due to the non-traction demand, such as air conditioning, lights and so on. The traction energy is required for the power up to 800 kW. The recovery energy is mostly lower than 500 kW.

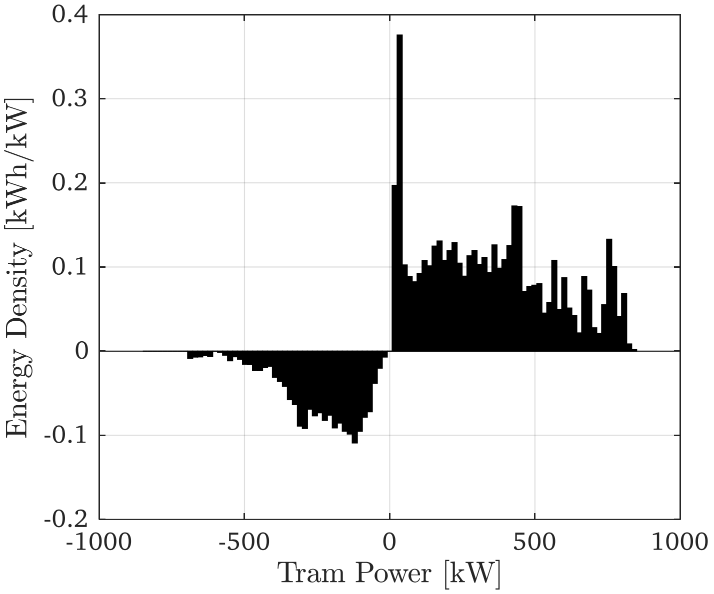

Fig. 3-4 Calculated statistical diagram based on the measured tram power in Fig. 3-3, showing the energy distribution of consumption and regeneration for different power levels

3.2.2 Parameters of the Flywheel and Grid Limits

The investigated flywheel has the parameters shown in Table 3-1. The storage capacity is chosen to be 2 kWh here, and a further analysis for varying capacity is carried out in Chapter 3.2.4. The maximum power is determined to be 500 kW, which covers almost all the regenerative power as shown in Fig. 3-4. The pressure P in the flywheel is chosen to be 0.3 Pa. This value is the typical lower limit of rotary vane pumps. Higher vacuum can be obtained if turbo-molecular pumps are used, which are significantly more expensive. The flywheel rotor body is dimensioned for a construction with carbon fiber reinforced composite material. The power efficiency considers 0.95 for an inverter and 0.95 for a permanent magnet (PM) machine. The auxiliary power demand for the magnetic bearings, vacuum pump and control and cooling systems is difficult to estimate here. A constant value is assumed for the preliminary simulation and the influence will be discussed afterwards in a parametric study.

Table 3-1 Parameters of the flywheel used in the investigated tram system

Parameter	Symbol	Value	Parameter	Symbol	Value
Storage capacity	C	2 kWh	Rotor outer radius	R_o	260 mm
Maximum speed	n_{max}	24000 min^{-1}	Rotor height	h	196 mm
Maximum power	$P_{FW,max}$	500 kW	Power efficiency	η_{ch}/η_{dch}	0.90/0.90
State of charge	$SOC_{min}/$ SOC_{max}	0.25/1	Auxiliary power demand	P_e	1 kW
Air pressure	P	0.3 Pa	Air friction losses	$P_{fr}(n_{max})$	87 W @ 60 °C

Table 3-2 Assumed parameters of the grid for the power feed-in

Parameter	Symbol	Value
Maximum grid feed-in power	$P_{g,max}$	50 kW
Grid feed-in efficiency	η_g	0.72

3.2.3 Simulation Results

Based on the established model and the driving cycle as input data, the simulation was carried out in *Matlab*. The aim of the case study is to investigate the energy saving potential by using a FESS compared to the tram without storage devices.

1) Energy Allocation without Storage Devices

A segment of the full driving cycle is shown in Fig. 3-5 (top). The correlating power is shown by the outline in Fig. 3-5 (bottom), including the consumption power denoted with positive values and regenerative power denoted with negative values. The area under the outline which is filled with different colors demonstrates the energy allocation of the tram. For a tram without storage device, the traction power is completely supplied by the grid (positive blue area). The regenerative energy is fed back to the grid in the first place. Due to the power limit for the feeding back, the excessive energy is consumed by the braking resistor (negative red area).

2) Energy Allocation with a 2 kWh Flywheel

For the same excerpted driving cycle, the energy allocation of the tram with a 2 kWh flywheel is shown in Fig. 3-6. The FESS (green area) has the first priority for both providing the driving power and accumulating the regenerative energy. The power supply from the grid (positive blue area) is required only if the FESS is fully discharged or the power demand exceeds power limit of the FESS. Regarding the regenerative energy, they are used to charge the flywheel in the first place. When the FESS is fully charged or the power exceeds the power limit of the FESS, the excessive energy is fed back to the grid. The resistor (red area) is only active when the grid feed-in power limit is surpassed.

The remaining energy will be consumed in the resistor and dissipated by heat. The *SOC* of the FESS is also presented in Fig. 3-6, in which a charge/discharge cycling period of less than 60 s can be seen.

3) Energy Saving and FESS Energy Efficiency

The total energy consumption of the tram is calculated for the complete driving cycle of 60 min. A comparison can be seen in Table 3-3. As the regenerative energy are accumulated by the storage device and used for the next traction period, the total energy consumption from the grid is reduced from 4.21 kWh/km to 2.94 kWh/km (approx. 30.2 %) if an ideal storage device without any internal losses is used. For a 2 kWh FESS considering the internal losses, the energy consumption of 3.33 kWh/km can be achieved, which is 20.9 % reduced.

The FESS has an overall energy efficiency of 74.8 %, close to the round trip power efficiency of 81 % (calculated by $\eta_{ch} \cdot \eta_{dch}$ in Table 3-1). That indicates that the energy loss due to the idling of the flywheel is small compared to the total converted energy. This is due to the relative short idling period in comparison to the charge/discharge period, which is different with the operating cycle in the residential PV systems in Chapter 2.

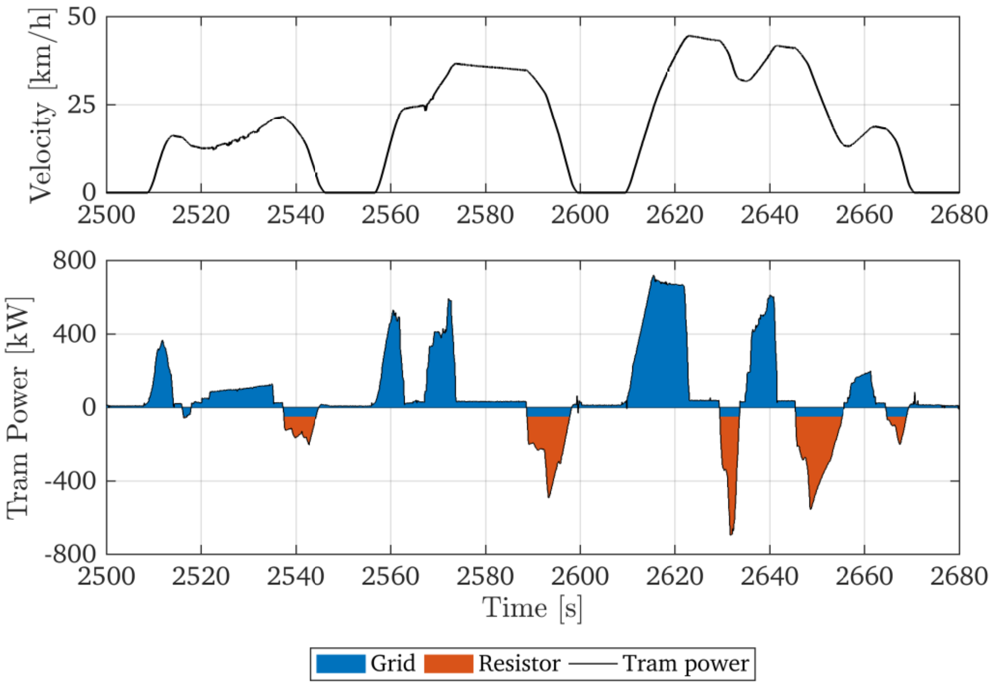

Fig. 3-5 Calculated energy allocation (bottom graph) for the tram without energy storage devices, presented for an excerpt of the complete measured driving cycle in Fig. 3-3

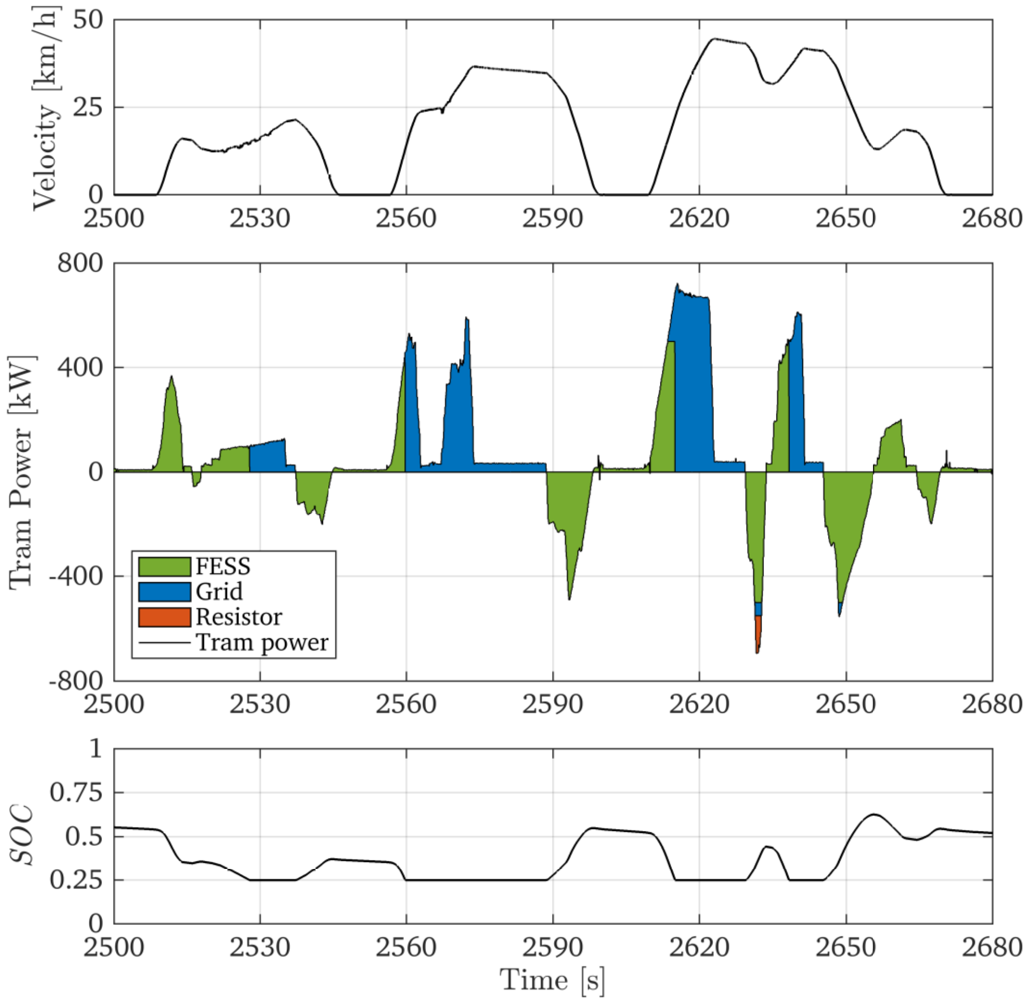

Fig. 3-6 Calculated energy allocation (middle graph) for the tram with a 2 kWh FESS and the calculated *SOC* of the FESS (bottom graph), presented for an excerpt of the complete measured driving cycle in Fig. 3-3

Table 3-3 Calculated energy performance of the tram without storage, with an ideal storage and with a 2 kWh FESS (E_{Tram}: overall tram energy consumption in kWh, s_{Tram}: total traveling distance of 17.6 km)

Parameter	No storage	With a 2 kWh ideal storage	With a 2 kWh FESS
Specific energy consumption $E_{\mathrm{Tram}}/s_{\mathrm{Tram}}$	4.21 kWh/km	2.94 kWh/km	3.33 kWh/km
Energy saving	0 (reference)	30.2 %	20.9 %
Storage energy efficiency η	-	100 %	74.8 %

3.2.4 Sizing of FESS

A parametric study of the FESS capacity C and maximum power $P_{\mathrm{FW,max}}$ is carried out in order to investigate their influence on the specific energy consumption (kWh/km) and the energetic efficiency η of the FESS. The purpose is to find out the optimum specifications of the FESS. Similarly as in Chapter 2, the capacity C is varied by changing the height h of the flywheel rotor. The windage losses will change with h as well. $P_{\mathrm{FW,max}}$ varies independently. The power efficiency of 0.90 and auxiliary power demand of 1 kW are assumed to be constant.

As shown in Fig. 3-7, the specific energy consumption of the tram decreases as the FESS capacity increases up to 1.5 kWh. For higher capacities, further benefits are not available as the total amount of regenerated energy is no higher than 1.5 kWh for each braking period, which can be seen in Fig. 3-6. Power above 500 kW is also not necessary, as the regenerative power is almost no higher than 500 kW as shown in Fig. 3-4. The inflection point on each contour line in Fig. 3-7 indicates the optimum size of the FESS in terms of energy saving. A specific energy consumption of 3.33 kWh/km can be reached by using a FESS with the capacity of 1.5 kWh and power rating of 450 kW. Even though with higher power of 550 kW, a slightly lower specific energy consumption of 3.325 kWh/km can be achieved, the benefit is not considerable compared to the costs for investing 100 kW extra power in a machine. Therefore, a capacity of 1.5 kWh and power rating of 450 kW is regarded as a reasonable size of the FESS for the given cycle.

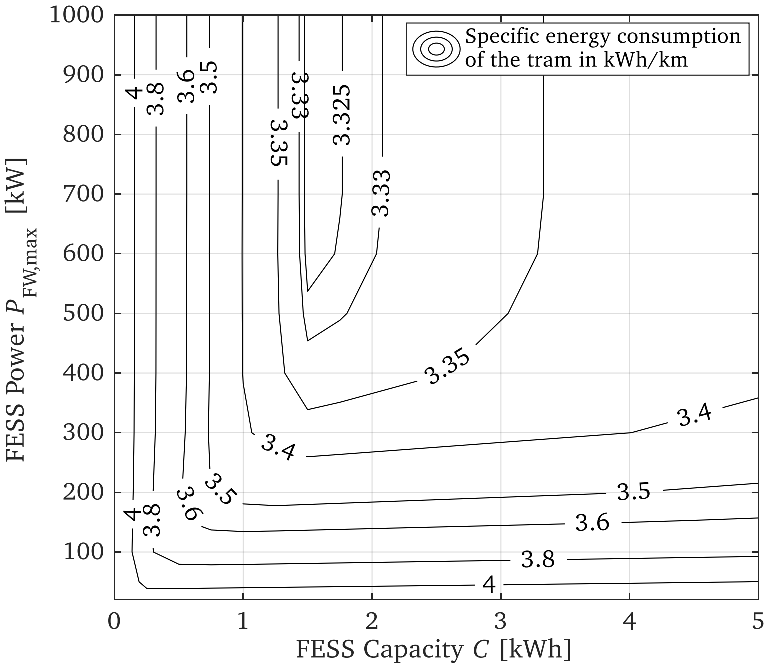

Fig. 3-7 Calculated specific energy consumption (kWh/km) of the tram by using FESS with varied capacities and power levels, based on the investigated driving cycle in Fig. 3-3 (FESS has constant power efficiency $\eta_{\mathrm{ch}} = \eta_{\mathrm{dch}} = 0.9$ and constant auxiliary power demand $P_{\mathrm{e}} = 1$ kW)

The energy efficiency of the FESS is shown in Fig. 3-8. An increased energy efficiency can be achieved for an increased power rating up to 200 kW, as more energy can be accumulated and released with increased power rating. Thus the total energy transfer via charge/discharge of the FESS accounts for a bigger portion compared to the idling losses. For the power higher than 200 W, no further increase of the energy efficiency can be seen, as the high power charging of the FESS leads to a higher degree of *SOC*, which also indicates higher idling losses. For a constant power rating, the energy efficiency slightly decreases with higher FESS capacities due to the higher idling losses of the high capacity FESS. For the chosen optimum size of the FESS with the capacity of 1.5 kWh and power rating of 450 kW, an overall energy efficiency of 75.5 % can be obtained.

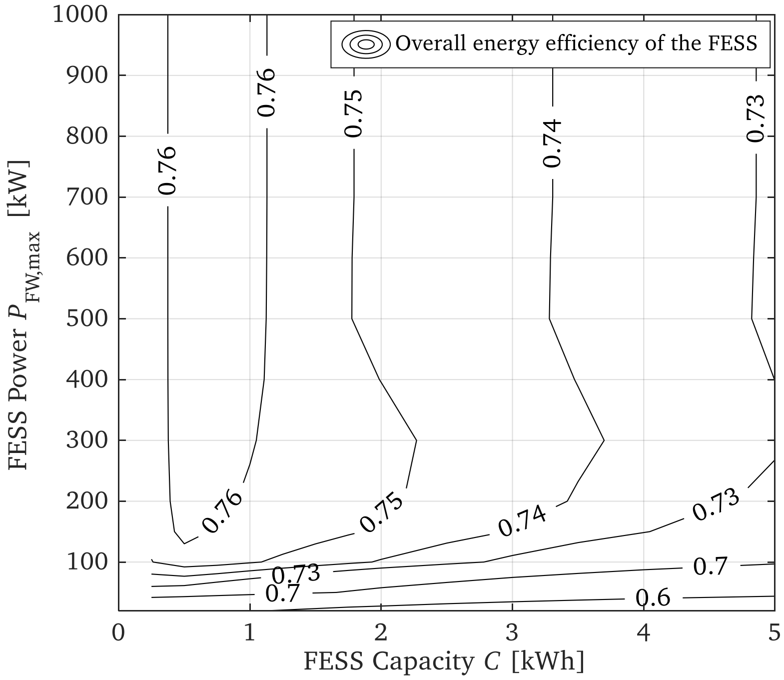

Fig. 3-8 Calculated overall energy efficiency of the FESS for varied capacities and power levels, based on the investigated driving cycle in Fig. 3-3 (FESS has constant power efficiency $\eta_{\mathrm{ch}} = \eta_{\mathrm{dch}} = 0.9$ and constant auxiliary power demand $P_{\mathrm{e}} = 1$ kW)

3.3 Comparison of Flywheel and EDLC

As EDLCs are more widely used as commercial products in the industry, a comparison of a FESS and an EDLC regarding the energetic performance for the same driving cycle is carried out.

The energy stored in an EDLC can be calculated by

$$E = \frac{1}{2} \cdot C_{\mathrm{cap}} \cdot U_{\mathrm{cap}}^2 , \tag{3-9}$$

where C_{cap} is the capacitance of EDLC and U_{cap} is the voltage. For a constant current charging, U_{cap} increases linearly with the charging time, as well as the charging power.

The *SOC* is defined in the same way as (3-4). The minimum *SOC* correlates to the energy when $U_{\mathrm{cap,min}}$ is reached.

$$E_{\mathrm{min}} = \frac{1}{2} \cdot C_{\mathrm{cap}} \cdot U_{\mathrm{cap,min}}^2 \tag{3-10}$$

In this simulation, $SOC_{\mathrm{min}} = 0.25$ is selected and thus the minimum voltage for maximum degree of discharge is $U_{\mathrm{cap,min}} = 0.5 \cdot U_{\mathrm{cap,max}}$.

3.3.1 Parameters of EDLC

Normally EDLCs are composed of a number of capacitor modules which are series or parallel connected. The selected capacitor module which is used in the simulation has the parameters in Table 3-4. The equivalent series resistance (ESR) and leakage current cause internal losses in each capacitor module and also lead to losses when they are series or parallel connected in the EDLCs.

The parameters of the composed EDLC are shown in Table 3-5. The EDLC is composed of 3900 capacitor modules (26 parallel branches with 150 modules in series connection for each branch) in order to reach the power rating of 450 kW even at lowest *SOC* and minimum voltage $U_{\mathrm{cap,min}}$. This power has the same rating as the optimum size of the FESS determined in Chapter 3.2.4 with a capacity of 1.5 kWh. By fulfilling the power rating demand, the storage capacity is, however, oversized to be 2.5 kWh. The internal losses are caused by the ESR and leakage current. The inverter efficiency and the auxiliary power demand for the control and cooling system are also taken into account.

Table 3-4 Parameters of one single capacitor module used in the simulation [42] (ESR: equivalent series resistance, $\Delta\vartheta$: temperature rise)

Parameter	Value	Parameter	Value
Rated voltage	2.7 V	Max. stored energy	0.66 Wh
Max. continuous current ($\Delta\vartheta = 15$ K)	54 A	Max. ESR	0.8 mΩ
Max. continuous current ($\Delta\vartheta = 40$ K)	88 A	Max. leakage current at 25 °C	1.5 mA

Table 3-5 Calculated parameters of the EDLC used in the investigated tram system, composed by 3900 modules given in [42] ($\Delta\vartheta$: temperature rise)

Parameter	Value	Parameter	Value
Storage capacity	2.5 kWh	State of charge (*SOC*)	0.25/1
Max. voltage	400 V	ESR	4.62 mΩ
Rated current ($\Delta\vartheta = 40$ K)	2.3 kA	Leakage current at 25 °C	39 mA
Number of series connected modules	150	Inverter efficiency	0.95 (charge) 0.95 (discharge)
Number of parallel branches	26	Auxiliary power demand	300 W

3.3.2 Simulation Results

By using the same driving cycle and load profile as shown in Fig. 3-3, the simulation results for the selected EDLC are compared with the FESS in Table 3-6. The specific energy consumption by using a 2.5 kWh EDLC is 3.22 kWh/km, which is 23.5 % lower than the tram without storage devices. Compared to a 1.5 kWh FESS with an energy saving potential of 20.9 %, EDLC can achieve slightly higher benefit. Concerning the storage overall energy efficiency, EDLC has 81.0 %, which is also slightly higher than FESS with 75.5 %.

Table 3-6 Calculated energetic performance of the tram with a EDLC and a FESS, based on the driving cycle in Fig. 3-3 (E_{Tram}: overall tram energy consumption in kWh, s_{Tram}: total traveling distance 17.6 km)

Parameter	With storage: 2.5 kWh EDLC	With storage: 1.5 kWh FESS	No storage
Power rating of the storage device	450 kW	450 kW	-
Specific energy consumption $E_{\mathrm{Tram}}/s_{\mathrm{Tram}}$	3.22 kWh/km	3.33 kWh/km	4.21 kWh/km
Energy saving	23.5 %	20.9 %	0 (reference)
Storage energy efficiency η	81.0 %	75.5 %	-

3.4 Influence of Grid Feed-in Power

The simulations above are based on the assumption that the allowed feed-in power of the grid is a constant value of 50 kW with feed-in efficiency of 0.72 considering the losses for the power transmission on the overhead lines. This is a much simplified assumption. In fact, the energy feed-in is only possible when the energy is required by the trains in vicinity. A precise calculation requires a time schedule and monitoring of the traffics, as well as a sophisticated model of the power supply network, which will not be discussed in this dissertation. However, concerning the uncertainty of the grid feed-in power, a simple approach is used here by varying the feed-in power level. The influence can be seen in Fig. 3-9.

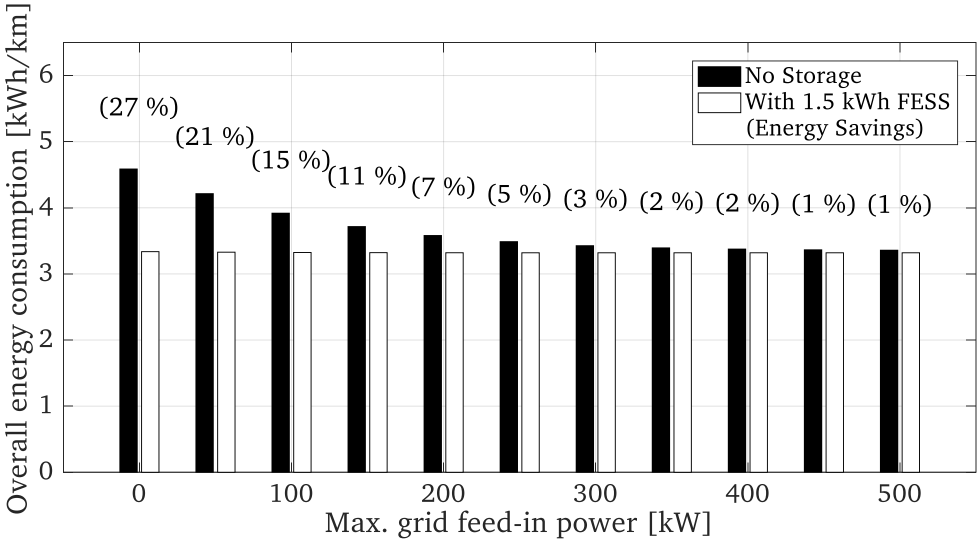

Fig. 3-9 Calculated overall energy consumption of the investigated tram without storage (black color) and with a 1.5 kWh FESS (white color) depending on various grid feed-in power level. The energy savings by using FESS are shown in brackets.

Without storage devices, the energy consumption is 4.6 kWh/km if no power is allowed to be fed into the grid. As the grid feed-in power increases, the energy consumption decreases from 4.6 kWh/km to 3.4 kWh/km for a 300 kW grid feed-in power level. Regarding the tram with FESS, the energy consumption is approx. 3.3 kWh/km, independent of the grid feed-in power. The energy saving (number shown in brackets) by using a FESS is 27 % and decreases for higher grid feed-in levels.

This graph indicates that the benefit of using storage device to accumulate the regenerative braking energy is only achievable if the grid feed-in power is low, or in other words, the probability for the power feeding to the other trains is low. If higher power is allowed to be fed back to the grid, for instance, in a very busy route line, using a storage device can hardly see benefits.

3.5 Summary and Outlook

This chapter analyzes the energetic performance of a tramway (driven by 570 kW nominal power) with an onboard FESS in comparison to an onboard EDLC. The analysis is based on a measured driving cycle and load profile for a traveling distance of 17.6 km in German city *Heidelberg*. Based on the assumption of 50 kW grid feed-in power limit, the simulation results show that, an onboard FESS with the storage capacity of 1.5 kWh and power rating of 450 kW has an energy saving potential of 20.9 % compared to a tram without storage devices, which is slightly lower than a 2.5 kWh onboard EDLC with the value of 23.5 %. Concerning the overall energy efficiency, FESS can reach 75.5 %, also a bit lower than EDLC, which is 81.0 %.

Concerning the energetic performance, FESS and EDLC are in comparable range. However, up to now EDLCs are dominant for the onboard storage in railway vehicles, despite of their degradation problems, while very few FESSs are developed. Two demonstrative vehicles developed so far are a regional train *LIREX* [43] and a *Citadis* tram operated in *Rotterdam* [44]. Both are developed by *Alstom*. FESSs are still meeting challenges concerning the energy density, costs and safety issue. Lighter, safer, more reliable and cost effective flywheels are expected in the future for the use as onboard storage devices.

The analysis in this chapter also gives a hint that, the benefit of onboard storage devices strongly depends on the grid feed-in power level or the probability of feeding the energy to the vehicles in vicinity. The energy saving potential of using onboard storage devices can be hardly seen if large amount of power can be fed to the grid. However, for the catenary-free city railways, the onboard storage devices are still essential.

4. Design Overview of a Flywheel Demonstrator

In order to verify the energetic performance and the implementations of high-speed technologies, a flywheel demonstrator was built in the *Institute for Electrical Energy Conversion, TU Darmstadt, Germany* [78]. This prototype will also be used for the students' experimental practice. The first stage of prototyping is to propose a valid design and technical solutions for the system construction, which will be presented in the following chapters in this thesis, including the component design, system build-up concept and assembly course, as well as the prototype construction.

4.1 Tasks and Design Specifications

The designed components and tasks include:

1) Complete design and validation of the flywheel rotor
2) Complete design of the E-machine
3) Validation of the critical performance: thermal performance, rotor dynamic behavior …
4) Bearing solutions: select magnetic levitation and safety bearing
5) Safety solutions against burst hazard
6) System build-up concept and validation course of assembly

The inverter is designed and provided by the *Institut für Stromrichtertechnik und Antriebsregelung* (SRT), *TU Darmstadt, Germany*. The design specifications are shown in Table 4-1. As the maximum current fed back to the grid is limited to be 50 A (r.m.s.) in the lab, the available rated apparent power is 35 kVA for the grid line-to-line voltage of 400 V (r.m.s.). The DC link voltage of the inverter U_{DC} is 560V. The output line-to-line voltage of the inverter is $U_{\mathrm{AC}} = U_{\mathrm{DC}} / \sqrt{2} = 396\,\mathrm{V}$, which is the maximum terminal voltage of the E-machine. The maximum speed $n_{\max} = 24000\,\mathrm{min}^{-1}$ is determined for this design. Higher speed is not realistic due to the following reasons:

1) Higher speed leads to higher stress in the rotor due to centrifugal force, which is proportional to the square of peripheral velocity $\Omega^2 \cdot r_{\mathrm{o}}^2$ (r_{o}: the outer radius of the flywheel body). Limited by the material strength, r_{o} should be proportionally reduced for

higher speed. While the energy is in proportional to $\Omega^2 \cdot r_o^4 \cdot h$ (*h:* the axial length of the flywheel body) according to (5-5). That means *h* should be quadratic increased in order to obtain the expected energy capacity. A long rotor leads to low rotor bending frequencies, which may cause resonance when rotational speed is close to the rotor bending frequency.

2) The switching frequency of the inverter is 12 kHz. For a higher speed machine, this switching frequency will lead to a low quality modulation. Significant harmonics and thus higher losses may be caused in the electric machine.

The minimum speed for the discharge of the flywheel is designed to be n_{min} = 12000 min^{-1}. This is equal to the values used in most flywheel designs, where 3/4 of the total stored energy is used.

Table 4-1 Design specifications and limitations of the inverter

Parameter	Symbol	Value	Unit
Flywheel			
Energy storage capacity	C_{FW}	0.5	kWh
Rated apparent power	S_{N}	35	kVA
Maximum speed	n_{max}	24000	min^{-1}
Minimum speed	n_{min}	12000	min^{-1}
Inverter			
DC-link voltage	U_{DC}	560	V
Nominal output voltage (r.m.s.)	U_{AC}	396	V
Nominal current (r.m.s.)	I_{N}	50	A
Switching frequency	f_{T}	12	kHz

4.2 System Design Overview

4.2.1 System Configuration

A sketch of the proposed system design with the assembly of the main components is shown in Fig. 4-1 a). The system configuration is determined to be a classical one: A disk-shape steel rotor mass is combined with an E-machine on one common shaft. This configuration has lower energy density compared to the integrated designs, e.g. inner-rotor outer-mass topology and outer-rotor topology. But the construction is relatively simple and therefore adopted in this design.

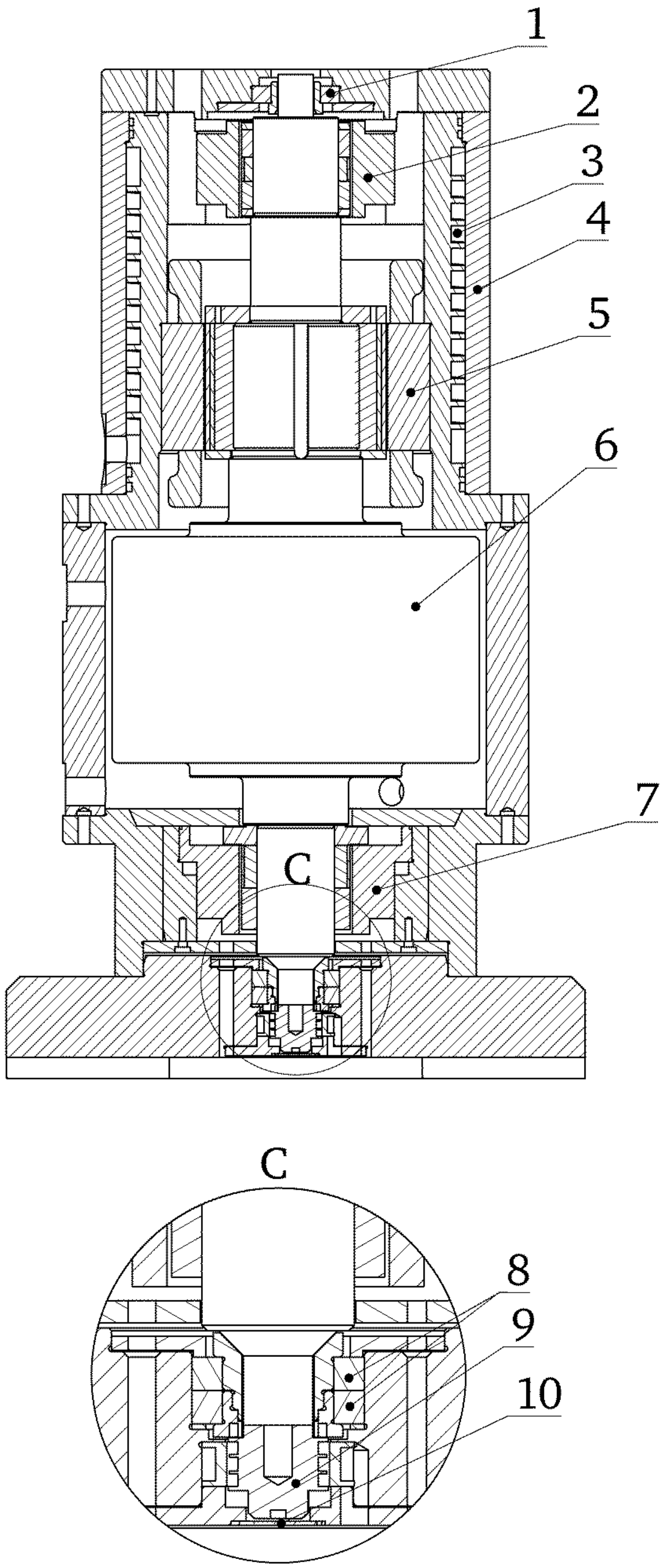

a)

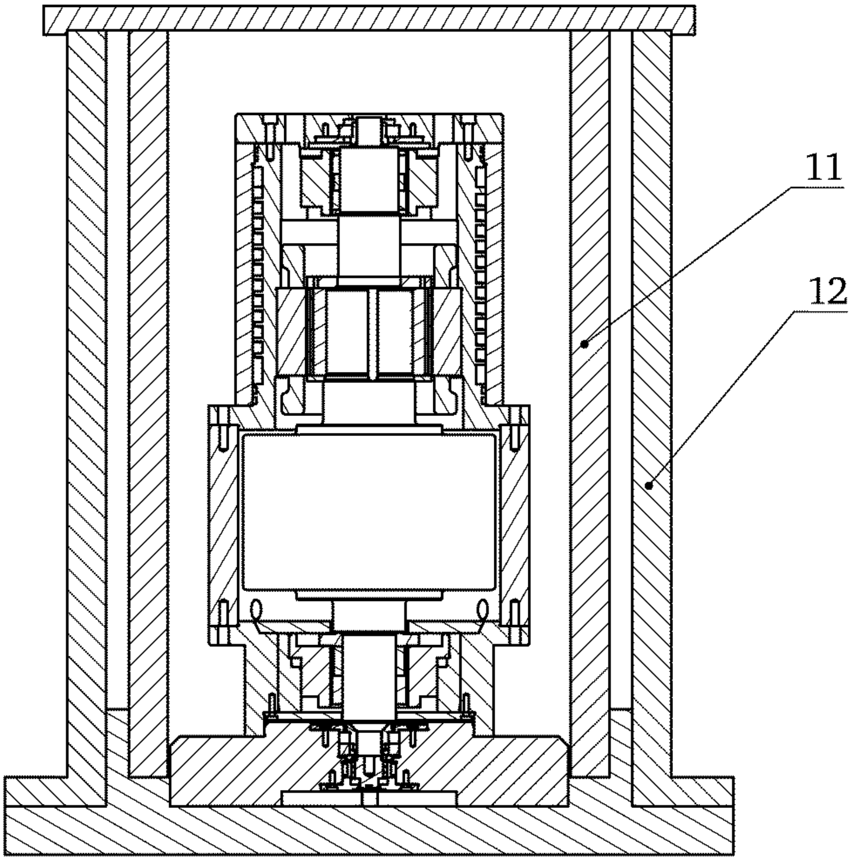

b)

Fig. 4-1 Flywheel assembled system [47] (*Autodesk Inventor 2018*):

a) System without burst containment: 1-safety bearing (top), 2-radial magnetic bearing, 3-water cooling channel, 4-housing, 5-E-machine stator, 6-flywheel rotor, 7-combined magnetic bearing, 8-safety bearing (bottom), 9-axial position sensor (rotor part), 10-revolusion sensor (stator part); b) System with burst containment: 11-inner containment, 12-outer containment & vacuum chamber

A vertical arranged system can be seen in Fig. 4-1 a). On each side of the shaft one magnetic bearing is placed for levitation. The radial magnetic bearing is placed on the top, which produces the levitation forces only in radial direction. The combined magnetic bearing on the bottom produces forces in both radial and axial direction and has to lift the total weight of the flywheel rotor. A back-up ball bearing is applied on each end of the shaft. In case of emergency when the failure of magnetic levitation occurs, they have to carry the complete flywheel rotor.

The disk-shaped flywheel body and the shaft are made to be one piece. If they are separately manufactured, the assembly will be problematic. It is not a good solution to drill a central hole in the disk and assemble on the shaft. This causes at least twice additional local stress near the hole area due to the centrifugal force [1]. Another possibility is to manufacture the flywheel body into a solid piece without central hole, and assemble two shafts on both sides with the help of bolts or by shrinking fit, but the local stress near these connection areas will be problematic under the load of high speed rotation, thermal expansion or vibrations, which should be carefully treated. Additionally, the dynamic behavior of the rotor would be also critical, as the bolts or fitting connection may result in a lower stiffness of the rotor, which lowers the critical speeds. Resonance occurs if the critical speed is in the operating speed range of the rotor, which may leads to damage on these "weak" connection parts due to the strong vibration. Besides, the rotating axis the flywheel body and the shaft should be aligned as precisely as possible, avoiding the unbalanced force. The precise alignment is difficult to be realized. Considering all these difficulties of the assembly solutions, a simple and robust design is to manufacture the flywheel body and the shaft into one piece. Thus the local effects are avoided and high rotor stiffness can be achieved.

For the stator side, water cooling is adopted for the E-machine and top magnetic bearing. The housing has 3 segmented pieces, and the function is to fix and correctly position all the components. As the high speed rotating rotor contains a considerable amount of energy, for safety concern in case of burst failure, two extra containments are used to enclose the system (Fig. 4-1 b)). The outer one is sealed and also serves as a vacuum chamber.

4.2.2 Critical Considerations

The following basic considerations are critical for the chosen flywheel design:

1) Rotor mechanical issue

The rotor mechanical issue concerns the following aspects:

- The dimensioning of the flywheel body to fulfill the inertia requirement
- The stress calculation in the rotor caused by the centrifugal force
- The assemble of the rotor components with correct fittings
- The balancing solutions
- The material hardening process in order to obtain high strength material
- The eigen-frequency analysis, avoiding resonance during rotation

2) System efficiency and losses

As an energy storage device, a high efficiency is always expected. Typically a round-trip efficiency is 85 … 95 %. As most losses occur in the E-machine, a high efficiency machine is required. Meanwhile, low stand-by losses are also required to reduce the self-discharge of the flywheel. Therefore, the losses in the magnetic bearings and friction losses are also critical. Another critical aspect is that, the losses in the rotor should be small, avoiding overheating due to the bad cooling condition in vacuum.

3) Thermal performance

One typical problem of the flywheel is the heat dissipation of the rotor in vacuum, relying mainly on the radiation. In order to achieve high power density and efficiency, a permanent magnet (PM) machine with surface mounted magnets is often used as the energy converter. The magnets are glued on the surface of the rotor iron and fixed by a prefabricated sleeve or bandage on the outer surface as a protection against the centrifugal force. Carbon fiber bandages are often used due to their high material strength. However, the material property of the carbon fiber bandages will be changed if the operating temperature is too high, leading to mechanical failure. The thermal performance of the rotor should be analyzed and the losses in the rotor components should be as small as possible to avoid overheating.

4) Safety concern

The safety issue of a high speed rotation system should always have the first priority. Especially for a flywheel system, where a considerable amount of energy is contained in a high speed rotating body. When sudden emergency occurs, the system should be able to dissipate the stored energy in a short time. Potential dangers include but not limited to: steel rotor burst, magnetic bearings out of control, voltage outage, inverter failure, short circuit …

4.2.3 Design Workflow

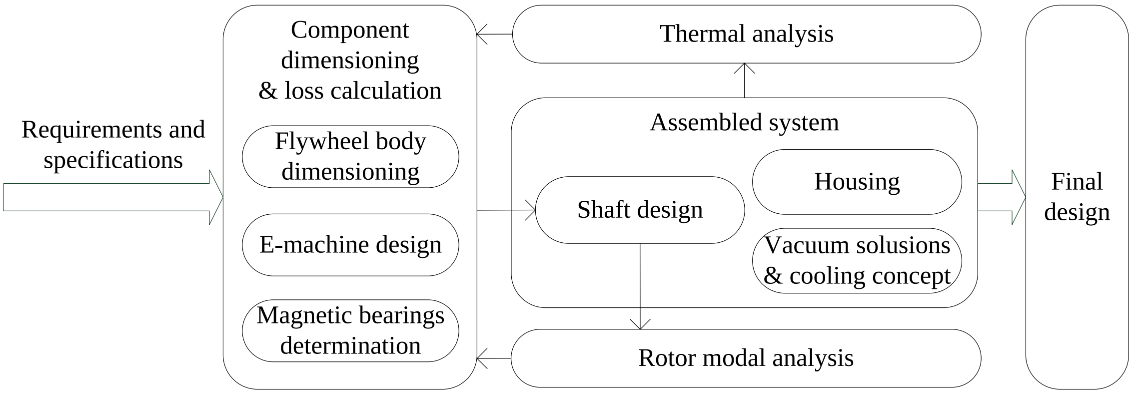

Fig. 4-2 Design workflow of the system

Fig. 4-2 shows a workflow chart for the system design. According to the given requirements (Table 4-1) and the proposed configuration in Fig. 4-1, the design starts from the component dimensioning and the loss calculations, including the flywheel body, E-machine and magnetic bearings. After they are determined, a shaft is designed to combine the rotor components. The rotor modal analysis is conducted to ensure the 1st bending frequency is far from the maximum speed of the rotor so that the rotor operates in the rigid body mode. If not, an iterative design should be done by re-dimensioning the rotor components. After obtaining the rotor structure, an assembled system will be carried out based on the housing design which considers the cooling and vacuum solutions. Finally, the thermal calculation of the system is carried out. If the overheat occurs, the losses in the components should be reduced. After the iterations, the final design is achieved.

5. Mechanical Design of the Flywheel Rotor

A preview of the designed flywheel rotor is depicted in Fig. 5-1. A flywheel body (Part 4) with big diameter is used for energy storage. A shaft with smaller diameter is designed to mount the rotor components of the E-machine (Part 5 … 9) and magnetic bearings (Part 1 … 3 and 10). The flywheel body and the shaft are designed to be one piece. The E-machine is a permanent magnet synchronous machine (PMSM) with the magnets (Part 7) mounted on the surface of a laminated rotor iron package (Part 8). The magnets are fixed and protected by a carbon fiber bandage (Part 6) on the outer surface. To fix the components 6 … 8 in axial direction, two end plates (Par 5 and 9) are used. The dimensions and fittings of the E-machine components 6 … 8 is presented in Chapter 6.5. The radial magnetic bearing produces levitation force in radial direction. The rotor iron (Part 10) is laminated in order to reduce losses. The rotor iron (Part 2) of the combined magnetic bearing is also laminated. It is used to produce radial force. The axial force is produced by using a solid steel rotor disk (Part 3). A position sensor (Part 1) is used for the axial position control of the combined magnetic bearing. The detailed configurations of the magnetic bearings are introduced in Chapter 7.

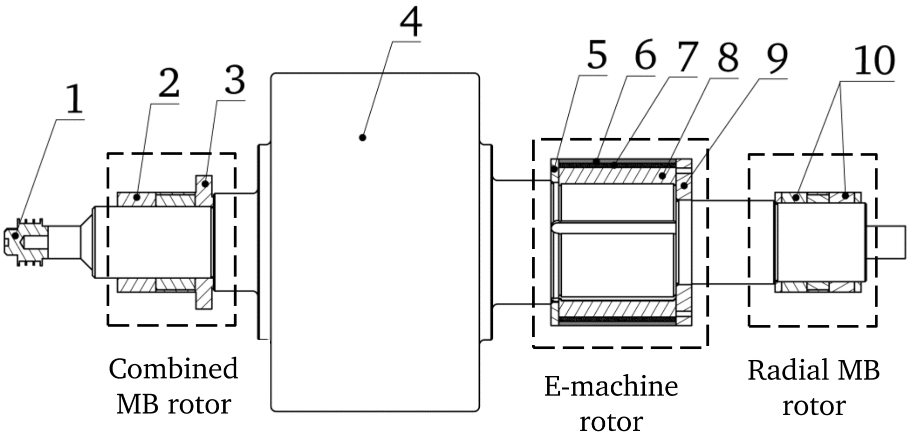

Fig. 5-1 Flywheel rotor components:

1-axial position sensor, 2-laminated rotor iron of combined MB, 3-axial disk of combined MB, 4-flywheel body, 5-E-machine end plate A, 6-E-machine bandage, 7-E-machine magnets, 8-E-machine laminated rotor iron, 9-E-machine end plate B, 10-laminated rotor iron of radial MB (MB: magnetic bearing)

This chapter deals with the mechanical design of the rotor, including the following aspects:

1) Dimensioning of the flywheel body

The dimensions of the flywheel body should not only fulfill the inertia requirement for energy storage, but also take the material strength into account, as tremendous stress will be caused due to high rotational velocity. For a solid disk (without central hole) with an outer radius of r_o and a constant height of h, the inertia $J \propto \rho \cdot r_o^4 \cdot h$ (ρ: material density) according to (5-4). The maximum equivalent stress due to the centrifugal force in the body is $\sigma_{\text{Mises,max}} \propto \rho \cdot \Omega^2 \cdot r_o^2$ according to (5-9). Basically, if the material strength is known, the maximum outer radius r_o can be calculated for a certain speed Ω. Then the height h can be calculated for this radius r_o in order to obtain the required inertia J. Quantitative calculations can be seen in Chapter 5.1.

2) Modal analysis of the rotor

In order to avoid resonance when the rotational speed coincides with the natural frequency of the rotor-bearing system, the rotor should operate in the subcritical range, i.e. the operating speed stays at least 70 % lower than the first critical speed. However, the arrangement of the rotor components given in Fig. 5-1 requires a relatively long shaft, which may lower the bending frequency. Therefore, the rotor modal analysis is important and carried out in Chapter 5.2.

3) Rotor balancing solutions

The rotor is balanced by adding or reducing some additional weights to compensate the eccentricity after manufacture. In our design, screw holes are drilled on the rotor in order to fix some bolts as additional weights for balancing. The detailed solutions are introduced in Chapter 5.3.

4) Rotor hardening process

A hardening process of the steel rotor was performed to achieve high material strength. However, a manufacture failure occurs due to the big local thermal stress. Therefore, the influence of the rotor structure on the hardening process is discussed in Chapter 5.4.

5.1 Flywheel Body Design

5.1.1 Flywheel Energy Capacity

As (1-1) shows, the kinetic energy stored in a flywheel with the rotational speed Ω (in rad/s) can be calculated by

$$E = \frac{1}{2} \cdot J \cdot \Omega^2 \,. \tag{5-1}$$

The flywheel body used in our system is a solid disk (without a central hole) with a constant height h. With the outer radius r_o, the inertia J is calculated by

$$J = \frac{1}{2} \cdot m_\mathrm{FW} \cdot r_\mathrm{o}^2 \,, \tag{5-2}$$

where m_FW is the mass of the disk, with

$$m_\mathrm{FW} = \rho \cdot \pi \cdot r_\mathrm{o}^2 \cdot h \,, \tag{5-3}$$

where ρ is the mass density of the material.
By substituting (5-3) into (5-2), the inertia can be written as

$$J = \frac{\pi}{2} \cdot \rho \cdot r_\mathrm{o}^4 \cdot h \,. \tag{5-4}$$

By substituting (5-4) into (5-1), the energy can be written as

$$E = \frac{\pi}{4} \cdot \rho \cdot \Omega^2 \cdot r_\mathrm{o}^4 \cdot h \,. \tag{5-5}$$

(5-4) indicates that a big radius disk is preferred as the inertia increases with the radius with the power of 4. A small radius may lead to a big height, which is not preferred considering rotor dynamic behavior. However, increasing radius causes higher stress in the body due to rotation.

5.1.2 Stress in a Rotating Disk

The stress due to rotation is the restriction for the dimensioning of the flywheel body. Other influences, such as torque, gyroscopic moment are negligible small and have nearly no influence on the body structure.
The stress in a rotating cylinder can be analyzed in a 2D circular plane which is perpendicular to the rotating axis. The analysis is based on two assumptions: plane stress and plane strain. The former one assumes the normal stress on this plane is zero. It is assumed for a very thin disk and is adequate enough if the thickness of the disk is small compared to the diameter. Plane strain assumes the normal stain on this plane is zero. It is correct for an infinite long cylinder and also can approximate the stress in the mid-plane of a very thick disk. The deviation of these two assumptions is about 3 % for isotropic materials [1].

Since the dimensions of the disk are not well known in the beginning of the design, a thin disk is assumed at first and the assumption of plane stress is used. The stress field of a disk is a function of one-dimensional parameter: the radius *r*. For a disk without a central hole, the stresses in radial direction σ_r and circumferential direction σ_θ due to rotation are given by [1]

$$\sigma_\mathrm{r} = \rho \cdot \Omega^2 \cdot r_\mathrm{o}^2 \cdot \frac{3+\nu}{8} \cdot \left(1 - \frac{r^2}{r_\mathrm{o}^2}\right), \tag{5-6}$$

$$\sigma_\theta = \rho \cdot \Omega^2 \cdot r_\mathrm{o}^2 \cdot \frac{3+\nu}{8} \cdot \left(1 - \frac{1+3\cdot\nu}{3+\nu} \cdot \frac{r^2}{r_\mathrm{o}^2}\right), \tag{5-7}$$

where ρ and ν are the density and *Poisson*'s ratio of the material.

In Fig. 5-2 the per unit stress $\sigma / (\rho \cdot \Omega^2 \cdot r_\mathrm{o}^2)$ are plotted with respect to the per unit radius r/r_o. This specific stress distribution is independent of speed and outer radius. The maximum stress occurs in the center of the disk ($r = 0$) for both directions which can be calculated by (5-8). An equivalent stress, named *von Mises* stress, can be calculated by (5-11) to consider the composed effect from both directions. The maximum equivalent stress also occurs in the center of the disk, calculated by (5-9).

$$\sigma_\mathrm{r,max} = \sigma_\mathrm{\theta,max} = \rho \cdot \Omega^2 \cdot r_\mathrm{o}^2 \cdot \frac{3+\nu}{8} \tag{5-8}$$

$$\sigma_\mathrm{Mises,max} = \rho \cdot \Omega^2 \cdot r_\mathrm{o}^2 \cdot \frac{3+\nu}{8} \tag{5-9}$$

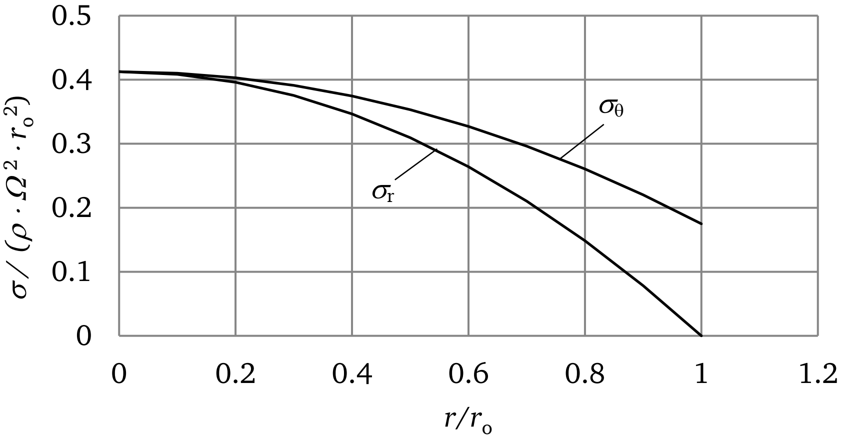

Fig. 5-2 Specific stress distribution $\sigma / (\rho \cdot \Omega^2 \cdot r_\mathrm{o}^2)$ vs. per unit radius r/r_o in a rotational constant height disk without a central hole, ρ: density, Ω: rotational speed, r_o: outer radius of the disk, σ_r: in radial direction, σ_θ: in tangential direction

5.1.3 Material Failure Criteria

For an isotropic material, the *von Mises* yield criterion is used as the failure criteria. The equivalent stress is

$$\sigma_{\mathrm{Mises}} = \sqrt{\frac{1}{2} \cdot \left[(\sigma_{11} - \sigma_{22})^2 + (\sigma_{22} - \sigma_{33})^2 + (\sigma_{33} - \sigma_{11})^2 + 6 \cdot \left(\tau_{12}^2 + \tau_{23}^2 + \tau_{31}^2 \right) \right]}, \tag{5-10}$$

where σ_{11}, σ_{22}, σ_{33} are the normal stresses and τ_{12}, τ_{23}, τ_{31} are shear stresses. They can be replaced by r, θ, z if the cylindrical coordinate system is applied.

The calculated flywheel body design has a constant height, which can be considered as axisymmetric in cylindrical coordinate system and the effects of small irregularities, such as holes for rotor balancing, etc. are neglected. Based on the plane stress assumption, the stress $\sigma_z = 0$ and the shear stress $\tau_{\mathrm{r\theta}} = \tau_{\mathrm{\theta z}} = \tau_{\mathrm{zr}} = 0$. The normal stresses are equal to the principle stresses. The equivalent stress can be written as

$$\sigma_{\mathrm{Mises}} = \sqrt{\sigma_{\mathrm{r}}^2 - \sigma_{\mathrm{r}} \cdot \sigma_{\mathrm{\theta}} + \sigma_{\mathrm{\theta}}^2}\,. \tag{5-11}$$

To avoid yielding of the material, the maximum *von Mises* stress $\sigma_{\mathrm{Mises,max}}$ in the flywheel body should be within a permitted value, which is determined by the material yield strength $R_{\mathrm{p0.2}}$ and the safety factor k_{sf} (>1)

$$\sigma_{\mathrm{Mises,max}} \le R_{\mathrm{p\,0.2}} / k_{\mathrm{sf}}\,. \tag{5-12}$$

As the failure of the flywheel rotors is destructive and usually not predictable, a high design margin should be reserved. A safety factor of 2 is recommended, with respect to the stress at maximum available operating speed in a qualification test. Namely, the rotor should operate no higher than 70 % of the speed attained in the qualification test. Assuming the mechanical failure happens when the material gets yield at the maximum over-speed, retaining a safety factor $k_{\mathrm{sf}} = 2$ indicates the stress at the nominal speed is half of the material yield strength. Thus at 40 % of over-speed, the material gets yield.

5.1.4 Flywheel Body Dimensioning

According to (5-6), (5-7) and (5-11), the maximum *von Mises* stress $\sigma_{\mathrm{Mises,max}}$ in a thin disk versus outer radius r_{o} can be plotted in Fig. 5-3 for the rotational speed 24000 min^{-1}. According to (5-5), to obtain a fixed amount of energy storage, the required height h can be calculated for varying outer radius r_{o}, and plotted also in Fig. 5-3 for the energy amount of 0.5 kWh. The maximum stress $\sigma_{\mathrm{Mises,max}}$ increases in proportional to r_{o}^{2}, while the required height h decreases in proportional to r_{o}^{-4}.

The solid lines in Fig. 5-3 are independent of material strength. If the material strength is known, the permitted $\sigma_{\mathrm{Mises,max}}$ in the body can be calculated by (5-12) and used as a limit in Fig. 5-3 to determine the maximum allowed outer radius $r_{\mathrm{o,max}}$. By using $r_{\mathrm{o,max}}$, the required height h can be determined on the other curve. This process is shown by dashed lines in Fig. 5-3.

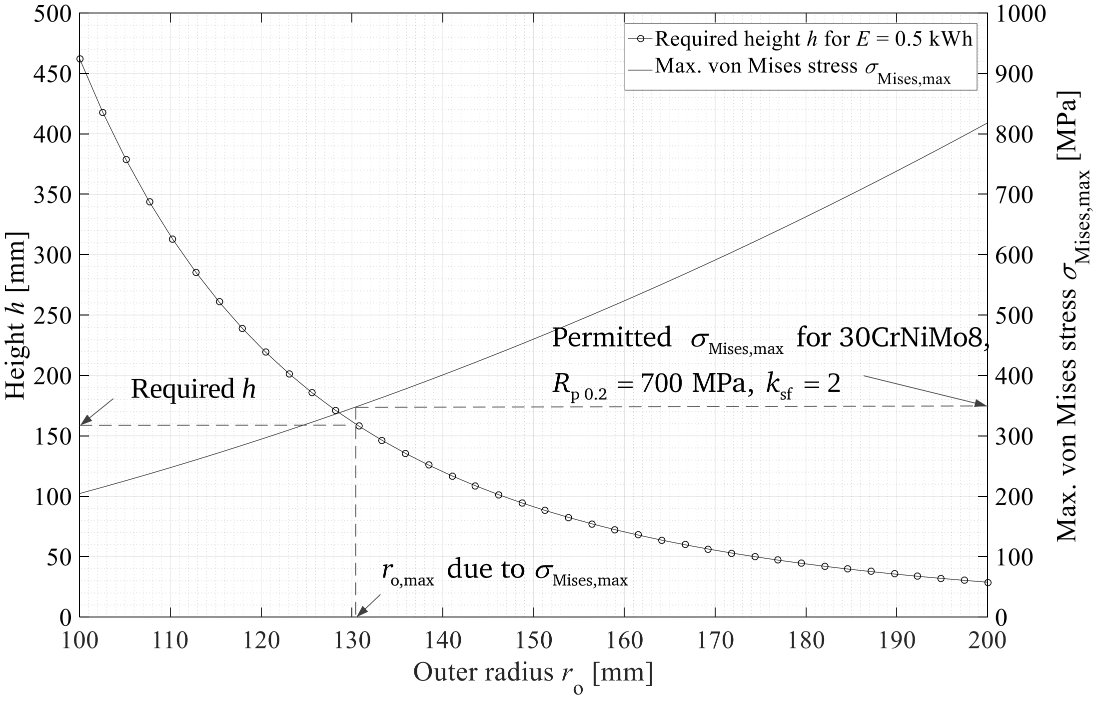

Fig. 5-3 Calculated dimensions and maximum equivalent stress $\sigma_{\mathrm{Mises,max}}$ of the rotating disk at $n_{\mathrm{max}} = 24000\ \mathrm{min}^{-1}$ to obtain the energy of $E = 0.5$ kWh for a body temperature of 20 °C (Dashed line: an example to determine the dimensions of the disk with the material 30CrNiMo8 according to (5-12), (5-9), (5-5))

Table 5-1 Calculated flywheel body dimensions determined from Fig. 5-3

Material	42CrMo4	30CrNiMo8
Yield strength $R_{\mathrm{p0.2}}$ [MPa]	551 (tested) 500 (standard)	700 (standard)
Safety factor k_{sf} (>1)	2	2
Permitted stress in flywheel body $R_{\mathrm{p0.2}}/k_{\mathrm{sf}}$ [MPa]	275.5	350
Flywheel body outer radius $r_{\mathrm{o,max}}$ [mm]	116.5	130
Flywheel body diameter $D = 2 \cdot r_{\mathrm{o,max}}$ [mm]	233	260
Flywheel body height h [mm]	253	160
Flywheel body mass m_{FW} [kg]	83.3	65.9
Specific energy E/m_{FW} [Wh/kg]	6.0	7.6

As calculation examples, two rotors are designed in Table 5-1 by using material 42CrMo4 and 30CrNiMo8 respectively. Their material strengths are shown in Table 5-2. A safety factor $k_{sf} = 2$ is used for both rotors. The material yield strengths are standardized values given by the manufactures [45, 46]. However, according to our testing for the material 42CrMo4 (explained in details in Chapter 5.1.6), the tested value (551 MPa) is higher than the standardized one (500 MPa). Thus the tested value is used for calculation. No strength testing was carried out for 30CrNiMo8, therefore, the yield strength given in the datasheet is used. By using Fig. 5-3 and the design method described above, the corresponding dimensions can be determined, shown in Table 5-1. A total mass of 65.9 kg is calculated for the rotor with 30CrNiMo8, which is 21 % lower than the design with 42CrMo4. Therefore, 30CrNiMo8 is used in the final design.

5.1.5 Influence of the Hardening Process on the Material Strength

As shown in Table 5-1, high strength material is preferred in order to increase the specific energy of the flywheel. The strengths of two optional materials: 42CrMo4 and 30CrNiMo8 are shown in Table 5-2. For steel materials, a hardening process (e.g. quenching process) is usually performed in order to obtain a high strength. The alloy will be firstly heated over the austenitic temperature A_{c3} as shown in Fig. 5-4. At that temperature ferrite will be completely transformed and converted into austenite [45]. Then it will be rapidly cooled in the coolant (e.g. water, oil, salt bath) in order to obtain the martensitic structure, which has high strength. If the cooling rate is too slow, it tends to build a mixture of bainite, ferrite and pearlite, which are weaker in terms of mechanical strength compared to martensite. The proportion of different phases depends strongly on the cooling rate. Fig. 5-4 shows the time-temperature-transformation (TTT) diagram of the material 42CrMo4 and illustrates how different microstructure will be developed due to different cooling rates, which determines different grades of hardness. For example, if the cooling temperature of the alloy follows curve 1) in Fig. 5-4, then in the end of the quenching process, one can obtain a mixture of 5 % bainite and 95 % of martensite. The resulting hardness is 566 Vickers. However, if the cooling is too slow, following curve 2) in the graph, then no martensite will be formed. Instead, a mixture of 3 % ferrite, 5 % pearlite and 92 % bainite will be obtained. The hardness is 286 Vickers, which is much lower. Usually the hardness corresponds to the material strength. A low hardness indicates a low strength.

Table 5-2 Mechanical strength of steel 42CrMo4 and 30CrNiMo8 [45, 46]

Diameter d [mm]	Yield strength $R_{p0.2}$ [MPa]	Ultimate strength R_m [MPa]	Elongation at fracture A_5 [%]	Section area shrinking Z [%]
42CrMo4				
$d \leq 16$	≥ 900	1100 - 1300	≥ 10	≥ 40
$16 < d \leq 40$	≥ 700	1000 - 1200	≥ 11	≥ 45
$40 < d \leq 100$	≥ 650	900 - 1100	≥ 12	≥ 50
$100 < d \leq 160$	≥ 550	800 - 950	≥ 13	≥ 50
$160 < d \leq 250$	≥ 500	750 - 900	≥ 14	≥ 55
30CrNiMo8				
$d \leq 16$	≥ 1050	1250 - 1450	≥ 9	≥ 40
$16 < d \leq 40$	≥ 1050	1250 - 1450	≥ 9	≥ 40
$40 < d \leq 100$	≥ 900	1100 - 1300	≥ 10	≥ 45
$100 < d \leq 160$	≥ 800	1000 - 1200	≥ 11	≥ 50
$160 < d \leq 250$	≥ 700	900 - 1100	≥ 12	≥ 50

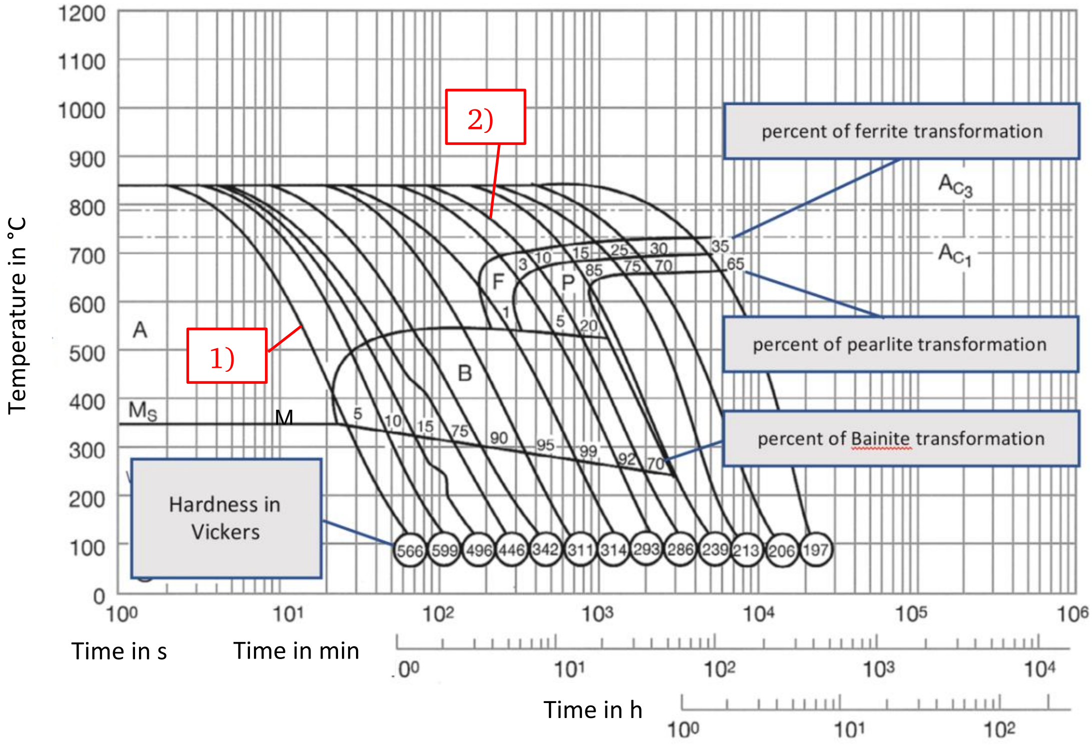

Fig. 5-4 Time-temperature-transformation diagram of the material 42CrMo4 [45, 80]

(A: austenite, F: ferrite, B: bainite, P: pearlite, M: martensite, M_s: martensite starting temperature, A_{c1}: lower transformation temperature, A_{c3}: upper transformation temperature)

The physical mechanism of this phase transition of steel is briefly introduced here. When the temperature is above A_{c3}, the phase is completely transformed to austenite. Austenite is γ-Fe (gamma-phase iron) with a face-centered cubic (FCC) crystal structure, which is open for the solution and diffusion of the carbon atoms, forming a homogenous distribution within the crystals of the iron. When temperature drops, the crystal structure of austenite changes to α-Fe, characterized by a body-centered cubic (BCC) structure and is insoluble for carbon atoms. The carbon atoms will migrate out of the crystals and group together at the interface between two grains, called the grain-boundaries. This forms two or more phases, for instance, with a laminated structure, which is softer compared to martensite. With a high cooling rate, the crystal structure of the iron atoms changes in a very short time, the carbon atoms are not able to diffuse and are trapped in the crystals, forming martensite structure with a high hardness and strength. Therefore, a high cooling rate is usually preferred to obtain a high strength.

The body volume and the geometry of the workpiece will influence the cooling rate. The core of the full body normally has a lower cooling rate than the surface. As shown in Fig. 5-1, the flywheel body is designed to be a constant thickness disk, in which the strength in the core of the disk is critical, as the maximum stress caused by the load of centrifugal force occurs in the center. However, due to the lowest cooling rate, the core center always has the lowest strength compared to the outer surface of the disk.

In order to investigate the cooling rate for different rotor geometries (Fig. 5-5 a)), a transient thermal calculation was carried out in *ANSYS*. Rotor I has a diameter $D = 260\,\mathrm{mm}$ and a length $h = 160\,\mathrm{mm}$, which are the dimensions of the designed flywheel body in Fig. 5-1. Rotor II is a flywheel body combined with a shaft. The total length is 670 mm. Rotor III has the same diameter with Rotor I and the same length with Rotor II. The rotors have an initial temperature of 850 °C and an ambient temperature of 180 °C corresponding to the temperature of the salt bath for quenching. A heat transfer coefficient of 800 W/(m^2· K) and a radiative emissivity of 0.79 are applied on the body surface as boundary conditions.

The cooling rates at the cores of different rotor geometries are compared in Fig. 5-5 b). Rotor I and Rotor II are faster cooled than Rotor III. The strength given in the standard is valid for a long rod, corresponding to Rotor III. Unlike the case in the standards, the axial length of the flywheel body is relatively small. The two end section surfaces can effectively improve the cooling rate of the center mass in the disk. Therefore, a higher strength of the center mass can be expected.

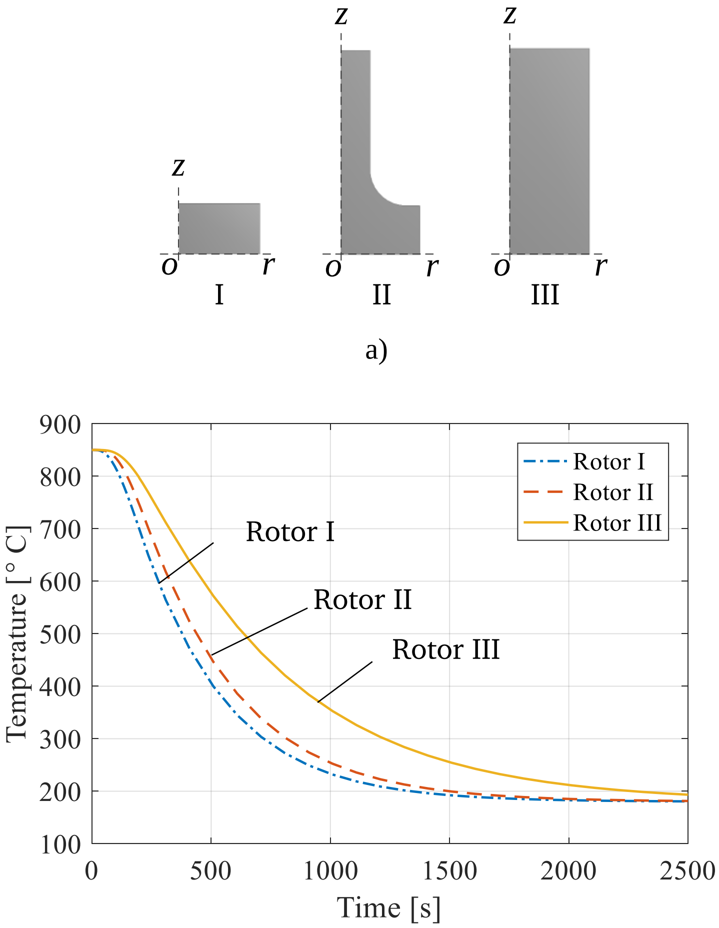

a)

b)

Fig. 5-5 Temperature calculations at the cores of different rotors:

a) calculated rotor geometries: Rotor I … III (axisymmetric by axis *o-z*, symmetric by axis *o-r*), b) calculated temperatures vs. time at the core of different rotors from a), calculated in *ANSYS* for an initial temperature 850 °C, cooled in a salt bath with a temperature of 180 °C

5.1.6 Strength Testing of Sampling Piece

The testing of the material strength is usually performed with a destructive method. To investigate the material strength after the hardening process, a sampling piece is produced and taken under test. The sampling flywheel body is a solid cylindrical disk with an outer diameter of 260 mm and an axial length of 170 mm. The material is 42CrMo4. After hardening, the sampling piece is cut into 3 pieces shown in Fig. 5-6 a). The middle piece III is further cut into 5 pieces shown in Fig. 5-6 b) and only the center piece is taken to perform the tensile testing, as the minimum tensile strength occurs in the center of the body. The testing was carried out by the *Staatliche Materialprüfungsanstalt, Darmstadt* according to the standard *DIN EN ISO 6507-1 edition 2014-06*. The tensile testing results are shown in Table 5-3. The yield tensile strength is $R_{p0.2} = 551$ MPa, which is about 10 % higher than the expected standard value given in Table 5-2. This value is used for the dimensioning of the flywheel body.

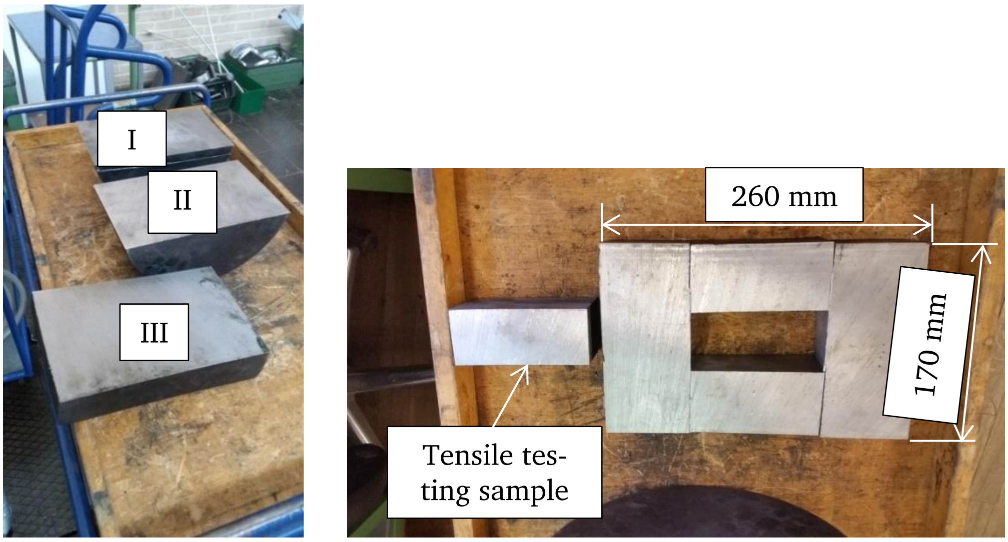

a) b)

Fig. 5-6 Preparation of the testing sample of the flywheel body for strength testing after hardening (material: 42CrMo4, diameter 260 mm, length 170 mm):

a) cutting the sampling flywheel body, b) cutting the piece III

Table 5-3 Tensile testing result of the core sampling piece after hardening (42CrMo4) compared to standard value in [45]

Sample	Yield strength $R_{p\,0.2}$ [MPa]	Ultimate strength R_m [MPa]	Elongation at fracture A_5 [%]	Section area shrinking Z [%]
Tested	551	847	11.5	34
Standard	≥ 500	750 - 900	≥ 14	≥ 55

5.2 Rotor Modal Analysis

Rotor modal analysis is a static analysis which calculates the natural frequency (or eigen-frequency) and the mode shape of a rotor-bearing system without external excitation or load. The natural frequency and mode shape are determined by the density, stiffness and damping of the system. When the rotational speed coincides with the natural frequency, resonance occurs, leading to tremendous vibration and noise. In order to avoid this, the rotor should operate in the subcritical range, i.e. the operating speed stays at least 70 % lower than the first critical speed (bending frequency).

5.2.1 Finite Element Model Set-up in *ANSYS*

The rotor modal analysis is performed numerically in *ANSYS Workbench 17.2*. Fig. 5-7 shows the modeled 3D geometry and the mesh elements of the rotor. Fig. 5-8 shows the modeled rotor components. The materials of the rotor components are shown in Table 5-4.

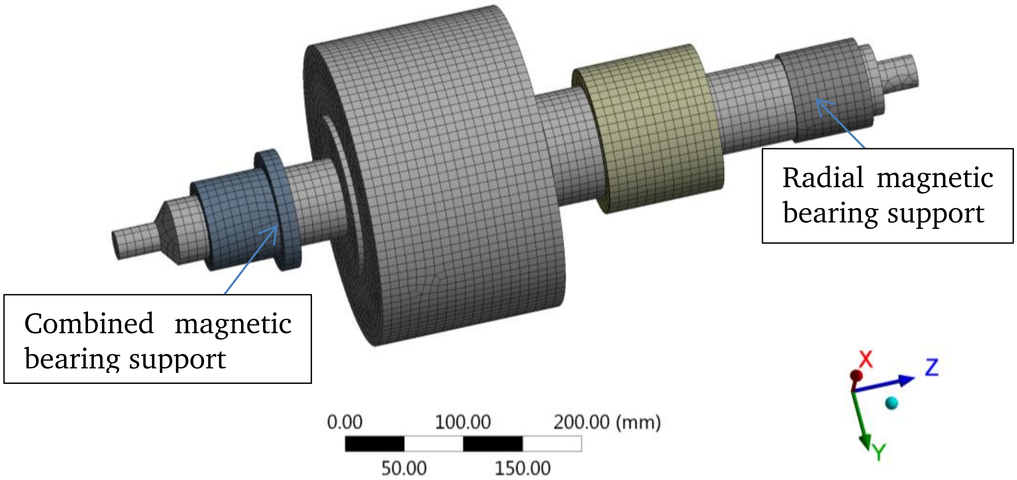

Fig. 5-7 Modeled flywheel rotor with bearing support (characterized by the setting of stiffness and damping coefficient) and laminated rotor iron package in the E-machine and magnetic bearings, built in *ANSYS* for modal analysis

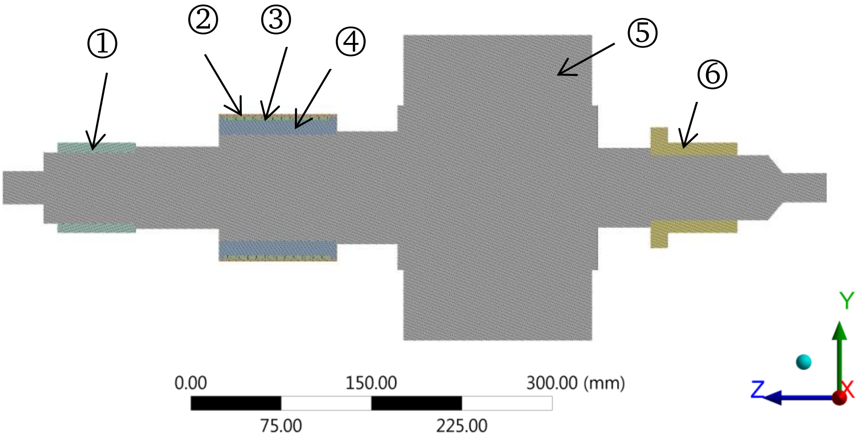

Fig. 5-8 Rotor components modeled in *ANSYS* for modal analysis (1-Radial MB rotor, 2-E-machine bandage, 3-E-machine magnets, 4-E-machine rotor iron, 5-Flywheel body & shaft, 6-Combined MB rotor)

Table 5-4 Materials for rotor components in Fig. 5-8
(‖: parallel direction of fibers, ⊥ : transversal direction of fibers)

	Component	Material	Mass density [kg/m^3]	E-modulus [GPa]	*Poisson*'s ratio
1	Radial MB rotor	Laminated iron NO20	7650	200 (radial) Varied (axial)	0.3
2	E-machine bandage	HTS5631+Epoxy resin	1540	145.28 (‖) 12.02 (⊥)	0.278 (‖⊥) 0.023 (⊥‖) 0.388(⊥⊥)
3	E-machine magnets	VACOMAX225	8400	140-170	0.24
4	E-machine rotor iron	Laminated iron NO20	7650	200 (radial) Varied (axial)	0.3
5	Flywheel body & shaft	42CrMo4	7720	210	0.3
6	Combined MB rotor	Laminated iron NO20	7650	200 (radial) Varied (axial)	0.3

Materials

Linear properties are considered for all the materials, based on the elastic deformation assumption. The material of the flywheel body and shaft is 42CrMo4. In fact, the material 30CrNiMo8 is used in our final design. Since the density (7720 kg/m^3 for 42CrMo4 and 7760 kg/m^3 for 30CrNiMo8) and E-modulus (210 GPa for both 42CrMo4 and 30CrNiMo8) of these two materials are very close, the calculations are also valid for the material 30CrNiMo8. The E-machine bandage is made of carbon fiber reinforced composite material which has orthotropic properties. The E-modulus in the parallel direction (‖) of the fiber is 145.28 MPa, higher than 12.02 MPa in the perpendicular direction (⊥). Laminated iron packages are used in the E-machine rotor and the rotor of the magnetic bearings. In the axial laminated direction, the E-modulus should be zero. As in *ANSYS* the E-modulus must be given as a positive value (>0). Therefore, 3 positive values: 2 GPa, 20 GPa, 60 GPa, are given in the simulation and their influences on the eigen-frequency are compared in Table 5-5.

Components Contacts

As the modal analysis is linear, these rotor components are connected to the shaft by using the *Bonded* connection setting. The increased rotor stiffness due to the shrink fit of the rotor components was not considered in the simulation.

Bearing Support

The model of radial suspension is simulated by applying the setting of *bearing* connection, which is characterized by the *stiffness* and the *damping* coefficient in the *x*- and *y*-

direction, respectively. No coupling coefficient is included. As the damping coefficients in the magnetic bearings are very small, which are neglected in the simulation. Only the stiffness is considered. The stiffness is varied from 500 … 50000 N/mm in order to investigate their influence. The results are shown in Table 5-6.

Mesh Element

The mesh element is chosen to be Hex 20, which is 20-node non-linear Hexahedron element. Mesh size is 8 mm.

5.2.2 Eigen-mode Shape

According to the calculation, the rotor presents rigid body modes (Fig. 5-9, Fig. 5-10) at low frequencies, which are characterized by translational and rotational rigid body motions. The vibration due to the rigid body modes will not cause a problem for the rotor, as the suspension forces and stiffness of the magnetic bearings are controllable. The first bending mode (Fig. 5-11), which is characterized by a flexural rotor bending at higher frequency, is more critical. It may cause destructive damage on the rotor when resonance occurs. Therefore, the operating speed should stay at least 70 % below the 1st bending frequency.

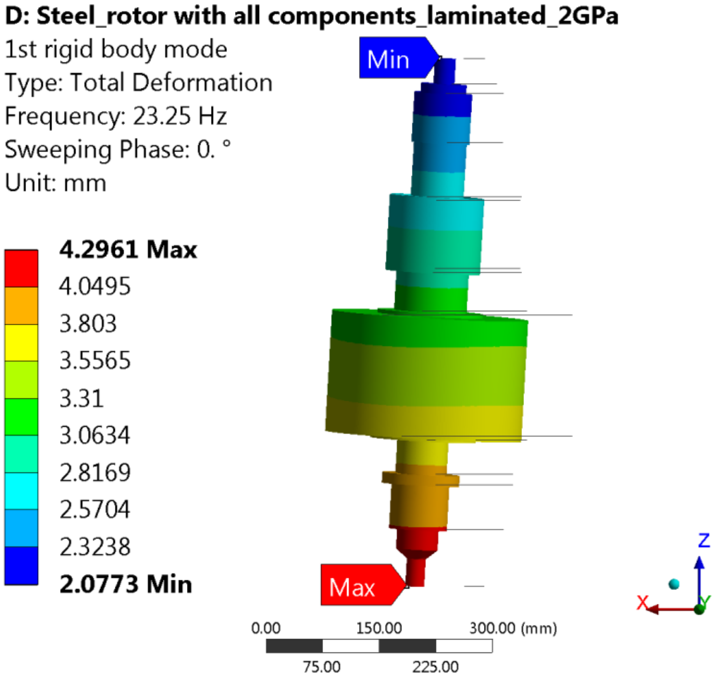

Fig. 5-9 Shape of the 1st rigid body mode at $n = 0$, calculated in *ANSYS* for E-modulus of laminated iron 2 GPa in axial direction, bearing stiffness 1000 N/mm, damping coefficient 0, shaft material 42CrMo4

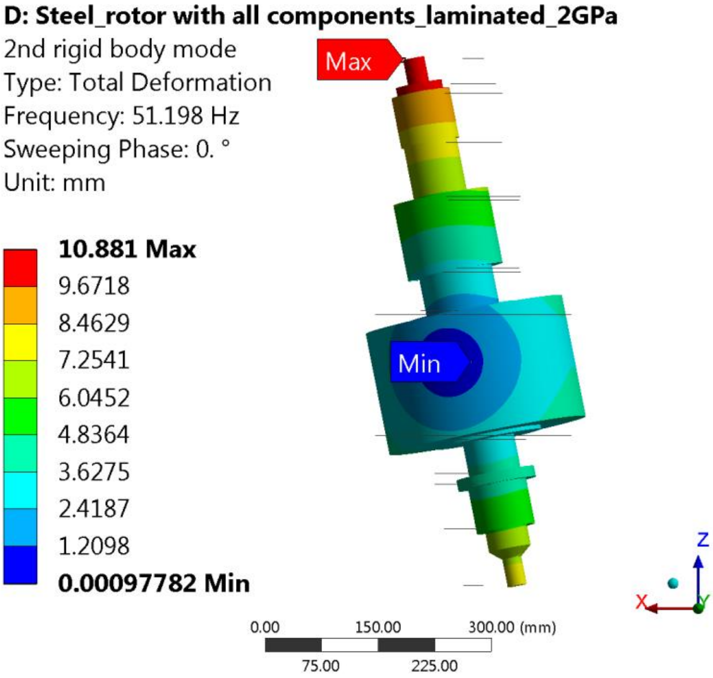

Fig. 5-10 Shape of the 2nd rigid body mode at $n = 0$, calculated in *ANSYS* for E-modulus of laminated iron 2 GPa in axial direction, bearing stiffness 1000 N/mm, damping coefficient 0, shaft material 42CrMo4

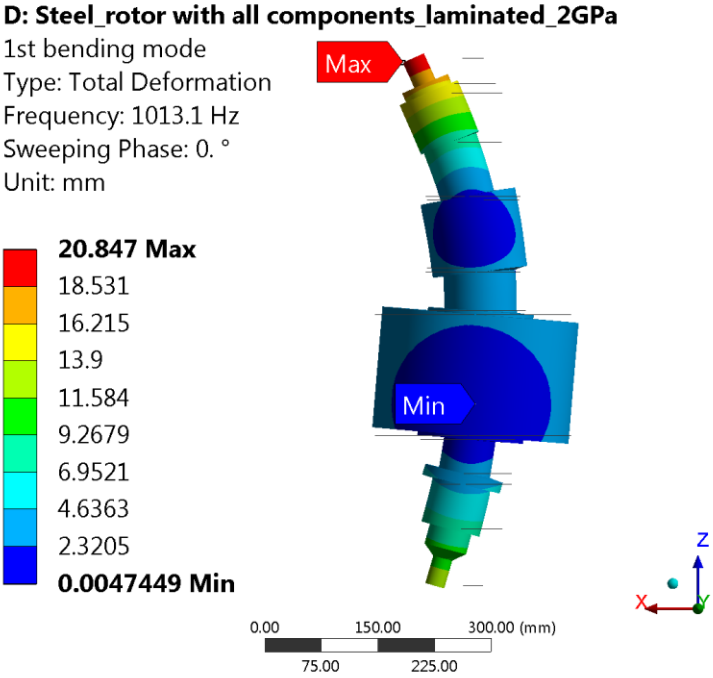

Fig. 5-11 Shape of the 1st bending mode at $n = 0$, calculated in *ANSYS* for E-modulus of laminated iron 2 GPa in axial direction, bearing stiffness 1000 N/mm, damping coefficient 0, shaft material 42CrMo4

5.2.3 Eigen-frequency

The eigen-frequency calculations at speed $n = 0$ are carried out based on varied parameters of E-modulus of the laminated iron and the varied bearing stiffness, shown in Table 5-5 and Table 5-6. As can be seen from Table 5-5, the E-modulus of the laminated iron has almost no influence on the eigen-frequency of the rigid body mode. While the 1st bending frequency increases slightly with higher E-modulus of the laminated iron. Table 5-6 shows the eigen-frequencies for varying bearing stiffness. The eigen-frequency of rigid body mode increases by increasing bearing stiffness, as well as the 1st bending frequency. However, the influence of the bearing stiffness on the 1st bending frequency is very small. The 1st bending frequency is dominant by the material stiffness or E-modulus of the rotor components.

Table 5-5 Calculated eigen-frequency of the rotor (shaft material 42CrMo4), calculated in *ANSYS* for $n = 0$, bearing stiffness 1000 N/mm, damping coefficient 0, calculated with 3 different E-modulus of the laminated iron

E-modulus of laminated iron [GPa]	60	20	2
1st rigid body mode [Hz]	23.26	23.26	23.25
2nd rigid body mode [Hz]	51.22	51.22	51.20
1st bending frequency [Hz]	1073.3	1038.9	1013.1

Table 5-6 Calculated eigen-frequency of the rotor (shaft material 42CrMo4), calculated in *ANSYS* for $n = 0$, E-modulus of laminated iron 2 GPa, bearing damping coefficient 0, calculated for different bearing stiffness

Bearing stiffness [N/mm]	500	1000	5000	10000	50000
1st rigid body mode [Hz]	16.46	23.25	51.55	72.14	149.18
2nd rigid body mode [Hz]	36.23	51.20	113.90	160.06	340.65
1st bending frequency [Hz]	1012.0	1013.1	1021.7	1032.5	1115.9

Investigating the performance with certain rotational speed, the eigen-frequency varies for different speeds due to gyroscopic effect. A *Campbell* diagram is often used to describe this effect, as shown in Fig. 5-12. The motion of the rotor for each eigen-mode can be split into two equivalent whirl motions: backward one and forward one. The eigen-frequency of the backward motion is smaller than the eigen-frequency at $n = 0$. Table 5-7 shows the eigen-frequency of the rotor for maximum speed of 24000 min^{-1} (mechanical frequency: 400 Hz). For the worst case neglecting the bearing stiffness, the eigen-frequency of the backward whirl at 24000 min^{-1} is 948.42 Hz. The operation frequency of 400 Hz is only 42.2 % of 948.42 Hz. Therefore, the 1st bending frequency is high enough to avoid the resonance of maximum speed operation. The rotor will operate in the rigid body mode.

Table 5-7 Calculated eigen-frequency of the rotor for the rotational speeds 0 and 24000 min^{-1}, calculated in *ANSYS* with the E-modulus of 2 GPa for the laminated iron, bearing damping coefficient 0, shaft material 42CrMo4 (BW: backward whirl, FW: forward whirl)

Bearing stiffness [N/mm]	0		1000	
Rotational speed [min^{-1}]	0	24000	0	24000
1st rigid body mode [Hz]	-	-	23.25	13.06 BW 23.65 FW
2nd rigid body mode [Hz]	-	-	51.20	24.37 BW 184.56 FW
1st bending frequency [Hz]	1010.9	948.42 BW 1088.0 FW	1013.1	950.74 BW 1090.0 FW

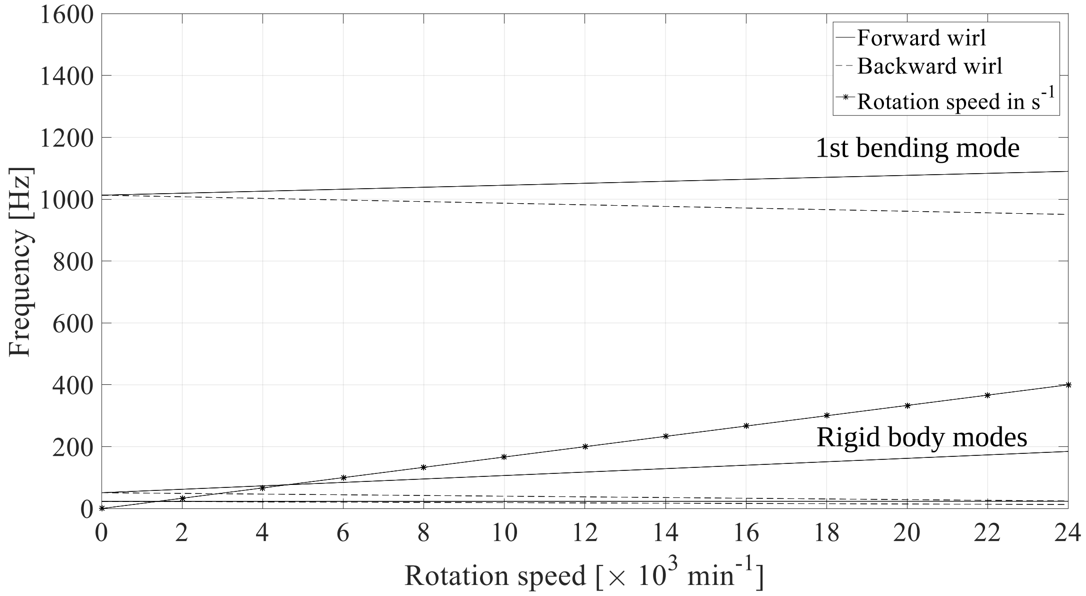

Fig. 5-12 Calculated *Campbell* diagram of the rotor (shaft material 42CrMo4), calculated with the E-modulus of laminated iron 2 GPa, stiffness of the magnetic bearing 1000 N/mm, bearing damping coefficient 0

5.3 Rotor Balancing

The rotor is balanced by adding or reducing some additional weights to compensate the unbalance caused by the inevitable eccentricity. In our design, screw bolts are used as additional weights and they are fixed on the rotor by drilled screw holes. The question is to determine where the balancing holes should locate.

The rotor is highly stressed due to rotation as shown in Fig. 5-13 for the case without balancing holes. The rotor without balancing holes has an axisymmetric structure and homogenous mass distribution, drilling holes on the body will interrupt the mass homogeneity and causes local stress due to centrifugal force. Assuming the balancing holes are directly drilled on the body (with the diameter of 260 mm), in order to calculate the local stress in the balancing hole, a 3D model is set up in *ANSYS* as shown in Fig. 5-14 a) with the dimension of the drilled hole shown in Fig. 5-14 b). 24 balancing bolts are circumferentially symmetric distributed, therefore, only a segmented rotor containing one balancing hole is modeled with the symmetry boundaries on both circumferential section surfaces. In axial direction, ½ model is used with the symmetry boundary on the axial section surface. The mesh elements adopt a mixture of Tet 10 (10-node non-linear tetrahedron) and Wed 15 (15-node non-linear wedge).

The calculated stress distribution is shown in Fig. 5-15. The maximum equivalent stress due to rotation is 481 MPa, which is concentrated distributed on the fillet with the radius of 0.2 mm on the hole bottom surface. As the neighboring masses have a big strain due to the centrifugal force, the stress concentration occurs at the position with big curvatures. Considering the material yield strength $R_{p0.2} = 700$ MPa, a safety factor of 1.46 is obtained due to this local effect, lower than the required safety factor of 2.

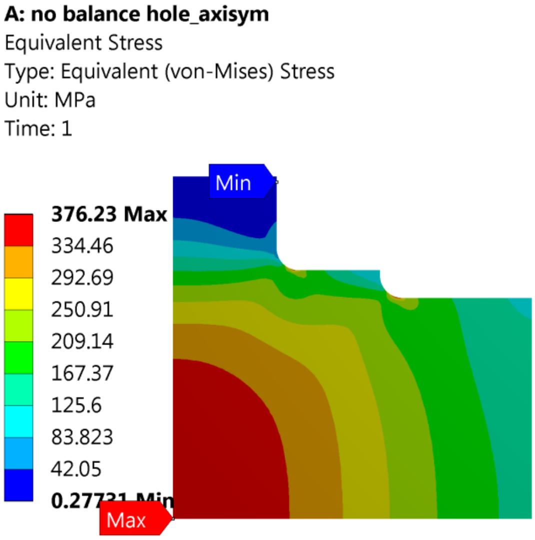

Fig. 5-13 Calculated *von Mises* stress in a flywheel body without balancing holes due to centrifugal force, calculated with an axisymmetric ½ model in *ANSYS Workbench*, for rotational speed 24000 min^{-1}, 20 °C, body material 30CrNiMo8

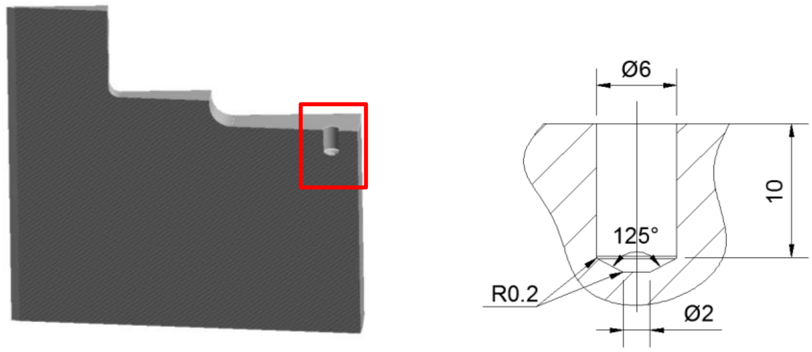

a) b)

Fig. 5-14 Balancing holes on the flywheel body, modeled in *ANSYS Workbench*:
a) section view of the 3D model for a segmented rotor with one hole pitch (15°), b) dimension of the drilled balancing hole

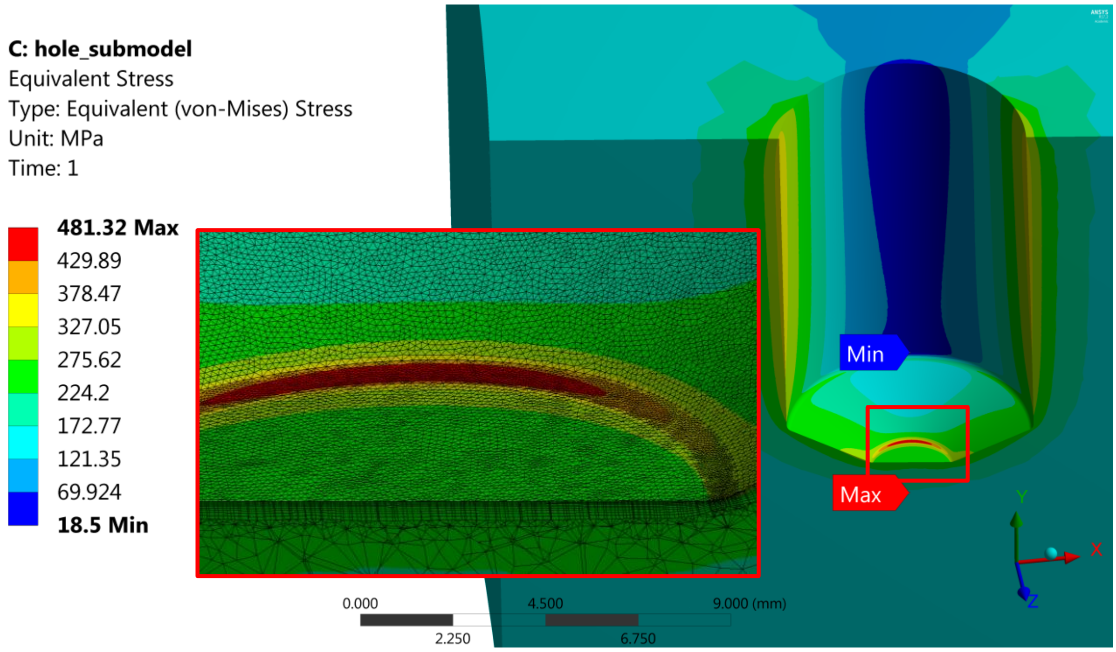

Fig. 5-15 Calculated local stress on the balancing hole on the flywheel body, calculated in *ANSYS Workbench* for rotational speed 24000 min^{-1}, 20 °C, body material 30CrNiMo8

5.3.1 Design of the Balancing Plane

Instead of direct drilling on the flywheel body, two balancing plane are chosen in our design as shown in Fig. 5-16 and Fig. 5-17 with the positions of the screw holes. Each balancing plane has 24 screw holes evenly distributed circumferentially. On the one side, the screw holes are drilled on an additional plane with a diameter of 150 mm on the end surface of the flywheel body. Compared to the plane on the flywheel body with a diameter of 260 mm, this plane has lower velocity and the height of this plane is variable, which will improve the stress distribution (explained in next chapter). However, the plane and the screw holes on the plane still should be carefully designed until the resulting stress distribution and the local stress concentration are acceptable.

The balancing plane on the other side is chosen to be on the aluminum end plate of the E-machine (Fig. 5-17). Also the stress in the end plate should be carefully calculated due to rotation, thermal expansion and press fit.

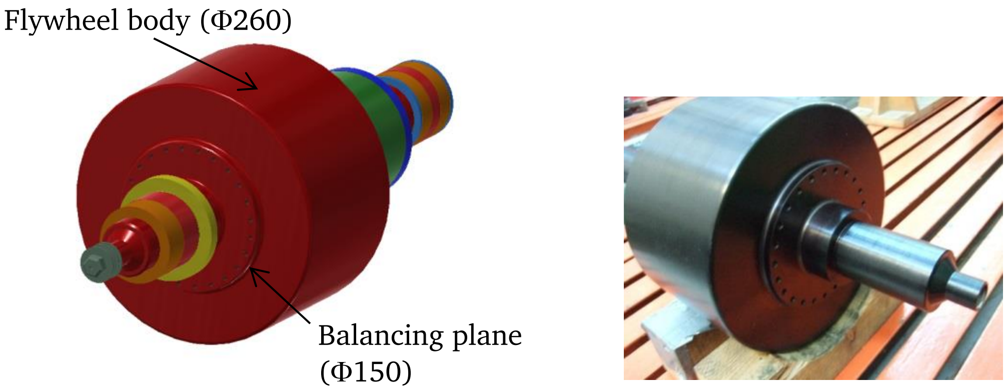

a) b)

Fig. 5-16 Rotor balancing screw holes on the additional plane with a diameter of 150 mm: a) 3D drawing [47], b) photo of the prototype

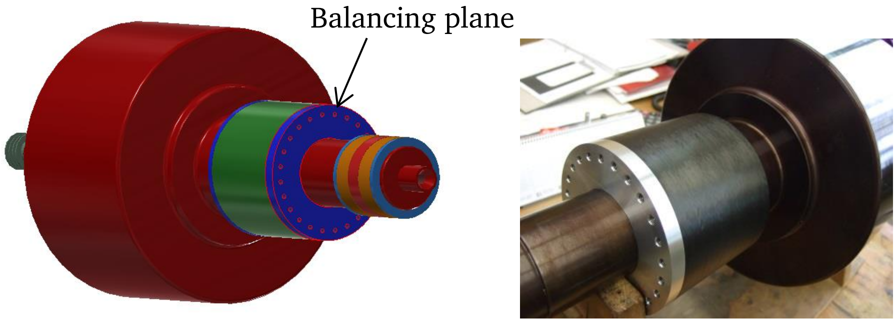

Fig. 5-17 Rotor balancing screw holes on E-machine end plate (aluminum) in Fig. 5-1: a) 3D drawing [47], b) photo of the prototype

5.3.2 Balancing Plane 1: on the Additional Plane with the Diameter of 150 mm

The section view of the flywheel rotor is shown in Fig. 5-18 with a drilled screw hole on the additional plane with the diameter of 150 mm. On this plane 24 screw holes are drilled, circular evenly distributed on a smaller diameter of 137 mm. The size of the screw holes is M6. The distance between the screw hole bottom and the flywheel body is defined to be h_{sr}.

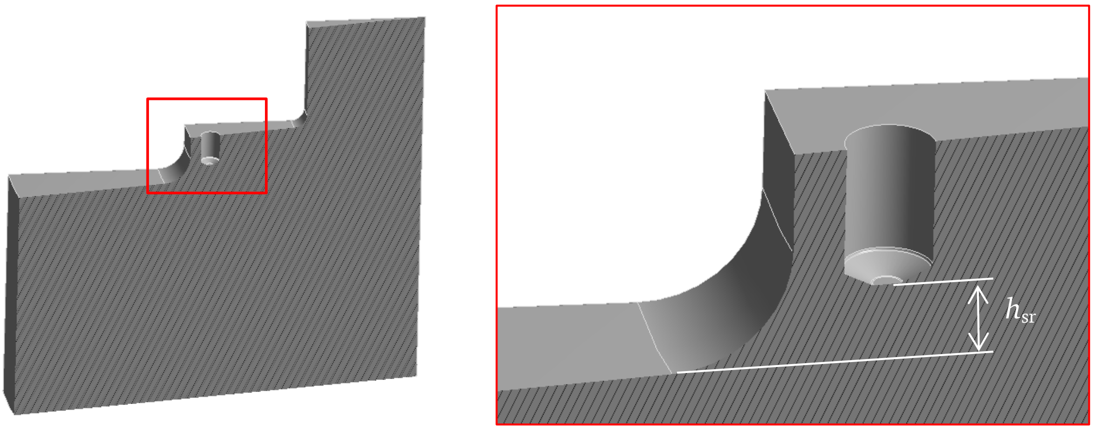

Fig. 5-18 Balancing plane on the flywheel rotor with balancing holes, where h_{sr} is the distance between the screw hole bottom and the flywheel body, modeled in *ANSYS Workbench*

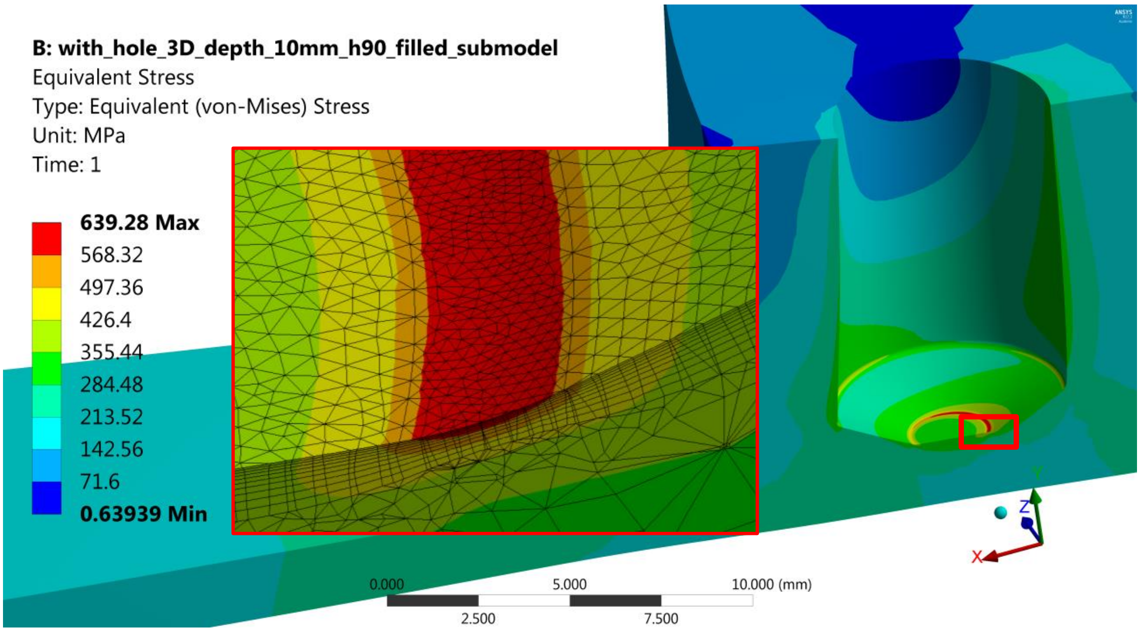

Fig. 5-19 Local stress on the balancing hole of the flywheel body for h_{sr} = 0 mm, calculated in *ANSYS Workbench* for rotational speed 24000 min^{-1}, 20 °C, body material 30CrNiMo8

The stress due to rotation is also calculated in *ANSYS Workbench*. Fig. 5-19 shows the local stress due to the screw hole for $h_{sr} = 0$ mm, i.e. the screw hole bottom is in line with the flywheel body surface. The maximum local stress is calculated to be 639.3 MPa, occurring on the edge of the screw hole bottom. Compared to the stress in Fig. 5-15, this stress is increased, which is reasonable as this position is higher stressed than Fig. 5-15 due to rotation according to Fig. 5-13. However, if the distance h_{sr} is increased, the stress will be decreased. Table 5-8 shows the stress for different distance h_{sr}. This can be understood that the hole is far from the highly stressed region as h_{sr} increases. A safety factor of 2 can be obtained for the yield strength $R_{\mathrm{p0.2}}$ = 700 MPa if h_{sr} is 10 mm.

Table 5-8 Local stress on the screw hole of the flywheel body for different hole positions, calculated in *ANSYS Workbench* for rotational speed 24000 min^{-1}, 20 °C, body material 30CrNiMo8

Distance h_{sr} [mm]	Max. *von Mises* stress [MPa]	Safety factor ($R_{\mathrm{p0.2}}$ = 700 MPa)
0	639.3	1.1
5	478	1.5
8	390	1.8
10	346	2.0

5.3.3 Balancing Plane 2: on E-machine End Plate

The E-machine end plates are used to fix the axial position of the magnets of the E-machine. They are made of aluminum or non-magnetic streel. The second balancing plane is chosen to be on the upper end plate (Part 9 in Fig. 5-1). Compared to non-magnetic steel, the high strength aluminum has lower mass density but higher yield strength (Table 5-9). Therefore, aluminum is used in our design. However, it should be noted that the strength decreases as the temperature increases. For aluminum 3.4365, the yield strength is 450 MPa at 20 °C and is estimated to be 290 MPa at 150 °C [48].

Table 5-9 Material properties of high strength aluminum 3.4365 and non-magnetic steel 1.3964 used for the end plate of the E-machine

Material	Al 3.4365	Steel 1.3964
Density ρ [kg/m^3]	2780	7910
E-modulus E [GPa]	70	195
CTE [$\times 10^{-6}$ 1/K]	23.4	16.4
Poisson's ratio	0.33	0.3
Yield strength $R_{\mathrm{p0.2}}$ [MPa]	450 (20°C) 290 (estimated, 150°C)	430 (20°C) 285 (150°C)
Ultimate strength R_{m} [MPa]	530 (20°C)	700-950(20°C) 675 (150°C)

The end plate has an inner diameter of 65 mm, outer diameter of 128 mm. 24 screw holes M6 are drilled, circular distributed on the diameter of 110 mm. The stress in this end plate is more complicated, which is due to not only rotation, but also thermal expansion and press-fittings with the shaft. An undersize of 0.2 mm is required for a valid connection of the end plate and the shaft without detach.

The stress in the end plate is calculated by a 2D model in *ANSYS Workbench* as shown in Fig. 5-20. A segmented rotor with one hole pitch is modeled. The mesh element is nonlinear Quad 8 with the size of 1 mm on the body surface and 0.02 mm on the hole edge. Two cases are considered:

- An empty screw hole;
- A screw hole, filled with a balancing mass with an additional fitting of 0.01 mm.

Calculated conditions include: standstill and 20 % over-speed rotation at 28800 min^{-1}, applied for the temperature of 20 °C and 150 °C, respectively, as shown in Table 5-11.

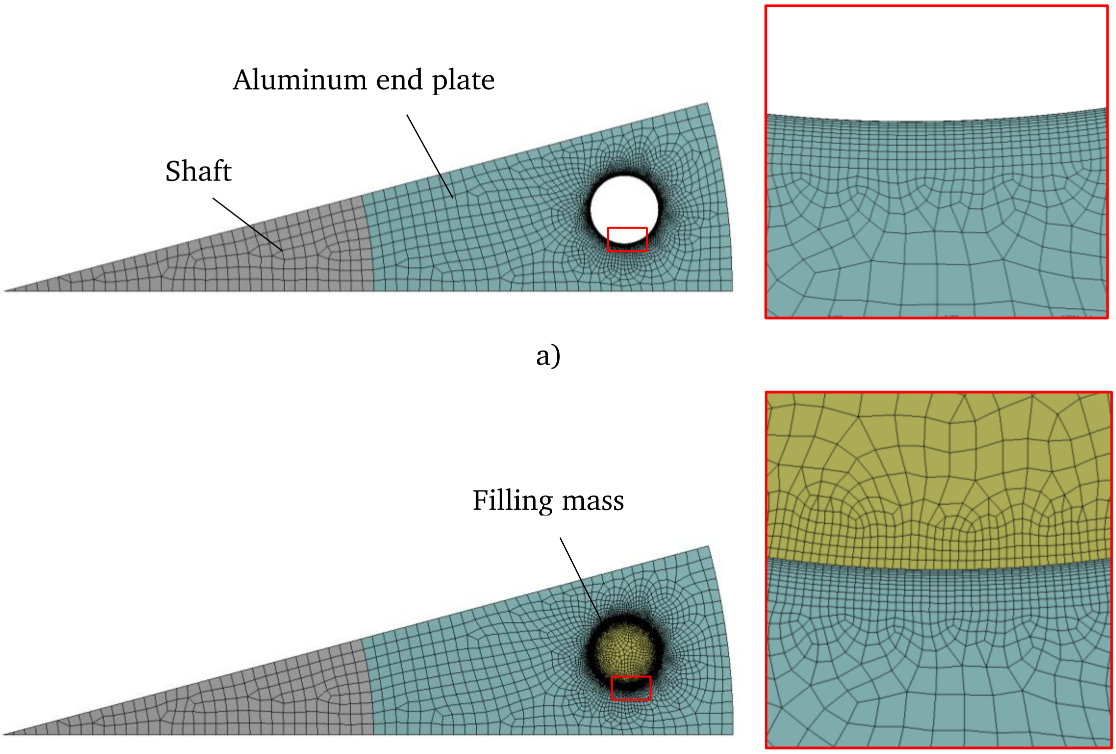

Fig. 5-20 Shaft and E-machine end plate, modeled in *ANSYS Workbench* (shaft material: steel 30CrNiMo8, end plate material: Al 3.4365, mesh size: 1 mm for shaft and end plate body surface, 0.02 mm on the hole edge): a) without filling mass, b) with filling mass

The contour plot in Table 5-10 shows the stress on the end plate at the rotational speed of 28800 min^{-1}, 20 °C. High stress occurs on the inner bore of the plate due to press fitting with the shaft and centrifugal force. Meanwhile, a local stress occurs on the balancing hole due to the tension in tangential direction, indicating the hole tends to have a tensile deform in the tangential direction. The maximum stress is approx. 245 MPa for the plate without filling mass. Compared to the material strength of 450 MPa, a safety factor of 1.84 is obtained. But this case is not critical, even though a plastic deform occurs for the worst estimation, the stress is more likely to cause an irreversible deformation instead of material fracture. When a balance mass is filled in the screw hole with an assumed interference fitting of 0.02 mm, the fitting causes additional stress in the hole which reaches approx. 312 MPa. The safety factor decreases to 1.44.

Table 5-10 Stress contour plot of the aluminum end plate of the E-machine, calculated in *ANSYS Workbench* at 28800 min^{-1}, 20°C

Empty hole	With filling mass (fitting 0.02 mm)
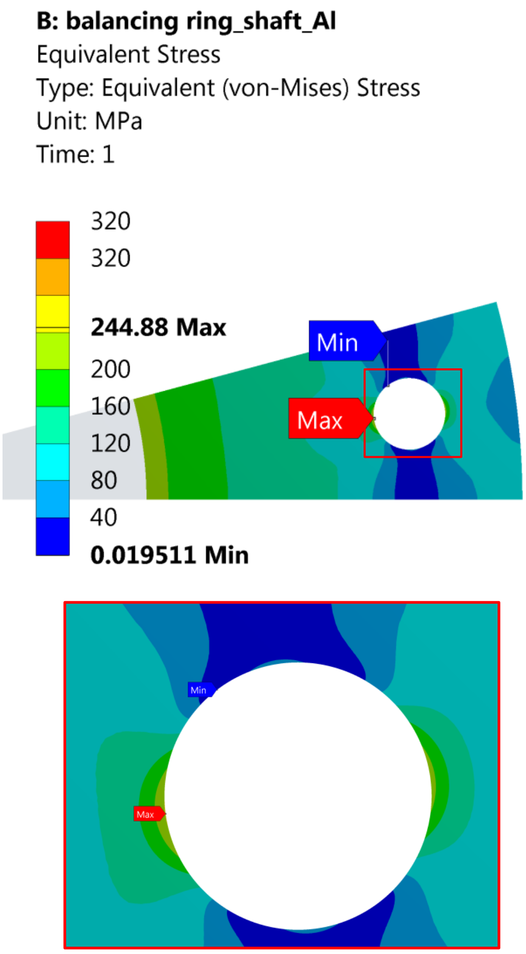	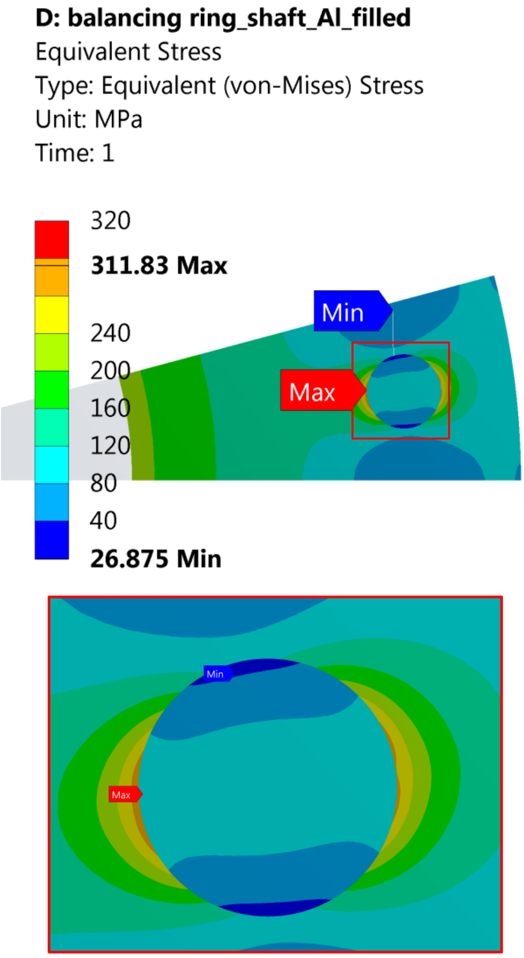

For different operating conditions, the stress are calculated in Table 5-11, as well as the safety factors compared to the material yield strengths at 20 °C or 150 °C in Table 5-9. The minimum safety factor is 1.44 for the holes filled with balancing mass, operating at

28800 min^{-1} and 20 °C (contour plot shown in Table 5-10). As stated above, the local stress is more likely to cause an irreversible deformation instead of material fracture. Therefore, this safety factor is acceptable.

Table 5-11 Stress calculation (in *ANSYS Workbench*) in the aluminum end plate of the E-machine with balancing holes (Δu: interference fitting of the end plate and shaft, n: rotational speed, ϑ: temperature, p_c: contact pressure between the shaft and the end plate)

Dimension	End plate inner diameter 65 mm, outer diameter 128 mm Screw hole M6×24, circular distributed on the diameter of 110 mm							
	Empty hole				With filling mass (fitting 0.02 mm)			
Δu [mm]	0.2	0.2	0.2	0.2	0.2	0.2	0.2	0.2
n [min^{-1}]	0	0	28800	28800	0	0	28800	28800
ϑ [°C]	20	150	20	150	20	150	20	150
p_c [MPa]	87.4	47.1	51.2	11.0	86.6	47.6	48.4	8.2
$\sigma_{\mathrm{Mises,max}}$ on end plate bore [MPa]	222	119	220	120	221	119	219	120
$\sigma_{\mathrm{Mises,max}}$ on balancing hole[MPa]	221.8	119.7	244.9	148.5	296.7	119.8	311.7	146.9
Safety factor	2.03	2.42	1.84	1.95	1.52	2.42	1.44	1.97

5.4 Rotor Hardening

5.4.1 Rotor Structural Failure during Hardening Process

Heat treatment is usually used to obtain a high material strength. As stated in Chapter 5.1.5, the alloy will be firstly heated up to 830 … 860 °C and then rapidly cooled in the coolant to 180 °C. The first flywheel rotor with the material 30CrNiMo8 and the dimensions shown in Fig. 5-21 was manufactured and taken to the hardening process. During the cooling process 830 … 860 °C to 180 °C, a big crack occurs at the flywheel body (Fig. 5-22). The crack starts from the intersection of flywheel body and the shaft, continues through the flywheel body axially to the other side. The width of the crack is about 0.1 mm. Two additional cracks start from the same intersection, but are much smaller and stay local. The reason for the crack lies in the stress concentration on the small fillet R2 in Fig. 5-21. During the cooling process, the temperature on the rotor surface drops much faster than the inner mass, leading to a big temperature gradient in the mass under but close to the surface. Temperature gradient causes thermal stress, which behaves as a tensile stress or a shrinking effect of the surface. The fillet area is under the load of tensile stress from two different directions: due to the shrinking the flywheel body surface (Surface A in Fig. 5-22) and due to the shrinking of the shaft surface (Surface B in Fig. 5-22). The tension effect on the fillet may lead to the structural failure.

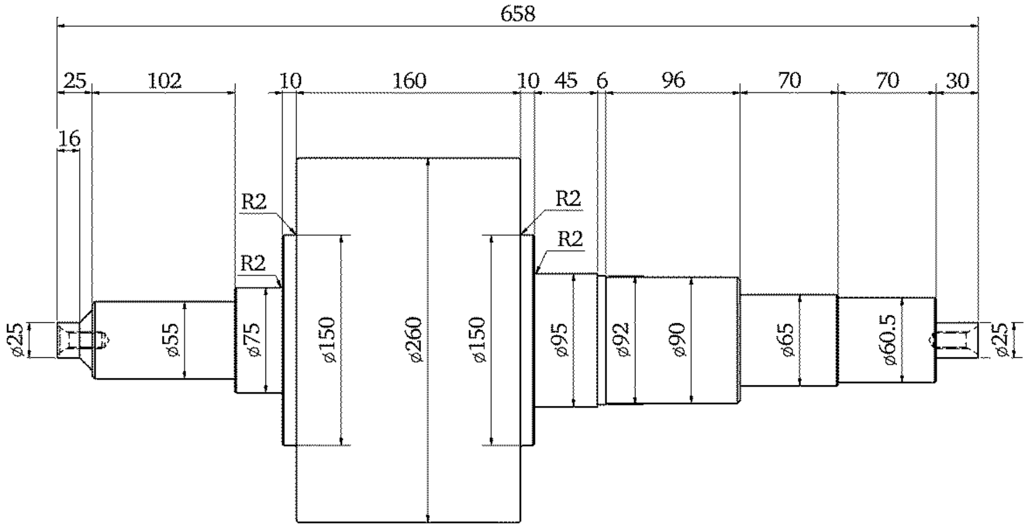

Fig. 5-21 Dimensions (unit: mm) of the rotor for hardening

a)　　b)　　c)

Fig. 5-22 Cracks occurred on the flywheel rotor during quenching process from 850 °C to 180 °C: a) view on the side connected with the shaft Φ95 in Fig. 5-21, b) view on the flywheel body outer surface, c) view on the side connected with the shaft Φ75 in Fig. 5-21

5.4.2 Thermal Stress Calculation for Quenching Process

In order to investigate the reason for the failure and the behavior of the flywheel rotor during the quenching process, a combined thermal and structural model is built in *ANSYS Workbench* for the destructed rotor. The rotor structure is simplified with the dimensions shown in Fig. 5-23. The built model is axisymmetric and only half length is built in axial direction with a symmetric boundary. The fillet connecting the shaft and the flywheel body has a radius of 2 mm, the same dimension as manufactured on the rotor in Fig. 5-21. The mesh element is non-linear element Quad 8 with the size of 3 mm on the body surface and 0.05 mm on the fillet edge.

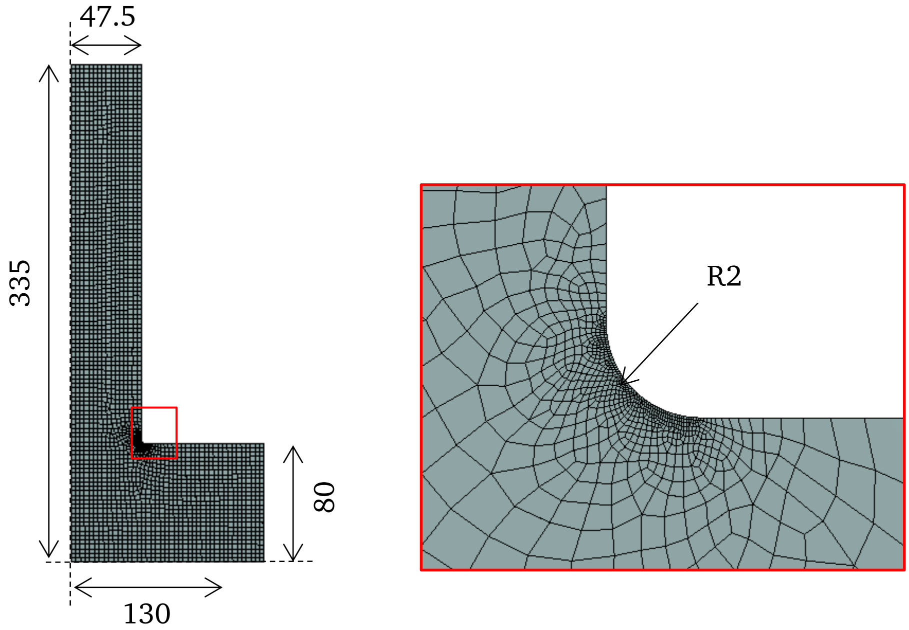

Fig. 5-23 Axisymmetric model of the destructed rotor built in *ANSYS Workbench* for thermal stress calculation (dimensions in mm, rotor material 30CrNiMo8, mesh size: 3 mm on the body surface and 0.05 mm on the fillet edge)

A temperature of 850 °C is applied as initial temperature and an ambient temperature of 180 °C is used corresponding to the temperature of the salt bath for quenching. The boundary conditions applied on the rotor outer surface are: convectional boundary with a constant heat transfer coefficient of $\alpha = 800\ \mathrm{W/(m^2{\cdot}K)}$ [41] and a radiative heat transfer boundary with emissivity of $\varepsilon = 0.79$ [49]. The density of the material is assumed to be constant, neglecting the influence of the martensitic transformation. A linear material property is assumed with a constant modulus, neglecting the plastic deformation. By using these conditions, the FEM program performs a transient calculation for the temperature in a thermal model and imports the results into a structural model to calculate the thermal stress. This model is a simple and ideal model which cannot completely describe the complicated quenching process with respect to the vaporization of the coolant, the martensitic transformation in the material and so on, the calculation here gives a hint for the reason of the failure in Fig. 5-22.

The calculated temperature distributions for different time are shown in Fig. 5-24. The rotor surface is faster cooled than the inner body. A graph of the temperature vs. time is plotted in Fig. 5-25 for the inner core position and the fillet edge.

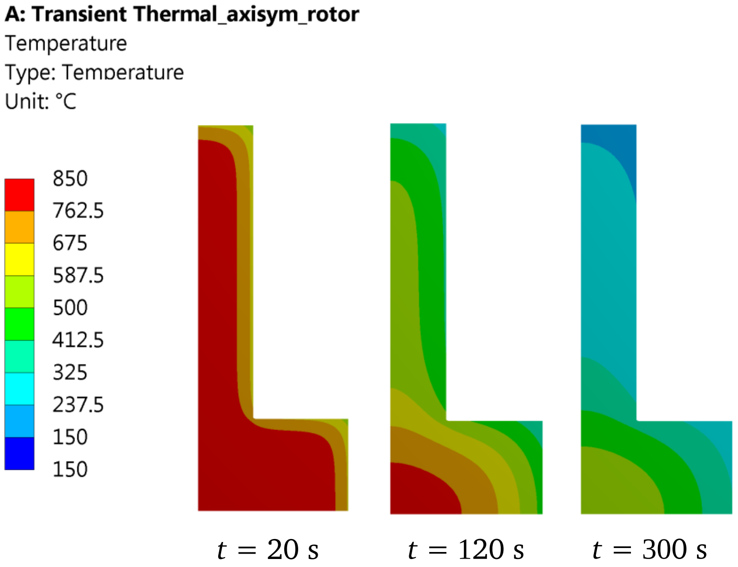

Fig. 5-24 Calculated temperature distribution in the rotor to simulate the quenching process, calculated in *ANSYS Workbench* with the initial temperature of 850 °C and the boundary condition: $\alpha = 800$ W/(m^2·K) and $\varepsilon = 0.79$ on the rotor outer surface

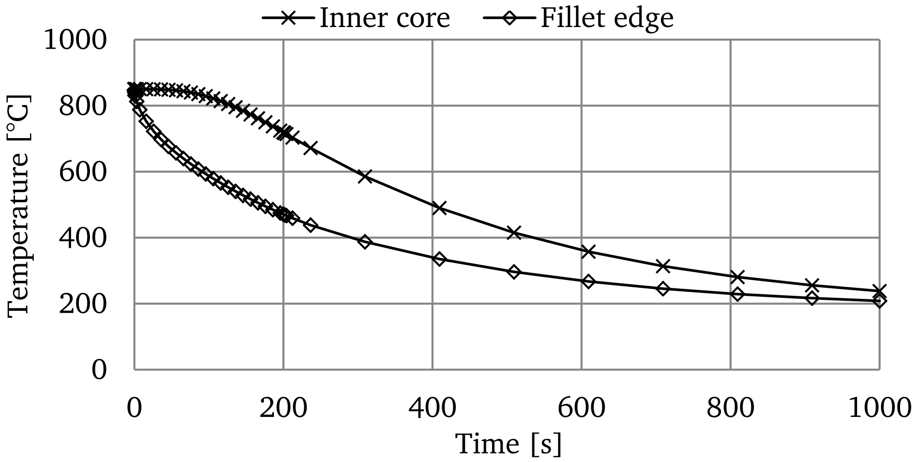

Fig. 5-25 Calculated temperature vs. time at the inner core and the fillet edge, calculated in *ANSYS Workbench* with the initial temperature of 850 °C and the boundary condition: $\alpha = 800$ W/(m^2·K) and $\varepsilon = 0.79$ on the rotor outer surface

The calculated stress distribution is shown in Table 5-12 and the stress vs. time at the fillet position is show in Fig. 5-26. The maximum equivalent stress on the filled edge is 2396 MPa, occurring 120 s after the cooling starts. According to Table 5-2, the material ultimate strength is 1250 … 1450 MPa for a rod with the diameter smaller than 16 mm. Compared to this value, the stress during quenching process is much higher and this explains the failure in Fig. 5-22.

Table 5-12 Calculated equivalent thermal stress in the rotor, calculated in *ANSYS Workbench* with the initial temperature of 850 °C and the boundary condition: $\alpha = 800$ W/(m^2·K) and $\varepsilon = 0.79$ on the rotor outer surface

t = 20 s	t = 120 s	t = 300 s
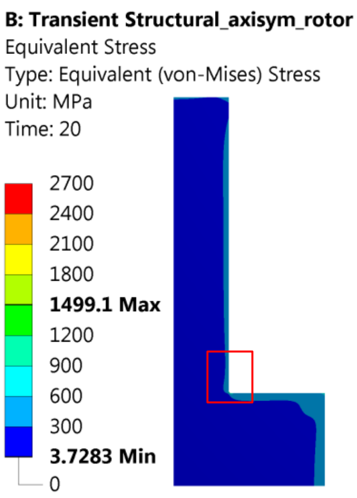	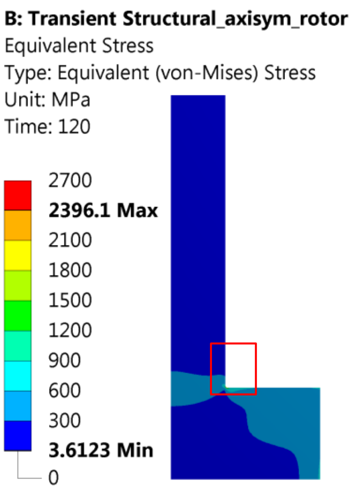	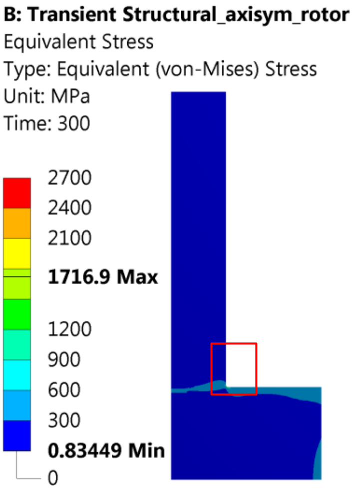
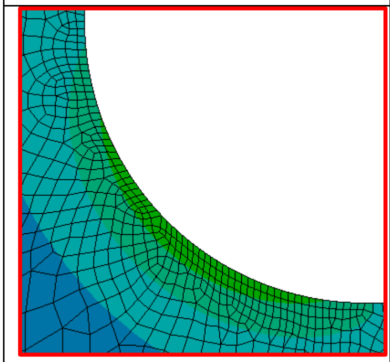	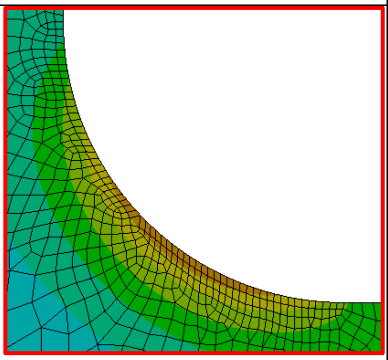	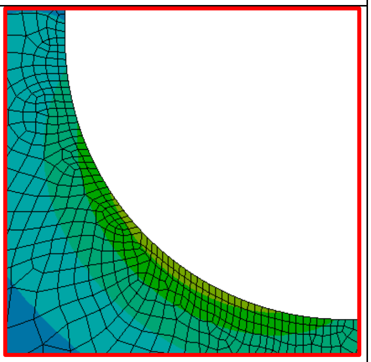

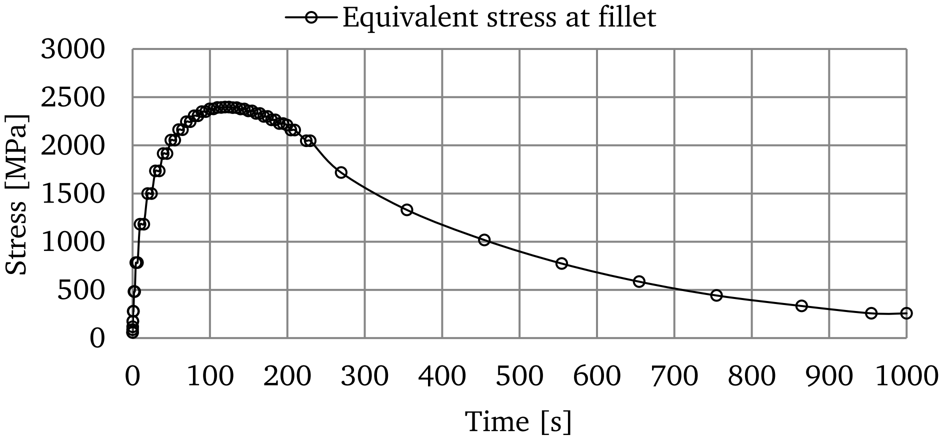

Fig. 5-26 Calculated equivalent thermal stress vs. time at the fillet edge, calculated in *ANSYS Workbench* with the initial temperature of 850 °C and the boundary condition: $\alpha = 800$ W/(m^2·K) and $\varepsilon = 0.79$ on the rotor outer surface

5.4.3 Modified Rotor Geometry

The rotor geometry should be modified in order to reduce the thermal stress. Table 5-13 compares the maximum thermal stress occurred in different rotor geometries.

Table 5-13 Calculated maximum stress in the rotor during thermal quenching process for different rotor geometries, calculated in *ANSYS Workbench* with body initial temperature 850 °C, heat transfer coefficient on the body surface 800 W/(m^2· K), radiative emissivity on the body surface 0.79 (axisymmetric and vertical symmetric model)

Rotor I: damaged rotor	Rotor II: fillet radius 40 mm
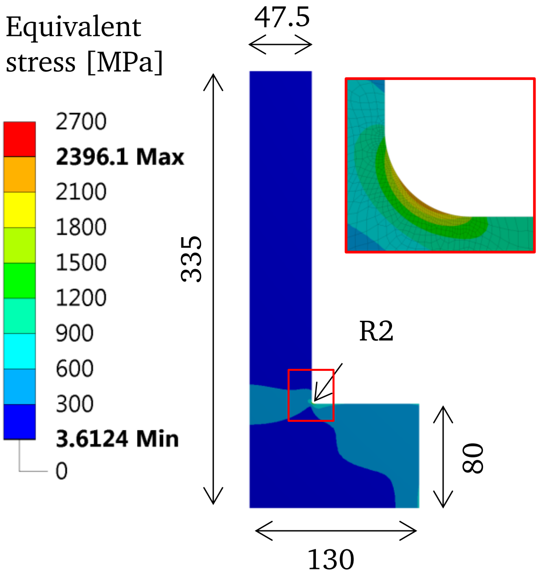	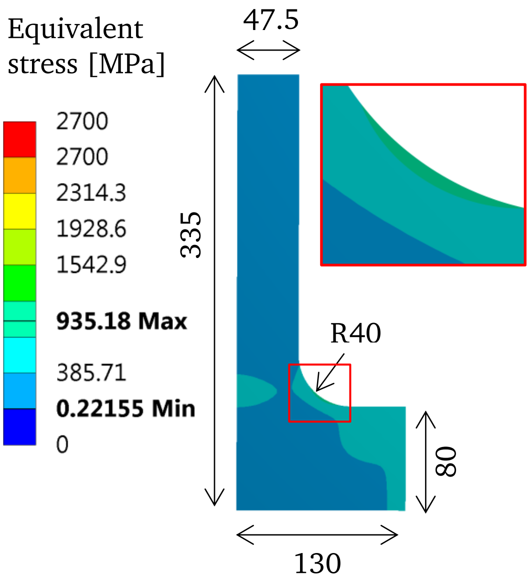
Rotor III: conical shape	**Rotor IV: fillet radius 60 mm**
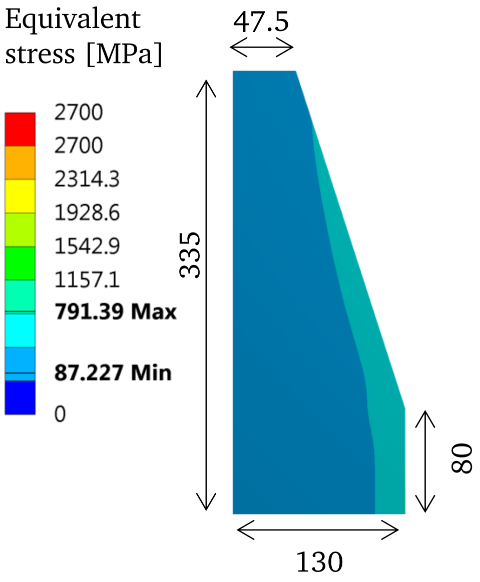	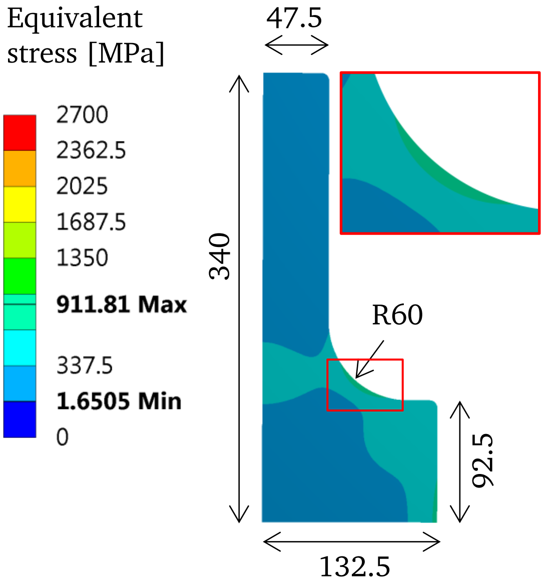

To reduce the local stress, one approach is to increase the fillet radius as Rotor II shown in Table 5-13. By using a fillet radius of 40 mm, the maximum stress decreases from 2396 MPa to 935 MPa. Another approach is to use a conical shape as Rotor III shown in Table 5-13. The maximum stress can be further reduced to 791 MPa. However, the disadvantage of the conical shape rotor is the lower cooling rate compared to the other rotors as shown in Fig. 5-27. As stated in previous chapters, a faster cooling rate is always preferred to obtain high strength in the center, as the maximum stress due to rotation occurs in the center. Therefore, Rotor III is not chosen.

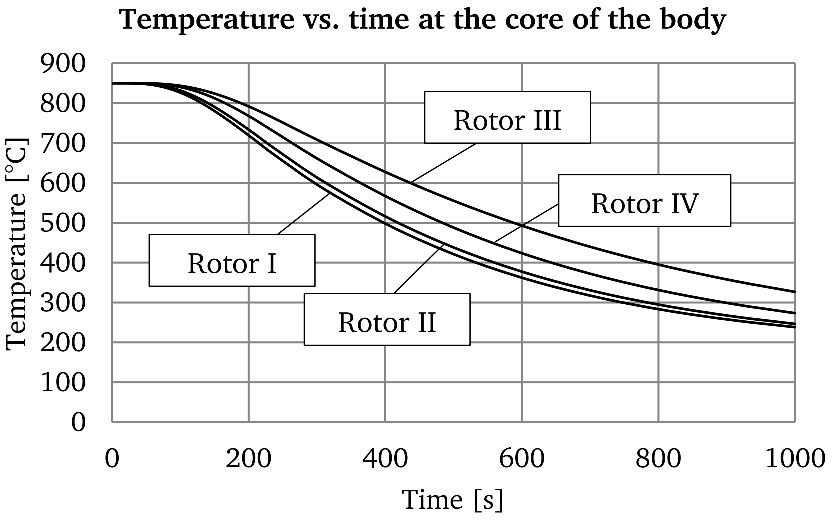

Fig. 5-27 Calculated temperature vs. time at the cores of rotors in Table 5-13 during quenching process, calculated in *ANSYS Workbench*

In the end, the geometry of Rotor IV was chosen and a new rotor with this geometry was manufactured for the second time hardening. A bigger fillet radius of 60 mm is used and the flywheel body has a thickness of 185 mm, which is larger compared to Rotor II in order to accommodate the geometry of the balancing plane. The second time quenching was successfully carried out and no damage was observed. After hardening, the rotor was then manufactured to the designed shape in Fig. 5-1.

5.5 Rotor Spin Testing

Spin testing of the rotor is highly recommended and important before the commission in the system, not only to test the strength of the rotor, but also get well known of the ultimate speed for the safety concern. After the rotor is completely assembled with all the components and with the designed fittings (Chapter 8.1.1) in the *Institute for Elec-*

trical Energy Conversion, *TU Darmstadt*, the rotor spin testing was performed by *Schenck RoTec GmbH, Darmstadt, Germany*. The rotor is vertically placed in the vacuum container of the test bench and was fixed to a quill shaft, which was driven by a motor though a gear box. The test was performed at room temperature for the vacuum level of around 1 mbar. Fig. 5-8 shows the measured speed, air pressure and vibration.

The designed maximum operating speed is 24000 min^{-1}. For the spin testing, the rotor was speed up by the driving motor to 1.2 times maximum speed, which is 28800 min^{-1} and remained a constant speed rotation for 2 minutes. After that the rotor was decelerated to standstill. Next round, the rotor was accelerated to the speed of 24000 min^{-1} and also performed a constant speed rotation for 2 minutes. Then the rotor was decelerated to standstill.

In order to monitor the inadmissible rotor vibrations that can cause damage to the driving gear, a displacement sensor is positioned on the drive shaft. This sensor triggers the automatic braking process if the vibration exceeds the limit value, which is 250 μm (peak-to-peak). The measured displacement of the rotor is depicted in Fig. 5-8, where 100 % corresponds to 250 μm (peak-to-peak). Resonance occurred at the speed of 4000 min^{-1}, but the rotor passed through with a big acceleration. The rotor vibration remained constant during the constant speed rotation.

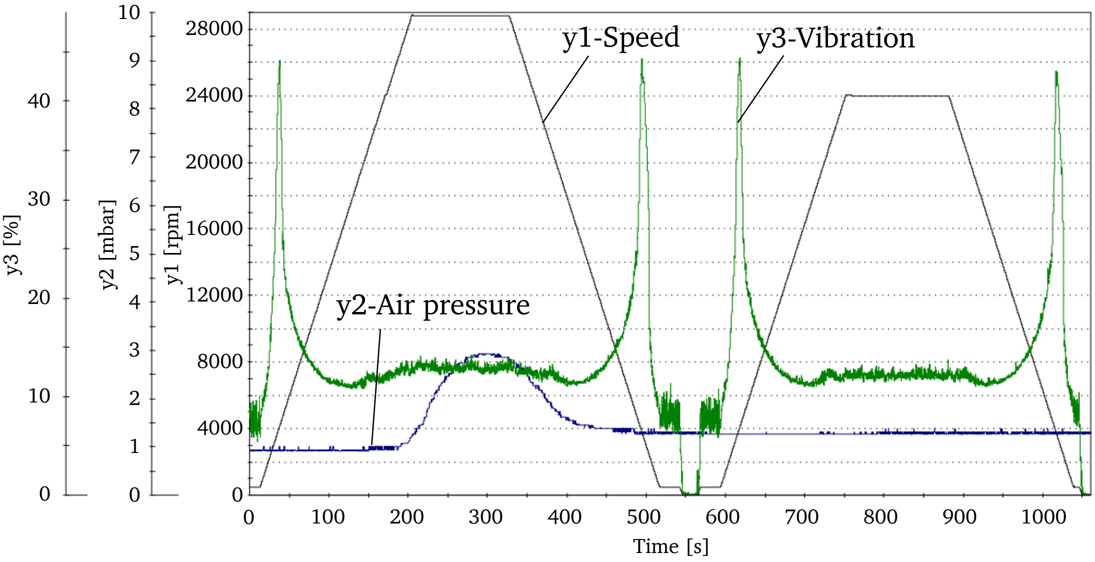

Fig. 5-28 Measured speed and vibration of the rotor during spin testing and the measured air pressure in the container, measured by *Schenck RoTec GmbH, Darmstadt, Germany*

The result shows that the rotor survived from the testing without visible damage occurred on the rotor. The rotor components remained an active assembly without separation or slipping. Therefore, the strength calculation and the fitting design are valid. The rotor can be implemented for the rotation at the designed speed without mechanical failure.

6. E-Machine Design

A high-speed E-machine is responsible for the kinetic and electric energy conversion in a flywheel system. It is used as a motor for the charge of the flywheel and as a generator for the discharge. The basic requirements for electric machines in flywheels are:

- High robustness;
- High efficiency;
- No cooling problems for the rotor.

A permanent magnet (PM) machine is chosen in our design based on the comparison in Table 1-6 for the commonly used E-machines in the flywheel systems. The reluctance machine is not considered in our design, due to the low power factor for synchronous reluctance machine (SynRM) and the high torque ripple for the switching reluctance machine (SRM). The induction machine has high robustness with high efficiency. The drawback is high rotor losses. As our system operates in vacuum, the high rotor losses in the induction machine lead to high rotor temperature without effective cooling, which is not acceptable. Compared to reluctance machine and induction machine, PM machine has low rotor losses, high power density and high efficiency. Therefore, it is used in our system. A proper design is required dealing with the typical downsides of the PM machine: the rotor mechanical strength, the rotor losses and the demagnetization problems, etc.

6.1 E-machine Design Overview

6.1.1 Design Specifications and Operating Characteristics

The E-machine design specifications are shown in Table 6-1. The speed range is predefined in Table 4-1 according to the speed of the flywheel. The rated apparent power $S_\mathrm{N} = 35$ kVA is also predefined. Considering the losses and the power factor of the E-machine, the rated output power $P_\mathrm{N} = 28$ kW is expected for motor mode. To avoid over modulation, the output voltage of the inverter for modulation index $m = 1$ is limited to $U_\mathrm{AC} = 396$ V. The machine has a star connection, therefore the phase voltage limit is $U_\mathrm{s,max} = 228.6$ V. A continuous operation is expected, considering the extreme case when the flywheel is fully utilized with continuous charge and discharge.

According to the specifications, the operating characteristics of the machine is defined in Fig. 6-1. The E-machine should provide a constant power P_N in the speed range of $n_{min} \dots n_{max}$. The power is positive if the machine operates as a motor and negative as a generator. Two operating points OP_1 and OP_2 are defined for the operations at n_{min} and n_{max}, respectively. As the induced voltage increases in proportional to speed, terminal voltage reaches the limit of the inverter $U_{s,max}$ at n_{max}. Therefore, for the operation between n_{min} and n_{max}, the flux is weakened by applying negative current in *d*-axis. The torque M_{max} decreases for increasing speed, while the power is constant. For the speed lower than n_{min}, the machine operates with constant torque.

Table 6-1 E-machine design specifications

Parameters	Symbol	Value	Unit
Maximum speed	n_{max}	24000	min^{-1}
Minimum speed	n_{min}	12000	min^{-1}
Nominal output voltage (r.m.s.) of inverter	U_{AC}	396	V
Max. phase voltage (r.m.s., Y connection)	$U_{s,\ max}$	228.6	V
Inverter switching frequency	f_T	12	kHz
Rated output power (motor)	P_N	28	kW
Max. current (r.m.s.)	I_{max}	50	A
Operation duty type	Continuous duty		

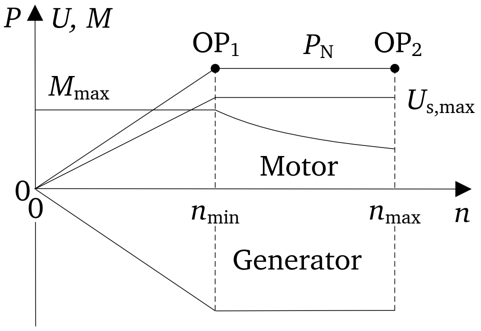

Fig. 6-1 Operating characteristics of the E-machine, P_N = 28 kW, n_{min} = 12000 min^{-1}, n_{max} = 24000 min^{-1}, $U_{s,\ max}$: max. terminal voltage, *M*: torque

6.1.2 E-machine Preview

The proposed design is a 4-pole PM machine with surface mounted rotor magnets, shown in Fig. 6-2. The main parameters are shown in Table 6-2. The detailed design parameters can be found in Chapter 6.2.

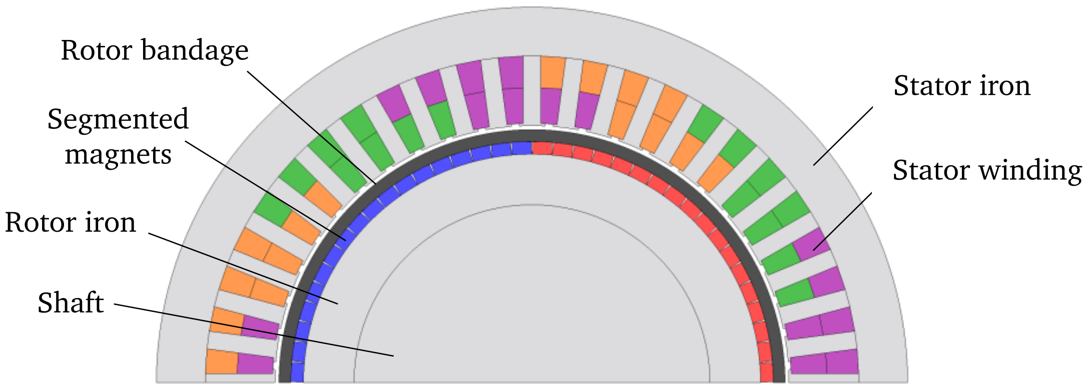

Fig. 6-2 Section view of the E-machine geometry, 1/2 model in *JMAG* (with surface mounted magnets and bandage)

Table 6-2 E-machine main dimensions and design parameters

Parameter	Symbol	Value
Stator inner diameter	d_{si}	130 mm
Stator outer diameter	d_{so}	190 mm
Shaft diameter	d_{sh}	90 mm
Iron stack length	L_{Fe}	90 mm
Air gap length	δ	1 mm
Bandage thickness	h_{B}	3 mm
Magnet dimension	$l_{\mathrm{m}} \cdot b_{\mathrm{m}} \cdot h_{\mathrm{m}}$	22.5 mm×4.9 mm×3.2 mm
Segmentation per pole	$c_{\mathrm{m}} \cdot z_{\mathrm{m}}$	18 (circumferential)×4 (axial)
Air gap flux density	$B_{\delta,1}$	0.45 T
Thermal loading	$A \cdot J$	2181 A/cm· A/mm^2
Material	Bandage	Carbon fiber HTS5631+epoxy resin
	Magnet	VACOMAX 225 (Sm_2Co_{17})
	Iron sheet	NO 20
Cooling	Water cooled with jacket on the stator outer surface	

Main critical considerations for the machine design are as follows:

1) Rotor mechanical strength

The magnets are glued on the surface of a laminated rotor iron package and fixed with a carbon fiber bandage on the outer surface. Compared to interior PM machine with magnets buried in the rotor iron, this configuration is more endurable for high velocity. The potential failure is the bandage damage due to high tensile stress in circumferential direction. Even though carbon fiber bandage has very high tensile strength (2615 MPa for the used material HTS5631+epoxy resin), a big safety factor (>3) should be reserved as the strength will decrease for high temperatures. A temperature of 141 °C should not be exceeded for safe operation. Chapter 6.5 presents the detailed stress calculation in the bandage.

2) Rotor losses and thermal limit in vacuum

The magnets are segmented in both radial and axial direction to reduce eddy current losses, which are the dominant heat sources on the rotor. As the rotor operates in vacuum, the heat is dissipated by radiation, which relies on the emissivity of the surface material and the surface area. A rough estimation of the rotor temperature in vacuum is necessary in order to determine the permissible rotor losses for the given temperature limit of 141 °C.

A rough thermal calculation is done by assuming a homogeneous rotor located in an enclosed containment as shown in Fig. 6-3.

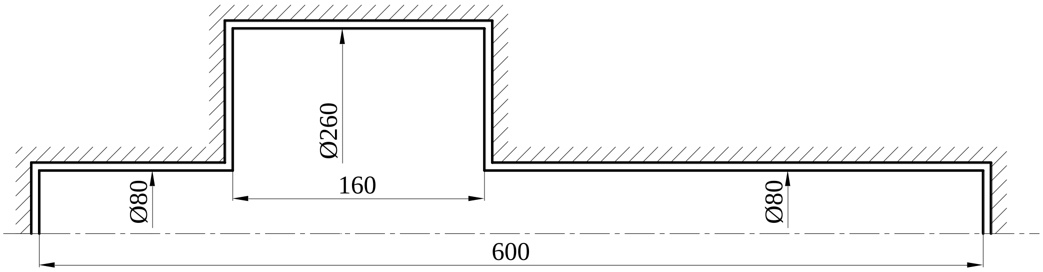

Fig. 6-3 Simplified rotor contour for a rough calculation of the rotor radiative heat transfer

The emissivity of the containment inner surface is assumed to be $\varepsilon_s = 0.95$, which is the value for a black-painted surface. A constant temperature of 60 °C is assumed for the containment. This is also reasonable for a water cooled stator based on the thermal analysis in Chapter 9. According to the calculation in Chapter 9, the rotor steady state temperature is almost homogeneous distributed. A rotor temperature ϑ_r and emissivity ε_r are assumed on the rotor surface. The radiative heat transfer from the rotor to the stator is calculated by

$$P_{\mathrm{rad}} = \frac{\sigma \cdot (T_r^4 - T_s^4)}{\frac{1-\varepsilon_r}{\varepsilon_r \cdot A_r} + \frac{1}{A_r \cdot F_{\mathrm{sr}}} + \frac{1-\varepsilon_s}{\varepsilon_s \cdot A_s}}, \tag{6-1}$$

where the subscript *s* denotes the stator inner surface, *r* denotes the rotor outer surface. F_{sr} is the facing factor depending on the position of the two surfaces. $F_{\mathrm{sr}} = 1$ for a body in an enclosed containment. *A* is the surface area, *T* is the absolute temperature (in K) on the surface (The corresponding celsius temperature is denoted by ϑ in °C), σ is *Stefan-Boltzmann* constant, $\sigma = 5.67\times10^{-8}$ W/(m$^2 \cdot$ K^4), and ε is the surface emissivity.

Fig. 6-4 shows the temperatures for different emissivity ε_r on the rotor surface. If an emissivity $\varepsilon_r = 0.242$ is assumed for a grinded steel rotor surface [49], at the temperature of 141 °C, the radiative heat transfer of 86 W can be calculated from (6-1). That means the rotor losses should be no higher than 86 W to obtain a rotor temperature lower than 141 °C. An efficient radiative heat transfer can be realized by an increased emissivity, e.g. on a black-painted rotor surface.

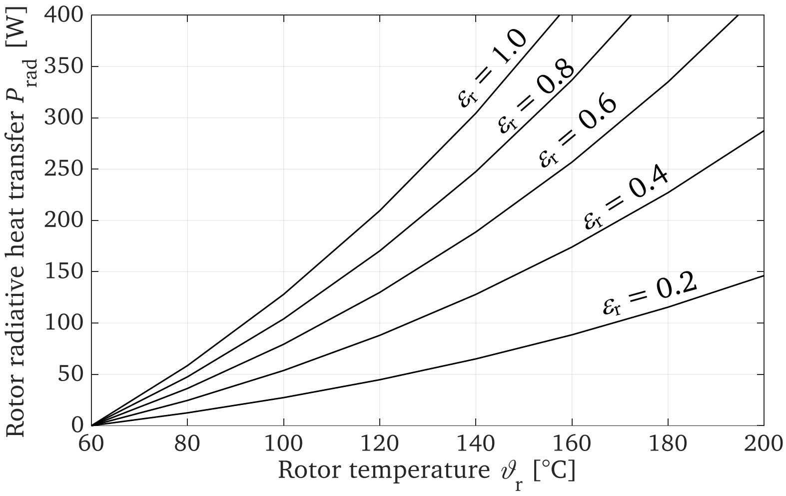

Fig. 6-4 Calculated rotor radiative heat transfer versus rotor temperatures for different rotor surface emissivity ε_r, calculated for an enclosed stator with constant temperature $\vartheta_s = 60$ °C and emissivity $\varepsilon_s = 0.95$ on the inner surface.

3) Efficiency and loss calculation

Loss calculation is important concerning efficiency and thermal performance. The loss calculation (in Chapter 6.3) is performed in numerical program *JMAG*, taking the additional losses due to inverter feeding into account.

4) Demagnetization

The irreversible demagnetization of the magnets should be always avoided for safety, even when failure occurs in the inverter. The demagnetizing performance of the machine is analyzed in Chapter 6.4.3 in case of a three phase short circuit, which is regarded as the most dangerous failure. The used magnet material is VACOMAX 225 (Sm_2Co_{17}). With an almost linear demagnetizing curve, it has a good anti-demagnetizing performance, even at a high temperature of 300 °C.

6.1.3 Outline of This Chapter

This chapter is organized in the following way:

Chapter 6.1 gives an overview of the designed machine and points out the critical considerations in the design. Chapter 6.2 presents the basic design parameters of the machine, including the geometric parameters, stator winding type and magnet material. Based on these parameters, Chapter 6.3 calculates the loss components in *JMAG* program, taking the harmonics caused by the inverter feeding into account. The harmonics are analyzed in Chapter 6.4, as well as the other two electromagnetic performances: the flux weakening performance and the demagnetization at three phase short circuit. Chapter 6.5 introduces the mechanical design of the rotor components, determining the bandage thickness and the fitting.

6.2 E-machine Design Parameters

6.2.1 Stator Design

The stator iron is laminated. The iron sheet type is NO 20 with a thickness of 0.2 mm. The stacking factor is 0.95. The iron is slotted and wound with a three-phase short pitched distributed two-layer winding with $q = 4$. Table 6-3 shows the design parameters of the stator. Fig. 6-5 shows the dimensions of the stator iron sheet. The winding diagram is shown in Appendix B.

The designed current density in the stator winding is 6.9 A/mm^2 and the current loading is 316.1 A/cm for operation at OP$_1$, leading to a thermal loading of $A \cdot J = 2181$ A/cm · A/mm^2. The thermal loading at OP$_2$ is slightly lower than OP$_1$ due to a lower current (Table 6-5). The machine is water cooled with the cooling jacket on the housing. The cooling design is presented in Chapter 9.5.

As the designed machine is a high speed machine. The current frequency is 800 Hz at the maximum operating speed of 24000 min^{-1}. Thus the skin depth of the copper wires is calculated to be 2.36 mm by (6-2). The diameter of the copper wire is determined to be 0.75 mm which is smaller than the skin depth.

$$d_{\mathrm{E}} = \sqrt{\frac{1}{\pi \cdot f \cdot \mu_0 \cdot \mu_{\mathrm{r}} \cdot \sigma}}, \tag{6-2}$$

where f is frequency, $\mu_0 = 4\pi \times 10^{-7}$ is the permeability in vacuum. μ_{r} is the relative permeability and σ is the electrical conductivity of the material. For copper material, $\mu_{\mathrm{r}} = 1$ and $\sigma = 57 \times 10^6$ S/m are used.

Table 6-3 Stator design parameters

Parameter	Symbol	Value	Parameter	Symbol	Value
Pole count	$2p$	4	Nr. of strands per turn	a_i	4
Slot number	Q_s	48	Slot area	A_slot	88.8 mm^2
Short pitching	w/τ_s	10/12	Slot filling factor	k_fill	0.438
Nr. of turns per phase	N_s	44	Current loading at OP_1	A	316.1 A/cm
Nr. of turns per coil	N_c	11	Current density at OP_1	J	6.9 A/mm^2
Parallel branches	a	4	Resistance (phase)	$R_{\mathrm{s},20\,°\mathrm{C}}$	43.81 mΩ
Diameter of wires	d_Cu	0.75 mm		$R_{\mathrm{s},150\,°\mathrm{C}}$	66.15 mΩ

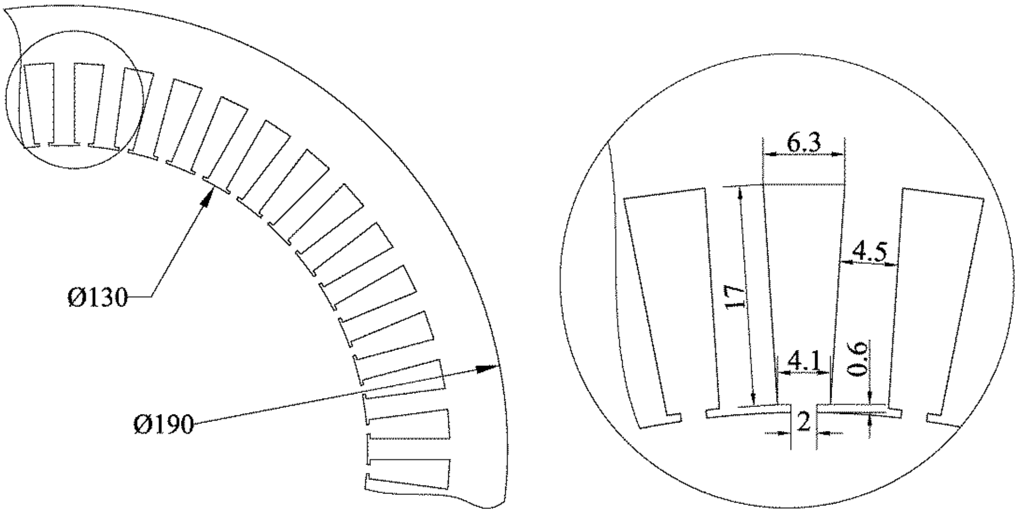

Fig. 6-5 Stator iron design, iron sheet NO 20 (dimensions in mm)

6.2.2 **Rotor Design**

The rotor magnets are mounted on the laminated rotor iron package surface. The iron type is NO 20. The magnets on the rotor are segmented. Each pole has 18 segments in circumferential direction and 4 segments in axial direction. The size of each segment is shown in Table 6-2. A carbon fiber bandage with the thickness of 3 mm is used for protection. The dimension of the rotor components, mainly the height of magnets h_m and the bandage thickness h_B determine the electromagnetic and mechanical performance, which will be discussed in the following chapters.

Table 6-4 Properties of magnet VACOMAX225HR at 20 °C [50]

Parameter	Symbol	Value
Remanence	B_r	1.03 T
Coercivity	H_{cB}	720 kA/m
Magnetic polarization	H_{cJ}	1590 kA/m
Relative permeability	μ_M	1.14
Energy density	$(BH)_{max}$	190 kJ/m^3
Temperature coefficient of remanence	TK_{B_r}	- 0.035 %/K (20-150 °C)
Temperature coefficient of coercivity	$TK_{H_{cJ}}$	- 0.19 %/K (20-150 °C)
Max. continuous temperature	T_{max}	350 °C

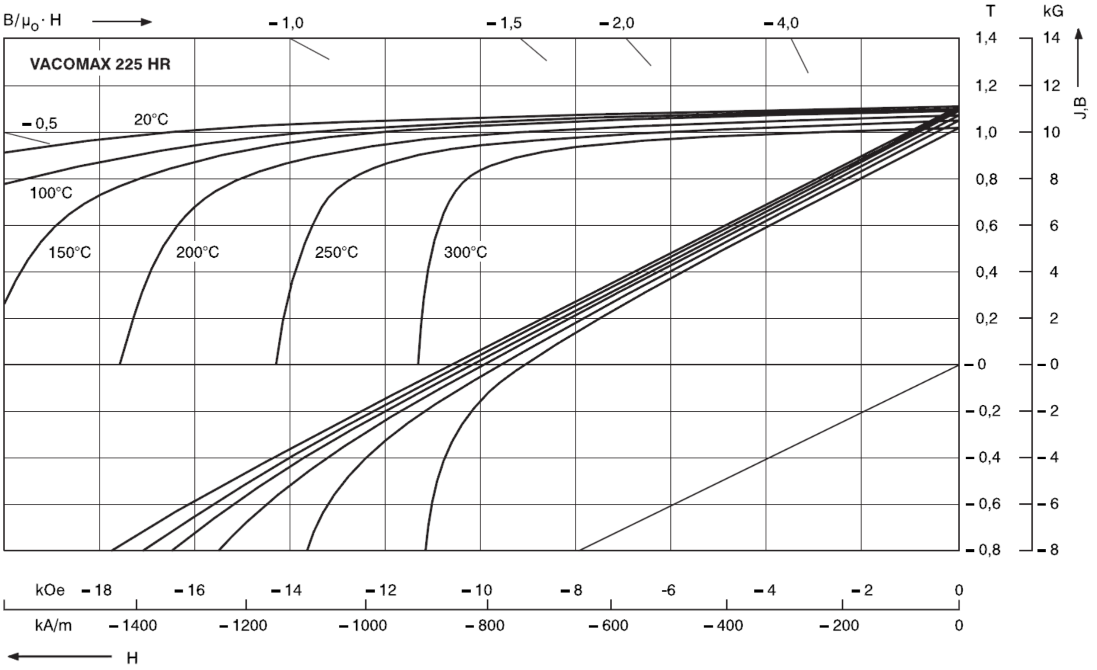

Fig. 6-6 Demagnetizing curves of magnet VACOMAX225HR at different temperatures [50]

The inductance of the designed machine is low due to big air gap, leading to a high short circuit current and high demagnetizing field. To avoid irreversible demagnetization in magnets, the magnet should be “strong” enough against the demagnetizing field. The magnets are more easily get demagnetized at high temperatures, which is critical in our case as the flywheel rotor normally has no effective cooling in vacuum. Compared to NdFeB, the Sm_2Co_{17} material has higher coercivity and magnetic polarization at high temperatures. Therefore, it is used in the design with the properties shown in Table 6-4 and Fig. 6-6.

6.2.3 Air Gap Flux Density

The air gap flux density $B_{\delta,1}$ can be calculated by (6-3) and (6-4), which depends on the thickness of magnets h_m and electromagnetic air gap length δ_e, for which $\delta_\mathrm{e} = \delta + h_\mathrm{B}$ (δ: mechanical air gap, h_B: bandage thickness). A coefficient k_f is introduced in (6-4) considering the effect of the geometry and flux leakage which is calculated by (6-5). The coefficient k_cv considers the effect due to the curvature of the air gap. The air gap in a high speed machine is usually bigger considering the space of the bandage. Since the flux is constant, the flux density on the stator surface is smaller than the rotor surface due to the curvature. This effect is considered by the coefficient k_cv in (6-6). Due to the big air gap, the flux on the stator surface is no longer perpendicular to the geometry, but with a tangential component. Here only the radial component is useful, therefore, the factor k_2D is used to consider this effect and calculated by (6-7). The effect of inter-pole flux leakage is considered by k_str in (6-8). k_gap in (6-9) is due to the small gap between each magnet segment. As the segments are in rectangular shape, the small gaps between each segment occur when they are mounted on the rotor surface.

$$B_{\delta,1} = \frac{4}{\pi} \cdot B_\mathrm{p} \cdot \sin(\alpha_\mathrm{e} \cdot \frac{\pi}{2}) \tag{6-3}$$

$$B_\mathrm{p} = \frac{B_\mathrm{r} \cdot k_\mathrm{f}}{1 + \frac{\delta_\mathrm{e}}{h_\mathrm{m}} \cdot \mu_\mathrm{M}} \tag{6-4}$$

$$k_\mathrm{f} = k_\mathrm{cv} \cdot k_\mathrm{2D} \cdot k_\mathrm{str} \cdot k_\mathrm{gap} \tag{6-5}$$

$$k_\mathrm{cv} = \frac{d_\mathrm{si} - 2 \cdot \delta_\mathrm{e}}{d_\mathrm{si}} \tag{6-6}$$

$$k_\mathrm{2D} = \frac{\pi \cdot \frac{\delta_\mathrm{e}}{\tau_\mathrm{p}}}{\sinh(\pi \cdot \frac{\delta_\mathrm{e}}{\tau_\mathrm{p}})} \tag{6-7}$$

$$k_\mathrm{str} = \sin(\alpha_\mathrm{str} \cdot \frac{\pi}{2}),\ \alpha_\mathrm{str} = \frac{\tau_\mathrm{p} - 2 \cdot \delta_\mathrm{e}}{\tau_\mathrm{p}} \tag{6-8}$$

$$k_\mathrm{gap} = \frac{c_\mathrm{m} \cdot b_\mathrm{m}}{\tau_\mathrm{p}} \tag{6-9}$$

The flux density $B_{\delta,1}$ depending on different combinations of h_m and δ_e can be seen in Fig. 6-7. There are some limitations for the selection of these parameters [76]. One of them is due to the mechanical strength. The thickness of bandage h_B should also be taken into account. As it is influenced by the height of magnets h_m, an iterative calculation should be done to determine $B_{\delta,1}$, h_m and h_B. Other limitations are the performance of the machine, such as the speed range for flux weakening operation, the demagnetization at sudden short circuit, the eddy current losses in the rotor, etc. Therefore, these parameters should be designed very carefully with validations of these performances.

Taking all the performance into account, thickness of magnet $h_\mathrm{m} = 3.2$ mm and the electromagnetic air gap length $\delta_\mathrm{e} = 4$ mm ($h_\mathrm{B} = 3$ mm, $\delta = 1$ mm) are determined in the final design as shown in Fig. 6-7. The corresponding flux density is $B_{\delta,1} = 0.45$ T.

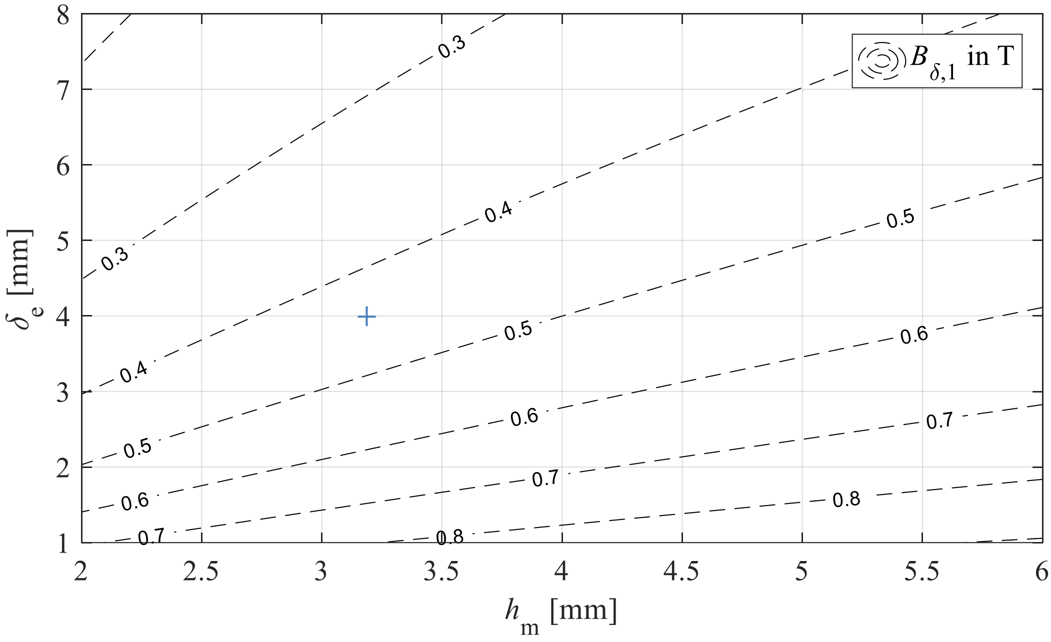

Fig. 6-7 Calculated air gap flux density $B_{\delta,1}$ depending on different combinations of magnet height h_m and electromagnetic air gap δ_e for stator design in Table 6-3, magnet: VACOMAX225HR, 150 °C ("+" final design)

6.3 E-Machine Loss Calculation

The losses in the machine are calculated numerically by a 2D-model in *JMAG*. In order to take the additional losses caused by the harmonics due to the modulation of the inverter into account, the machine is fed by a current source which is superposed by the fundamental and the harmonics. They are obtained from the *Matlab Simulink* model introduced in Chapter 6.4.1. The loss components include iron losses, stator winding losses, losses in the magnets. The overall results are given in Table 6-5 for the operation points OP_1, OP_2 and no load. The air friction loss calculation with low air pressure will be presented in details in Chapter 8.3.

Table 6-5 Calculated E-machine electromagnetic performance and loss components

Parameter	Symbol	Value			
		OP_1	OP_2	No load	
Speed [min^{-1}]	n	12000	24000	12000	24000
Frequency [Hz]	f	400	800	400	800
Back EMF [V]	U_p	191.5	383.0	191.5	383.0
Current [A]	I_s	48.90	46.24	0	31.47
	I_d	0	-39.21	0	-31.47
	I_q	48.90	24.50	0	0
Current angle [°]	β	0	59.73	0	90
Phase voltage (r.m.s.) [V]	$U_{s, ph}$	228.32	228.18	191.5	228.47
Power factor	$\cos\varphi$	0.8489	0.9027	-	-
Electromagnetic torque [Nm]	M_e	22.25	11.2	-	-
Electromagnetic power [kW]	P_e	27960	28149	-	-
Copper losses at 150 °C [W]	$P_{Cu, DC, 150\,°C}$	473.5	424.2	0	196.3
	$P_{Cu, AC, 150\,°C}$	496.4	486.4	0	221.8
Iron losses in stator teeth [W]	$P_{Fe,st}$	135.8	277.2	116.4	277.5
Iron losses in stator yoke [W]	$P_{Fe,sy}$	226.3	211.1	164.4	219.2
Losses in magnets [W]	P_{PM}	26.4	28.4	0.4	29.4
Losses in rotor iron [W]	$P_{Fe,r}$	4.8	5.4	1.0	4.1
Air friction losses [W]	P_{fr}	0.104	0.417	0.104	0.417
Total losses [W]	P_d	875.9	975.5	282.3	740.4
Efficiency [%]	η	96.96	96.65	-	-

6.3.1 Losses in Laminated Iron

A 2D model is built in *JMAG* for the field calculation. After that the iron losses are computed by a loss solver in *JMAG* which is a post processing based on the magnetic field analysis results. The excess losses are considered to be negligible small, thus the total iron losses are divided into hysteresis and eddy current losses. In the simulation, the loss table of the iron sheet, which is usually provided by the manufacture, is given as the input data. *JMAG* performs the frequency separation treatment with the loss table in order to obtain the loss coefficients. The specific iron loss in W/kg is expressed as [51]

$$p_{Fe} = a(B) \cdot f + b(B, f) \cdot f^2, \tag{6-10}$$

where B is the flux density in T and f is the frequency in Hz. a (in W/(kg·Hz)) and b (in in W/(kg·Hz^2)) are the coefficients for arbitrary B and f. Based on the given loss table, *JMAG* computes the coefficients $a(B)$ and $b(B, f)$ for the given B and f in the loss table. After performing the field analysis of the existing model and obtaining the flux density of each element, *JMAG* performs a *Fourier* decomposition of the flux density in time domain and generates the flux density B_k and the corresponding frequency f_k for k-th harmonic. Thus the specific iron loss can be calculated by

$$p_{\mathrm{Fe}} = \sum_k f_k \cdot a\left(\left|B_k\right|\right) + \sum_k f_k^2 \cdot b\left(\left|B_k\right|, f_k\right), \tag{6-11}$$

where $a(|B_k|)$ and $b(|B_k|, f_k)$ are obtained by linear interpolation of the computed coefficients from the loss table.

This method is a straightforward approach for the loss calculation based on the interpolant fitting of the given loss table. A low precision occurs if the calculated frequency exceeds the given frequency due to the linear interpolation. Also the effect of rotational magnetization of the iron is not considered.

After getting the numerical results, two correction factors are used considering the effect of the bridging between the iron sheets due to the insulation damage during the laser cutting process. A loss increase factor of $k_{\mathrm{Vd}} = 1.8$ is used for the stator teeth and $k_{\mathrm{Vy}} = 1.5$ is used for the stator yoke and rotor laminated iron. The calculated iron losses are shown in Table 6-5.

6.3.2 Losses in Stator Winding

Due to the switching effect of the inverter, the current fed into the stator winding is not an ideal sinusoidal waveform, but can be regarded as a sum of sinusoidal waveforms with different amplitudes and frequencies after *Fourier* analysis. The resistive losses for the k-th current harmonic I_{sk} can be calculated by (6-12), with the resistance R_{s} at operating temperature ϑ in °C, which is calculated by (6-13). $R_{\mathrm{s},\vartheta_0}$ is the resistance (in Ω) measured at temperature ϑ_0 in °C.

$$P_{\mathrm{Cu,\,DC},\,k} = 3 \cdot I_{sk}^2 \cdot R_{\mathrm{s}} \tag{6-12}$$

$$R_{\mathrm{s}} = R_{\mathrm{s},\vartheta_0} \cdot \left(1 + \frac{\vartheta - \vartheta_0}{235 + \vartheta_0}\right) \tag{6-13}$$

R_s is called DC resistance which is measured for a DC current feeding. If the current is alternating, additional eddy current will be induced due to the slot stray flux, leading to additional copper losses.

According to [52], the copper losses $P_{\mathrm{Cu,AC},k}$ consist of the resistive losses $P_{\mathrm{Cu,DC},k}$ calculated by (6-12) and the additional eddy current losses due to skin and proximity effect $P_{\mathrm{Cu,add,pr}}$ and due to the circulating current $P_{\mathrm{Cu,add,circ}}$, as described by

$$P_{\mathrm{Cu,\,AC,}\,k} = P_{\mathrm{Cu,\,DC,}\,k} + P_{\mathrm{Cu,\,add,\,pr}} + P_{\mathrm{Cu,\,add,\,circ}}\,. \tag{6-14}$$

The skin and proximity effect refers to the unevenly distributed current density on the cross section of each single copper wire in the slot, regardless of the circuit connections of these wires. The effect depends on the slot shape, slot stray flux, wire shapes, etc. The designed E-machine adopted round wires in trapezoidal slots (Fig. 6-8). To estimate this effect, a simplified assumption is made for multiple square wires in a rectangular slot as shown in Fig. 6-8. The equivalent square wire has the same cross section area as the round wires and the dimension is calculated by

$$b_{\mathrm{T}} = \sqrt{\frac{\pi}{4} \cdot d_{\mathrm{Cu}}^2}\,, \tag{6-15}$$

where d_{Cu} is the round wire diameter.

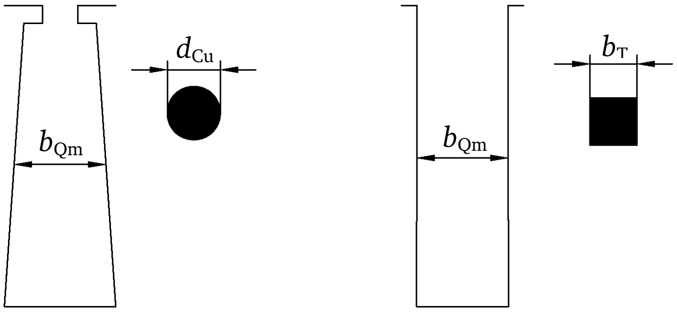

Fig. 6-8 Designed (left) and equivalent (right) slot shape and wire section (b_{Qm}: average slot width)

6.3.2.1 Additional Losses due to Skin and Proximity Effect

The additional losses $P_{\mathrm{Cu,add,pr}}$ due to skin and proximity effect can be calculated by [52]

$$P_{\mathrm{Cu,\,add,\,pr}} = 3 \cdot I_{sk}^2 \cdot R_{\mathrm{s}} \cdot \left(\overline{k}_{sk,\,\mathrm{pr}} - 1\right) = P_{\mathrm{Cu,\,DC,}\,k} \cdot \left(\overline{k}_{sk,\,\mathrm{pr}} - 1\right), \tag{6-16}$$

with

$$\bar{k}_{sk,\,\mathrm{pr}} = \frac{l_{\mathrm{Fe}} \cdot k_{sk,\,\mathrm{pr}} + l_{\mathrm{b}}}{l_{\mathrm{Fe}} + l_{\mathrm{b}}}, \tag{6-17}$$

$$k_{sk,\,\mathrm{pr}} = \varphi\left(\xi_{\mathrm{T}k}\right) + \frac{m_{\mathrm{T}}^{2} - 1}{3} \cdot \psi\left(\xi_{\mathrm{T}k}\right), \tag{6-18}$$

$$\varphi\left(\xi_{\mathrm{T}k}\right) = \xi_{\mathrm{T}k} \cdot \frac{\sinh\left(2 \cdot \xi_{\mathrm{T}k}\right) + \sin\left(2 \cdot \xi_{\mathrm{T}k}\right)}{\cosh\left(2 \cdot \xi_{\mathrm{T}k}\right) - \cos\left(2 \cdot \xi_{\mathrm{T}k}\right)}, \tag{6-19}$$

$$\psi\left(\xi_{\mathrm{T}k}\right) = 2 \cdot \xi_{\mathrm{T}k} \cdot \frac{\sinh\left(\xi_{\mathrm{T}k}\right) - \sin\left(\xi_{\mathrm{T}k}\right)}{\cosh\left(\xi_{\mathrm{T}k}\right) + \cos\left(\xi_{\mathrm{T}k}\right)}, \tag{6-20}$$

$$\xi_{\mathrm{T}k} = b_{\mathrm{T}} \sqrt{\mu_0 \cdot \pi \cdot \kappa_{\mathrm{Cu}} \cdot f_{sk} \cdot a_{\mathrm{T}} \cdot b_{\mathrm{T}} / b_{\mathrm{Qm}}}, \tag{6-21}$$

where a_{T} is the number of horizontally placed wires in one slot and m_{T} is the total number of vertically placed wires in one slot. They can be calculated by (6-22) and (6-23). b_{Qm} is the average slot width. l_{Fe} is the length of the laminated iron package, l_{b} is the length of the overhang winding. As stray flux at the winding overhang can be neglected, no current displacement occurs in this part. Thus a corrected coefficient $\bar{k}_{sk,\,\mathrm{pr}}$ is used in (6-17) instead of $k_{sk,\,\mathrm{pr}}$.

$$a_{\mathrm{T}} = \frac{b_{\mathrm{Qm}} \cdot \sqrt{k_{\mathrm{fill}}}}{b_{\mathrm{T}}} \tag{6-22}$$

$$m_{\mathrm{T}} = \frac{2 \cdot N_{\mathrm{c}} \cdot a_{\mathrm{i}}}{a_{\mathrm{T}}} \tag{6-23}$$

In (6-22), k_{fill} is the slot filling factor, which is the ratio of total copper wires section area to the slot area. N_{c} is number of turns per coil.

The winding of the designed machine has $N_{\mathrm{c}} = 11$ turns for each coil with $a_{\mathrm{i}} = 4$ parallel strands for each turn. Thus in each slot, 44 wires should be arranged for both upper and lower layer. The diameter of the round wire is $d_{\mathrm{Cu}} = 0.75$ mm, thus the equivalent dimension of the assumed squre wire, calculated by (6-15), is $b_{\mathrm{T}} = 0.665$ mm. An average slot width $b_{\mathrm{Qm}} = 5.2$ mm is obtained from the stator geometry in Fig. 6-5. With the slot filling factor of $k_{\mathrm{fill}} = 0.438$, a feasible arrangement of the wires in one slot is: $a_{\mathrm{T}} = 5$ and $m_{\mathrm{T}} = 18$ as shown in Fig. 6-9 a).

6.3.2.2 Additional Losses due to Circulating Current in Parallel Wires

The second type additional losses $P_{\mathrm{Cu,add,circ}}$ occurs when a coil contains several parallel strands. Depending on the positions of these parallel strands in one slot, the induced

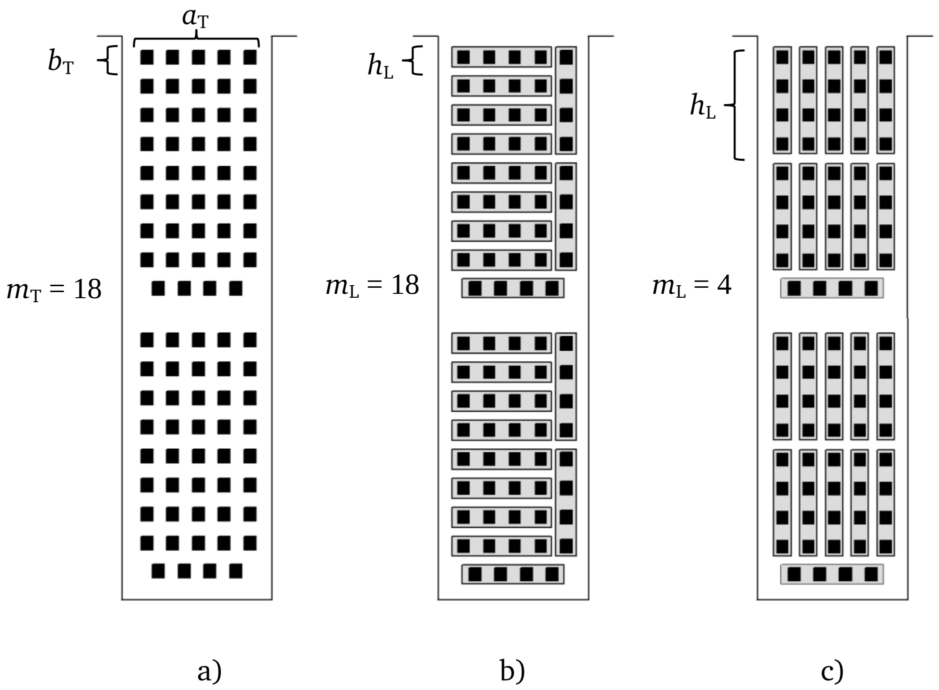

Fig. 6-9 Wire arrangements for the additional losses calculation: a) due to skin and proximity effect, b) due to circulating current: best case, c) due to circulating current: worst case

voltage in each parallel strands differs and thus leads to a circulating current within these parallel strands. As in real case, the arrangement of the wires are irregular, the losses can be estimated by considering an average of the best case and worst case as shown in Fig. 6-9. As the voltage induced in one single wire varies depending on the vertical position in the slot, the best case is to arrange the parallel strands horizontally as much as possible, thus reducing the voltage potential between two parallel strands and therefore the circulating current. For the worst case, on the contrary, the parallel strands are prioritized to be placed vertically as shown in Fig. 6-9 c).

Concerning the arrangement of parallel strands, the best case is shown in Fig. 6-9 b): 9 turns have horizontally arranged parallel strands and 2 turns have vertically arranged parallel strands. The equivalent h_L is $(1 \times 9 + 4 \times 2) / 11 \cdot b_T = 1.55 \cdot b_T$ and $m_L = 18$. The worst case is shown in Fig. 6-9 c): 10 turns have vertically arranged parallel strands and 1 turn has horizontally arranged parallel strands. The equivalent h_L is $(4 \times 10 + 1 \times 1) / 11 \cdot b_T = 3.73 \cdot b_T$ and $m_L = 4$.

The additional losses $P_{Cu,add,circ}$ can be calculated by [52]

$$P_{\mathrm{Cu,\,add,\,circ}} = 3 \cdot I_{sk}^2 \cdot R_s \cdot \left(k_{sk,\,\mathrm{circ}} - 1\right) = P_{\mathrm{Cu,\,DC},\,k} \cdot \left(k_{sk,\,\mathrm{circ}} - 1\right), \tag{6-24}$$

with

$$k_{sk,\,\mathrm{circ}} = \varphi(\xi_k) + \eta \cdot (\eta + 1) \cdot \psi(\xi_k), \tag{6-25}$$

$$\xi_k = h_{\mathrm{L}} \cdot \sqrt{\mu_0 \cdot \pi \cdot \kappa_{\mathrm{Cu}} \cdot f_{sk} \cdot \frac{l_{\mathrm{Fe}}}{l_{\mathrm{Fe}} + l_{\mathrm{b}}} \cdot a_{\mathrm{T}} \cdot b_{\mathrm{T}} / b_{\mathrm{Qm}}}\ , \tag{6-26}$$

$$\eta = \frac{m_{\mathrm{L}} - 1}{2}, \tag{6-27}$$

where h_{L} is the height of vertically placed wires of the parallels strands.

Table 6-6 Calculated copper losses in the winding for the current harmonics calculated in Chapter 6.4.1, winding resistance $R_{\mathrm{s}} = 0.06615\ \Omega$ at temperature $\vartheta = 150$ °C

(f: harmonic frequency, $\hat{I}_{sk}$: current amplitude, $P_{\mathrm{Cu,DC},k}$: DC resistive losses, $P_{\mathrm{Cu,AC},k}$: AC resistive losses, $P_{\mathrm{Cu,add,pr}}$: additional losses due to skin and proximity effect, $P_{\mathrm{Cu,add,circ}}$: additional losses due to circulating current in the winding)

OP$_1$: 12000 min^{-1}								
f [Hz]	$\hat{I}_{sk}$ [A]	$P_{\mathrm{Cu,add,pr}}/P_{\mathrm{Cu,DC},k}$	$P_{\mathrm{Cu,add,circ}}/P_{\mathrm{Cu,DC},k}$			$P_{\mathrm{Cu,DC},k}$ [W]	$P_{\mathrm{Cu,AC},k}$ [W]	$P_{\mathrm{Cu,AC},k}/P_{\mathrm{Cu,DC},k}$
			best case	worst case	average			
400	69.1	1.01	1.02	1.03	1.03	473.15	488.55	1.03
10400	0.8	7.93	14.42	14.58	14.50	0.06	1.19	18.78
11200	1	9.01	16.52	15.80	16.16	0.10	2.10	21.17
12800	0.9	11.40	21.13	18.08	19.60	0.080	2.11	26.25
13600	0.6	12.70	23.63	19.12	21.38	0.036	1.03	28.92
22000	0.3	30.23	57.15	27.02	42.09	0.0089	0.55	62.21
23600	0.2	34.27	64.81	28.07	46.44	0.0040	0.28	69.52
24400	0.2	36.36	68.76	28.56	48.66	0.0040	0.29	73.27
26000	0.2	40.67	76.90	29.47	53.19	0.0040	0.32	80.97
Σ	-	-	-	-	-	473.45	496.42	1.05
OP$_2$: 24000 min^{-1}								
f [Hz]	$\hat{I}_{sk}$ [A]	$P_{\mathrm{Cu,add,pr}}/P_{\mathrm{Cu,DC},k}$	$P_{\mathrm{Cu,add,circ}}/P_{\mathrm{Cu,DC},k}$			$P_{\mathrm{Cu,DC},k}$ [W]	$P_{\mathrm{Cu,AC},k}$ [W]	$P_{\mathrm{Cu,AC},k}/P_{\mathrm{Cu,DC},k}$
			best case	worst case	average			
800	65.4	1.04	1.08	1.13	1.11	423.84	478.94	1.13
8800	0.9	5.98	10.67	11.97	11.32	0.08	1.15	14.32
10400	1.1	7.93	14.42	14.58	14.50	0.12	2.25	18.78
13600	0.8	12.70	23.63	19.12	21.38	0.063	1.83	28.92
15200	0.5	15.51	29.04	21.04	25.04	0.025	0.86	34.55
20000	0.3	25.47	48.09	25.56	36.82	0.0089	0.48	53.48
23200	0.2	33.24	62.86	27.82	45.34	0.0040	0.27	67.67
24800	0.2	37.42	70.77	28.79	49.78	0.0040	0.30	75.17
28000	0.2	46.30	87.46	30.51	58.99	0.0040	0.36	90.91
Σ	-	-	-	-	-	424.15	486.43	1.15

In case of short pitching, several slots are filled with windings in different phases. The induced voltages of the upper and lower winding in such slots have a phase shift. A correction factor $k_{\mathrm{s,ph}}$ is used to consider this effect. Thus (6-16) and (6-24) should be corrected by

$$P_{\mathrm{Cu,\,add,\,pr}} = P_{\mathrm{Cu,\,DC,}\,k} \cdot k_{\mathrm{s,\,ph}}^2 \cdot \left(\bar{k}_{\mathrm{s}k,\,\mathrm{pr}} - 1\right), \tag{6-28}$$

$$P_{\mathrm{Cu,\,add,\,circ}} = P_{\mathrm{Cu,\,DC,}\,k} \cdot k_{\mathrm{s,\,ph}}^2 \cdot \left(k_{\mathrm{s}k,\,\mathrm{circ}} - 1\right). \tag{6-29}$$

The designed machine adopts a double-layer short pitching winding in 48 slots with w/τ_{s} = 10/12. The winding arrangement leads to 24 slots filled with different phases. Therefore, the correction factor $k_{\mathrm{s,ph}}$ is 0.933.

The copper losses of the designed machine are calculated in Table 6-6 concerning the current harmonics calculated in Chapter 6.4.1. At the operation speed of 12000 min^{-1} and rated power, the current displacement effect causes 5 % additional losses. At the operation speed of 24000 min^{-1} and the rated power, 15 % additional losses will be caused.

6.3.3 Losses in the Magnets

The eddy current losses in the magnets are induced by the fields in the air gap which are asynchronously rotating with the rotor field. These fields are from the m.m.f. excited by the stator side and from the current time harmonics. The stator winding, fed by a time-sinusoidal current, excites the stator field in the air gap which can be described by

$$B_{\delta,\mathrm{s}} = \sum_{\mu=1}^{\infty} B_{\delta,\mu} \cdot \cos\left(\mu \cdot p \cdot \theta - \omega_{\mathrm{s},1} \cdot t - \varphi_{\mu}\right). \tag{6-30}$$

μ is order of the spatial-distributed harmonics. p is the pole count. ω_{s} is the angular frequency of the current, with subscript “1” denoting fundamental, i.e. a sinusoidal current feeding.

If the stator winding is fed by a non-sinusoidal current, which contains k-th time harmonics, each harmonic excites a series of spatial harmonics. The sum of all the spatial and time harmonics can be described by

$$B_{\delta,\mathrm{s}} = \sum_{\mu,k=1}^{\infty} B_{\delta,\mu,k} \cdot \cos\left(\mu \cdot p \cdot \theta - k \cdot \omega_{\mathrm{s},1} \cdot t - \varphi_{\mu,k}\right). \tag{6-31}$$

The distribution of these harmonics can be regarded as a series of rotating waves in the air gap with a wave length λ and mechanical rotating speed Ω, calculated by

$$\lambda = \frac{2\cdot\pi}{\mu\cdot p} = \frac{\lambda_1}{\mu},\ \lambda_1 = \frac{2\cdot\pi}{p}, \tag{6-32}$$

$$\Omega = \frac{k\cdot\omega_{\mathrm{s,1}}}{\mu\cdot p} = \frac{k}{\mu}\cdot\Omega_1,\ \Omega_1 = \frac{\omega_{\mathrm{s,1}}}{p}, \tag{6-33}$$

where λ_1 and Ω_1 are expressions for the fundamentals ($\mu = 1$, $k = 1$).

Table 6-7 shows the characteristics of various harmonic waves. The time and spatial fundamentals ($\mu = 1$, $k = 1$) have the same rotating speed with the rotor, inducing no losses in the rotor. The spatial harmonics ($\mu \neq 1$, $k = 1$) have shorter spatial wave length and lower rotating speed compared to the fundamental, thus inducing eddy current in the rotor. In terms of time harmonics ($\mu = 1$, $k \neq 1$), the spatial field distribution excited by each time harmonic have the same spatial harmonic order and wave length. But the traveling speed is proportionally increased for higher order time harmonics, as the current alternates in higher frequencies. These harmonics will also induce eddy current losses in the rotor which normally have larger contribution than the spatial harmonics, if the current waveform is not ideally sinusoidal.

Table 6-7 Characteristics of the rotating waves in the air gap concerning various time and spatial harmonic orders (fundamental described with subscript 1)

Time harmonic order k	Spatial harmonic order μ	Wave frequency (ele.) f	Wave length (mech.) λ	Rotating speed (mech.) Ω
1	1	f_1	λ_1	Ω_1
1	μ	f_1	λ_1/μ	Ω_1/μ
k	1	$k\cdot f_1$	λ_1	$k\cdot\Omega_1$
k	μ	$k\cdot f_1$	λ_1/μ	$k\cdot\Omega_1/\mu$

In this thesis, the magnetic losses are calculated numerically with a 2D-model in *JMAG*. Each magnet segment is modeled to consider the effect of radial segmentation. To consider the effect of the axial segmentation, the conductivity of the magnets κ_{m} used in the 2D-model is modified by [53]

$$\kappa_{\mathrm{m,eff}} = \kappa_{\mathrm{m}}/(1 + b_{\mathrm{m}}/l_{\mathrm{m}}), \tag{6-34}$$

where κ_{m} is the physical conductivity of the magnet material. b_{m} and l_{m} are the width and length of each segment. The total calculated eddy current losses in the magnets are shown in Table 6-5.

The harmonics in the air gap penetrate the magnets and also cause losses in the rotor iron package which are also calculated and included in Table 6-5.

6.4 E-machine Electromagnetic Performance

6.4.1 Harmonic Analysis due to PWM Drive

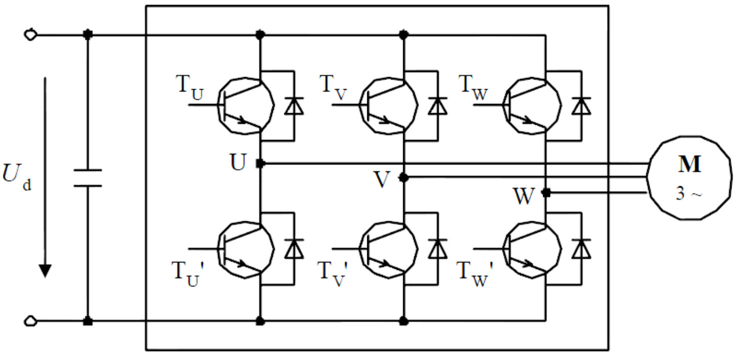

Fig. 6-10 Scheme of 3-phase voltage source inverter, U_d: DC link voltage, figure source: [52]

The machine is fed by a voltage source inverter with the DC link voltage of 560 V. By turning the switches on and off, the output voltage is modulated, distinguished by multiple pulses of variable widths and constant amplitude. The spectrum of the voltage due to the pulse width modulation (PWM) contains a fundamental signal and a series of harmonics, depending on the modulation depth, switching frequency and the frequency of modulating wave. These harmonics cause additional losses in the machine which should be taken into account. This chapter analyzes these harmonics and the results (Table 6-8) will be used as the current feeding source in the *JMAG* model in Chapter 6.3. In order to analyze the harmonics of the power supply due to the PWM control, a simulation model is built in *Matlab Simulink*. This model simulates open loop operation of the machine, i.e. the machine is fed by a modulated voltage source without active control of speed or current. By applying the modulation index and the phase angle of the carrier wave, the model generates the corresponding switching control signals which are applied to the IGBTs, thus the output voltage of the inverter is modulated and fed to the machine. With given machine parameters: inductance, resistance and pole numbers, the current and electromagnetic torque with parasitic harmonics can be calculated. Compared to the sophisticated control loop in a real inverter, this model calculates straightforward the harmonic components due to PWM in a machine with a much simplified driving topology.

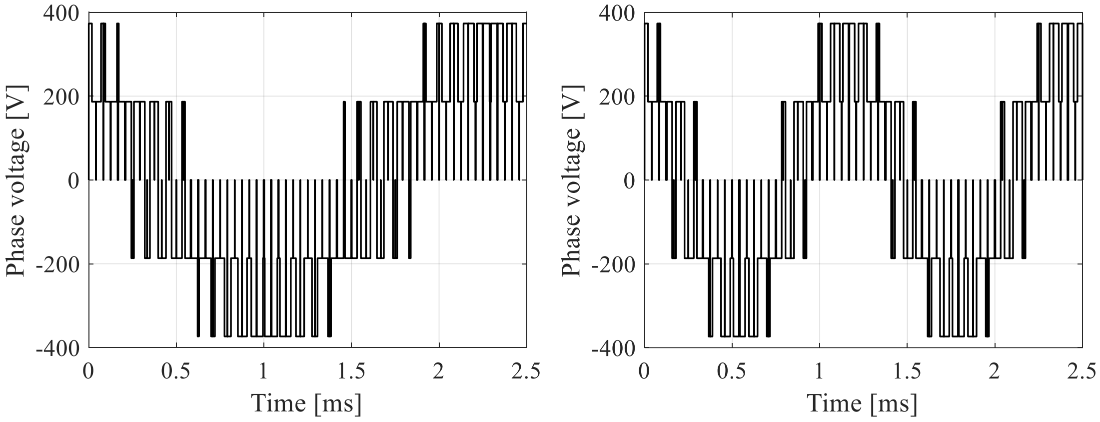

a) 400 Hz 800 Hz

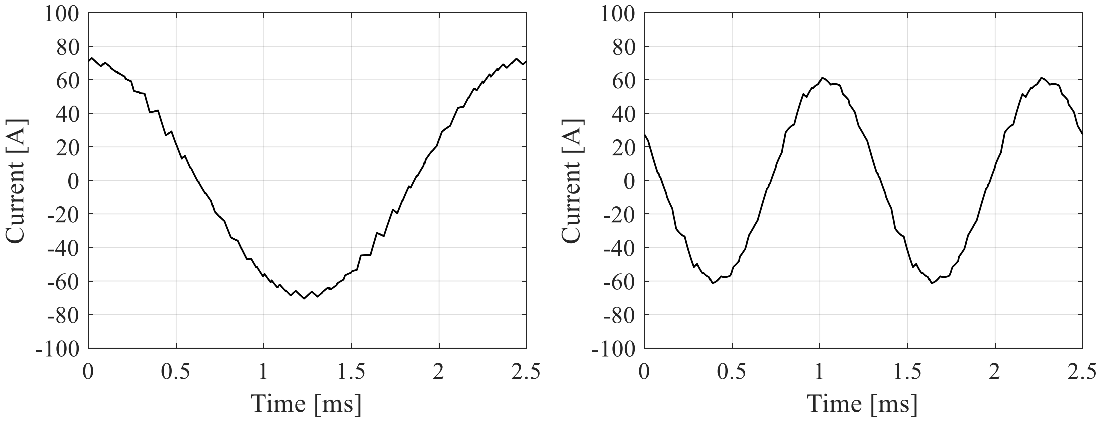

b) 400 Hz 800 Hz

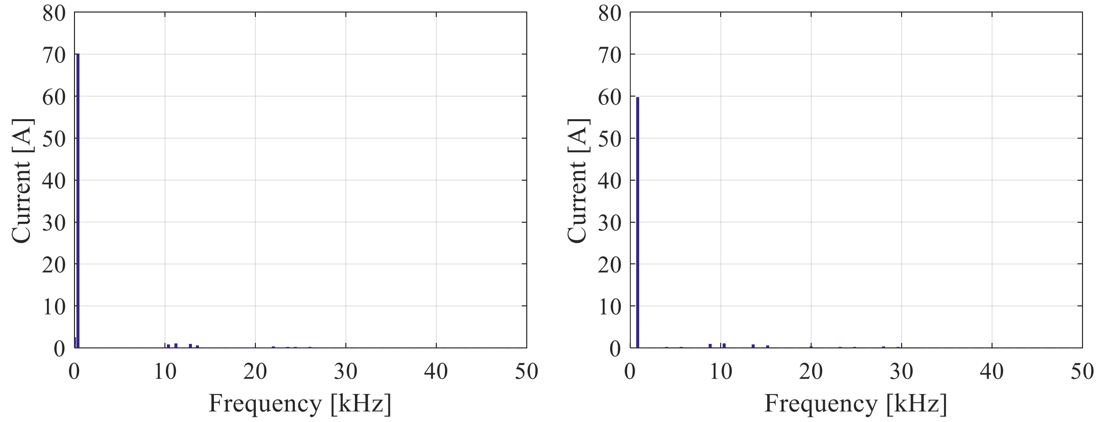

c) 400 Hz 800 Hz

Fig. 6-11 Calculated voltage and current waveforms and current harmonics of phase *U* in the inverter-fed PM machine, switching frequency $f_{\mathrm{T}} = 12$ kHz : a) phase voltage, b) current, c) harmonics of current

The modulated voltage and current waveform of a single phase *U* for OP_1 and OP_2 are shown in Fig. 6-11, as well as the current harmonic analysis. The fundamental and 8 main harmonic components of current are shown in Table 6-8. The switching frequency is $f_\mathrm{T} = 12\ \mathrm{kHz}$.

Table 6-8 Calculated main harmonic components of the current of phase *U* in Fig. 6-11 c), switching frequency $f_\mathrm{T} = 12\ \mathrm{kHz}$

OP$_1$: 12000 min^{-1}				OP$_2$: 24000 min^{-1}		
Frequency [Hz]		Current [A]	Phase angle [°]	Frequency [Hz]	Current [A]	Phase angle [°]
f_s	400	69.1	0	800	65.4	58
$f_\mathrm{T} - 4 \cdot f_\mathrm{s}$	10400	0.8	-36	8800	0.9	-40.6
$f_\mathrm{T} - 2 \cdot f_\mathrm{s}$	11200	1	-153.1	10400	1.1	-154.7
$f_\mathrm{T} + 2 \cdot f_\mathrm{s}$	12800	0.9	-27.2	13600	0.8	-25.1
$f_\mathrm{T} + 4 \cdot f_\mathrm{s}$	13600	0.6	-144.4	15200	0.5	-138.9
$2 \cdot f_\mathrm{T} - 5 \cdot f_\mathrm{s}$	22000	0.3	-67.6	20000	0.3	-69.4
$2 \cdot f_\mathrm{T} - f_\mathrm{s}$	23600	0.2	58.4	23200	0.2	56.9
$2 \cdot f_\mathrm{T} + f_\mathrm{s}$	24400	0.2	121	24800	0.2	122.9
$2 \cdot f_\mathrm{T} + 5 \cdot f_\mathrm{s}$	26000	0.2	-113.2	28000	0.2	-124.6

6.4.2 Field Oriented Control and Flux Weakening

The machine operates with field oriented control following the operating characteristics in Fig. 6-1. Flux weakening is required for the speed from n_min to n_max with a constant power. For the surface mounted magnet rotor configuration, the electromagnetic air gap is relatively big due to the use of bandage, leading to a rather low inductance. The flux weakening range cannot be infinite but limited by the maximum current. Considering only the fundamental and neglecting the resistance, the restrictions for a constant power field weakening operation can be described by the following equations:

1) Voltage limit:

$$\left(\omega \cdot \Psi_\mathrm{p} + \omega \cdot L_\mathrm{d} \cdot \hat{I}_\mathrm{d}\right)^2 + \left(\omega \cdot L_\mathrm{q} \cdot \hat{I}_\mathrm{q}\right)^2 = \hat{U}_\mathrm{s}^2 \le \hat{U}_\mathrm{s,max}^2 \tag{6-35}$$

2) Current limit:

$$\hat{I}_\mathrm{d}^2 + \hat{I}_\mathrm{q}^2 = \hat{I}_\mathrm{s}^2 \le \hat{I}_\mathrm{s,max}^2 \tag{6-36}$$

3) Power requirement:

$$P_\mathrm{e} = \frac{m}{2} \cdot \omega \cdot \Psi_\mathrm{p} \cdot \hat{I}_\mathrm{q} \tag{6-37}$$

6.4.2.1 Voltage and Current Circle Diagram

By modifying (6-35), the voltage limit can be further written as:

$$\left(\Psi_{\mathrm{p}} + L_{\mathrm{d}} \cdot \hat{I}_{\mathrm{d}}\right)^2 + \left(L_{\mathrm{q}} \cdot \hat{I}_{\mathrm{q}}\right)^2 \le \left(\frac{\hat{U}_{\mathrm{s,max}}}{\omega}\right)^2 . \tag{6-38}$$

The pole coverage ratio is approximated to be one for the surface mounted magnet rotor configuration in Fig. 6-2, neglecting the small gaps between each segmentation. The inductance $L_{\mathrm{d}} = L_{\mathrm{q}}$. Thus, the voltage limit can be drawn in the *d*-*q* reference frame as a circle with the origin on the *d*-axis shown in Fig. 6-12. The origin is shifted from the coordinate center by a distance of $\Psi_{\mathrm{p}}/L_{\mathrm{d}}$. The radius of the circle is $\hat{U}_{\mathrm{s,max}}/\omega$, which becomes smaller as the operating speed increases.

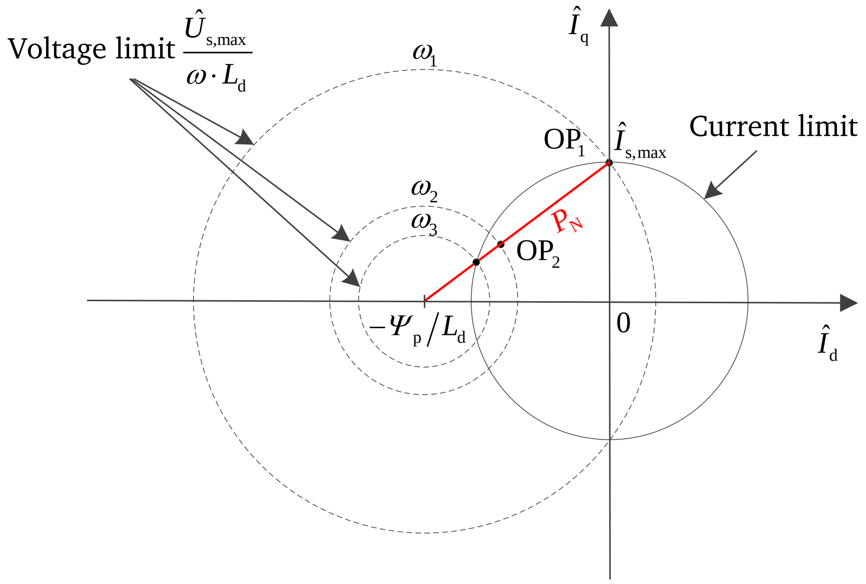

Fig. 6-12 Circle diagram of stator current limit $\hat{I}_{\mathrm{max}}$ and voltage limit $\hat{U}_{\mathrm{s,max}}$ for flux weakening operation, $\omega_1 < \omega_2 < \omega_3$, red line: constant power line, P_{N}: rated power.

The current limit can be also drawn in the same coordinate, which is a circle with the center on the origin. The feasible operating points should locate in the intersection area of the voltage limit and current limit. The constant power line (red line) is also drawn. The operating points on the constant power line produce a constant power. Here define the speed ω_1 to be the maximum speed for constant torque operation, corresponding to the minimum operating speed of the flywheel n_{min} in Fig. 6-1. When the speed is higher than ω_1, the field weakening starts and the voltage limit circle becomes smaller. For a constant power field weakening, the operating point is the intersection of the voltage limit and the constant power line, which moves along the constant power line towards the point ($-\Psi_p / L_d$, 0) until the speed reaches ω_3, when the current limit is reached. Then operating point moves along the current limit circle towards *d*-axis with a decreasing power until zero.

According to the requirements in Fig. 6-1, the operating point OP_1 is defined as shown in Fig. 6-12 which is the intersection of the current limit circle and the *q*-axis, which means $\hat{I}_d = 0$, $\hat{I}_q = \hat{I}_{s,\max}$ and produces the maximum torque which is regarded as the rated torque. OP_1 should not locate outside of the voltage circle at ω_1. Otherwise the operating point at $n_{\min}$ in Fig. 6-1 cannot be fulfilled. The operating point OP_2 should locate on the constant power line and the speed at OP_2 which is ω_2 (or $n_{\max}$ corresponding to the maximum operating speed of the flywheel), should be between ω_1 and ω_3 as shown in Fig. 6-12. This also means the intersection of the voltage limit circle and the constant power line should locate inside of the current limit at ω_2, otherwise the constant power at ω_2 cannot be fulfilled in Fig. 6-1.

Fig. 6-12 can be used to judge if the designed machine fulfills the field weakening requirements. As the diagram is determined by the parameters Ψ_p and L_d, for different Ψ_p and L_d different cases may occur as shown in Fig. 6-13, where ω_1 and ω_2 correspond to $n_{\min}$ and $n_{\max}$ of the flywheel in Fig. 6-1 and Ψ_p and L_d are variable. For a simplified assumption, Ψ_p / L_d remains constant. As the purpose here is to point out how the voltage and current limitations are surpassed for different design parameters, Ψ_p / L_d is not relevant for the judgment criteria.

For OP_1, different inductance L_d result in 3 locations of the voltage limit circle at the same speed ω_1. Circle 1) and 2) are feasible. If the inductance L_d is relatively big, a smaller circle 3) will occur which is infeasible as OP_1 locates outside of the voltage limit circle 3), which means the voltage limit is surpassed when the current is applied to obtain the required power.

For OP_2 at the speed ω_2, circle 1') and 2') are feasible as the intersection of the voltage limit circle and the constant power line locates inside of the current limit. Similarly a big inductance L_d leads to a smaller voltage circle 3'), thus the intersection of the voltage circle and the constant power line is outside of the current limit or the intersection of the voltage limit circle and the current circle leaves the constant power line. Therefore, circle 3') is not feasible.

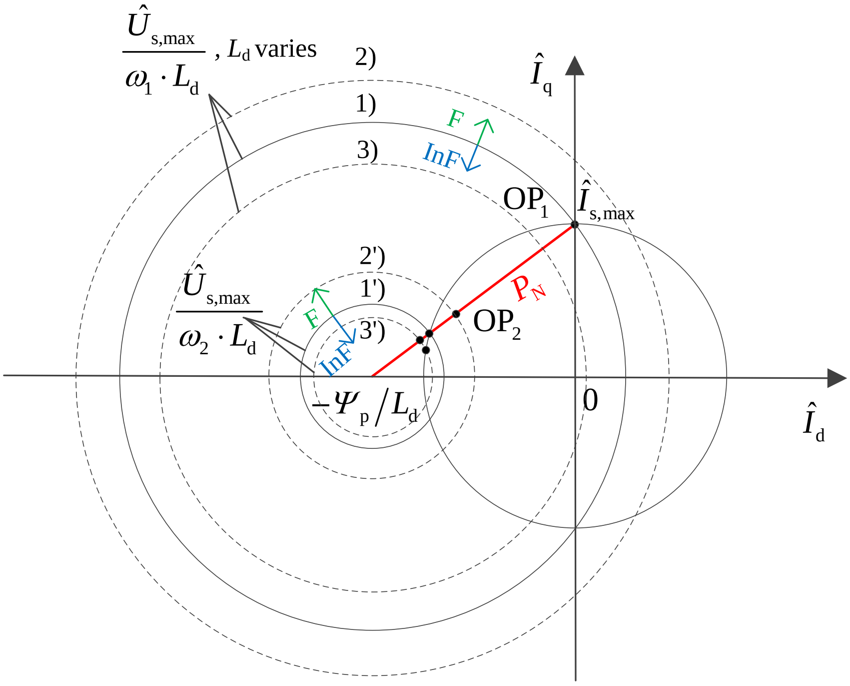

Fig. 6-13 Different locations of the voltage and current limit circles for different design parameters Ψ_p and L_d (ω_1 and ω_2 correspond to n_{min} and n_{max} for the flywheel, F: feasible region, InF: infeasible region)

6.4.2.2 Influences of the Design Parameters on the Field Weakening Performance

The circle diagram provides a straightforward way to evaluate the field weakening performance of a designed machine. However, the influence of the independently varying flux Ψ_p is not considered, as it is rather complicated to be presented in the diagram. Therefore, this chapter introduce a mathematical way based on the calculation from the equations (6-35) … (6-37).

The parameters Ψ_p and L_d are determined by the machine dimensions and winding parameters. The stator design is assumed to be fixed here. The discussion will be focused on the rotor parameters: magnet height h_m and electromagnetic air gap length δ_e which are critical parameters in high speed machine as they influence not only air gap flux density $B_{\delta,1}$ (discussed in Chapter 6.2.3) but also the mechanical stress in the bandage (Chapter 6.5), short circuit performance (Chapter 6.4.3), as well as the field weakening performance, which will be discussed in this chapter.

For a given stator design, Ψ_p and L_d are calculated by

$$\Psi_\text{p} = N_\text{s} \cdot k_\text{w1} \cdot \frac{2}{\pi} \cdot B_{\delta,1} \cdot \tau_\text{s} \cdot L_\text{Fe}, \tag{6-39}$$

$$L_\text{d} = L_\text{q} = L_\text{h} + L_{\text{s}\sigma}, \tag{6-40}$$

$$L_\text{h} = \frac{2}{\pi^2} \cdot \frac{m}{p} \cdot \mu_0 \left(N_\text{s} \cdot k_\text{w1}\right)^2 \cdot \frac{\tau_\text{s} \cdot L_\text{Fe}}{h_\text{m} + \delta_\text{e}}, \tag{6-41}$$

where N_s is the number of turns per phase of the winding, k_w1 is the winding factor, τ_s is the pole pitch, L_Fe is the iron stack length, m is the phase number, p is the pole count, μ_0 is the permeability in vacuum, L_h is the main inductance, $L_{\text{s}\sigma}$ is the stator leakage inductance.

The inductance L_d and L_q are equal which are the sum of the main inductance L_h and leakage inductance $L_{\text{s}\sigma}$. $L_{\text{s}\sigma}$ is regarded as a constant, independent of the rotor parameters. The calculated Ψ_p and L_d for varying magnet height h_m and electromagnetic air gap length δ_e are plotted in Fig. 6-14 and Fig. 6-15. The parameters for the final design can also be seen on the graphs.

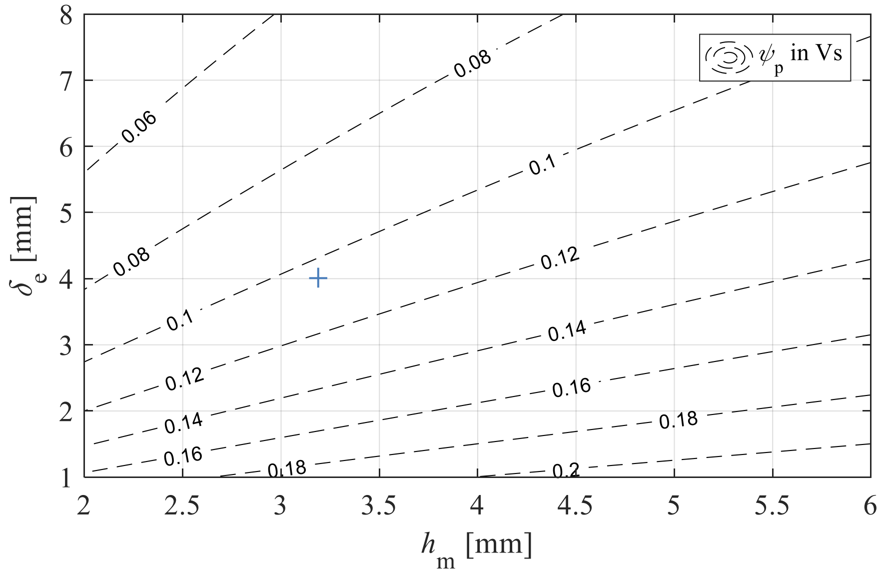

Fig. 6-14 Calculated main flux Ψ_p excited by the magnet on the rotor depending on varying magnet thickness h_m and electromagnetic air gap length δ_e, for fixed stator design in Table 6-3, magnet: VACOMAX225HR, 150 °C ("+" final design)

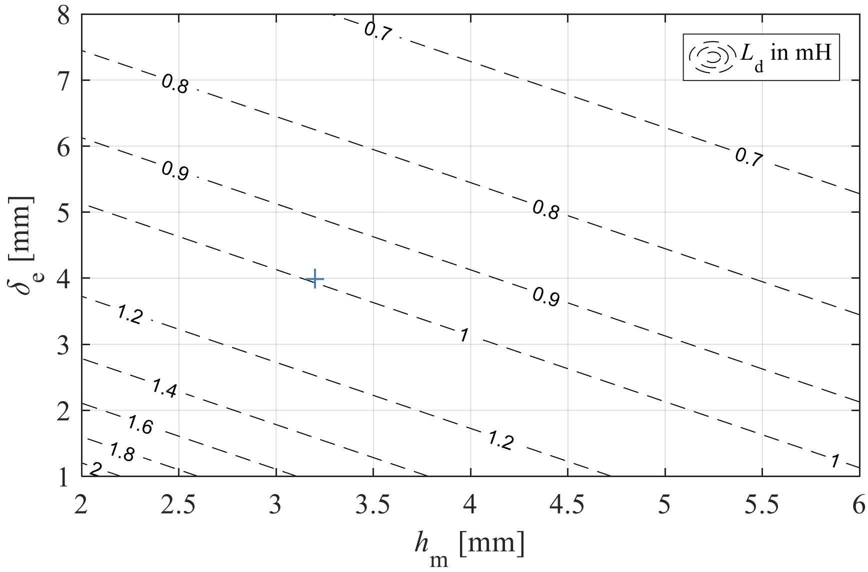

Fig. 6-15 Calculated inductance L_d depending on varying magnet thickness h_m and electromagnetic air gap length δ_e, for fixed stator design in Table 6-3, magnet: VACOMAX225HR, 150 °C ("+" final design)

In order to evaluate the field weakening performance, the operation requirements at two operating points are firstly given:

- OP$_1$: $\hat{I}_d = 0$, $n = n_{min}$, $P_e = P_N$, $\hat{U}_s \le \hat{U}_{s,max}$, $\hat{I}_s \le \hat{I}_{s,max}$
- OP$_2$: $\hat{I}_d < 0$, $n = n_{max}$, $P_e = P_N$, $\hat{U}_s = \hat{U}_{s,max}$, $\hat{I}_s \le \hat{I}_{s,max}$

For a constant power requirement at OP$_1$, the required $\hat{U}_s$ and $\hat{I}_s$ can be calculated based on (6-37) and (6-35) by

$$\hat{I}_{s1} = \hat{I}_{q1} = \frac{P_e}{\frac{m}{2} \cdot \omega_1 \cdot \Psi_p}, \tag{6-42}$$

$$\hat{U}_{s1} = \sqrt{\left(\omega_1 \cdot \Psi_p + \omega_1 \cdot L_d \cdot \hat{I}_{d1}\right)^2 + \left(\omega_1 \cdot L_q \cdot \hat{I}_{q1}\right)^2}, \tag{6-43}$$

where subscript "1" denotes the variables for OP$_1$. They should be smaller than the voltage and current limits.

For OP$_2$ as the voltage limit is reached $\hat{U}_s = \hat{U}_{s,max}$, the critical is $\hat{I}_s$, calculated by

$$\hat{I}_{s2} = \sqrt{\hat{I}_{d2}^2 + \hat{I}_{q2}^2}, \tag{6-44}$$

$$\hat{I}_{q2} = \frac{P_e}{\frac{m}{2} \cdot \omega_2 \cdot \Psi_p}, \tag{6-45}$$

$$\hat{I}_{d2} = \frac{\sqrt{\hat{U}_{s,max}^2 - \left(\omega_2 \cdot L_q \cdot \hat{I}_{q2}\right)^2} - \omega_2 \cdot \Psi_p}{\omega_2 \cdot L_d}, \tag{6-46}$$

where subscript “2” denotes the variables for OP_2.

The calculated voltage and current at OP_1 are plotted in Fig. 6-16 and Fig. 6-17. The current at OP_2 is plotted in Fig. 6-18.

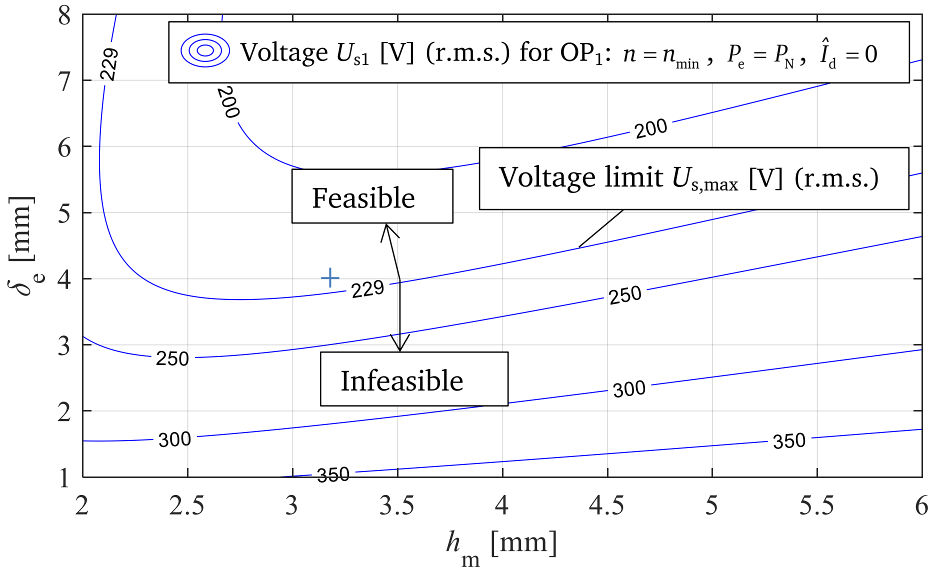

Fig. 6-16 Calculated phase voltage U_{s1} (r.m.s.) depending on varying magnet thickness h_m and electromagnetic air gap length δ_e, for fixed stator design in Table 6-3, magnet: VACOMAX225HR, 150 °C (“+” final design)

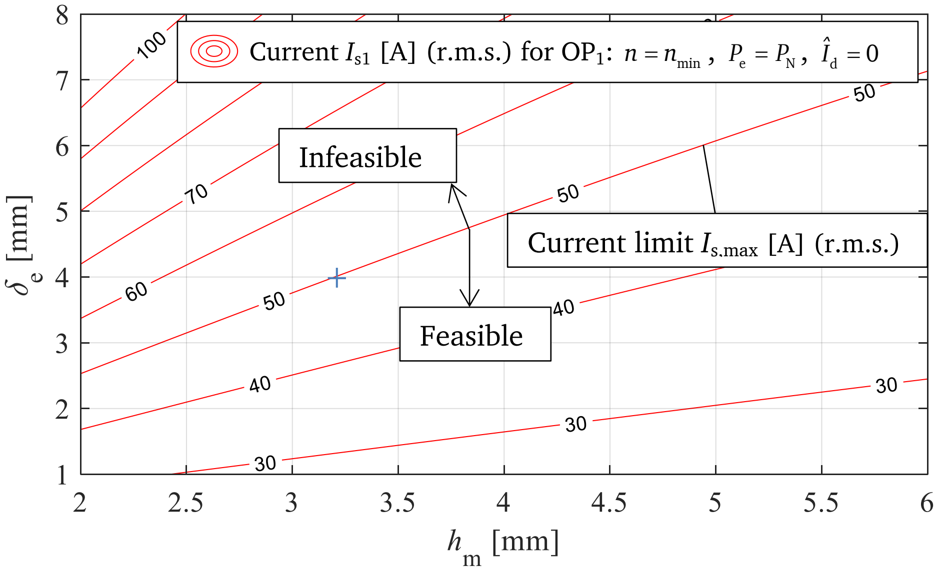

Fig. 6-17 Calculated phase current I_{s1} (r.m.s.) depending on varying magnet thickness h_m and electromagnetic air gap length δ_e, for fixed stator design in Table 6-3, magnet: VACOMAX225HR, 150 °C (“+” final design)

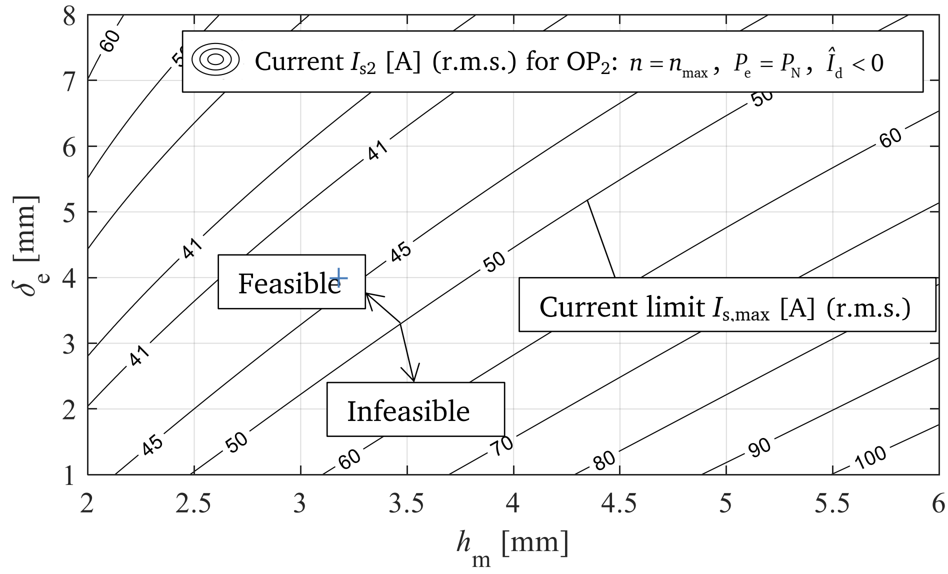

Fig. 6-18 Calculated phase current I_{s2} (r.m.s.) depending on varying magnet thickness h_m and electromagnetic air gap length δ_e, for fixed stator design in Table 6-3, magnet: VACOMAX225HR, 150 °C ("+" final design)

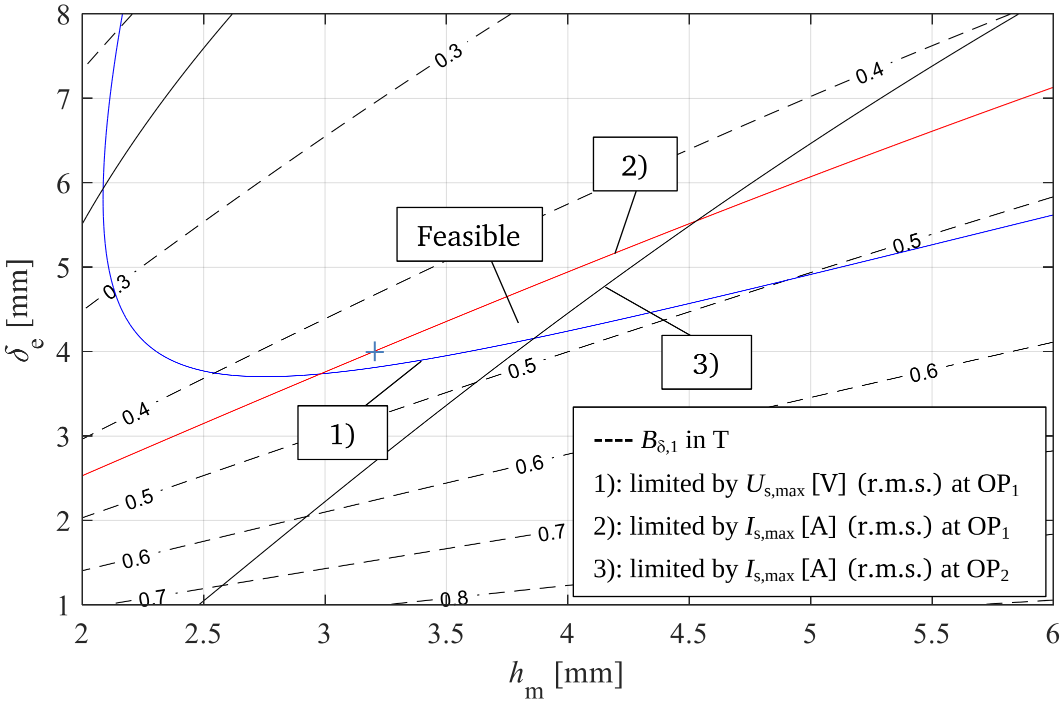

Fig. 6-19 Calculated voltage and current limits (r.m.s.) for different combinations of magnet height h_m and electromagnetic air gap δ_e for the stator parameters in Table 6-3: d_{si} = 130 mm, L_{Fe} = 90 mm, N_s = 44, magnet: VACOMAX225HR, 150 °C ("+" final design)

The feasible parameters can thus be determined by taking all these limitations into account, which should be the intersection region in Fig. 6-19. Within the region, one can choose freely the combinations of the parameters. Normally low magnet height which means low costs is preferred. But low magnet height may cause demagnetization problems. If selecting the parameters outside the feasible region, the operating characteristics in Fig. 6-1 cannot be fulfilled.

It should be noted that if the dimensions or the stator design are changed, the graphs also changes accordingly. Then a group of different designs should be proposed and compared.

6.4.3 Demagnetization at Three Phase Sudden Short Circuit

Sudden short circuit may happen when an inverter failure or a winding failure occurs. A three phase short circuit is considered in this chapter. An overshooting current usually occurs when the short circuit happens. Especially when it happens at the moment when the induced voltage of a certain phase is zero, i.e. the main field of the rotor is fully coupled by the stator winding of this phase, a maximum overshooting current will be obtained. At short circuit, the magnetic field excited by the stator current opposes the rotor field, which is excited by the magnets. It may cause an irreversible demagnetization of the magnets.

The characteristics of the permanent magnet material can be described by a *B*-*H* curve (solid line) in the second quadrant as shown in Fig. 6-20, characterized by the remanence B_r and coercivity H_c. At no load condition, the flux density B and the filed strength H in the magnets are related to the height of the magnets and the air gap, which is represented by a zero-crossing straight line with an inclination. The crossing point of these two lines yields the operating point P_0 of the magnets at no load. At short circuit, due to the opposing field caused by the stator current $\hat{I}_\mathrm{sc}$, the straight line is shifted to the left, leading to the shift of the operating point from P_0 to P on the *B*-*H* curve. If the demagnetizing curve of the magnet is linear, the operating point moves back reversely along the path P-P_0 to the original point after the opposite field is removed. But normally the demagnetizing curve is not perfect linear, especially for high temperatures, as shown in Fig. 6-20. A higher opposite field leads to a further movement of the operating point to P'. Then the recovery of the operating point is irreversible, namely it moves back following a new path ($P' - B'_\mathrm{r}$) which is parallel to the linear part of the original *B*-*H* curve. This new path is called recoil curve. As a result, the original remanence B_r cannot be restored, but a lower one B'_r, meaning the magnet is demagnetized. And this demagnetization is irreversible.

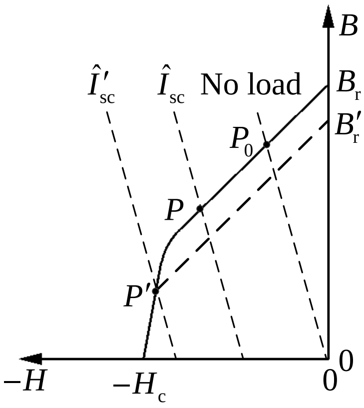

Fig. 6-20 Irreversible demagnetization of the permanent magnet caused by opposite field due to short circuit current $\hat{I}_{sc}$. (P_0: operating point at no load, P, P': operating points due to opposite fields, B_r: remanence, H_c: coercivity)

The magnet used in this machine is Sm_2Co_{17} with the demagnetizing curve shown in Fig. 6-21. The demagnetizing curve has no obvious “knee” point like in Fig. 6-20 at the temperature of 150 °C, but almost a linear curve. A parameter, the polarization J, is used to evaluate the anti-demagnetization capability of the magnet and is written by

$$J = B - \mu_0 \cdot H. \tag{6-47}$$

It can be derived from the *B-H* curve and drawn in Fig. 6-21.

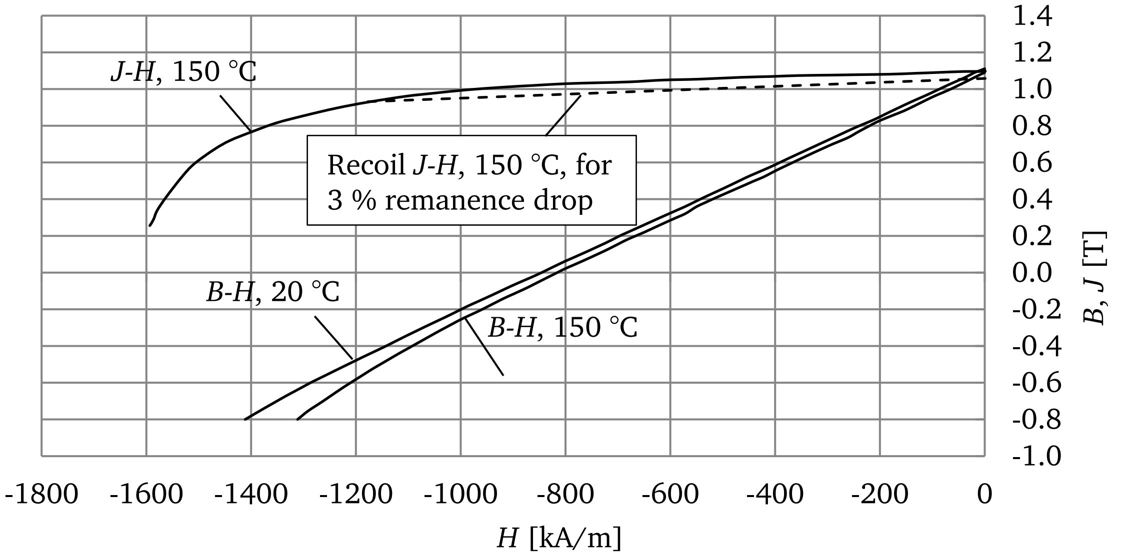

Fig. 6-21 Demagnetizing curve of the magnet: VACOMAX225HR [50]

A recoil *J-H* curve (dashed line) is also drawn in Fig. 6-21, which is parallel to the tangent of *J-H* curve (solid line) at the point (B_r, 0). If 3 % of remanence is acceptable, the intersection of the *J-H* curve and the recoil curve indicates that the demagnetizing field strength should be lower than 1177 kA/m. It is necessary to verify if the demagnetization is acceptable at sudden short circuit.

The induced current at sudden short circuit is the sum of a DC component which decays with a stator armature time constant and a steady state current. The maximum peak value can be calculated by (6-48), neglecting the decay of the DC component. Table 6-9 shows the numerical results calculated in *JMAG*. The maximum demagnetizing field in magnets is 936.4 kA/m, which is lower than 1177 kA/m. Three phase short circuit leads to no irreversible demagnetization in magnets at 150 °C.

$$\hat{I}_{\mathrm{sc,\ pk}} \approx \frac{2 \cdot \hat{U}_{\mathrm{p}}}{\sqrt{R_{\mathrm{s}}^2 + \left(\omega \cdot L_{\mathrm{d}}\right)^2}} \tag{6-48}$$

Table 6-9 Calculated demagnetization for three phase sudden short circuit at 24000 min^{-1}, 150 °C, calculated in *JMAG*, initial condition: No load

Parameter	Symbol	No load
Induced voltage	$\hat{U}_{\mathrm{p}}$	383.0 V
Max. sudden short circuit current	$\hat{I}_{\mathrm{sc,\ pk}}$	211.8 A
Demagnetizing field in magnets	$\lvert H_{\mathrm{sc,\ max}}\rvert$	936.4 kA/m
Max. sudden short circuit torque	$M_{\mathrm{sc,\ max}}$	35.4 Nm

6.5 Mechanical Design of the E-Machine Rotor

The magnets are glued on the rotor surface and have to be fixed by a prefabricated sleeve or bandage made of carbon fiber composite material due to the centrifugal forces. The bandage is assembled by cold shrinking with an undersize between the inner surface of the bandage and the outer surface of the glued magnets. The bandage thickness has to be determined based on the material strength and the maximum stress due to the rotation and thermal expansion. The bandage should be thick enough to withstand the tensile force. However, a thick bandage also leads to a big effective air gap, which is not preferred as more magnets are required for the magnetization.

6.5.1 Rotor Material Properties

The material properties of the rotor components are shown in Table 6-10. The bandage material in this design has the maximum tensile strength of 2615 MPa, which is a calculated value as a composite property of the fiber and epoxy resin. During the manufacture and the assembly the strength may be reduced. Therefore a safety factor of 2 is considered. An additional factor of 1.5 should also be taken into account due to the influence of the alternating temperature on the material strength and modulus. Considering these two factors the permissible tensile strength of bandage is 872 MPa. In the analytical calculation, the strength limit should be smaller in order to reserve a safety margin considering the additional stress caused by the sharp edges of the segmented magnets, which is difficult to calculate analytically as well as numerically.

Table 6-10 Material properties for E-machine rotor components
($\parallel$: parallel direction of fibers, $\perp$: transversal direction of fibers, CTE: coefficient of thermal expansion.)

	Bandage	Magnets	Rotor iron	Shaft
Material	HTS5631 +Epoxy resin [54]	VACOMAX225 [50]	NO 20 [55]	30CrNiMo8 [56]
Density ρ [kg/m^3]	1540	8400	7650	7760
Tensile modulus E [GPa]	$E_\parallel = 145.28$ $E_\perp = 12.02$	140-170	200	210
Shear modulus G [GPa]	$G_{\parallel\perp} = G_{\perp\parallel} = 5.562$ $G_{\perp\perp} = 4.329$	-	-	-
Poisson's ratio ν	$\nu_{\parallel\perp} = 0.278$ $\nu_{\perp\parallel} = 0.023$ $\nu_{\perp\perp} = 0.388$	0.24	0.3	0.3
Tensile strength [MPa]	$R_\parallel^+ = 2615$ $R_\perp^+ = 90$	-	400	700
Compressive strength [MPa]	$R_\perp^- = 205$	400-900	505	-
Shear strength S [MPa]	105	-	-	-
CTE [$10^{-6}/{}^\circ\mathrm{C}$]	$\alpha_\parallel = 0.139$ $\alpha_\perp = 34.3$	10	11.5	11.5

6.5.2 Analytical Calculation of the Stress in Rotor Components

6.5.2.1 Restrictions

The stress in the rotor components are caused by centrifugal force due to rotation, press-fitting due to assembly and the material thermal expansion. They can be calculated analytically following the model and method introduced in [54]. The formulas are summarized in Appendix C. The used model is 3-layer ring model, representing bandage, magnet, shaft respectively for each layer. In reality, a laminated iron package is used in the rotor. It is regarded as part of the shaft here since they have similar properties as shown in Table 6-10. The magnet segmentation is not considered. The purpose of the stress calculation is to determine the thickness of the bandage h_B and the interference fitting Δu between the magnet and the bandage, fulfilling the following restrictions:

1) The total tensile stress $\sigma_{t,B}$ in the bandage due to press fit, thermal expansion and rotation should be within the material strength limit $\sigma_{t,B,limit}$ in (6-49), which is calculated by $R_{\parallel}^{+}/k_{sf}$ (k_{sf} : safety factor) for safety.

2) The contact pressure p between each component should always be positive (under pressure on each contact surface) to assure they are successfully assembled and able to transmit torque as in (6-50).

3) The undersize Δu between magnets and bandage should be within a reasonable range for the possibility of shrink fitting assembly (6-51).

$$\sigma_{t,B} = \sigma_{tp,B} + \sigma_{t\vartheta,B} + \sigma_{t\omega,B} \leq \sigma_{t,B,limit} \tag{6-49}$$

$$p = p_{\Delta u} - p_{\vartheta} - p_{\omega} \geq p_{min} > 0 \tag{6-50}$$

$$0 \leq \Delta u \leq \Delta u_{max} \tag{6-51}$$

σ is stress, p is contact pressure, Δu is the undersize. The subscripts p, ϑ, ω denote the effect due to contact pressure, thermal expansion and rotation respectively. The subscript t denotes the tangential direction.

The dimension restrictions are:

- Stator inner diameter d_{si} = 130 mm (Fig. 6-5)
- Electromagnetic air gap length δ_e = 4 mm (Fig. 6-7)
- Magnet height h_m = 3.2 mm (Fig. 6-7)

They are determined considering the electromagnetic performance designed in Chapter 6.2. Based on these dimensions, the rotor parameters to be determined here are: the bandage thickness h_B and the undersize Δu between magnets and bandage inner surface.

6.5.2.2 Stress Calculation

A parametric stress calculation of h_B and Δu was carried out and the results are presented in Table 6-11 for 9 cases. A maximum over-speed of $1.2 \cdot n_{max} = 28800\ \text{min}^{-1}$ is taken into account in case of over-speed testing for at least 2 min (IEC60034-1). A maximum temperature ϑ is 150 °C. The maximum stress in the bandage $\sigma_{t,B,max}$ is calculated, as well as the pressure on the contact surfaces of shaft-to-magnet ($p_{\text{sh-m}}$) and magnet-to-bandage ($p_{\text{m-B}}$). A ratio of $R_{\parallel}^{+}/\sigma_{\text{t,B,max}}$ evaluates the safety margin to the maximum tensile strength $R_{\parallel}^{+}=2615\ \text{MPa}$ of the bandage.

For each case in Table 6-11, the maximum stress in the bandage occurs when the rotor rotates at maximum speed and maximum temperature, which is marked in the table with a red color filling. A thicker bandage h_{B} or smaller interference fitting Δu can reduce the stress in the bandage. The minimum contact pressure between shaft and magnet $p_{\text{c,sh-m}}$ is also critical, which occurs at maximum rotational speed and low temperature (marked with blue color filling in Table 6-11). In order to assure a reliable contact, a thicker bandage h_{B} and bigger interference fitting Δu are required. Therefore, a compromise should be made for the determination of h_{B} and Δu.

Table 6-11 Analytical calculation of the stress and pressure for E-machine rotor components (h_{B}: bandage thickness, Δu: undersize between the bandage and the magnets, n: speed, ϑ: temperature, $p_{\text{sh-m}}$: contact pressure between shaft and magnets, $p_{\text{m-B}}$: contact pressure between magnets and bandage, $\sigma_{\text{t,B,max}}$: maximum tangential stress in bandage)

h_{B}	mm	2.8											
Δu	mm	0.15				0.16				0.17			
n	min^{-1}	0		28800		0		28800		0		28800	
ϑ	°C	20	150	20	150	20	150	20	150	20	150	20	150
$p_{\text{sh-m}}$	MPa	15.7	33.9	1.1	19.4	16.7	35.0	2.1	20.4	17.7	36.0	3.2	21.5
$p_{\text{m-B}}$	MPa	15.4	29.1	14.1	27.8	16.5	30.2	15.1	28.8	17.5	31.2	16.1	29.8
$\sigma_{\text{t,B,max}}$	MPa	346.6	637.5	372.4	663.2	369.7	660.6	395.5	686.3	392.8	683.7	418.6	709.4
$R_{\parallel}^{+}/\sigma_{\text{t,B,max}}$		7.54	4.10	7.02	3.94	7.07	3.96	6.61	3.81	6.66	3.82	6.25	3.69
h_{B}	mm	3.0											
Δu	mm	0.14				0.15				0.16			
n	min^{-1}	0		28800		0		28800		0		28800	
ϑ	°C	20	150	20	150	20	150	20	150	20	150	20	150
$p_{\text{sh-m}}$	MPa	15.6	34.8	0.9	20.2	16.7	35.9	2.0	21.3	17.8	37.1	3.1	22.4
$p_{\text{m-B}}$	MPa	15.4	30.0	13.9	28.6	16.5	31.1	15.0	29.6	17.6	32.2	16.1	30.7
$\sigma_{\text{t,B,max}}$	MPa	322.7	612.8	348.5	638.6	345.8	635.8	371.6	661.6	368.8	658.9	394.6	684.7
$R_{\parallel}^{+}/\sigma_{\text{t,B,max}}$		8.10	4.27	7.50	4.09	7.56	4.11	7.04	3.95	7.09	3.97	6.63	3.82
h_{B}	mm	3.2											
Δu	mm	0.13				0.14				0.15			
n	min^{-1}	0		28800		0		28800		0		28800	
ϑ	°C	20	150	20	150	20	150	20	150	20	150	20	150
$p_{\text{sh-m}}$	MPa	15.4	35.6	0.6	20.8	16.5	36.8	1.8	22.0	17.7	37.9	2.9	23.2
$p_{\text{m-B}}$	MPa	15.1	30.8	13.6	29.2	16.3	31.9	14.7	30.3	17.5	33.1	15.9	31.5
$\sigma_{\text{t,B,max}}$	MPa	298.9	588.2	324.8	614.1	321.9	611.2	347.8	637.1	344.9	634.2	370.8	660.1
$R_{\parallel}^{+}/\sigma_{\text{t,B,max}}$		8.75	4.45	8.05	4.26	8.12	4.28	7.52	4.10	7.58	4.12	7.05	3.96

For a better understanding, Fig. 6-22 shows the stress components in the bandage caused by press-fitting, thermal expansion and rotation respectively, for the bandage thickness of 3 mm as an example. As can be seen from the graph, the stress in the bandage is mainly due to the pressfitting and thermal expansion, the effect of rotation is small. The stress in the bandage can be reduced by using a smaller undersize, however, Δu shouldn't be too small, avoiding a loose contact between the magnet and the shaft. A minimum contact pressure of $p_{\min} = 2$ MPa is given as the restriction value in (6-50).

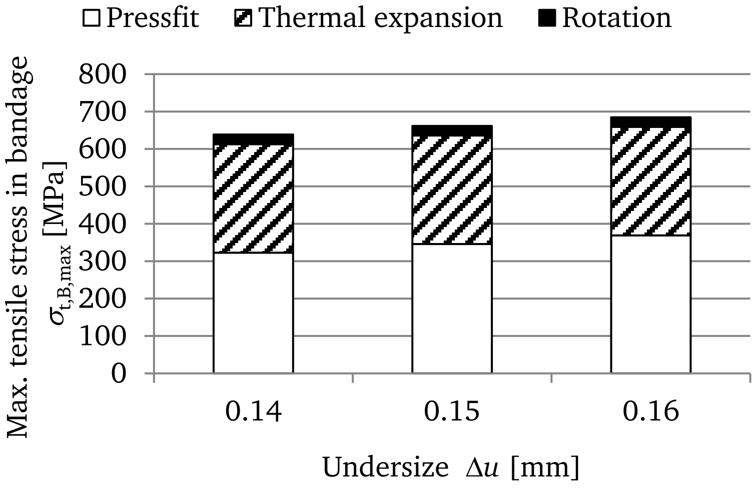

Fig. 6-22 Calculated maximum tensile stress $\sigma_{t,B,max}$ in the bandage caused by press-fit, thermal expansion at 150 °C and rotation at 28800 min^{-1} for the bandage thickness of 3.0 mm, magnet height of 3.2 mm.

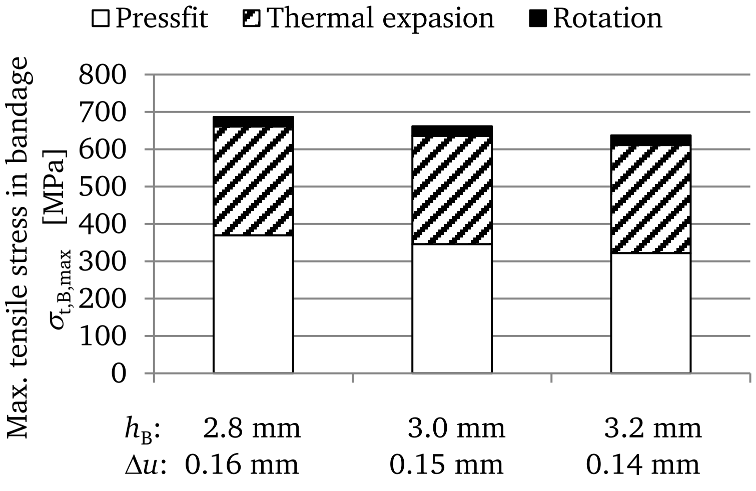

Fig. 6-23 Calculated maximum tensile stress $\sigma_{t,B,max}$ in the bandage caused by press-fit, thermal expansion at 150 °C and rotation at 28800 min^{-1} for different combinations of bandage thickness h_m and undersize Δu (magnet height 3.2 mm)

For the same pressure of 2 MPa on the contact surface magnet-to-shaft, three combinations of h_B and Δu are selected and compared in Fig. 6-23. For a thicker bandage, the required undersize is smaller due to the smaller bandage deformation, leading to a smaller stress in the bandage. However, the thickness of the bandage is limited by the stator inner diameter. A reasonable mechanical air gap considering the rotor displacement should be reserved.

Finally the bandage parameters are chosen with a height $h_{\mathrm{B}} = 3\ \mathrm{mm}$, and an undersize $\Delta u = 0.15\ \mathrm{mm}$. Thus the mechanical air gap is $\delta = 1$ mm. For the chosen design, the resulting maximum stress in the bandage is $\sigma_{\mathrm{t,B,max}} = 661.6\ \mathrm{MPa}$ at 28800 min^{-1} and a bandage temperature of 150 °C. Compared to the maximum material strength $R_{\|}^{+} = 2615\ \mathrm{MPa}$ of the bandage, a safety factor of 3.95 is used. The minimum contact pressure occurs between the shaft and the magnets $p_{\mathrm{sh\text{-}m}} = 2\ \mathrm{MPa}$, ensuring the fixation of the magnets at high speed rotation of 28800 min^{-1} at a temperature of 20 °C.

7. Magnetic Levitation

In order to reduce the friction losses, the flywheel rotor is suspended by magnetic bearings. This chapter introduces the configuration of the magnetic bearings and the force and loss calculations in the designed system.

7.1 Requirements of Levitation

The rotor mass is calculated to be 90 kg for the chosen design in Fig. 5-1. The flywheel will be vertically positioned, so that the axial magnetic bearing has to carry the full rotor weight. Therefore, the axial magnetic bearing should produce a force of at least 900 N for the levitation.

In the radial direction, the two radial magnetic bearings should compensate for the unbalanced force of the rotor due to eccentricity. According to the standard of balance quality requirements of rigid rotors *ISO 1940/1* [57], the balance quality G is defined by the eccentricity e and the rotational speed Ω of the center mass around the axis of rotation with

$$G = e \cdot \Omega \,. \tag{7-1}$$

The unbalanced force due to the eccentricity can be calculated by

$$F = m \cdot e \cdot \Omega^2 = m \cdot G \cdot \Omega, \tag{7-2}$$

where m is the rotor mass, e is the eccentricity in meter, Ω is the rotational speed in rad/s. G is the balance quality. For a flywheel rotor with the balance quality of G 6.3, which means $G = 6.3$ mm/s, the designed flywheel rotor with the mass of 90 kg will produce an unbalance force of 1425 N, which is allowed, at the rotational speed 24000 min^{-1}.

Mechanical bearings are usually able to produce the force at this level. However, due to the big stiffness, mechanical bearings will force the rotor to rotate around its axis of symmetry, which causes a big vibration and noise. In terms of magnetic bearings, to produce such a force requires a large amount of current, which is not realistic. However, due to the low stiffness and the characteristics of the free suspensions by magnetic bearings, it is possible to rotate the rotor in its principle axis of inertia with a required orbit instead of the axis of symmetry. This can effectively reduce the forces that are applied to compensate the unbalance.

The rotor balancing was carried out by the company *Schenck RoTec GmbH, Darmstadt, Germany*. In order to reduce the load of the magnetic bearings, the balancing quality in our system is required to be G 2.5, which was realized. Thus the maximum allowed unbalance force is 565 N for 90 kg rotor mass. Considering the worst case, where the total force is compensated by the magnetic bearing, rotational frequent 282.5 N radial force is required for each magnetic bearing.

7.2 Magnetic Bearing Configuration and Specifications

The five-axis suspension of the rotor is realized by a homo-polar radial magnetic bearing on the top and a combined axial-radial magnetic bearing on the bottom (Fig. 1-1). According to the force requirements, the magnetic bearings of the company *KEBA LTI Motion, Lahnau* are chosen. The section views of the magnetic bearings can be seen in Fig. 7-1 and the stator is shown in Fig. 7-2.

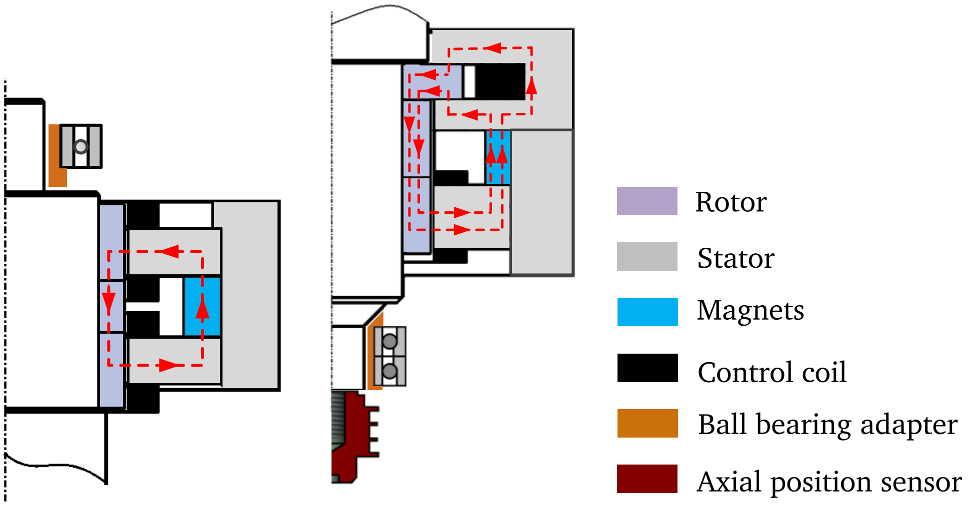

a) b)

Fig. 7-1 Configuration of the magnetic bearings from company *KEBA LTI Motion, Lahnau*: a) homo-polar radial magnetic bearing on the top of the flywheel rotor, b) combined axial-radial magnetic bearing on the bottom of the flywheel rotor; biased field (red dashed lines)

The homo-polar radial magnetic bearing has 4 poles and consists of two stator parts. Each part has 4 control coils. A bias field is excited by the magnets mounted between the two stators and are magnetized in axial direction. The resulting biased field is shown in Fig. 7-1 a). The 4 magnets are magnetized axially in the same direction, therefore the polarities in the air gap are the same in circumferential direction, which are N-N-N-N (or S-S-S-S) instead of N-S-N-S alternating. This arrangement causes lower losses in the rotor compared to the hetero-polar magnetic bearings, where the polarity varies alternatively in the rotor circumference.

On the bottom of the flywheel rotor, a combined magnetic bearing is placed, shown in Fig. 7-1 b). It consist two parts: a homo-polar magnetic bearing for the radial forces and a homo-polar axial magnetic bearing for the axial force. One ring shape coil is used for the axial force control. The stator components of the combined magnetic bearing are shown in Fig. 7-3. The axial control coils are placed inside of the C-shaped stator and covered by a steel sheet, therefore cannot be seen in Fig. 7-3.

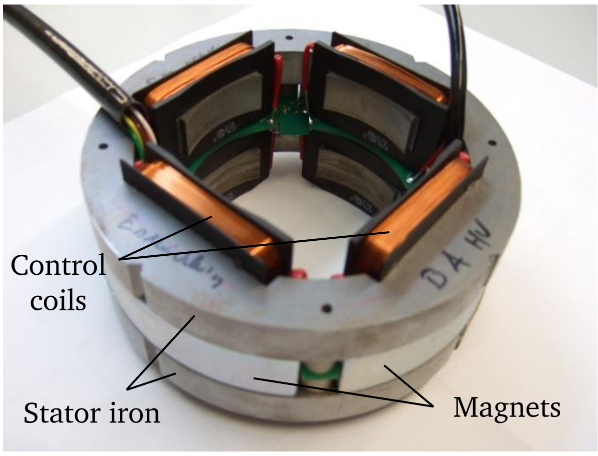

Fig. 7-2 Stator of the radial magnetic bearing, showing magnets and control coils

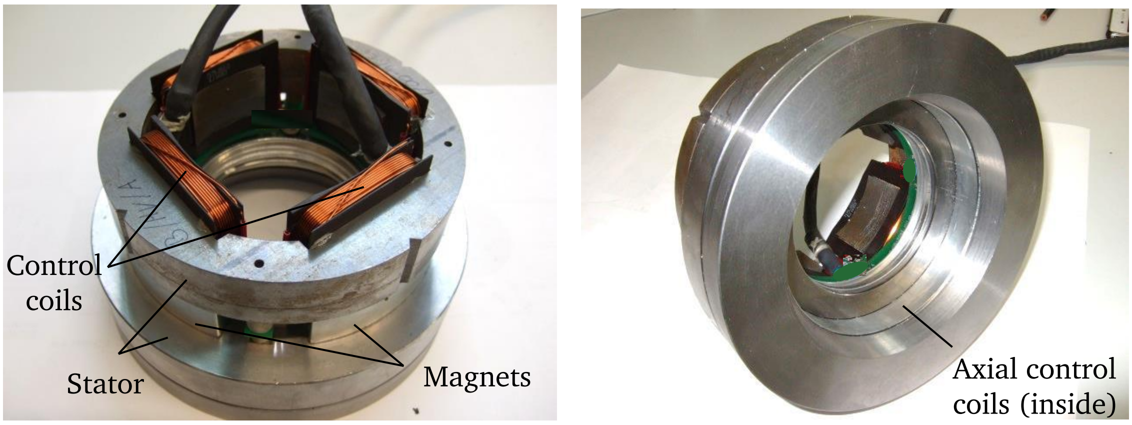

a) b)

Fig. 7-3 Stator of the combined magnetic bearing: a) top view, b) bottom view

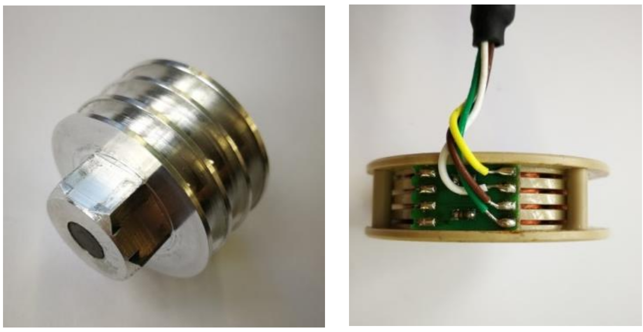

Fig. 7-4 Axial position sensor for combined magnetic bearing:
a) rotor part, b) coils on the stator side

The axial position sensor (Fig. 7-4) is an eddy current type with an aluminum rotor part and coils on the stator side. The rotor part is mounted on the bottom of the shaft, as shown in Fig. 7-1 b).

7.3 Field and Force in Magnetic Bearings

7.3.1 Combined Magnetic Bearing

In order to calculate the field and force in the magnetic bearing, a 3D model (Fig. 7-5) is built in *JMAG* with the main dimensions and specifications of the combined magnetic bearing in Table 7-1.

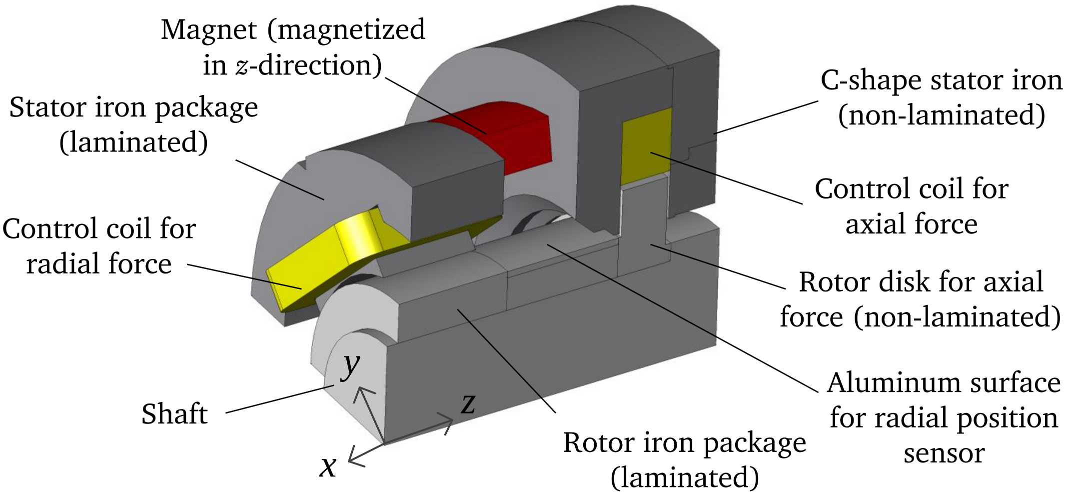

Fig. 7-5 3D model of the combined magnetic bearing, built in *JMAG*

Table 7-1 Main dimensions and specifications of the combined magnetic bearing

Radial components		
Stator inner diameter	d_{si}	80 mm
Rotor outer diameter	d_{ro}	76.7 mm
Axial length of stator iron	$L_{Fe,s}$	25 mm
Axial length of rotor iron	$L_{Fe,r}$	29.5 mm
Air gap length	δ_r	1.65 mm
Axial components		
Outer diameter of rotor disk	$d_{ro,disk}$	102.5 mm
Inner diameter of rotor disk	$d_{ri,disk}$	79 mm
Air gap length	δ_z	0.6 mm
Magnet parameters		
Inner diameter	$d_{i,mag}$	116 mm
Outer diameter	$d_{o,mag}$	139 mm
Axial length	L_{mag}	20 mm
Control coil parameters		
Number of turns of control coil	N	60 (radial), 91 (axial)
Wire diameter	d_{Cu}	0.8 mm
Max. current	I_{max}	8 A

7.3.1.1 Biased Field in 3D Model

The biased field distribution excited by the magnets is calculated in a 3D model in *JMAG* and presented in Fig. 7-6. The fields in the air gaps are presented in Fig. 7-7. The field gradients under the pole areas vary not much. The average flux density under the pole area is 0.38 T in the axial air gap and 0.62 T in the radial air gap.

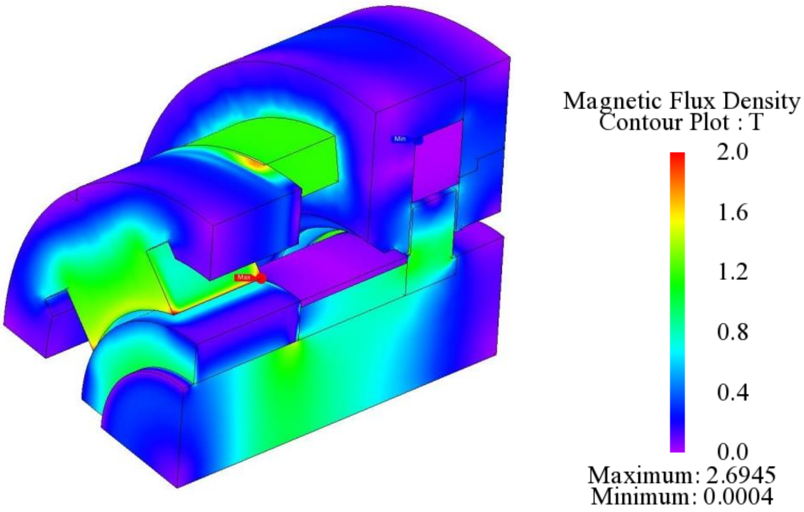

Fig. 7-6 Calculated biased field distribution in the combined magnetic bearing, calculated in *JMAG*

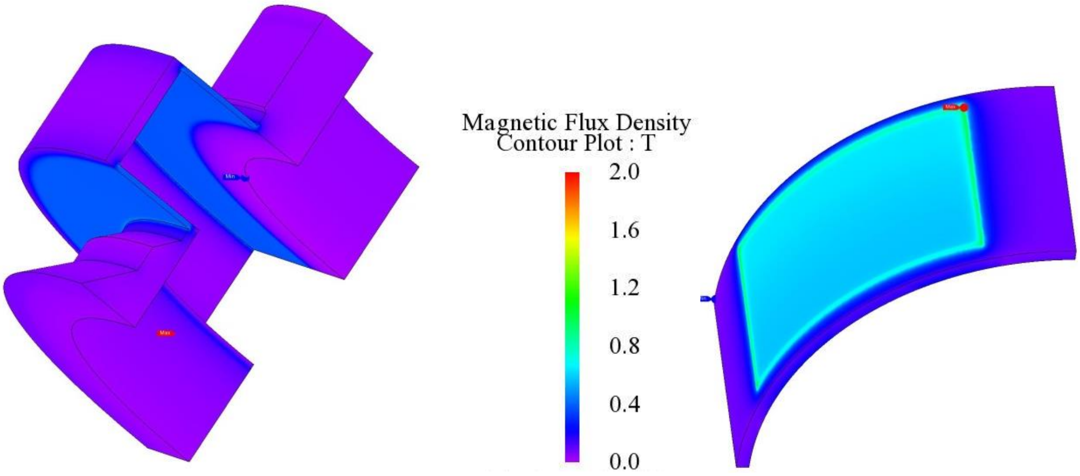

a) b)

Fig. 7-7 Calculated biased field distribution in the air gap of the combined magnetic bearing, calculated in *JMAG*: a) field in axial air gap, b) field in radial air gap

7.3.1.2 Axial Force

As the radial flux has little influence on the axial force, the 3D model in Fig. 7-5 is simplified to a 2D model in Fig. 7-8 to calculate the axial force. The radial control coils are neglected. In the 3D model, the magnets consist of 4 pieces, evenly distributed in circumferential direction. Each piece has a pole coverage angle of less than 90°. In the axisymmetric 2D model, modeling such 3D geometry is no more feasible. Therefore, the geometry of the magnets is modified by using a ring-shaped magnet with an increased

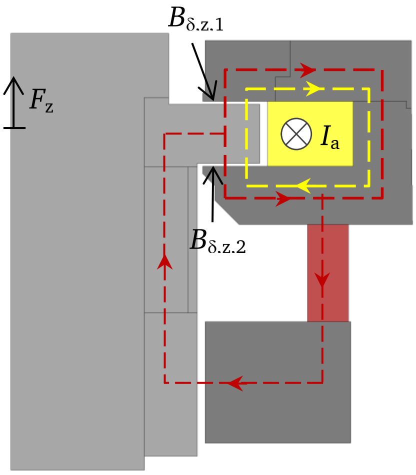

Fig. 7-8 Simplified 2D axisymmetric model for the axial force calculation in *JMAG* (red dashed line: biased field excited by the magnet, yellow dashed line: control field excited by the current in the control coil)

inner radius, so that the axial cross section areas of the magnets remain the same as in the 3D model, thus the total flux is the same.

The magnet excites a biased field $B_{\delta,z,0}$, shown in Fig. 7-8 with the red dashed line. The current in the control coil excites a control field B_a, shown in Fig. 7-8 with the yellow dashed line. Thus in the air gap, a superposition of these two fields is obtained by

$$B_{\delta,z,1} = B_{\delta,z,0} + B_a \, , \tag{7-3}$$

$$B_{\delta,z,2} = B_{\delta,z,0} - B_a \, . \tag{7-4}$$

The force acting on the disk is calculated by (7-5) and can be written as (7-6) by substituting (7-3) and (7-4) into (7-5).

$$F_z = \frac{A}{2 \cdot \mu_0} \cdot \left(B_{\delta,z,1}^2 - B_{\delta,z,2}^2 \right) \tag{7-5}$$

$$F_z = \frac{A}{2 \cdot \mu_0} \cdot \left[\left(B_{\delta,z,0} + B_a \right)^2 - \left(B_{\delta,z,0} - B_a \right)^2 \right] = \frac{2 \cdot A}{\mu_0} \cdot B_{\delta,z,0} \cdot B_a \tag{7-6}$$

In (7-5) and (7-6), A is the facing area of the C-shape stator and the rotor disk on each side, μ_0 is the permeability in vacuum.

The fields and forces are calculated numerically in *JMAG* with the simplified 2D axisymmetric model and the results are compared with the 3D model as shown in Table 7-2. For varying control current, the results of the two models fit well. The biased field is 0.379 T in the upper air gap and 0.388 T in the lower air gap, which are slightly different due to the asymmetric leakage paths on the yoke legs.

Table 7-2 Numerically calculated (in *JMAG*) axial field and force of the combined magnetic bearing, in dependence of the axial excitation current I_a

	2D axisymmetric model			3D model
Current I_a [A]	$B_{\delta,z,1}$ [T]	$B_{\delta,z,2}$ [T]	Axial force F_z [N]	Axial force F_z [N]
-8	-0.377	1.061	-1388.8	-1356.1
-6	-0.194	0.9	-1091.4	-1065.0
-4	-0.005	0.732	-758.6	-740.4
-2	0.186	0.56	-397.7	-388.3
0	0.379	0.388	-12.5	-11.6
2	0.571	0.215	392.9	385.8
4	0.761	0.044	814.4	800.4
6	0.948	-0.124	1245.4	1226.2
8	1.127	-0.285	1675.5	1654.1

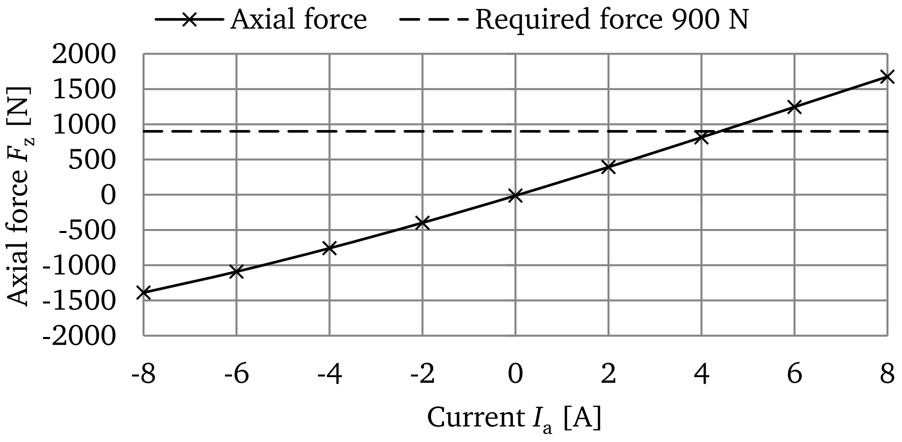

Fig. 7-9 Calculated axial force produced in the combined magnetic bearing for various control currents I_a, calculated by 2D axisymmetric model in *JMAG*

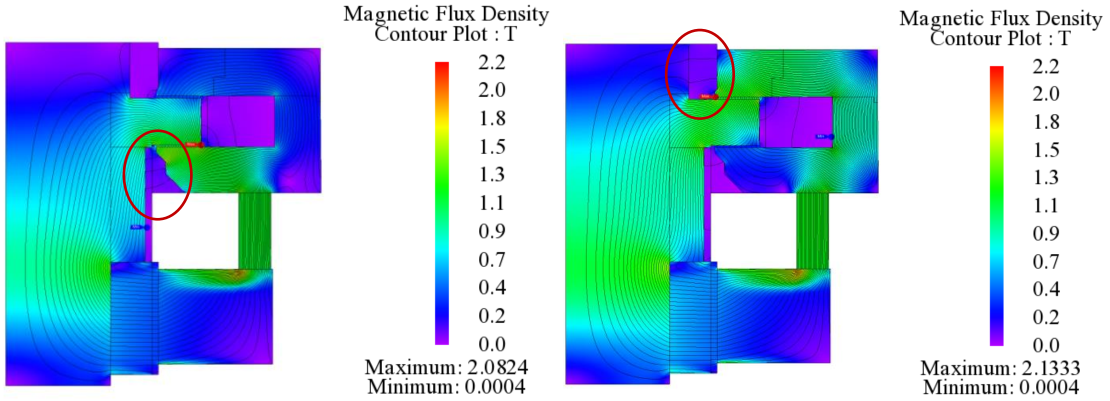

a) I_a = -8A   b) I_a = 8 A

Fig. 7-10 Flux lines in the combined magnetic bearing for the control current I_a, showing an asymmetric flux leakage

Fig. 7-10 shows the field distribution and flux lines in the magnetic bearing with a current feeding of 8 A in the coil. Different leakage (red circle) caused by the asymmetric structure on each side can be seen. The produced force for the current feeding of 8 A is calculated to be 1675.5 N, as shown in Table 7-2. If the current direction is inversed, which is – 8 A in Table 7-2, the produced force is – 1388.8 N due to the asymmetric leakage. This asymmetric force can be used as extra benefit if the magnetic bearing is properly oriented. For example for the current arrangement, in order to fulfill the axial force requirement of 900 N to levitate the flywheel rotor, the control current of $I_a = 4.40$ A is required as shown in Fig. 7-9. But if the magnetic bearing is flipped upside down, the required current is $I_a = -4.85$ A.

7.3.1.3 Radial Force

1) $I_{\mathrm{x}} = 0$ A

The radial force is produced by the field in the radial air gap due to the interaction of the biased field and the radial control field as shown in Fig. 7-11.

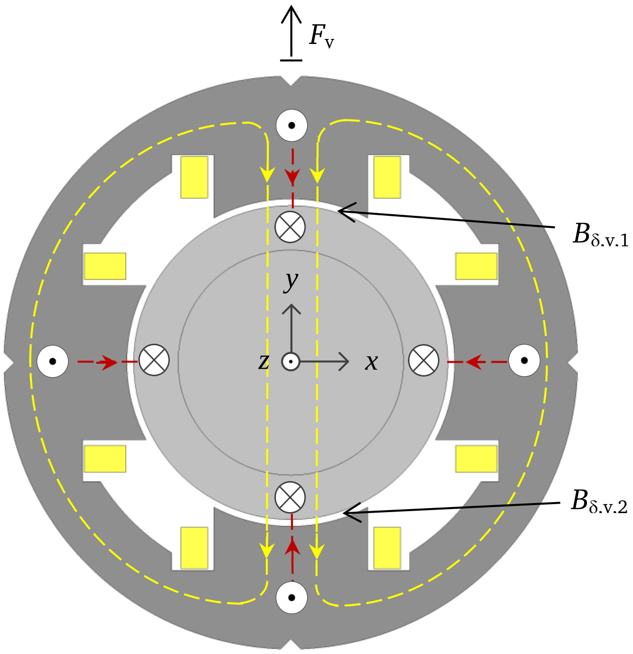

Fig. 7-11 2D planar model for the radial control field calculation in *JMAG* (red dashed line: biased field excited by the magnet, yellow dashed line: control field excited by the current in the control coil, the symbol “dot” and “cross” show the direction of the biased field)

Assuming the control field in x-direction is zero, i.e. $I_{\mathrm{x}} = 0$ A, the air gap field in y-direction can be described by

$$B_{\delta,\mathrm{y},1} = B_{\delta,\mathrm{r},0} + B_{\delta,\mathrm{y,c}}\,, \tag{7-7}$$

$$B_{\delta,\mathrm{y},2} = B_{\delta,\mathrm{r},0} - B_{\delta,\mathrm{y,c}}\,, \tag{7-8}$$

where $B_{\delta,\mathrm{r},0}$ is the biased field, $B_{\delta,\mathrm{y,c}}$ is the control field in y-direction. $B_{\delta,\mathrm{y},1}$ and $B_{\delta,\mathrm{y},2}$ are depicted in Fig. 7-11.

The non-identical fields will generate force in y-direction which can be calculated by (7-9) and (7-10). The geometry parameter $L_{\mathrm{Fe,s}}$ is the stator iron length and α_{p} is the coverage angle of each stator pole, which are presented in Table 7-1. By substituting (7-7) and (7-8) into (7-10), the force in (7-11) can be obtained.

$$F_{\mathrm{y}} = \int_{-\alpha_{\mathrm{p}}/2}^{\alpha_{\mathrm{p}}/2} \frac{\left(B_{\delta,\mathrm{y},1}^{2} - B_{\delta,\mathrm{y},2}^{2}\right)}{2\cdot\mu_0} \cdot \frac{d_{\mathrm{si}}}{2} \cdot L_{\mathrm{Fe,s}} \cdot \cos\left(\theta\right) d\theta \tag{7-9}$$

$$F_{\mathrm{y}} = \frac{\left(B_{\delta,\mathrm{y},1}^2 - B_{\delta,\mathrm{y},2}^2\right)}{2 \cdot \mu_0} \cdot d_{\mathrm{si}} \cdot L_{\mathrm{Fe,s}} \cdot \sin\left(\alpha_{\mathrm{p}}/2\right) \tag{7-10}$$

$$F_{\mathrm{y}} = \frac{2}{\mu_0} B_{\delta,\mathrm{r},0} \cdot B_{\delta,\mathrm{y,c}} \cdot d_{\mathrm{si}} \cdot L_{\mathrm{Fe}} \cdot \sin\left(\alpha_{\mathrm{p}}/2\right) \tag{7-11}$$

The biased field $B_{\delta,\mathrm{r},0}$ is calculated in the 3D static model (Fig. 7-5) in *JMAG* for a constant current feeding in axial coil $I_{\mathrm{a}} = 4.4$ A, corresponding to the required current to axially lift the flywheel rotor mass. The flux density decreases along the axial length of the laminated stator iron due to the big magnetic resistance between each laminated sheet. Therefore, here the flux density at middle axial position of the stator iron is used as an average value. The circumferential distribution of the radial field is shown in Fig. 7-12 a). Under the pole area, the biased field (radial component) is constant $B_{\delta,\mathrm{r},0} = 0.62$ T.

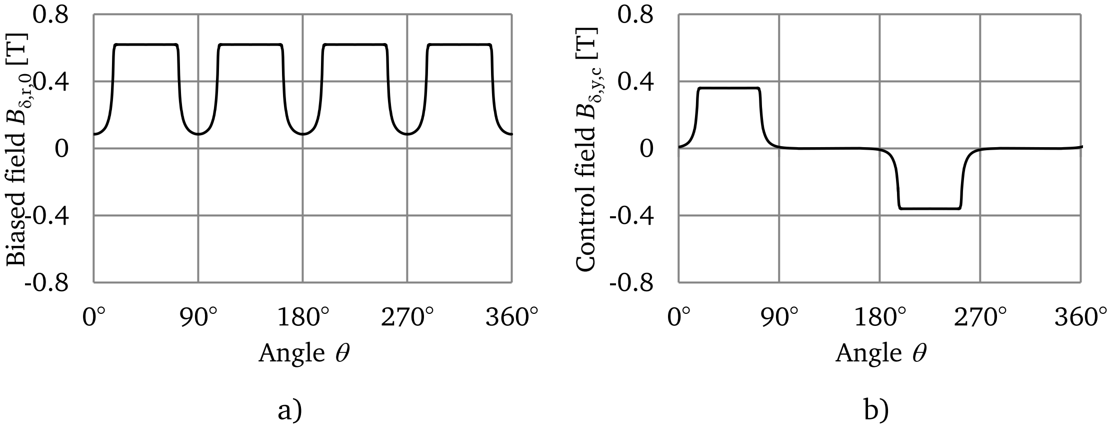

a) b)

Fig. 7-12 Calculated biased and control field in the radial air gap of the combined magnetic bearing: a) biased field calculated in the 3D model in Fig. 7-5 for $I_{\mathrm{a}} = 4.4$ A in axial coil, b) control field in *y*-direction for a DC current feeding $I_{\mathrm{y}} = 8$ A, $I_{\mathrm{x}} = 0$ A, calculated in 2D model in Fig. 7-11.

As the control field $B_{\delta,\mathrm{y,c}}$ locates in the *x*-*y* plane and decoupled with the axial magnetic bearing, it can be calculated independently by using a 2D planar model in Fig. 7-11, without considering the biased field. By feeding current I_{y} only in the coil in *y*-direction and $I_{\mathrm{x}} = 0$ A, the field distribution $B_{\delta,\mathrm{y,c}}$ in Fig. 7-12 b) can be obtained for $I_{\mathrm{y}} = 8$ A.

Table 7-3 shows the calculated biased field $B_{\delta,\mathrm{r},0}$ and the control field $B_{\delta,\mathrm{y,c}}$ for various I_{y}. The air gap fields $B_{\delta,\mathrm{y},1}$ and $B_{\delta,\mathrm{y},2}$ are calculated by a superposition of $B_{\delta,\mathrm{r},0}$ and $B_{\delta,\mathrm{y,c}}$ following (7-7) and (7-8). Thus the radial forces F_{y} can be calculated by (7-11) and also presented. The maximum control current is $I_{\mathrm{y,max}} = 8$ A, leading to a current density of 16 A/mm^2. Higher currents are not allowed due to the thermal limit.

Table 7-3 Calculated field in the radial air gap and radial force in the combined magnetic bearing for $I_x = 0$ A

	Current	Biased field	Axial force	Current	Control field	Air gap field		Radial force
	I_a [A]	$B_{\delta,r,0}$ [T]	F_z [N]	I_y [A]	$B_{\delta,y,c}$ [T]	$B_{\delta,y,1}$ [T]	$B_{\delta,y,2}$ [T]	F_y [N]
Obtained from	(3D)	(3D)		applied	(2D)	Eq.(7-7)	Eq.(7-8)	Eq.(7-11)
2D & 3D Super-positon	4.4	0.62	900	-8	-0.360	0.26	0.98	-333.5
				-6	-0.269	0.351	0.889	-249.2
				-4	-0.179	0.441	0.799	-165.8
				-2	-0.088	0.532	0.708	-81.5
				0	0	0.62	0.62	0.0
				2	0.088	0.708	0.532	81.5
				4	0.179	0.799	0.441	165.8
				6	0.269	0.889	0.351	249.2
				8	0.360	0.980	0.260	333.5
3D model	4.4	0.62	909	8	-	0.972	0.255	350.6

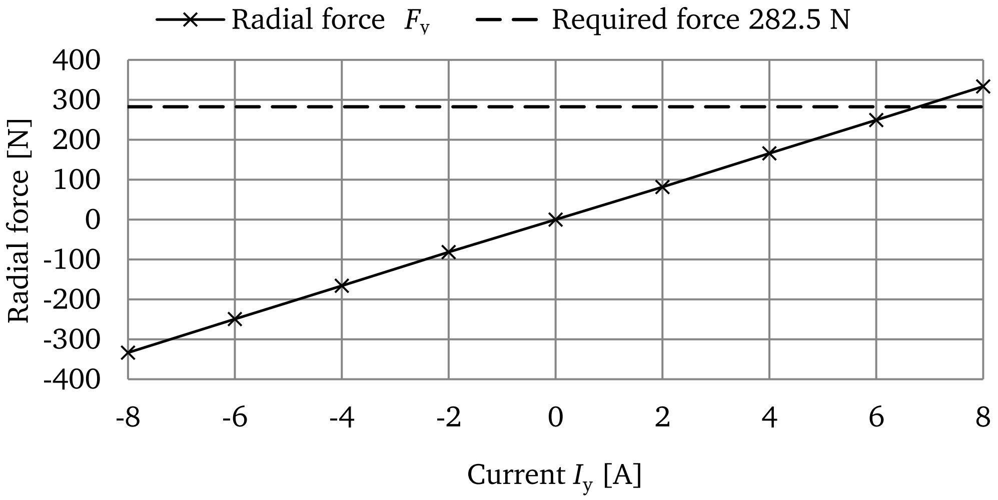

Fig. 7-13 Calculated force (superposition method) in y-direction for various currents feeding in the y control coil in the combined magnetic bearing, calculated for $I_a = 4.4$ A in axial coil and $I_x = 0$ A in control coil

In the bottom row of Table 7-3, calculation results obtained completely from a 3D model are presented, with the current feeding in both axial coil and y coil. In a complete 3D model, the air gap field $B_{\delta,y,1}$ and $B_{\delta,y,2}$ and the radial force F_y can be directly obtained instead of superposition calculation. Therefore the results are used here as a comparative reference in order to verify the method of superposition calculation. For a current feeding $I_y = 8$ A, the force calculated from the superposition method is 333.5 N. Compared to the 350.6 N calculated from the 3D model, a deviation of 4.9 % is acceptable.

The calculated forces F_y in Table 7-3 for various currents I_y are plotted in Fig. 7-13 for $I_a = 4.4$ A in the axial coil and $I_x = 0$ A in the control coil. The required force for the worst case is 282.5 N as calculated in Chapter 7.1, which can be fulfilled by the magnetic bearing.

2) $\underline{I}_x \neq 0$ A

The force space vector $\underline{F}_r$ on the rotor is a superposition of the force space vector $\underline{F}_x$ in x-direction and $\underline{F}_y$ in y-direction, as described by (7-12). By feeding sinusoidal currents in both x- and y-coils with a phase shift of 90° (Fig. 7-14 a)), the magnitude of the forces in both directions are time-varying, as described by (7-13) and (7-14). Thus the superimposed force vector $\underline{F}_r$ can be written by (7-15). If the forces in x and y direction have the same amplitude (in (7-16)), then $\underline{F}_r$ has a constant amplitude and rotates with the frequency ω, where $\omega = 2 \cdot \pi \cdot f$ (f is the current frequency). f is determined by the rotating speed n. With $f = n$, the force vector $\underline{F}_r$ is synchronous with the rotor, compensating the unbalanced force.

The amplitude F_r depends on the amplitude of the feeding current in the control coils. Fig. 7-14 b) shows rotating trajectory of the superimposed force vector $\underline{F}_r$ for different current amplitudes.

$$\underline{F}_\mathrm{r} = \underline{F}_\mathrm{x} + \underline{F}_\mathrm{y} \tag{7-12}$$

$$\underline{F}_\mathrm{x} = F_\mathrm{x} \cdot \cos(\omega \cdot t) \cdot e^{j0} \tag{7-13}$$

$$\underline{F}_\mathrm{y} = F_\mathrm{y} \cdot \sin(\omega \cdot t) \cdot e^{j\frac{\pi}{2}} \tag{7-14}$$

$$\underline{F}_\mathrm{r} = F_\mathrm{x} \cdot \cos(\omega \cdot t) \cdot e^{j0} + F_\mathrm{y} \cdot \sin(\omega \cdot t) \cdot e^{j\frac{\pi}{2}} \tag{7-15}$$

$$\underline{F}_\mathrm{r} = F_\mathrm{r} \cdot \cos(\omega \cdot t) \cdot e^{j0} + F_\mathrm{r} \cdot \sin(\omega \cdot t) \cdot e^{j\frac{\pi}{2}} = F_\mathrm{r} \cdot e^{j\omega t}, \text{ with } F_\mathrm{x} = F_\mathrm{y} = F_\mathrm{r} \tag{7-16}$$

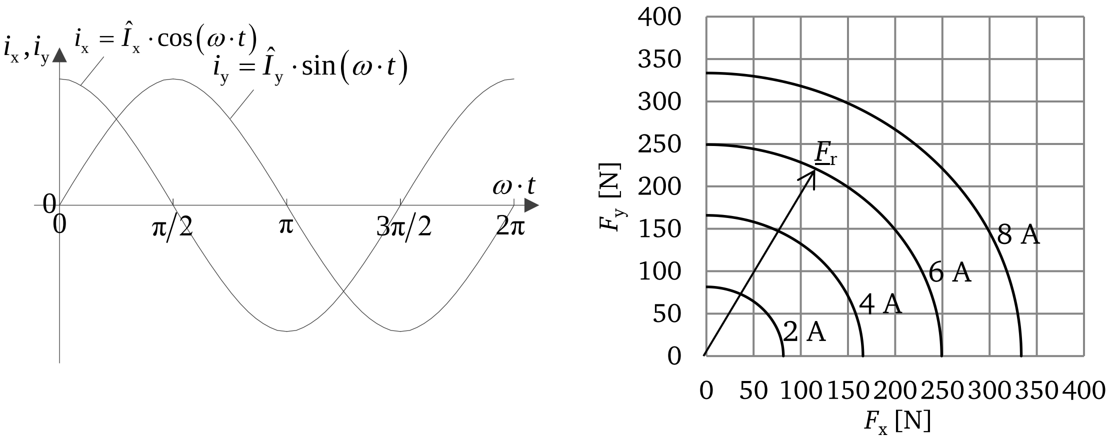

a) b)

Fig. 7-14 Calculated current feeding and generated radial force in combined magnetic bearing: a) sinusoidal current fed in the *x* and *y* control coils, b) generated radial force for different control current amplitudes $\hat{I}_x$ and $\hat{I}_y$, showing rotating trajectory of the superimposed force vector f_r with the amplitude of F_r, expressed by (7-16)

7.3.2 Radial Magnetic Bearing

The radial magnetic bearing is assembled on the upper side of the rotor and produces only the radial force. For field and force calculation, a 3D model is built in *JMAG* as shown in Fig. 7-15 with the dimensions and parameters shown in Table 7-4.

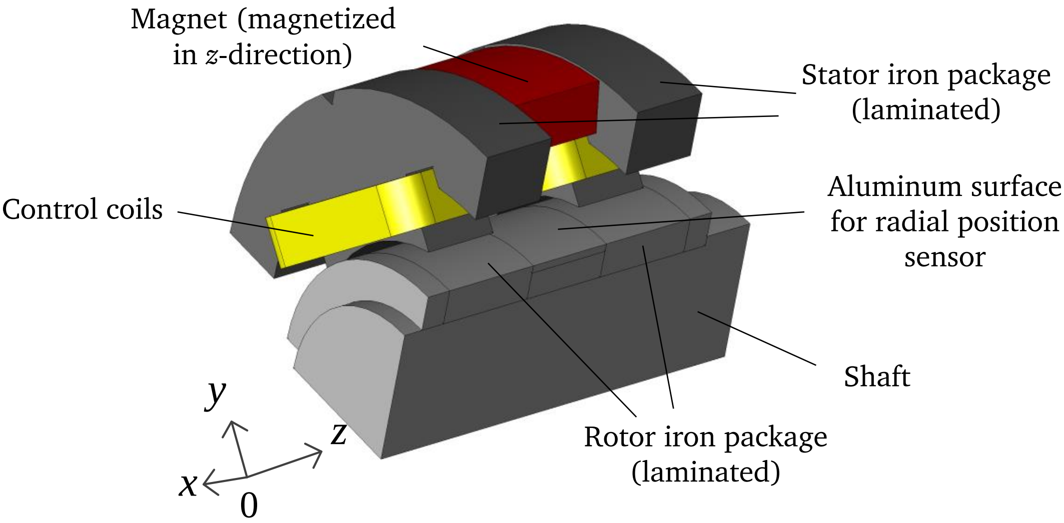

Fig. 7-15 3D model of the radial magnetic bearing, built in *JMAG*

Table 7-4 Main dimensions and specifications of the radial magnetic bearing

Stator parameters		
Stator inner diameter	d_{si}	80 mm
Axial length of stator iron	$L_{Fe,s}$	15 mm
Rotor parameters		
Rotor outer diameter	d_{ro}	76.7 mm
Axial length of rotor iron	$L_{Fe,r}$	19.5 mm
Air gap length	δ_r	1.65 mm
Magnet parameters		
Inner diameter	$d_{i,mag}$	116 mm
Outer diameter	$d_{o,mag}$	139 mm
Axial length	L_{mag}	20 mm
Control coil parameters		
Number of turns of control coil	N	60
Wire diameter	d_{Cu}	0.8 mm
Max. current	I_{max}	8 A

The biased field distribution excited by the magnets is calculated in a 3D model in *JMAG* and presented in Fig. 7-16. The fields in the air gaps are presented in Fig. 7-17. The field gradients under the pole areas vary not much. The average flux density under the pole area is 0.75 T.

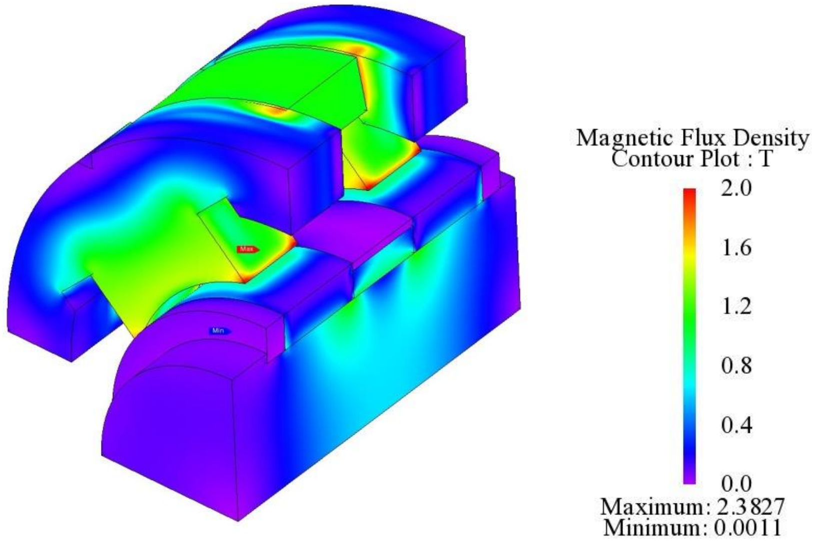

Fig. 7-16 Calculated biased field distribution in the radial magnetic bearing, calculated in *JMAG*

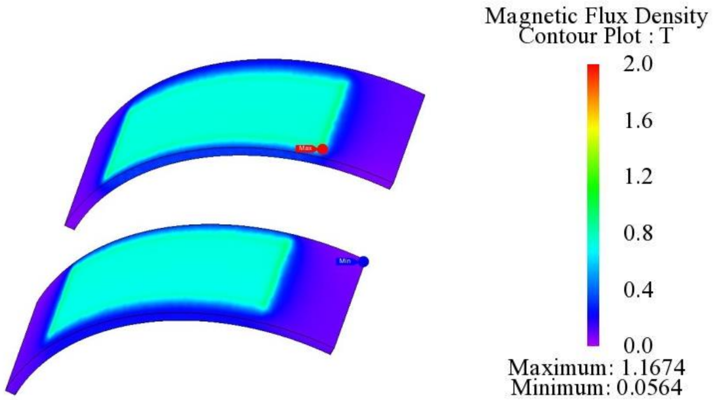

Fig. 7-17 Calculated biased field distribution in two air gaps of the radial magnetic bearing, calculated in *JMAG*

The force calculations are similar to the radial force in the combined magnetic bearing. The biased field $B_{\delta,r,0}$, which is excited by the magnets, is calculated in the 3D model and is shown in Fig. 7-18 a). The control field $B_{\delta,y,c}$ in y-direction is calculated in a 2D planar model with the current I_y fed in the y-coils and $I_x = 0$ A in the x-coils. The calculated control field $B_{\delta,y,c}$ for $I_y = 8$ A is shown in Fig. 7-18 b).

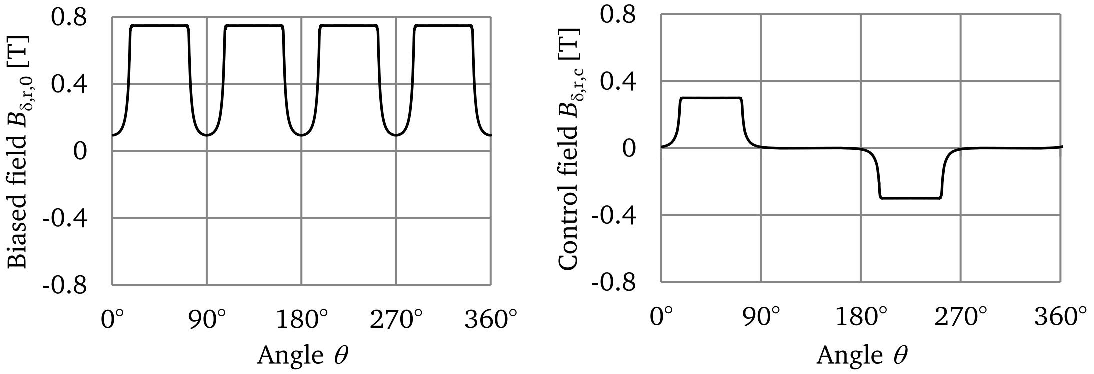

a) b)

Fig. 7-18 Calculated biased and control field in the air gap of the radial magnetic bearing: a) biased field calculated in the 3D model in Fig. 7-15 without control current, b) control field in y-direction for a DC current feeding $I_y = 8$ A, $I_x = 0$ A, calculated in a 2D planar model.

The superimposed air gap field $B_{\delta,y,1}$ and $B_{\delta,y,2}$ are calculated by (7-7) and (7-8), which are presented in Table 7-5, as well as the radial force calculated by (7-11). The forces F_y for various current I_y are plotted in Fig. 7-19. The maximum force $F_y = 402$ N can be obtained for the maximum current feeding of $I_y = 8$ A. The calculated maximum force requirement of 282.5 N can be fulfilled.

Table 7-5 Calculated field in the air gap and force in the radial magnetic bearing for $I_x = 0$ A

	Biased field	Current	Control field	Air gap field		Radial force
	$B_{\delta,r,0}$ [T]	I_y [A]	$B_{\delta,y,c}$ [T]	$B_{\delta,y,1}$ [T]	$B_{\delta,y,2}$ [T]	F_y [N]
Obtained from	(3D)	applied	(2D)	Eq.(7-7)	Eq.(7-8)	Eq.(7-11)
2D & 3D superpositon	0.749	-8	-0.299	0.450	1.048	-402.0
		-6	-0.224	0.525	0.973	-300.6
		-4	-0.148	0.601	0.897	-199.3
		-2	-0.074	0.675	0.823	-98.7
		0	0	0.749	0.749	0
		2	0.074	0.823	0.675	98.7
		4	0.148	0.897	0.601	199.3
		6	0.224	0.973	0.525	300.6
		8	0.299	1.048	0.450	402.0

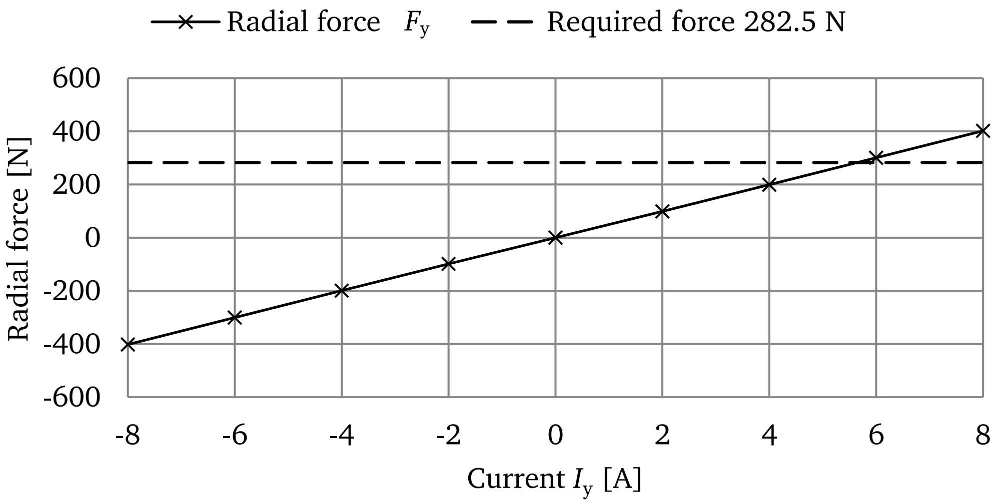

Fig. 7-19 Calculated force (superposition method) in y-direction for various currents feeding in the control coil in y-direction for the radial magnetic bearing, calculated for $I_x = 0$ A in the coil in x-direction

7.4 Loss Calculation in Magnetic Bearings

7.4.1 Copper Losses

Assuming the rotor is stably lifted up in axial direction without any bobbing or vibration, only a DC current is required in the axial coil of the combined bearing to support the rotor gravity. The DC resistive losses are calculated by (7-17).

AC current is fed in radial coils, producing a rotational radial force to compensate the rotor unbalanced force. Therefore, the amplitude depends on the rotor balancing quality, rotor speed and rotor dynamic behavior. The copper losses are roughly estimated by (7-18), assuming a sinusoidal current form, neglecting the harmonics due to PWM voltage.

$$P_{\mathrm{Cu,\,MB,\,a}} = I_{\mathrm{a}}^2 \cdot R_{\mathrm{MB,\,a}} \tag{7-17}$$

$$P_{\mathrm{Cu,\,MB,\,r}} = I_{\mathrm{r,\,rms}}^2 \cdot R_{\mathrm{MB,\,r}}\,,\ I_{\mathrm{r,\,rms}} = \hat{I}_{\mathrm{r}} \big/ \sqrt{2} \tag{7-18}$$

R denotes the coil resistance and the subscripts *a* and *r* denote axial and radial direction, respectively. *r* is the general symbol for direction *x* or *y*. The total losses should be the sum of both directions, which are presented in Table 7-6.

Table 7-6 Calculated copper losses in the used magnetic bearings for ideal sinusoidal current supply with an amplitude $\hat{I}_{\mathrm{r}}$

Combined bearing				Radial bearing	
$R_{\mathrm{MB,a}}$ [Ω] at 60 °C		$R_{\mathrm{MB,r}}$ [Ω] at 60 °C		$R_{\mathrm{MB,r}}$ [Ω] at 60 °C	
1.525		0.807		1.336	
Current I_{a} [A]	Copper losses $P_{\mathrm{Cu,MB,a}}$ [W]	Current $\hat{I}_{\mathrm{r}}$ [A]	Copper losses $P_{\mathrm{Cu,MB,r}}$ [W]	Current $\hat{I}_{\mathrm{r}}$ [A]	Copper losses $P_{\mathrm{Cu,MB,r}}$ [W]
4.4	29.5	0	0	0	0
		2	3.23	2	5.34
		4	12.9	4	21.4
		6	29.1	6	48.1
		8	51.6	8	85.5

7.4.2 Stator Iron Losses

In the axial magnetic bearing, if the rotor is ideally located in the central position, only DC current is required to support the rotor gravity, thus there is no loss in the stator iron as there is no flux variation. In case of disturbance or vibration, a varying control current is required and causes additional eddy current losses in the stator iron. But the current is unpredictable and will not be considered here.

In the radial magnetic bearing, the stator iron losses are caused by the flux variation due to the varying control current. The biased field does not cause stator iron losses. Therefore, the iron losses are calculated numerically with a 2D model in *JMAG* (Fig. 7-11) by feeding a sinusoidal control current in the control coils without biased field. After getting the numerical results, one correction factor $k_{\mathrm{Vd}} = 1.8$ is used considering the effect of the bridging between the iron sheets due to the insulation damage during the laser cutting process. The calculated iron losses are shown in Fig. 7-20 for the radial force actuator in the combined bearing and in Fig. 7-21 for the radial magnetic bearing.

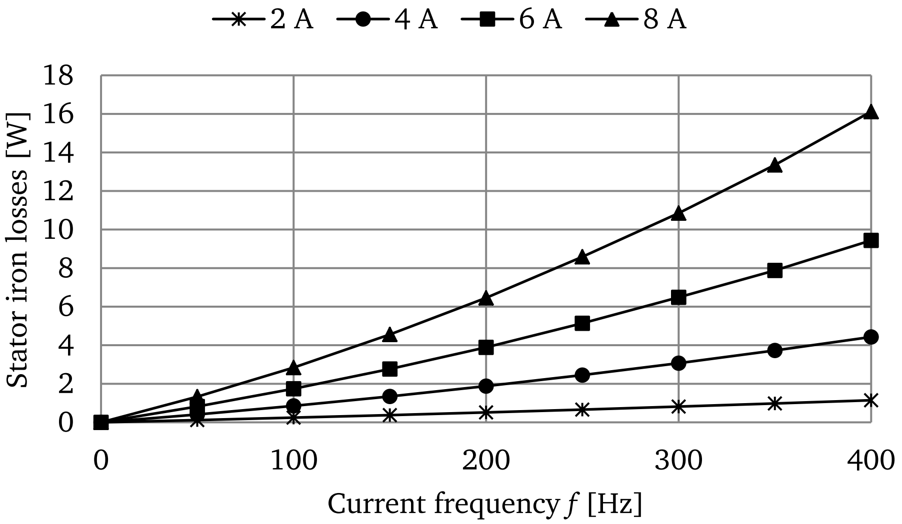

Fig. 7-20 Calculated stator iron losses in the combined magnetic bearing (radial force actuator) due to the sinusoidal current feeding in the control coils, neglecting biased field, which is excited by the magnets, calculated by 2D model in *JMAG* (The displayed lines correspond to different amplitudes of the applied control currents.)

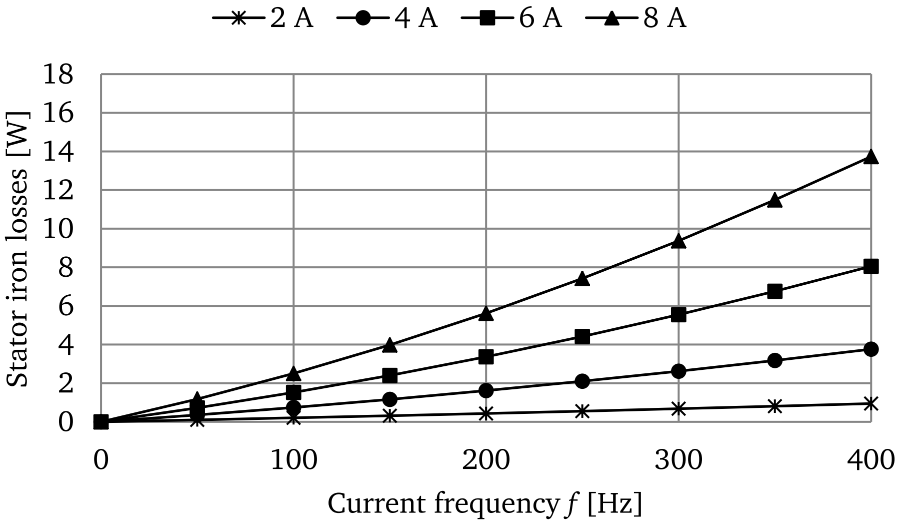

Fig. 7-21 Calculated stator iron losses in the radial magnetic bearing due to the sinusoidal current feeding in the control coils, neglecting the biased field, which is excited by the magnets, calculated by 2D model in *JMAG* (The displayed lines correspond to different amplitudes of the applied control currents.)

7.4.3 Rotor Iron Losses

The rotor is built with laminated iron, and the iron losses are much lower compared to a solid rotor, but still should be taken into account carefully due to the poor rotor heat dissipation in the flywheel system. The rotor iron losses calculated here include two parts: the one caused by the biased field and the one caused by the control field. These two loss components are calculated separately and summed up afterwards to obtain the total losses.

1) Rotor losses caused by biased field

The biased field distribution on the rotor surface is not ideally constant. Field sags can be seen in Fig. 6-10 a) in the air gap under the stator pole gap. After *Fourier* transform, the field can be described by (7-19) in stator reference frame. This field is non-rotating, therefore, in the rotor reference frame, all of these field harmonics have the same rotating speed Ω relative to the rotor, which will induce rotor losses.

$$B_{\delta,\mathrm{B,s}} = \sum_{\mu=1}^{\infty} B_{\delta,\mu,\mathrm{B}} \cdot \cos\left(\mu \cdot p \cdot \theta_{\mathrm{s}} - \varphi_{\mu}\right) \text{ (stator reference frame)} \tag{7-19}$$

$$B_{\delta,\mathrm{B,r}} = \sum_{\mu=1}^{\infty} B_{\delta,\mu,\mathrm{B}} \cdot \cos\left(\mu \cdot p \cdot \theta_{\mathrm{r}} - \mu \cdot p \cdot \Omega \cdot t - \varphi_{\mu}\right) \text{ (rotor reference frame)} \tag{7-20}$$

μ is the harmonic order, p is the pole counts, θ_{s} and θ_{r} are the angles in stator and rotor reference frames, φ_{μ} is the phase angle of each harmonic μ, $B_{\delta,\mu,\mathrm{B}}$ is the amplitude of each harmonic μ.

The rotor losses can be calculated numerically in *JMAG*. Usually a 3D transient simulation is required due to the unique 3D field distribution of a homo-polar magnetic bearing, which is rather time consuming. Therefore, a static model is used here as an alternative approach. Firstly, the static field calculation is performed in a 3D static model, as shown in Fig. 7-6. Then the rotor iron is segmented into small rings as shown in Fig. 7-22, with the created r-θ-z reference frame and a sample point A at the center position of one segmented ring. The aim is to obtain the spatial field distribution versus angle θ at the circle which is coincident with point A and it is used to represent the field distribution in this segmented ring.

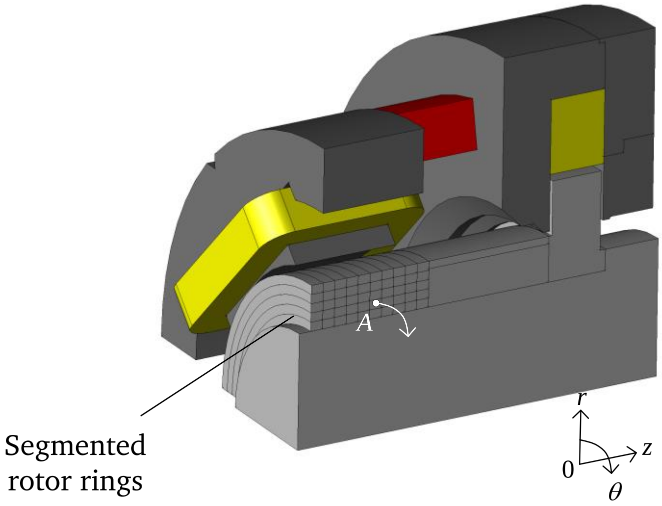

Fig. 7-22 Assumed segmented rotor core in order to obtain the field distribution (versus angle θ) in each segmented ring for rotor iron loss calculation based on the field calculation results in *JMAG*

Fig. 7-23 a) shows the field distribution in one ring of the simulation model as an example. By replacing θ with $\Omega \cdot t$ in Fig. 7-23 a), this spatial field distribution is converted to time domain in the rotor reference frame, which represents the field variation versus time of the sample point *A* in the rotor in Fig. 7-22. After performing the *Fourier* transform in time domain, the time harmonic field can be obtained (Fig. 7-23 b)) with the field amplitude B_μ and frequency f_μ for each harmonic order μ.

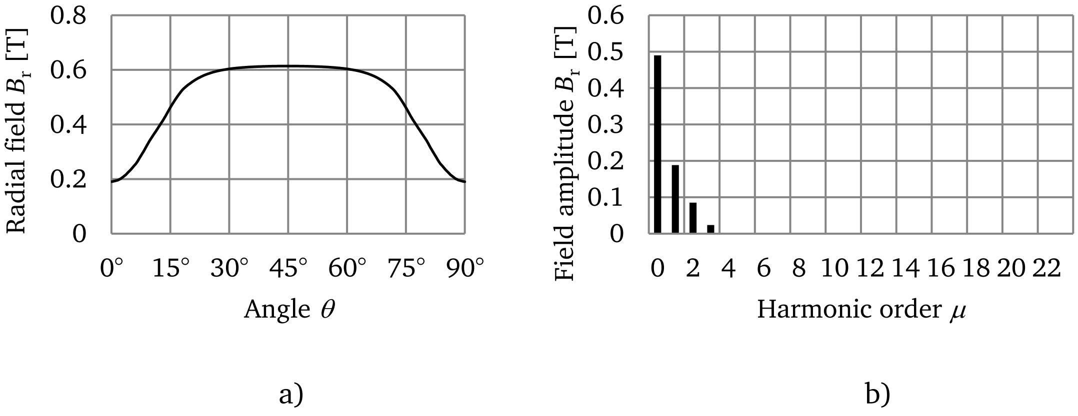

a) b)

Fig. 7-23 Calculated field distribution and harmonics in one segmented ring of the rotor iron of the combined magnetic bearing: a) radial field B_r under one pole pitch at the circle r = 33.603 mm, z = 9.145 mm, b) harmonics of radial field B_r, base frequency $f_1 = p \cdot n$ = 1600 Hz at speed n = 24000 min^{-1} with the pole number p = 4

Finally, by using B_μ and f_μ, the specific losses in each segment are calculated by classical specific iron loss formula (7-21) [58]. Due to the symmetric configuration, all the points of one segmented ring have the same field spectrum after *Fourier* transform. Therefore, the total iron losses (in W/kg) in the rotor can be calculated by (7-22), where m_{seg} (in kg) is the mass of each segmented ring.

$$p_{\mathrm{Fe,\,seg}} = \sum_{\mu=1}^{n} k_{\mathrm{h}} \cdot B_\mu^2 \cdot f_\mu + k_{\mathrm{c}} \cdot B_\mu^2 \cdot f_\mu^2 + k_{\mathrm{e}} \cdot B_\mu^{1.5} \cdot f_\mu^{1.5} \tag{7-21}$$

$$P_{\mathrm{Fe}} = \sum_{seg} p_{\mathrm{Fe,\,seg}} \cdot m_{\mathrm{seg}} \tag{7-22}$$

In (7-21), k_{h}, k_{c}, k_{e} are the iron loss coefficients considering hysteresis loss in W/(kg·T^2·Hz), eddy current loss in W/(kg·T^2·Hz^2) and excess loss in W/(kg·T$^{1.5}$·Hz$^{1.5}$). These coefficients can be determined by performing the curve fitting for a given loss table of certain iron sheet type. For the used iron sheet NO20 in this design, the coefficients in Table 7-7 are obtained based on the loss table in Appendix B. The root mean squared error (RMSE) calculates the square root of the quadratic mean values of the differences between predicted values and observed values. It evaluates the accuracy of the predicted values calculated by (7-21) compared to the given data in the loss table. The calculated RMSE value for the fitting is 3.985 W/kg, which is scale dependent. But compared to the absolute losses especially at high frequency (hundreds of W/kg), the RMSE is small enough and acceptable.

Table 7-7 Calculated iron loss coefficients for iron sheet NO20, obtained by data fitting of the loss table in Appendix B (RMSE: root mean squared error)

Coefficient	k_{h} [W/(kg·T^2·Hz)]	k_{c} [W/(kg·T^2·Hz^2)]	k_{e} [W/(kg·T$^{1.5}$·Hz$^{1.5}$)]	RMSE [W/kg]
Value	**0.**03395	9.939×10^{-6}	4.353×10^{-4}	3.985

The calculated static field is already obtained in Fig. 7-6 for the combined magnetic bearing and in Fig. 7-16 for the radial magnetic bearing. The rotor irons, taken out from these two graphs, are presented in Fig. 7-24. The mesh size is 0.3…0.5 mm.

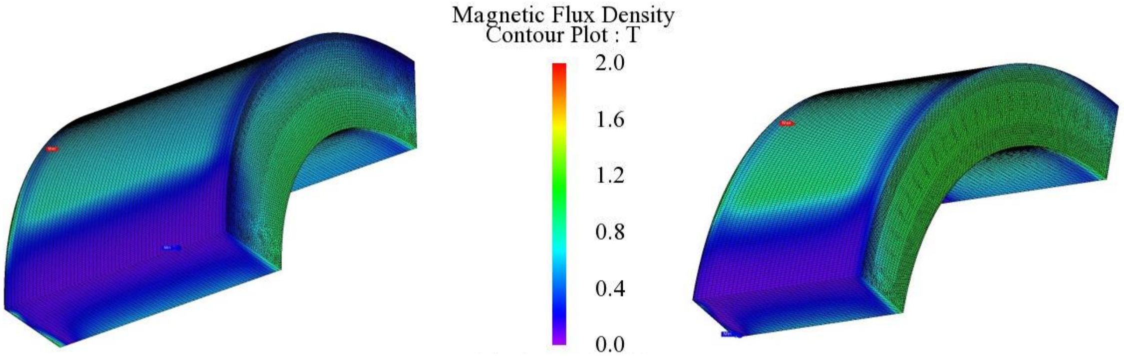

a) b)

Fig. 7-24 Static field distribution in the rotor irons, calculated in *JMAG*: a) in combined magnetic bearing, b) in radial magnetic bearing

For the rotor iron loss calculation, the rotor iron in combined magnetic bearing is divided into 40 segmented rings in radial direction and 50 segmentations in axial direction. In the radial magnetic bearing, the rotor iron is divided into 30 segmented rings in radial direction and 40 segmentations in axial direction. The size of each division is close to the mesh element size. After getting the losses, one correction factor $k_{\mathrm{vy}} = 1.5$ is used considering the effect of bridging between the iron sheets due to the insulation damage during the laser cutting process. The calculated losses of two magnetic bearings are shown in Table 7-8.

Table 7-8 Analytically calculated losses in the rotor iron of magnetic bearings caused by biased field, which is obtained in *JMAG*

Rotational speed n [min^{-1}]	Losses in rotor iron caused by biased field [W]	
	Combined MB	Radial MB
0	0	0
6000	2.20	2.57
12000	5.82	6.78
18000	10.50	12.21
24000	16.08	18.71

2) Rotor losses caused by control field

The second part of the rotor losses is due to the spatial harmonics of the control field by feeding a sinusoidal current. (The losses caused by time harmonics are calculated in Chapter 7.4.4.3.) The control field distribution (e.g. Fig. 7-12 b) and Fig. 7-18 b)) can be described by a sum of spatial harmonics in (7-23) in stator reference frame. These harmonics rotate with the speed Ω/ν, which are asynchronous with the rotor for $\nu \neq 1$ and induce rotor losses.

$$B_{\delta,\mathrm{c}} = \sum_{\nu=1}^{\infty} B_{\delta,\nu,\mathrm{c}} \cdot \cos\left(\nu \cdot p \cdot \theta_{\mathrm{s}} - \omega_{\mathrm{s},1} \cdot t - \varphi_{\nu}\right) \text{ (stator reference frame)} \qquad (7\text{-}23)$$

In (7-23), ν is the harmonic order, p is the pole counts, θ_{s} is the angle in stator reference frame, φ_{ν} is the phase angle for ν-th harmonic, $B_{\delta,\nu,\mathrm{c}}$ is the amplitude for ν-th harmonic. The rotor losses caused by the control field can be calculated by a 2D model without the biased field, thus neglecting the saturation effect due to the superposition of the biased field and control field. After getting the numerical results, one correction factor $k_{\mathrm{vy}} = 1.5$ is used considering the effect of the bridging between the iron sheets due to the insulation damage during the laser cutting process. For sinusoidal current feeding, the calculated rotor iron losses are shown in Fig. 7-25 for the combined magnetic bearing and Fig. 7-26 for the radial magnetic bearing. In the end, the losses in Table 7-8 and Fig. 7-25 and Fig. 7-26 should be summed up for the corresponding magnetic bearings to obtain the total rotor iron losses.

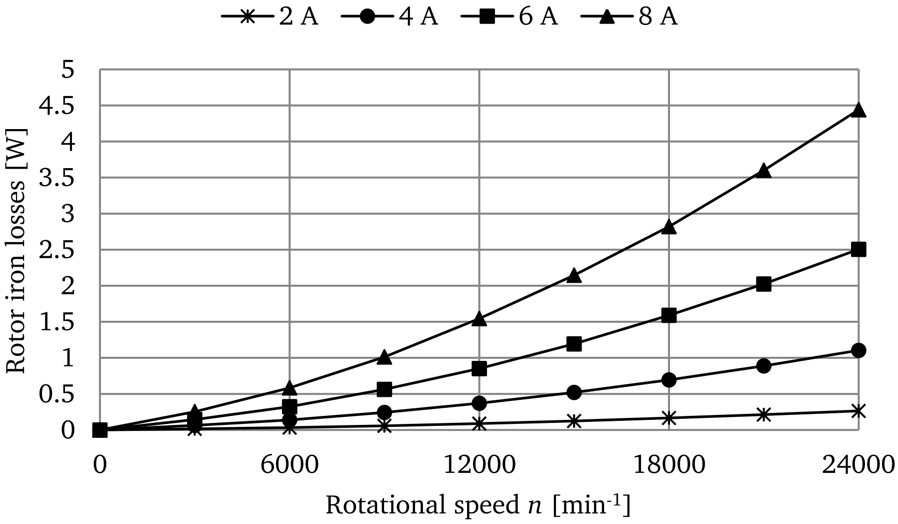

Fig. 7-25 Calculated rotor iron losses in the radial actuator of the combined magnetic bearing due to the sinusoidal current feeding in the control coil (current frequency f and rotational speed n fulfill: $f = n$, with n in s^{-1}), neglecting the biased field excited by the magnets, calculated by 2D model in *JMAG* (Displayed lines correlate to different amplitudes of the applied control current.)

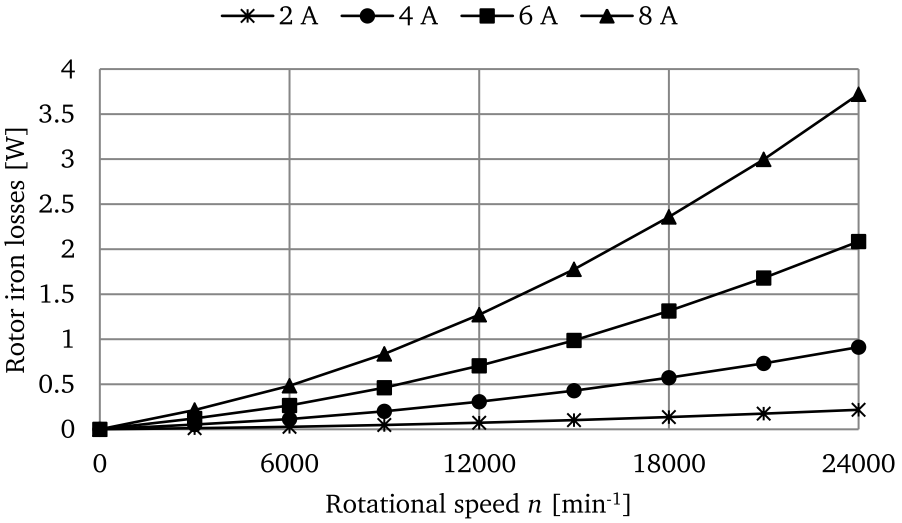

Fig. 7-26 Calculated rotor iron losses in the radial magnetic bearing due to the sinusoidal current feeding in the control coil (current frequency f and rotational speed n fulfill: $f = n$, with n in s^{-1}), neglecting the biased field excited by the magnets, calculated by 2D model in *JMAG* (The displayed lines correlate to different amplitudes of the applied control current.)

7.4.4 Additional Losses due to PWM Control

The coils of the magnetic bearings are fed by a voltage source inverter with the DC link voltage of 150 V. The output voltage is pulse-width modulated, which causes harmonics in the winding, resulting in additional losses. This chapter shows the additional loss calculation in the combined magnetic bearing as an example.

7.4.4.1 Harmonics due to Switching Effect

In order to obtain the harmonics, a simulation model (Fig. 7-27) was built in *Matlab Simulink* to generate the modulated voltage. The switching control signals are simply generated by comparing a given reference voltage and a modulation carrier. The modulated voltage is applied on an *R-L* series-connected component, representing the coils in magnetic bearings. Thus the current can be obtained and used as the current supply for the magnetic bearings in the 2D model in *JMAG* to calculate the additional losses.

The simulated modulated voltage and current waveforms of the x coil in the combined magnetic bearing are shown in Fig. 7-28, as well as the current harmonics. The fundamental and 7 main harmonic components of the current are shown in Table 7-9. The switching frequency is $f_{\mathrm{T}} = 16\ \mathrm{kHz}$. Here the maximum current of 8 A is chosen for the analysis, which is as the worst case for the loss and thermal calculations.

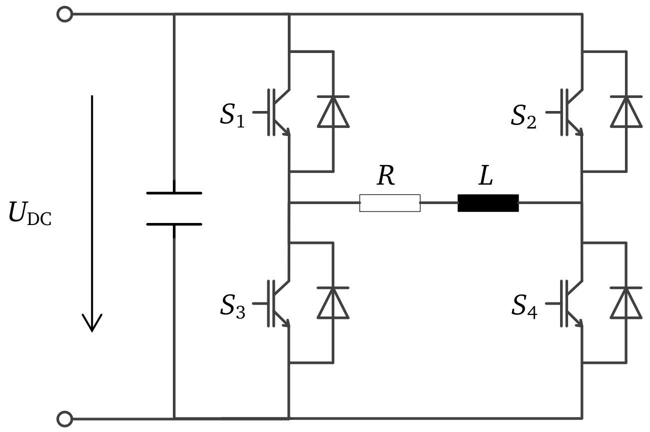

Fig. 7-27 Scheme of the modeled voltage source inverter to feed one coil of the magnetic bearing, U_{DC}: DC link voltage, R and L: resistance and inductance of the control coil, $S_1 \sim S_4$: switches

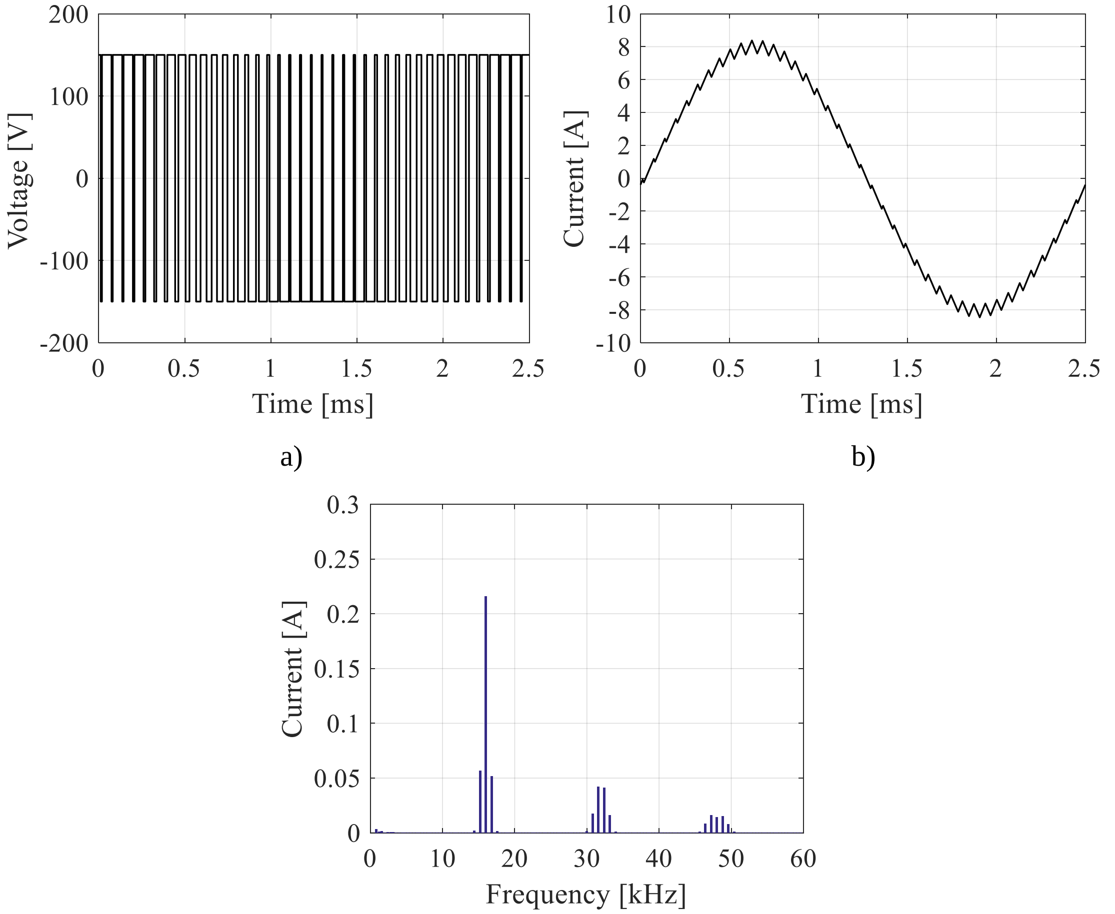

a)

b)

c)

Fig. 7-28 Calculated waveforms and harmonics in the x coils of the inverter-fed combined magnetic bearing, rotational speed 24000 min^{-1}, switching frequency $f_{\mathrm{T}} = 16\ \mathrm{kHz}$: a) modulated voltage, b) current (fundamental amplitude $\hat{I}_1 = 8.03\ \mathrm{A}$, frequency $f_{\mathrm{s}} = 400\ \mathrm{Hz}$), c) harmonics of the current (fundamental not shown)

Table 7-9 Calculated main harmonic components of the current in Fig. 7-28 c), switching frequency $f_T = 16$ kHz, fundamental frequency $f_s = 400$ Hz

Rotational speed: 24000 min^{-1}			
Frequency [Hz]		Current [A]	Phase angle [°]
f_s	400	8.03	-93.23
$f_T - 2 \cdot f_s$	15200	0.057	-167.91
f_T	16000	0.216	0.056
$f_T + 2 \cdot f_s$	16800	0.0516	168.03
$2 \cdot f_T - 3 \cdot f_s$	30800	0.0176	108.08
$2 \cdot f_T - f_s$	31600	0.0423	-83.97
$2 \cdot f_T + f_s$	32400	0.0413	-96.02
$2 \cdot f_T + 3 \cdot f_s$	33200	0.0164	71.97

7.4.4.2 Additional Copper Losses

The additional copper losses are calculated analytically by using the formulas in Chapter 6.3.2. The coils in the radial actuator are wound around each pole with the pole and slot shape shown in Fig. 7-29. To simplify the calculation, the coils are assumed to locate in a rectangular-shape slot as shown in Fig. 7-29. The flux leakage in the assumed rectangular-shape slot is supposed to be higher than in the real slot. Therefore, the additional losses will be over-estimated, which is as the worst case.

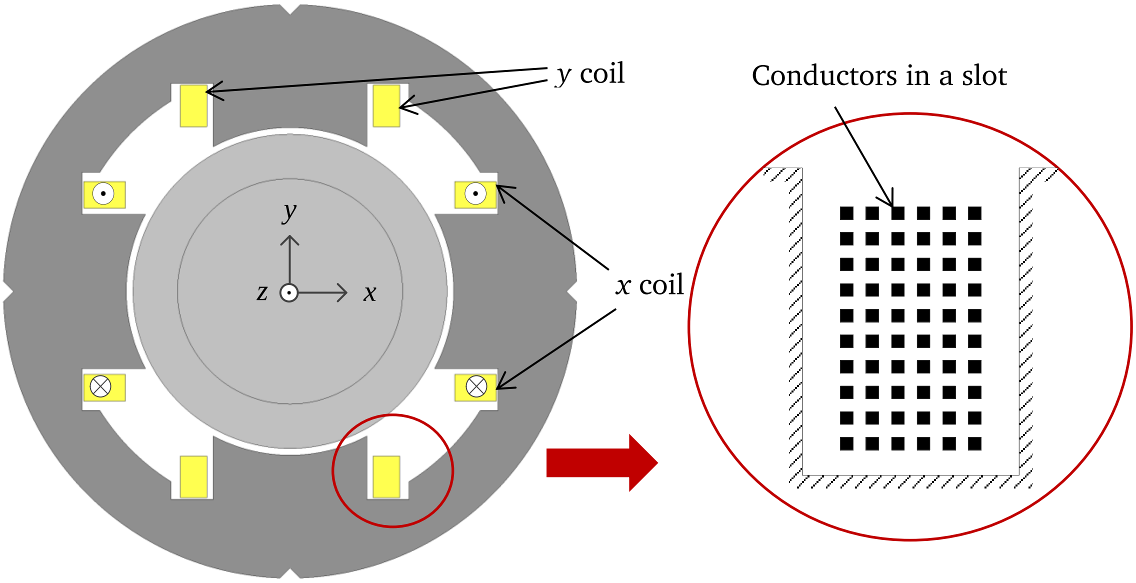

Fig. 7-29 Section view of the radial actuator of the magnetic bearings, modeled in *JMAG*

There are 60 turns of wires in each coil, which are series connected. According to the designed slot geometry in the actuator, their arrangements are shown in Fig. 7-29. 6 wires locate in the parallel direction of the slot bottom and 10 wires locate in the vertical direction of the slot bottom. As all the wires are series connected, no circulating current will occur. Therefore, the additional losses are only due to the skin and proximity effect.

The calculated results are shown in Table 7-10 for the rotor speed of 24000 min^{-1}, considering the current with the harmonics in Table 7-9. Compared to the DC resistive losses, which considers a pure sinusoidal current feeding in a DC resistance, the current harmonics and the skin and proximity effect cause 0.4 % higher additional losses, which is very small.

Table 7-10 Calculated copper losses in the coils of the radial actuator of the combined magnetic bearing, for the current harmonics in Table 7-9 (winding resistance $R_s = 0.807\ \Omega$ at temperature $\vartheta = 60$ °C)

Rotational speed n	Fundamental current $\hat{I}_1$	DC resistive losses $P_{\mathrm{Cu,DC,1}}$	AC resistive losses $\Sigma P_{\mathrm{Cu,AC},k}$	$\Sigma P_{\mathrm{Cu,AC},k}/P_{\mathrm{Cu,DC,1}}$
24000 min^{-1}	8.03 A	52.06 W	56.24 W	1.004

n: rotor speed,

$\hat{I}_1$: amplitude of the fundamental current,

$P_{\mathrm{Cu,DC,1}}$: DC resistive losses caused by fundamental current,

$\Sigma P_{\mathrm{Cu,AC},k}$: sum of the AC resistive losses considering the skin and proximity effect for the current harmonics in Table 7-9.

7.4.4.3 Additional Iron Losses

The iron losses are calculated numerically in the 2D model in *JMAG* (Fig. 7-11, without biased field). Instead of feeding a sinusoidal control current, the current with the harmonics in Table 7-9 is fed in the control coils. The calculated iron losses are shown in Table 7-11. The result shows that the current harmonics cause 1.94 times higher iron losses in the rotor and 1.77 times higher losses in the stator of the combined magnetic bearing. As the radial magnetic bearing has a similar structure as the radial actuator in the combined bearing, and the field distribution of both magnetic bearings are comparable, these ratios are also suitable when estimating the additional iron losses in the radial magnetic bearing.

Table 7-11 Calculated iron losses in the combined magnetic bearing, calculated in the 2D planer model in *JMAG* shown in Fig. 7-11

Rotational speed: n = 24000 min^{-1} Sinusoidal: feeding a sinusoidal current with the amplitude $\hat{I}_1$ = 8.03 A PWM: feeding the currents in Table 7-9			
	Sinusoidal	PWM	Ratio: PWM/Sinusoidal
Rotor iron	4.44 W	8.63 W	1.94
Stator iron	16.12 W	28.6 W	1.77

7.5 Dummy Set-up

To verify the levitation force of the magnetic bearings, a prototype containing the magnetic bearings and a shaft was built. The configuration is shown in Fig. 7-30. The electric machine and mechanical bearing are not mounted. The prototype and components are shown in Fig. 7-31. To load the magnetic bearings, an additional weight was hung on the shaft in order to achieve the same weight as the designed flywheel rotor.

The testing was only carried out for a static levitation, i.e. the rotor is not rotating. The testing shows that the rotor weight of 90 kg (900N) can be suspended by the magnetic bearings, but only in one axial direction. This is the case, when the prototype Fig. 7-30 is vertical positioned with the B-side on the top. If the rotor is flipped, it cannot be levitated. That indicates a significant asymmetric biased field of the axial magnetic bearing that can preferably produce force only in one direction. This asymmetric effect is even larger than the simulated results in Chapter 7.3.

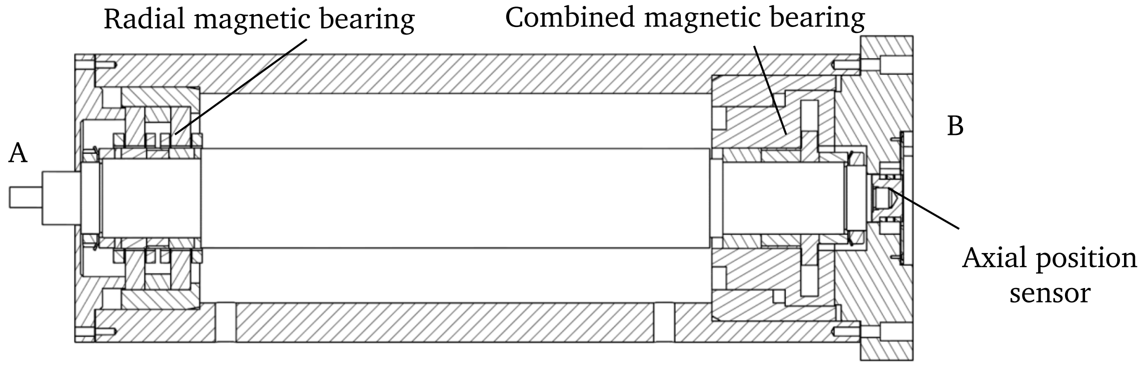

Fig. 7-30 Configuration of the prototype for the magnetic bearing testing under atmospheric pressure, including a shaft and radial magnetic bearing (A-side) and a combined magnetic bearing (B-side) without mechanical bearings or an E-machine [47]

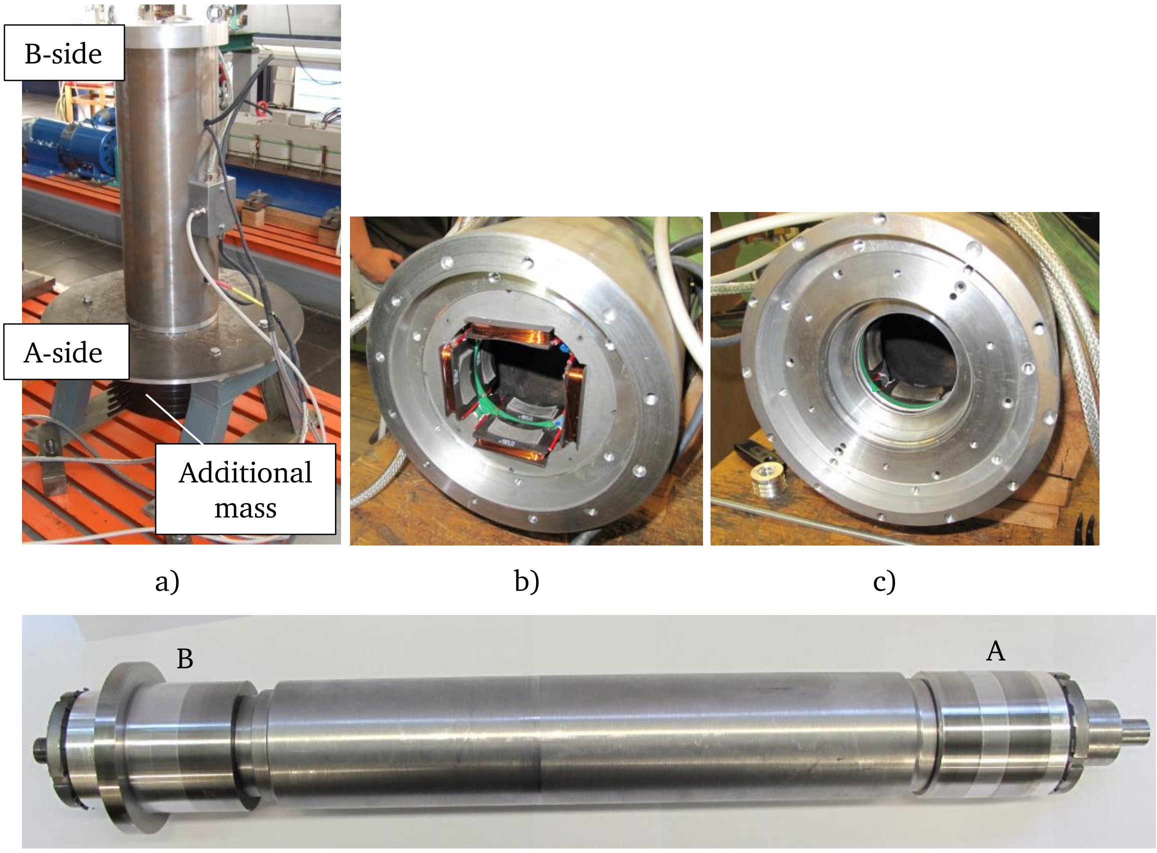

a) b) c)

d)

Fig. 7-31 Dummy prototype for magnetic bearing testing:

a) prototype, b) radial magnetic bearing stator (A-side), c) combined magnetic bearing stator (B-side), d) dummy rotor showing shaft and magnetic bearing rotor components

8. Flywheel System Set-up

8.1 System Construction

The system was constructed and set up in the *Institute for Electrical Energy Conversion (Institut für Elektrische Energiewandlung, EW), TU Darmstadt*. The system overview without burst containment is shown in Fig. 8-1.

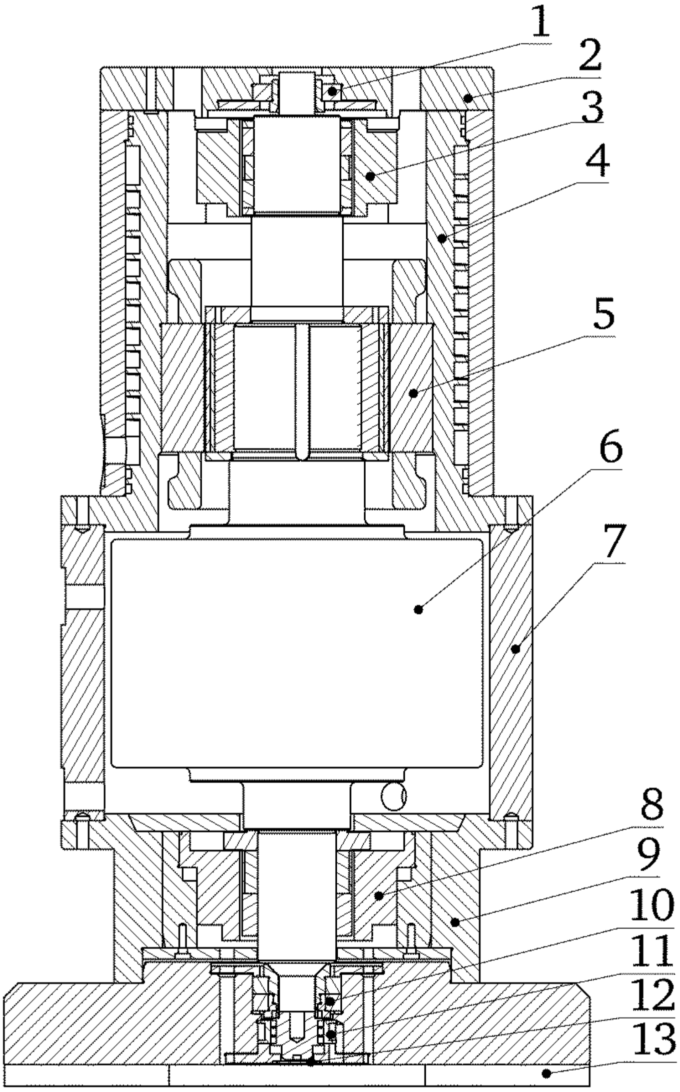

Fig. 8-1 Constructed flywheel system without burst containment [47] (*Autodesk Inventor 2018*): 1-safety bearing (top), 2-top lid, 3-radial magnetic bearing, 4-upper housing, 5-E-machine stator, 6-flywheel rotor, 7-middle housing, 8-combined magnetic bearing, 9-bottom housing, 10-safety bearing (bottom), 11-axial position sensor, 12-revolusion sensor, 13-bottom plate

8.1.1 Rotor Construction

The monolithic flywheel body and shaft is manufactured from steel 30CrNiMo8. In order to reduce the thermal stress concentration in the fillets, the rotor was firstly manufactured with the contour of rotor IV in Table 5-13. After that a quenching process was performed for the rotor hardening. The rotor was heated up to 830 … 860 °C and rapidly cooled in the salt bath of 180 °C. After obtaining the hardened piece, the rotor is tooled into the designed contour with correct dimensions. Then the rotor is painted black (Fig. 8-2) in order to increase the radiative emissivity.

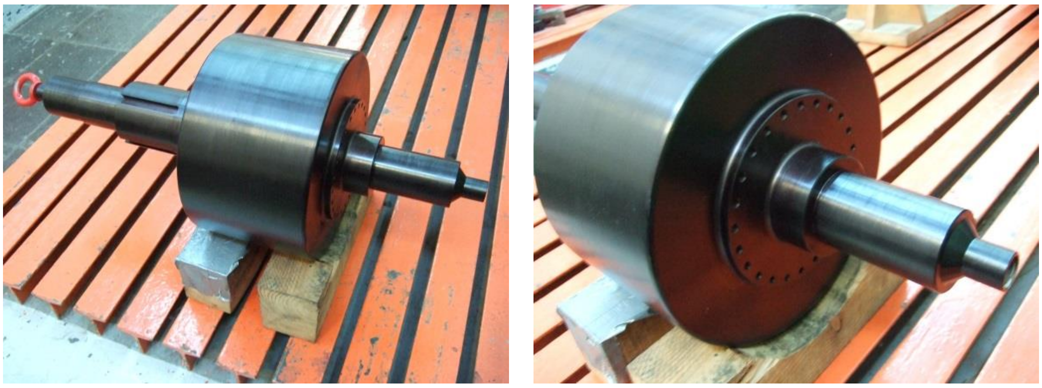

a) b)

Fig. 8-2 Black-pained rotor (material 30CrNiMo8, after quenching process): a) showing rotor contour, b) showing balancing holes

The rotor iron package of E-machine was mounted on the shaft with the shrink fitting in Table 8-1. The segmented magnets are glued on the rotor iron package and grinded afterwards to obtain the correct dimensions. Since the fitting between magnets and bandage is as large as 0.3 mm, mounting by press fit is prone to cause bandage damage due to enormous axial force. Therefore, cold shrink fitting is adopted by cooling the rotor to approx. - 20 °C in the fridge (Fig. 8-3). Liquid Nitrogen cooling is not used here as the transient temperature distribution due to rapid cooling may cause large thermal stress on the rotor. The bandage is then pressed on the cooled rotor and grinded to the correct dimension (Fig. 8-4).

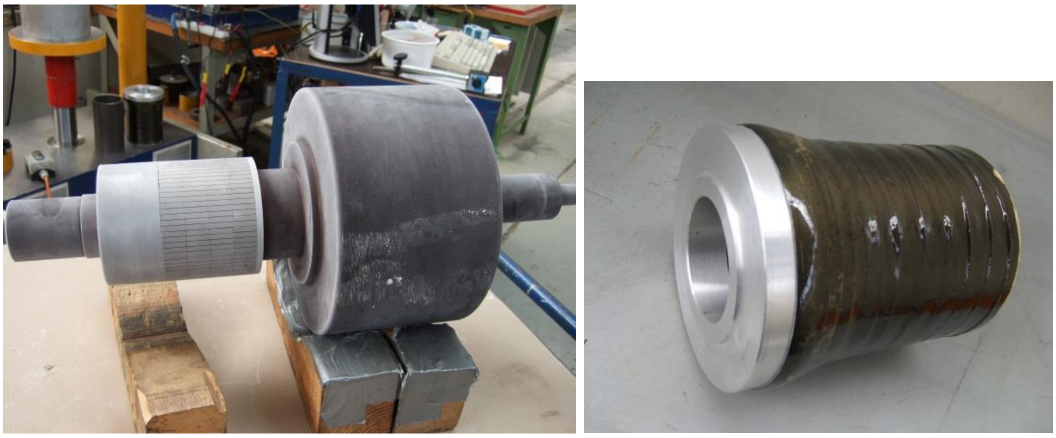

a) b)

Fig. 8-3 Cold flywheel rotor and carbon fiber bandage prepared for mounting: a) cold flywheel rotor with glued magnets, b) bandage sleeve

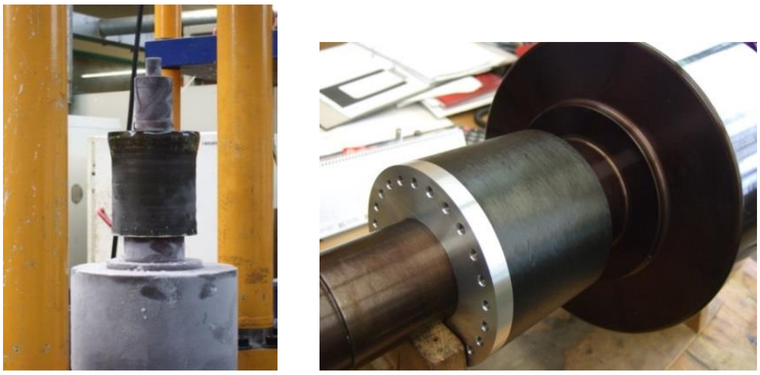

a) b)

Fig. 8-4 Flywheel rotor with mounted carbon fiber bandage: a) before bandage surface grinding, b) after bandage surface grinding

The rotor components are mounted on the shaft with shrink fittings shown in Table 8-1. The fittings are determined based on the stress calculation (formulas in Appendix C), fulfilling the following restrictions for maximum temperature of 150 °C and maximum speed of $1.2 \cdot n_{\max} = 28800\ \mathrm{min}^{-1}$:

1) The total tensile stress in the assembled rotor component due to press fit, thermal expansion and rotation should be within the material strength limit, considering the safety factor.

2) The contact pressure between each component should always be positive (under pressure on each contact surface) to assure they are successfully assembled, even for 20 % over-speed testing.

3) The undersize between each component should be within a reasonable range for the possibility of shrink fitting assembly.

Table 8-1 Fittings of flywheel rotor components

Component A	Component B	Fitting
E-machine		
Shaft	Rotor iron package	- 0.07 mm
Magnets	Bandage	- 0.3 mm
Shaft	Aluminum end ring (upper)	- 0.2 mm
Shaft	Aluminum end ring (lower)	- 0.3 mm
Combined MB		
Shaft	Axial disk	R5/s5
Shaft	Rotor iron package	M5/s5
Shaft	Magnetic steel	K5/s5
Magnetic steel	Aluminum sleeve	H5/u5
Radial MB		
Shaft	Rotor iron package	H5/u5
Shaft	Magnetic steel	G5/u5
Magnetic steel	Aluminum sleeve	H5/r5
Shaft	End ring	G6/u5
Safety bearing		
Shaft	Safety bearing adapter (upper)	+ 0.1 mm
Shaft	Safety bearing adapter (lower) radial surface	+ 0.1 mm
Shaft	Safety bearing adapter (lower) conical surface	+ 0.14 mm

8.1.2 Inner Housing

The inner housing is composed of 3-stage cylindrical housing, one top lid and one bottom plate. The upper part of the cylindrical housing (Fig. 8-5) has the function to fix the stator of the radial magnetic bearing and the E-machine (Fig. 8-6 a)). They are mounted by shrink fitting.

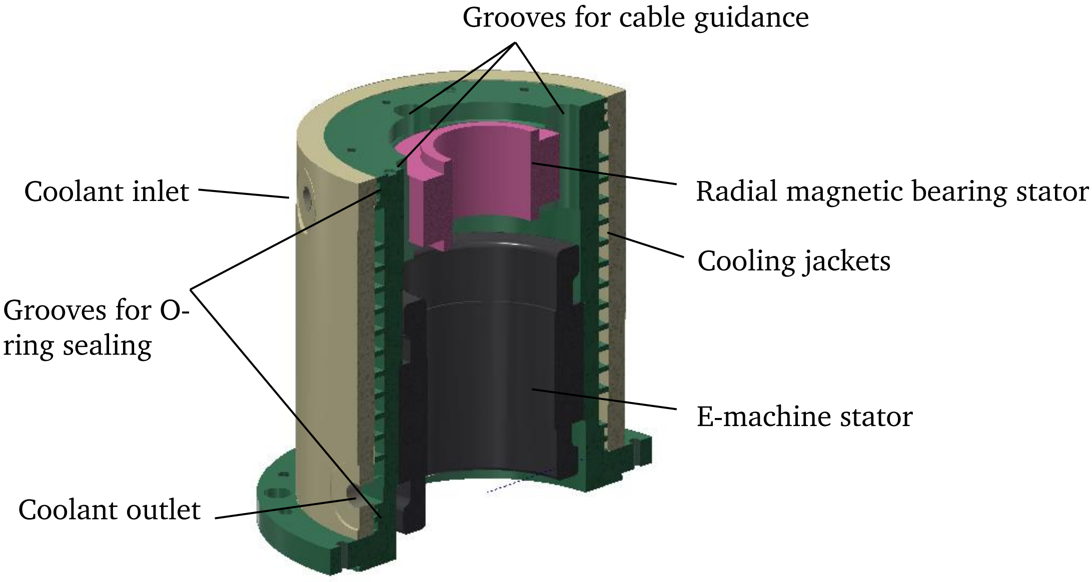

Fig. 8-5 Upper housing (*Autodesk Inventor 2018*) [47]

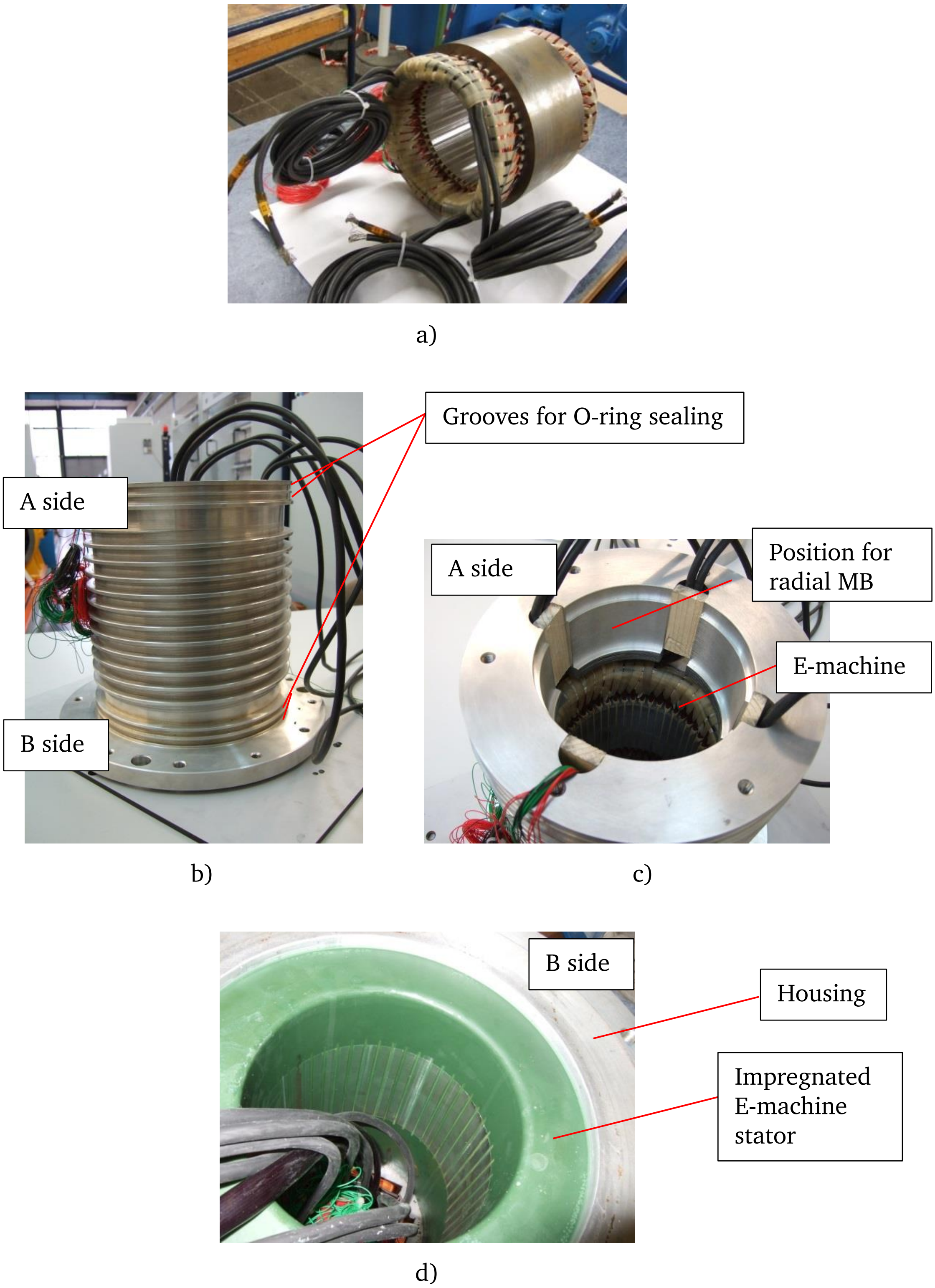

Fig. 8-6 Components of upper housing: a) E-machine stator, b) upper housing with spiral cooling jackets, c) top view of the upper housing with E-machine (before impregnation), d) bottom view of the upper housing with impregnated E-machine stator

The spiral cooling jackets (Fig. 8-6 b)) are manufactured on the housing to remove the heat of the E-machine. Two O-rings are used on both sides for sealing. For the cable guidance, 4 grooves (Fig. 8-6 c)) are manufactured for both power cables and signal wires of the E-machine and the radial magnetic bearing. The cables are extended through the top lid and fixed on the connectors on the vacuum chamber. After the E-machine stator was mounted on the upper housing, vacuum pressure impregnation (VPI, Fig. 8-6 d)) was performed in order to improve the insulation and thermal conductivity of the stator winding.

The bottom cylindrical housing (Fig. 8-7) is used to fix the combined magnetic bearing, also by shrink fitting. For a successful mounting, the end plate of magnetic bearing is constructed by two C-shape plate. They are assembled after the rotor is positioned and fixed on the bottom plate side by long screws bars.

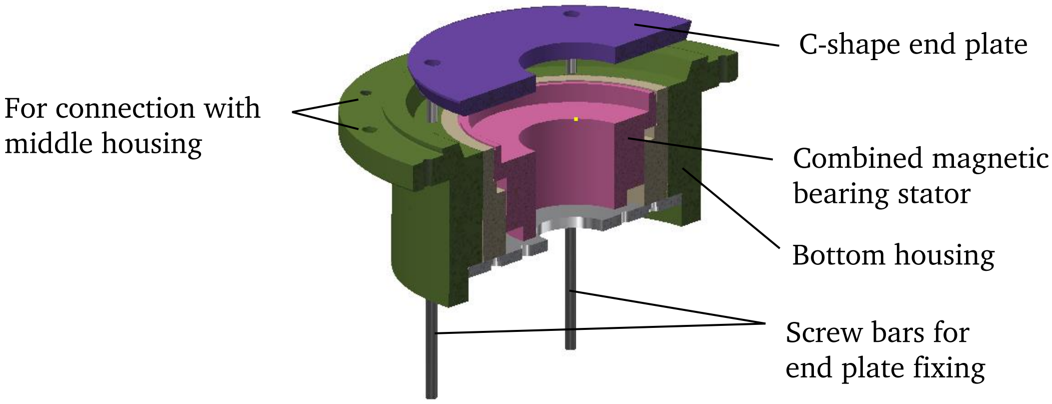

Fig. 8-7 Bottom housing (*Autodesk Inventor 2018*) [47]

The middle housing (Fig. 8-8) is connected to the top and bottom housings with screws. Three screw holes are manufactured along the lateral surface in order to fix the rotor at the center positon by brass screws during the assembly procedure (introduced in Chapter 8.1.4), avoiding scratch between the rotor and stator.

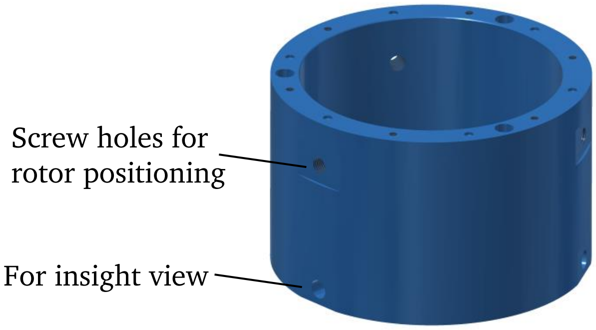

Fig. 8-8 Middle housing (*Autodesk Inventor 2018*) [47]

The top lid (Fig. 8-9) provides the fixing positions for the radial safety bearing. It is fixed with the upper housing by crews. 4 holes are manufactured on the lid as the outlet of cables.

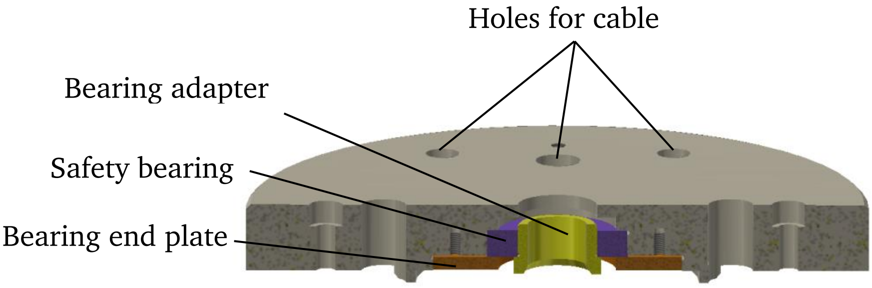

Fig. 8-9 Top lid (*Autodesk Inventor 2018*) [47]

The bottom lid (Fig. 8-10) provides the fixing positions for the bottom safety bearing and the stator part of the sensors. On the bottom surface, 2 grooves are manufactured for the guidance of cables.

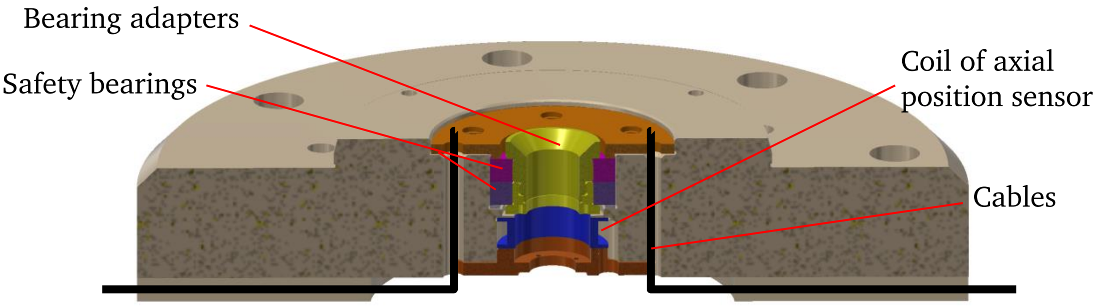

Fig. 8-10 Bottom plate (*Autodesk Inventor 2018*) [47]

8.1.3 Safety Bearing

Ball bearings are used as safety bearings in case of failure of the magnetic bearings (shown in Fig. 7-1). They are placed on the top and bottom side of the flywheel. On the top a deep groove ball bearing (hybrid bearing type 6008) is placed, which is loaded in radial direction. For the bottom an adapters is assembled on the inner ring of the two spindle ball bearings (71907 CD) which have a back-to-back arrangement. The adapter has a conical shape which can transmit axial force to the bearing and the rotor can be centered as well. The adapter consists of two parts which are combined by screwing them (Fig. 8-12). A force fit of the inner bearing ring and the adapter cause a preload in the bearings, which prevents the skidding of the inner ring at no load conditions.

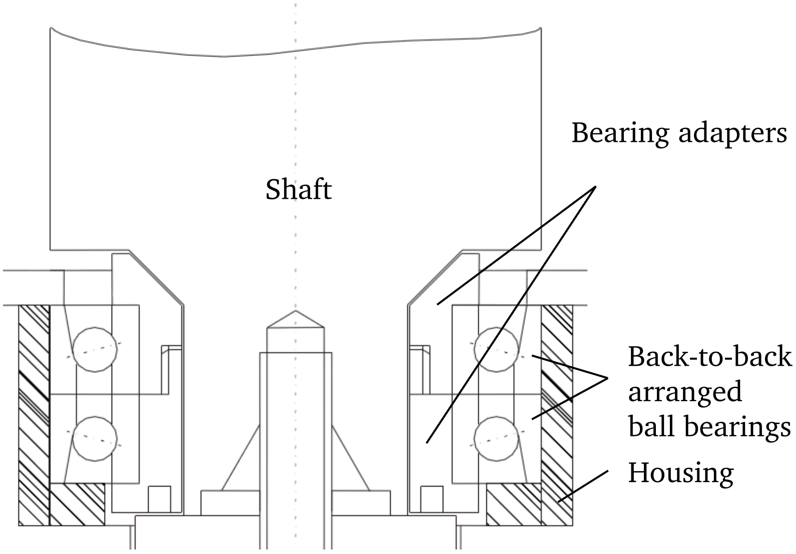

Fig. 8-11 Adapter design for the safety bearing (bottom) to ensure a centered flywheel rotor

Fig. 8-12 Safety bearing adapters (bottom)

8.1.4 System Assembly Course

Due to the rather complicated structure, a valid assembly course is required to make sure all the components can be mounted and positioned correctly. As the magnets in the E-machine and magnetic bearings produce considerable magnetic force, which influence the position control during assembly, the assembly should be properly handled avoiding the scratches or damage on the component surfaces.

A valid assembly course is proposed in the *Institute for Electrical Energy Conversion*, *TU Darmstadt*, containing mainly 4 steps, as shown from Fig. 8-13 to Fig. 8-15.

Step 1: The middle housing, bottom housing and the bottom plate are assembled, including all the mounted components inside, except the axial sensor and revolution sensor. In order to guide the rotor to slide in the center position, a guiding rod (component 1 in Fig. 8-13) and a guiding plate (component 2 in Fig. 8-13) are used to avoid touching to the magnetic bearing. To avoid scratch on the flywheel body, a guiding sleeve made of PVC material (component 3 in Fig. 8-13) is mounted on the middle housing. On the rotor there is an end plate (component 4 in Fig. 8-13), which belongs to the stator part of the combined magnetic bearing. This plate is not fixed on the rotor but should be fixed on the stator by long screw bars after the rotor is positioned.

Step 2: The rotor slides in the bottom housing, until it sits on the adapter of the bottom safety bearing, centered by the conical surface. Then 3 brass bolts (component 1 in Fig. 8-14) are screwed in to fix the flywheel body. After that the PVC guiding sleeve and the rotor guiding rod are removed. The components of axial positon sensor and revolution sensor are mounted from the bottom side. The long screw bars of the C-shape end plate are also fixed from the bottom side.

Step 3: The upper housing is pre-assembled with all the stator components and sealing parts. Similarly, the mounting of the upper housing is also guided by 3 guiding rods, fixed on the middle housing as shown in Fig. 8-15 a). After the upper housing slides to the corrected position and fixed, the guiding rods are removed.

Step 4: The top lid is mounted on the upper housing and the cables are guided through the 4 designed holes.

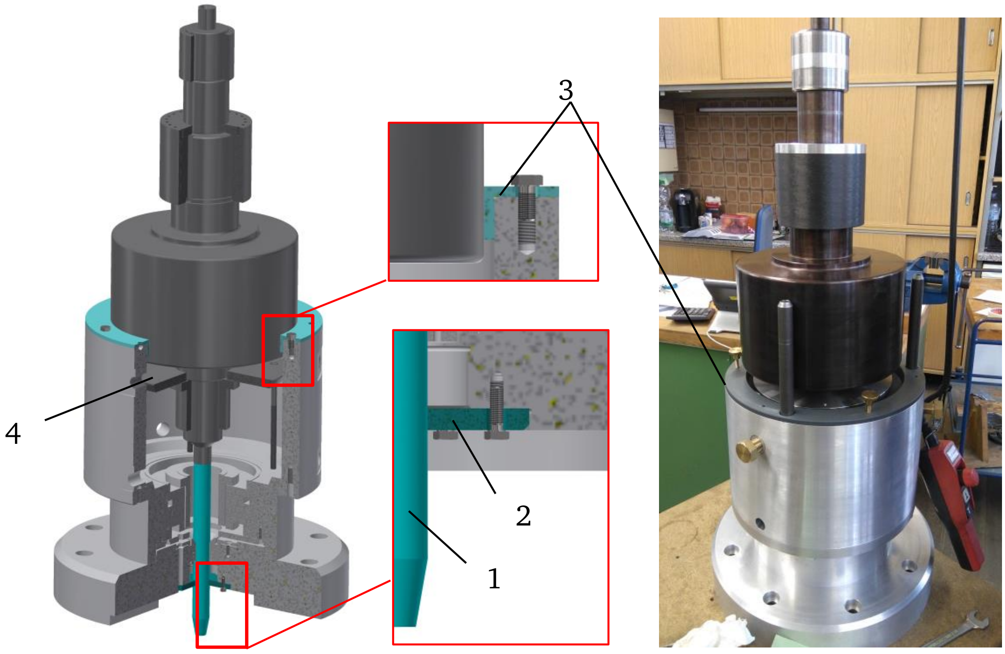

a) b)

Fig. 8-13 System assembly course, step 1: assembly of the rotor to bottom housing, 1-guiding rod, 2-guiding plate, 3-guiding sleeve, 4-C-shape end plate belonging to combined magnetic bearing (stator part): a) *Autodesk Inventor 2018* [47], b) prototype

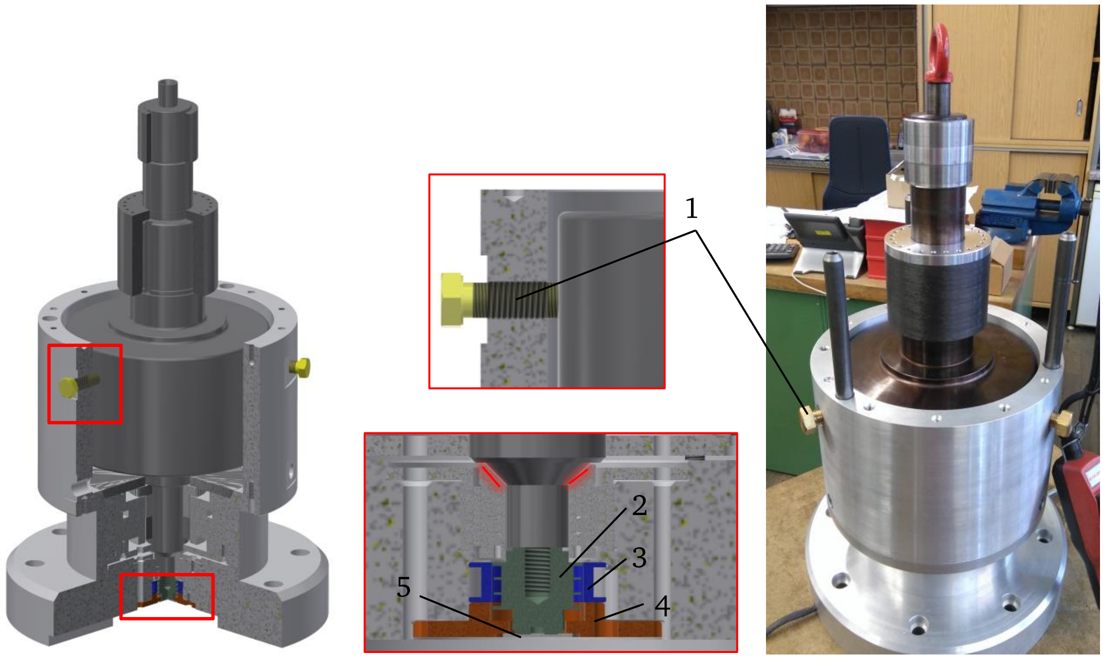

a) b)

Fig. 8-14 System assembly course, step 2: fix the rotor position, 1-fixing bolt, 2-axial position sensor (rotor part), 3-axial position sensor (stator part), 4-end plate for fixition, 5-revolusion sensor (stator part): a) *Autodesk Inventor 2018* [47], b) prototype

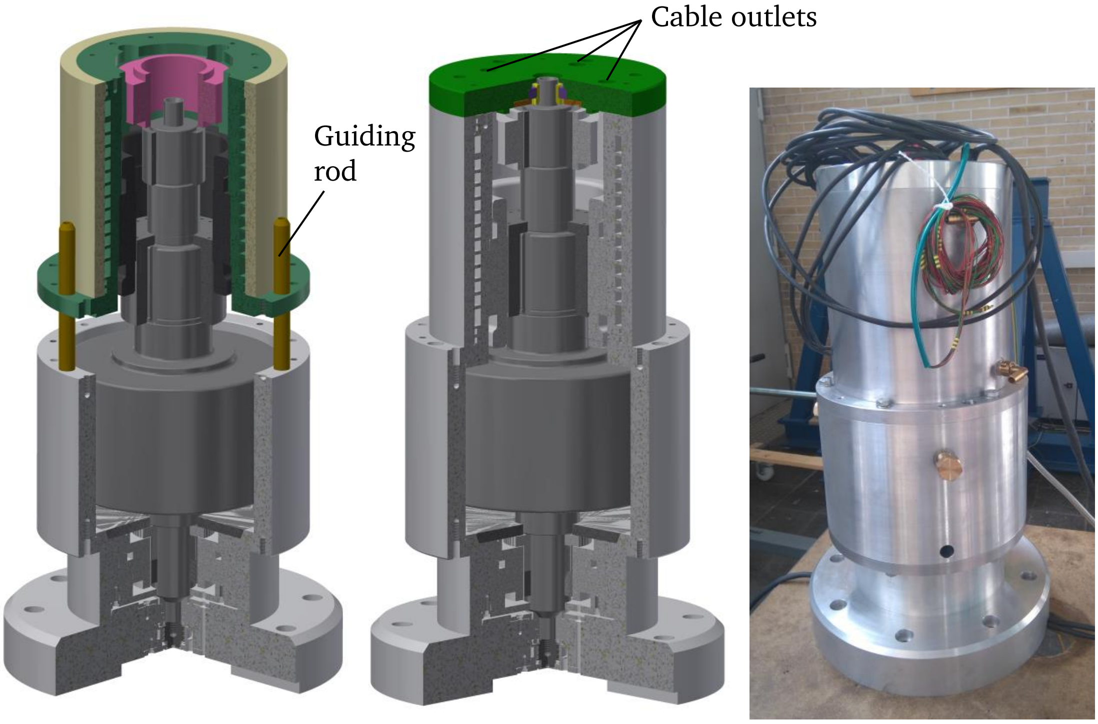

a) b) c)

Fig. 8-15 System assembly course: a) step 3: assemble the upper housing [47], b) step 4: assemble the top lid [47], c) assembled prototype

8.2 Burst Protection: Containment Design

Flywheels store appreciable energy and due to the big rotor mass high potential hazards exist. Safety must be assured for all operation conditions. The most serious potential hazard is a structural failure of the rotor [26]. The rotor disassembles into two or several projectiles and performs translational and rotational motions with significant energy, which is called a burst. In order to hold the energy, a robust burst protective housing should be designed.

8.2.1 Impact Process

The impact process is rather complicated to predict in practice and the relevant theories are still not completed so far. Most experiences are based on the experimental testing. In [59], a series of burst containment testing were carried out for a steel rotor which splits into 4 fragments and impact onto a housing with different thicknesses. The impact behavior and deformation of the housing were measured. The corresponding theory was proposed which will be used in this thesis for the burst containment design.

The theory presented in this chapter is extracted from [59], which describes the energy dissipation during the impact of a rotor fragment onto a housing. Two stages are defined during this process. The first stage is characterized by the compression of the housing material in face with the impact area and the shear deformation of the material along the perimeter of the impact area. If this local perforation failure does not occur, the second stage of containment will start. The translational energy of the system should be dissipated by the tensile strain of the housing for a successful containment.

8.2.1.1 Stage 1

Energy loss at stage 1

Before the impact, the fragment contains the kinetic energy

$$E_1 = \frac{1}{2} \cdot M_1 \cdot V_1^2 + \frac{1}{2} \cdot J_1 \cdot \Omega_1^2 , \tag{8-1}$$

where M_1 is the mass of the fragment, V_1 is the velocity, J_1 is the moment of inertia around the center of gravity of the fragment, Ω_1 is the angular velocity. During the impact, due to the conservation of momentum

$$M_1 \cdot V_1 = (M_1 + M_2) \cdot V_2 \text{ and } J_1 \cdot \Omega_1 = (J_1 + J_2) \cdot \Omega_2 , \tag{8-2}$$

where M_2, and J_2 are the effective mass and moment of inertia of the housing. After the impact, the fragment and the housing move with the same velocity V_2 and angular velocity Ω_2. Thus, the kinetic energy of the two bodies after impact is

$$E_2 = \frac{1}{2} \cdot (M_1 + M_2) \cdot V_2^2 + \frac{1}{2} \cdot (J_1 + J_2) \cdot \Omega_2^2 . \tag{8-3}$$

Thus, the kinetic energy dissipated in the momentum transfer is

$$\Delta E_1 = E_1 - E_2 = \frac{1}{2} \cdot M_1 \cdot V_1^2 \cdot \left(1 - \frac{M_1}{M_1 + M_2}\right) + \frac{1}{2} \cdot J_1 \cdot \Omega_1^2 \cdot \left(1 - \frac{J_1}{J_1 + J_2}\right). \tag{8-4}$$

The second term in (8-4) refers to the rotational energy, which acts as friction forces on the contact surfaces of the fragment and housing. This energy will be dissipated by heating and smearing of the material, which neither helps nor hinders the perforation [59]. The translational kinetic energy is more critical, as it acts as normal force imposed on the housing and may cause perforation. Therefore, only the translational part of the kinetic energy is considered here and the energy loss for stage 1 is

$$\Delta E_1 = \frac{1}{2} \cdot M_1 \cdot V_1^2 \cdot \left(1 - \frac{M_1}{M_1 + M_2}\right). \tag{8-5}$$

Effective mass of the housing

The calculation depends on the proper evaluation of the effective mass M_2 of the housing. Depending on the housing length, 2 cases are depicted in Fig. 8-16. The effective mass includes m_{21} in line with the fragment and the neighboring mass m_{22} which also acts and sustains shear forces.

1) For a long shell, the adjacent distance is considered to be $a = 3 \cdot T$ (T: thickness of the housing), according to the measurements in [59] for a fragment velocity of 213 … 274 m/s. For lower velocities this length is expected to be higher. The effective mass [59]

$$M_2 = m_{21} + 0.34 \cdot m_{22} , \tag{8-6}$$

where m_{22} is the adjacent mass which starts from the perimeter of the impact area and extends to a distance of $a = 3 \cdot T$.

2) For a short cylinder, where $a \leq 3 \cdot T$, the effective mass

$$M_2 = m_{21} + m_{22} \cdot \left(\frac{k_0^2/b^2}{k_0^2/b^2 + 1}\right), \tag{8-7}$$

where k_0 is the radius of gyration of m_{22} around the center of gravity, b is the distance from the center of the gravity to the perimeter of the impact area. For $a = 3 \cdot T$, $M_2 = m_{21} + 0.27 \cdot m_{22}$. For $a = 2 \cdot T$, $M_2 = m_{21} + 0.29 \cdot m_{22}$.

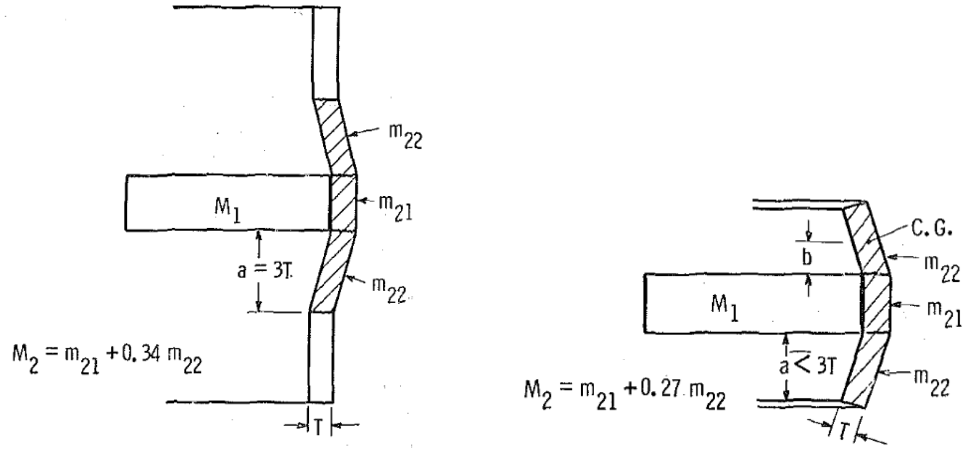

(a) Long Cylindrical Shell (b) Short Cylindrical Shell

Fig. 8-16 Effective mass of the housing [59]
(M_1: mass of the rotor fragment, M_2: effective mass of the housing, m_{21}: the mass of the housing in line with the rotor fragment, m_{22}: the housing mass adjacent to the impact area, a: the adjacent distance taken into account, T: thickness of the housing, C.G.: center of gravity)

Strain energy of stage 1

When the impact happens, the housing material in face with the rotor fragment is compressed and tends to move outwards. Therefore, simultaneously, the material on the perimeter of the contact area is sheared. The energy which leads to a plastic strain of the material due to compression is

$$E_c = A \cdot T \cdot \varepsilon_c \cdot \sigma_d , \tag{8-8}$$

where A is the contact area, T is the wall thickness of the housing, ε_c is the compressive plastic strain, and σ_d is the average dynamic plastic flow stress of the material in compression.

The energy of the material due to shear can be calculated by [59]

$$E_s = K \cdot \tau_d \cdot L_p \cdot T^2 , \tag{8-9}$$

where τ_d is the dynamic shear strength of the material, L_p is the perimeter of the sheared area, and K is an experimental constant with a value in the range of 0.3 to 0.5. Based on the testing results in [59], $K \cdot \tau_d = 0.27 \cdot \sigma_d$ can be used in (8-9) for the calculation of E_s.

Criterion for Non-perforation

A successful containment for stage 1 should assure that the energy ΔE_1 in (8-5) due to the momentum transfer should be dissipated by the compressive and shear deformation of the housing.

The criterion for non-perforation is

$$E_\mathrm{c} + E_\mathrm{s} > \Delta E_1 , \tag{8-10}$$

or

$$A \cdot T \cdot \varepsilon \cdot \sigma_\mathrm{d} + K \cdot \tau_\mathrm{d} \cdot L_\mathrm{p} \cdot T^2 > \frac{1}{2} \cdot M_1 \cdot V_1^2 \cdot \left(1 - \frac{M_1}{M_1 + M_2} \right) . \tag{8-11}$$

If (8-10) is not fulfilled, the perforation occurs and part of the housing mass is punched out. The residual energy of the fragment and punched-out housing should be recalculated if there is an outer housing as second containment. Details are introduced in [59].

8.2.1.2 Stage 2

If no perforation occurs at stage 1, the residual kinetic energy after the momentum transfer is $\Delta E_2 = E_2$ in (8-3). This energy causes tensile deformation of the housing and should be dissipated by essentially uniaxial tension strain (stretching) for a short housing, and by biaxial tension strain for a long housing. The criterion for containment in stage 2 is

$$E_\mathrm{t} > \Delta E_2 , \tag{8-12}$$

or

$$Q \cdot \varepsilon_\mathrm{t} \cdot \sigma_\mathrm{d} > \frac{1}{2} \cdot M_1 \cdot V_1^2 \cdot \left(\frac{M_1}{M_1 + M_2} \right) , \tag{8-13}$$

where ε_t is the allowed strain of the material before fracture, σ_d is an average plastic flow tensile stress, Q is the volume of housing material that involves in the tensile deformation.

1) For a short housing the entire volume of material is strained. With the fragment number n_f, the involved volume of material Q per fragment is

$$Q = \pi \cdot D_\mathrm{c} \cdot L_\mathrm{c} \cdot T / n_\mathrm{f} , \tag{8-14}$$

where D_c and L_c are the diameter and the length of the housing, and T is the wall thickness.

2) For a long housing, the volume Q per fragment is calculated by (8-15), which is the volume of the material involved in the determination of the effective mass M_2.

$$Q = 3 \cdot L_{\mathrm{p}} \cdot T^2 + A \cdot T \tag{8-15}$$

8.2.2 Burst Containment Design

The material S355J2H (1.0576) is used for the calculation of the burst containment. This material is often used as seamless circular steel tubes for mechanical and general engineering purposes. The density of this material is 7850 kg/m^3. The strengths for different dimensions are shown in Table 8-2. The outer diameter and thickness are standardized.

Table 8-2 Mechanical properties of steel tube S355J2H (1.0576) [60, 61]

Nominal thickness T [mm]	Upper yield point R_{eH} [N/mm^2]	Tensile strength R_{m} N/mm^2	Elongation at fracture min. %
$T < 3$	355	510-680	22
$3 < T \leq 16$		470-630	
$16 < T \leq 40$	345		
$40 < T \leq 63$	335		21
$63 < T \leq 80$	325		20
$80 < T \leq 100$	315		
$100 < T \leq 120$	295	450-600	18
Notched-bar impact value at a temperature of -20 °C is 27 J.			

The calculation was carried out with the dimensions and parameters shown in Table 8-3. The fragment number is assumed to be 4 according to [59]. For the housing, the permitted compressive strain is chosen to be $\varepsilon_c = 0.07$. The permitted tensile strain is chosen to be $\varepsilon_c = 0.10$ as the minimum and $\varepsilon_c = 0.15$ as the maximum according to [59]. The tensile strength for the wall thickness above 16 mm is chosen to be the lower limit $\sigma_u = 470$ MPa from Table 8-2 for safety. The dynamic tensile strength σ_d is assumed to be 1.4 higher than the apparent tensile strength σ_u according to the measured material properties in [59].

Table 8-3 Parameters and dimensions used for the calculation to determine the containment thickness

Material properties of the containment	
Density	7850 kg/m^3
Permitted compressive strain ε_c	0.07
Permitted tensile strain ε_t	0.10 … 0.15
Tensile strength σ_u	470 MPa
Dynamic strength $\sigma_d = 1.4 \cdot \sigma_u$	658 MPa
Rotor body fragment parameter	
Rotor body diameter	260 mm
Rotor body axial length	160 mm
Fragment number	4
Containment dimension	
Containment inner diameter	$D_{c,i}$ = 415 mm
Containment axial length	L_c = 180 mm (short)
	L_c = 800 mm (long)

Table 8-4 shows the calculated results for both short and long containment. As the containment thickness increases, the energy loss ΔE_1 of the impact of stage 1 increases, which should be dissipated by the compression and shear of the housing at stage 1. The containment deformed energy $E_c + E_s$, which indicates the ability to absorb the kinetic energy, also increases with the increasing thickness. If ΔE_1 is higher than $E_c + E_s$, the energy which should be dissipated cannot be completely absorbed by the compressive and shear deformation of the material, thus a perforation will happen. Therefore, the crossing point is critical which gives accordingly a minimum thickness for a successful protection at stage 1. The same criterion is also used for stage 2. The crossing point corresponds to a minimum thickness of the housing for a successful protection at stage 1, where the kinetic energy ΔE_2 should be absorbed by the tensile deformation of the housing for a valid containment.

By comparing the results of short (axial length L_c = 180 mm) and long (L_c = 800 mm) containments, we can see the effects of the adjacent mass of the housing around the contact surface. If the permitted tensile strain ε_t = 0.10 is used, a minimum thickness of 45 mm is required for a short containment. For a long containment, as the adjacent mass also performs deformation, which helps to absorb the impact energy, the required thickness is smaller than a short housing. The minimum thickness of the long containment can be determined to be 30 mm. The resulting mass is about 263 kg for the long containment.

Table 8-4 Containment dimensioning: Calculated results of the energy dissipation, deform work during the impact and the housing weight vs. containment thickness, calculated according to the method in [59]

<table>
<tr><td colspan="2">Notations in the graphs:
ΔE_1: Energy to be dissipated in the fragment at stage 1,
ΔE_2: Energy to be dissipated in the fragment at stage 2,
$E_s + E_c$: Containment deformed energy due to shear and compression,
E_t ($\varepsilon_t = 0.10$): Containment deformed energy due to tension, for the maximum allowed strain $\varepsilon_t = 0.10$,
E_t ($\varepsilon_t = 0.15$): Containment deformed energy due to tension, for the maximum allowed strain $\varepsilon_t = 0.15$.</td></tr>
<tr><th>Short containment (L_c = 180 mm)</th><th>Long containment (L_c = 800 mm)</th></tr>
<tr><td>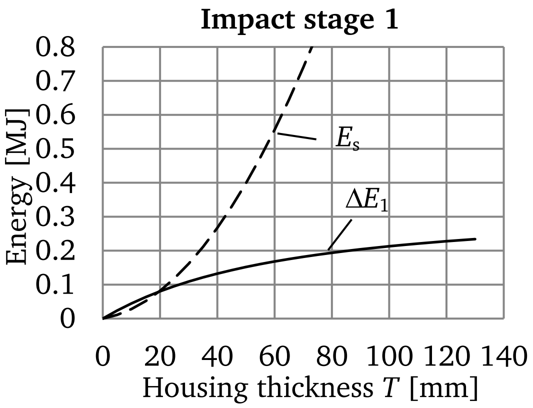Impact stage 1 </td><td>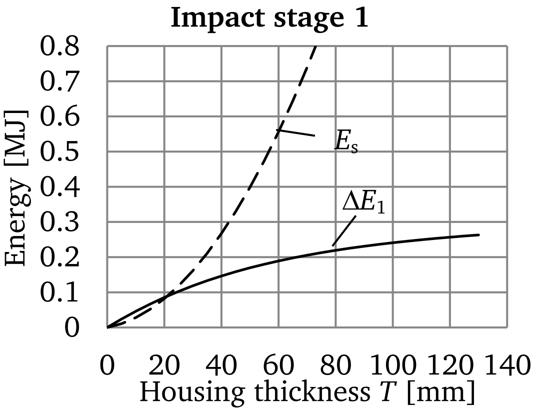Impact stage 1 </td></tr>
<tr><td>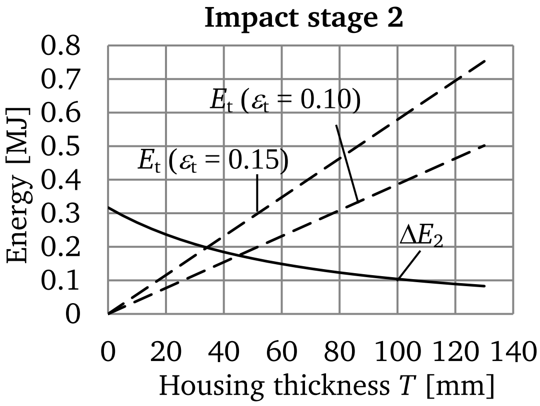Impact stage 2 </td><td>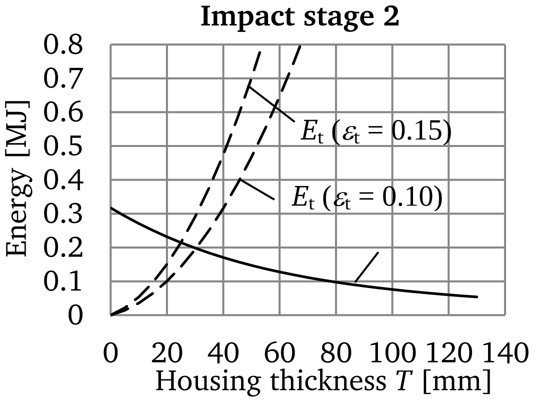Impact stage 2 </td></tr>
<tr><td>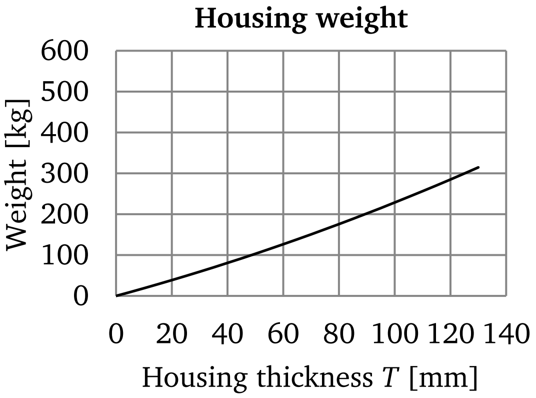Housing weight </td><td>Housing weight </td></tr>
</table>

For safety concern, 2 housings should be used in case the inner housing fails. A space between 2 housings should be reserved to allow the deformation of the inner housing. It can be calculated by

$$\delta_{\mathrm{c,\,gap}} = (D_{\mathrm{c,i}}/2 + T)\cdot \varepsilon_{\mathrm{t}}\,. \tag{8-16}$$

In our system, two burst containments are designed for a higher safety as shown in Fig. 8-17. The outer diameter and thickness are standardized values in [60]. The thicknesses of two containments are both determined to be 40 mm. A gap of 23.5 mm is reserved in between.

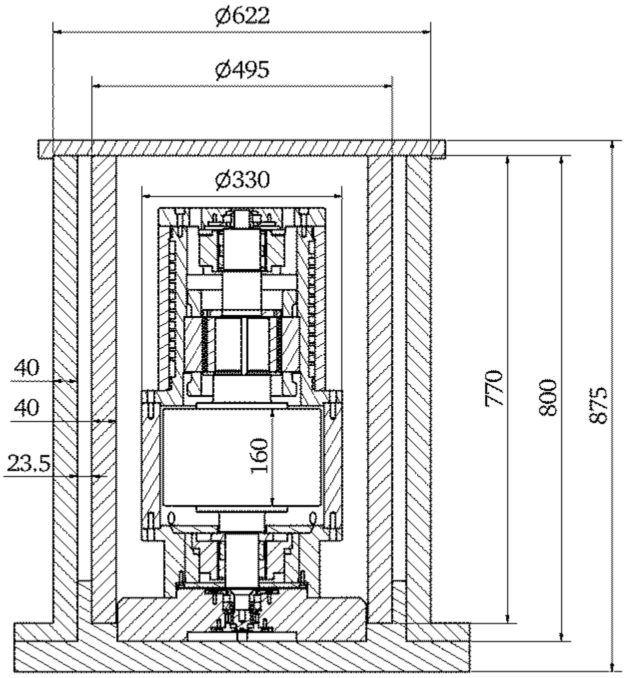

Fig. 8-17 Designed dimensions of the two burst containments

8.3 Vacuum: Air Friction Losses

In order to reduce the air friction losses of the high speed rotor, the flywheel system locates in a vacuum container. The vacuum level in this design is chosen to be 0.3 Pa, which is the lower pressure limit of a two-stage rotary vane pump [62]. Higher level of vacuum (10^{-5} … 10^{-8} Pa) requires a molecular pump which will significantly increase the costs.

Despite of the vacuum environment, air friction losses are not negligible, and even become important when considering the difficulty for the rotor heat transfer in vacuum.

Traditional air friction loss calculations are based on the assumption of continuum air flow, which is no more valid when the pressure is low, as the molecular mean free path is comparable or even bigger than the pertinent dimension of the flow field. However, one can hardly find a perfect theory for the friction loss calculation in this free molecule flow regime. A prediction method is proposed in [63] and verified by the experimental measurements. Therefore, this method is used in this thesis and summarized as follows according to [63].

8.3.1 Air Flow Regimes

The theory is regarding the flow of the fluid (or gas) in the gap between two concentric cylinder surfaces, one of which is tangentially moving relative to the other. The flow regime of the fluid can be divided into three categories (Table 8-5), depending on the rarefaction of the molecules.

One dimensionless parameter to define the regimes is called *Knudsen* number, calculated by

$$K_{\mathrm{n}} = \frac{\lambda}{\delta}, \tag{8-17}$$

where λ is the molecular mean free path and δ is a pertinent dimension of the flow field. For the involved two concentric cylindrical model, it refers to the radial air gap length. The *Knudsen* number indicates the degree of rarefaction of the fluid molecules.

The molecular mean free path λ is the average distance traveled by a gas molecule between two successive impact collisions. In case of local thermodynamic equilibrium, it can be calculated by (8-18) for the air in a range of 100 to 1900 K [63].

$$\lambda = \frac{3.1 \times 10^{-5} \cdot T^2}{(T + 110.4) \cdot P} \tag{8-18}$$

In (8-18), λ is in meters, T is the absolute temperature in Kelvins, and P is the pressure in pascals. Fig. 8-18 shows λ (in mm) in dependent of P for temperatures of 20 °C and 150 °C, as well as the air flow regimes for a radial air gap distance of 5 mm, corresponding to the value in the designed flywheel.

In classical continuum flow, the *Knudsen* number is very small, indicating very intensive molecules in the gap. The intermolecular collisions are decisive other than the molecule-surface collisions (the collisions of the molecules on the cylinder surface). The velocity and temperature transfer from the cylinder to the fluid is continuous, characterized by surface friction (due to fluid viscosity) and convection heat transfer [64]. In the continuum flow, various flow regimes exist, e.g. laminar, transition, vortex, and turbulent flows. The losses can be calculated by following the conventional formulas introduced in [64, 65]. Particularly, the parameters of the gas (e.g. density, viscosity, etc) vary with temperature and pressure, for which the dependency can be found in [1].

As the pressure drops, the gas becomes rare that the mean free path is not much smaller than the gap length. In the slip flow, the intermolecular and molecule surface collisions are of equal importance. A discontinuity or a slip occurs for the velocity and temperature transfer from the cylinder to the fluid. The effect of the velocity and temperature slip is the reduction of surface friction as well as heat transfer. According to [66], only in the range of atmospheric pressure heat transfer through convection is technically applicable.

In the free molecule flow, when the mean free path is much bigger than the air gap length, the intermolecular collisions can be neglected due to the large rarefaction. The flow is governed by the molecule surface collisions, which cause friction losses, even though very low. The presence of the boundary surfaces will not disturb the flow field.

Table 8-5 Flow regimes defined by *Knudsen* number K_n [63]

Knudsen number K_n	<0.01	0.01 … 3	>3
Flow regime	Continuum flow	Slip flow	Free molecule flow

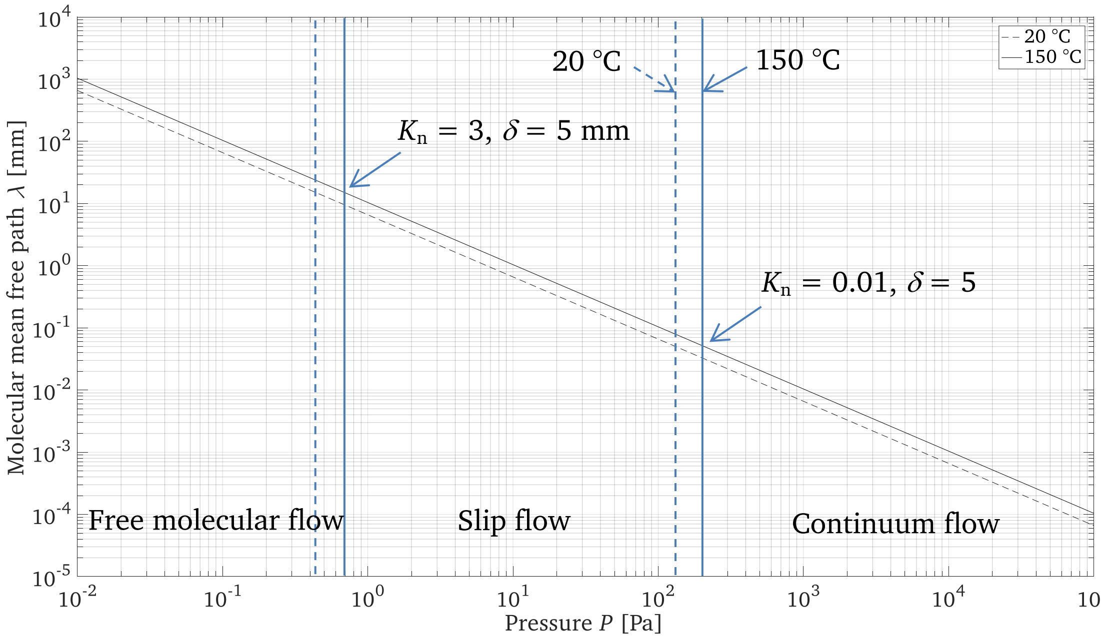

Fig. 8-18 Molecular mean free path λ versus air pressure P, showing different flow regimes for a radial air gap δ = 5 mm (solid line: 150 °C, dashed line: 20 °C), according to Table 8-5

8.3.2 Air Friction Loss for Free Molecule Flow Regime

The windage loss on a rotating disk is the sum of the loss on the cylinder surface and two end disk surfaces.

$$P_{\mathrm{fr,\ sum}} = P_{\mathrm{fr,\ C}} + P_{\mathrm{fr,\ D}} \tag{8-19}$$

According to [63], the windage loss for a free molecule flow in concentric rotating cylinders can be calculated by

$$P_{\mathrm{fr,\ free,\ C}} = P \cdot \sqrt{\frac{2 \cdot \pi}{R \cdot T}} \cdot L \cdot r_{\mathrm{o}}^{3} \cdot \Omega^{2}, \tag{8-20}$$

where R is the gas constant, r_{o} and L are the outer radius and the axial length of the rotating cylinder, Ω is the angular rotational speed. The windage loss on the two end disk surfaces are calculated by

$$P_{\mathrm{fr,\ free,\ D}} = \frac{P}{2} \cdot \sqrt{\frac{2 \cdot \pi}{R \cdot T}} \cdot r_{\mathrm{o}}^{4} \cdot \Omega^{2}. \tag{8-21}$$

For the calculation in slip flow regime, a correction is introduced based on the calculations in free molecule regime

$$P_{\mathrm{fr,\ slip}} = P_{\mathrm{fr,\ free}} \cdot \left(\frac{2 \cdot \lambda/\delta}{1 + 2 \cdot \lambda/\delta} \right). \tag{8-22}$$

By using the formulas above, the windage losses of each component of the flywheel rotor can be calculated.

In Table 8-6, each component is assumed to be a cylindrical segment with given dimensions and clearance in the table, in order to have a comparison of the losses on the cylinder surface and end surface for each component. As can be seen, the dominant losses occur on the flywheel body, mainly on cylinder surfaces and lower on the disk surfaces.

Table 8-6 Calculated air friction losses for the flywheel rotor components, air pressure P = 0.3 Pa, temperature 150 °C

Component	E-machine	Flywheel body	Radial MB	Combined MB
Outer diameter d_o [mm]	128	260	76.7	76.7
Length L [mm]	90	160	66	73.8
Radial clearance δ_r [mm]	1	5	1.65	1.65
Axial clearance δ_z [mm]	10	5	10	10
Molecular mean free path λ [mm]	34.7	34.7	34.7	34.7
Knudsen number in radial direction $K_{n,r}$	34.7	6.93	21	21
Knudsen number in axial direction $K_{n,z}$	3.47	6.93	3.47	3.47
Friction losses on cylinder surface $P_{fr,C}$ [W]	0.317	4.47	0.050	0.0554
Friction losses on two end surface $P_{fr,D}$ [W]	0.10	1.82	0.0129	0.0129
Total friction losses P_{fr} [W]	0.417	6.28	0.0624	0.0683

The designed rotor has a rather complicated structure as shown in Fig. 8-19 a), therefore, a simplified contour (Fig. 8-19 b)) is used for the air friction loss calculation. The calculated losses for different air pressure levels are shown in Fig. 8-20. For the chosen air pressure of 0.3 Pa, the friction losses are 6.7 W.

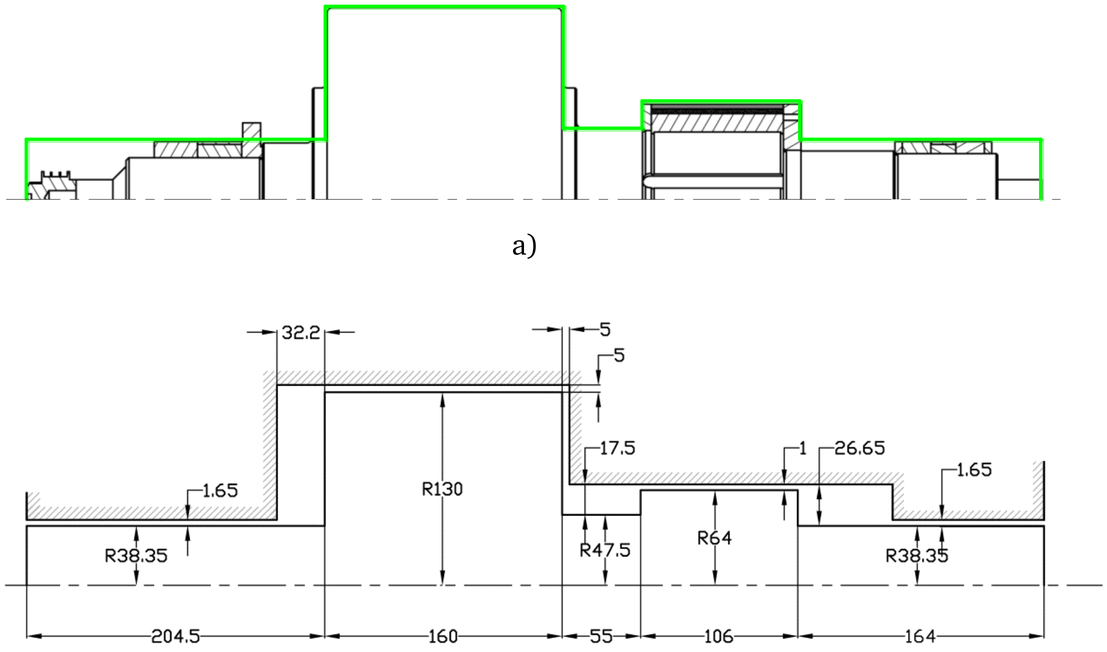
a)

b)

Fig. 8-19 Simplified rotor contour for air friction loss calculation: a) original designed rotor structure with simplified contour lines (green lines), b) dimensions (in mm) of the simplified rotor contour and gaps

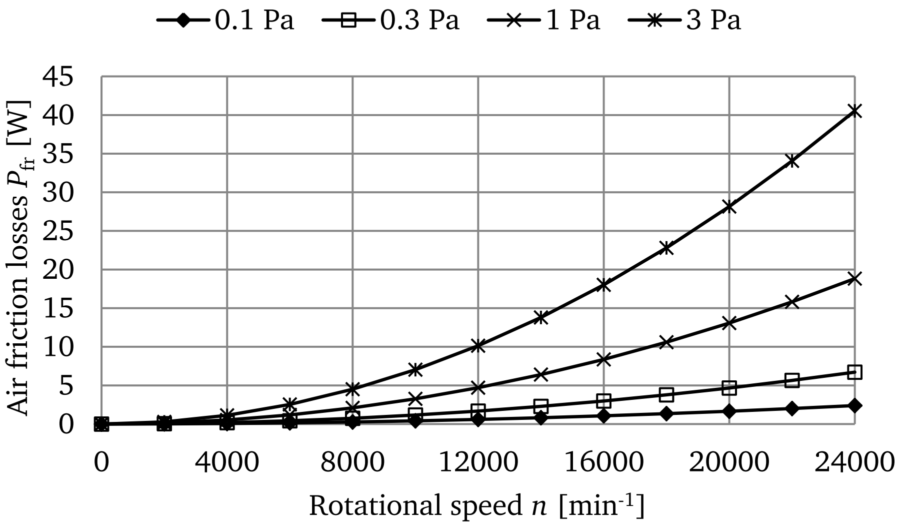

Fig. 8-20 Calculated flywheel rotor air friction losses for different pressure levels at temperature 150 °C

9. Thermal Performance

As the flywheel system operates in vacuum, the heat of the rotor is only dissipated through radiation, as the heat convection through the air is negligible at the low pressure of 0.3 Pa. Therefore, the thermal performance of the rotor is more critical than the water cooled stator.

This chapter presents the thermal calculation of the flywheel system. A T-equivalent lumped parameter thermal network is firstly modeled. The loss components of the system are summarized according to the calculated results in previous chapters and are used to calculate the temperatures and heat flows. The calculation is carried out for two operating conditions: continuous operation and the operation with a duty cycle which is assumed for a fully-utilized flywheel with continuous charging and discharging cycle. In the end, the design of the stator water cooling system is presented.

9.1 T-equivalent Lumped Parameter Network

Lumped parameter network is usually used to evaluate the thermal performance of a system, which can carry out both steady state and transient analysis. Traditionally, the conductive heat transfer is modeled by a thermal resistance which is analogous to a resistance in electric circuits. For example, for one-dimensional heat transfer in a rod in Fig. 9-1, an equivalent network in Fig. 9-2 a) is used. The thermal resistance is derived based on the solution of the one-dimensional steady state heat diffusion equation (9-1) for zero internal heat generation $q_\mathrm{i} = 0$ [67].

$$\lambda \cdot \frac{\partial^2 \vartheta}{\partial x^2} + q_\mathrm{i} = 0 \tag{9-1}$$

In (9-1), λ is the thermal conductivity, ϑ is the temperature distribution on the rod with respect to the axial position denoted by x, and q_i is the internal loss density in W/m^3.

However, in case of internal heat generation, this equalization may lead to high discretization errors, i.e. if the number of nodes is low, it will lead to an overestimated temperature [68]. A commonly used compensation approach is T-equivalent network [64] [67] [69] [70], which compensates the overestimated temperature by introducing a negative thermal resistance, as shown in Fig. 9-2 b). This negative thermal resistance is derived by the steady state heat diffusion equation (9-1) with internal heat generation

$q_\mathrm{i} > 0$. The derivation is described in Appendix D. Also a calculation example is presented in Appendix D for a comparison of the T-equivalent network and the conventional equivalent network. The comparison shows that, the T-equivalent network gives a good estimation for the body with internal heat generation, while conventional model is more suitable for the body heated up by the external source without internal heat generation. Therefore, in this thesis, the T-equivalent network is adopted for the components which have internal losses. While for the components without internal losses, the conventional one-node equivalent network is used.

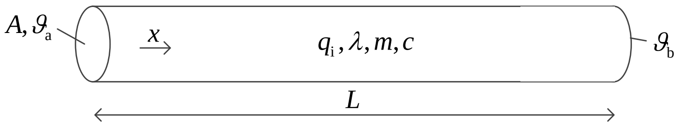

Fig. 9-1 One dimensional heat conduction in a rod with internal loss density q_i, axial length L, section area A, mass m, thermal conductivity λ, specific heat capacity c, constant temperatures ϑ_a, ϑ_b at the end surfaces of the rod

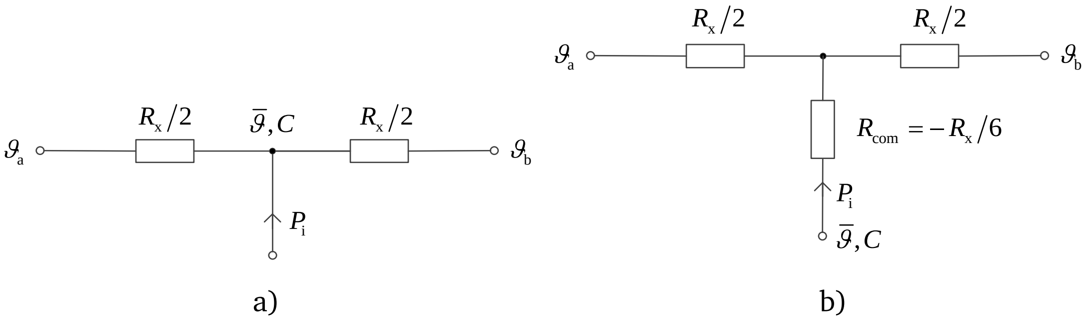

Fig. 9-2 Equivalent thermal network for steady state heat conduction in a single rod, internal heat source $P_\mathrm{i} = \int q_\mathrm{i} \mathrm{d}_\mathrm{V} = q_\mathrm{i} \cdot A \cdot L$, thermal capacitance $C = m \cdot c$, average temperature $\bar{\vartheta}$: a) conventional equivalent network, b) T-equivalent network

In our system, most components are of cylindrical shape. Therefore, the T-equivalent circuits (Fig. 9-3) proposed by [69] are used. They are modeled for both radial and axial directions and coupled by a common node where the internal heat flows in and the average temperature of the component is calculated. The thermal resistances are calculated by the formulas in Table 9-1.

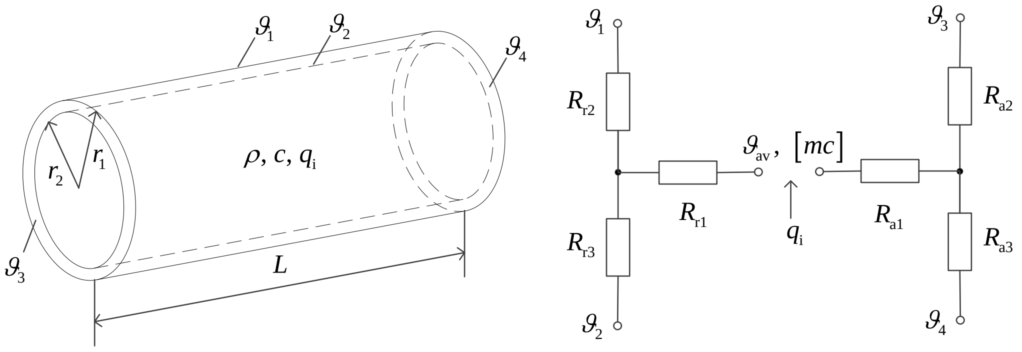

a) b)

Fig. 9-3 T-equivalent thermal network for a cylindrical component [69]: a) a cylindrical component, b) T-equivalent thermal networks in radial (with subscript r) and axial (with subscript a) directions

Table 9-1 Formulas for thermal resistance calculation in the thermal network in Fig. 9-3

$$R_\mathrm{r1} = -\frac{1}{8\cdot\pi\cdot\lambda_\mathrm{r}\cdot L\cdot\left(r_1^2-r_2^2\right)}\cdot\left[r_1^2+r_2^2-\frac{4\cdot r_1^2\cdot r_2^2\cdot\ln\left(r_1/r_2\right)}{r_1^2-r_2^2}\right],$$

$$R_\mathrm{r2} = \frac{1}{4\cdot\pi\cdot\lambda_\mathrm{r}\cdot L}\cdot\left[1-\frac{2\cdot r_2^2\cdot\ln\left(r_1/r_2\right)}{r_1^2-r_2^2}\right],\ R_\mathrm{r3} = \frac{1}{4\cdot\pi\cdot\lambda_\mathrm{r}\cdot L}\cdot\left[\frac{2\cdot r_1^2\cdot\ln\left(r_1/r_2\right)}{r_1^2-r_2^2}-1\right];$$

$$R_\mathrm{a1} = -\frac{R_\mathrm{a2}}{3},\ R_\mathrm{a2} = R_\mathrm{a3} = \frac{L}{2\cdot\pi\cdot\lambda_\mathrm{a}\cdot\left(r_1^2-r_2^2\right)}.$$

$$[mc] = \rho\cdot c\cdot\pi\cdot L\cdot\left(r_1^2-r_2^2\right).$$

ρ	kg/m^3	Mass density
m	kg	Mass
c	J/(kg·K)	Specific heat capacity
λ_r, λ_a	W/(m·K)	Thermal conductivity in radial (r) and axial (a) direction
q_i	W/m^3	Internal loss density
ϑ_av	°C	Average temperature
ϑ_1, ϑ_2, ϑ_3, ϑ_4	°C	Temperatures at cylinder boundary surfaces

9.2 System Thermal Network

A thermal network of the flywheel system is built as shown in Fig. 9-4 with different colors representing each component. The network consists of 14 nodes, taking the heat flows in both radial and axial directions into account. A detailed description of the modeling of the main components and parameter calculations of the thermal resistance and capacitances are presented in Appendix E.

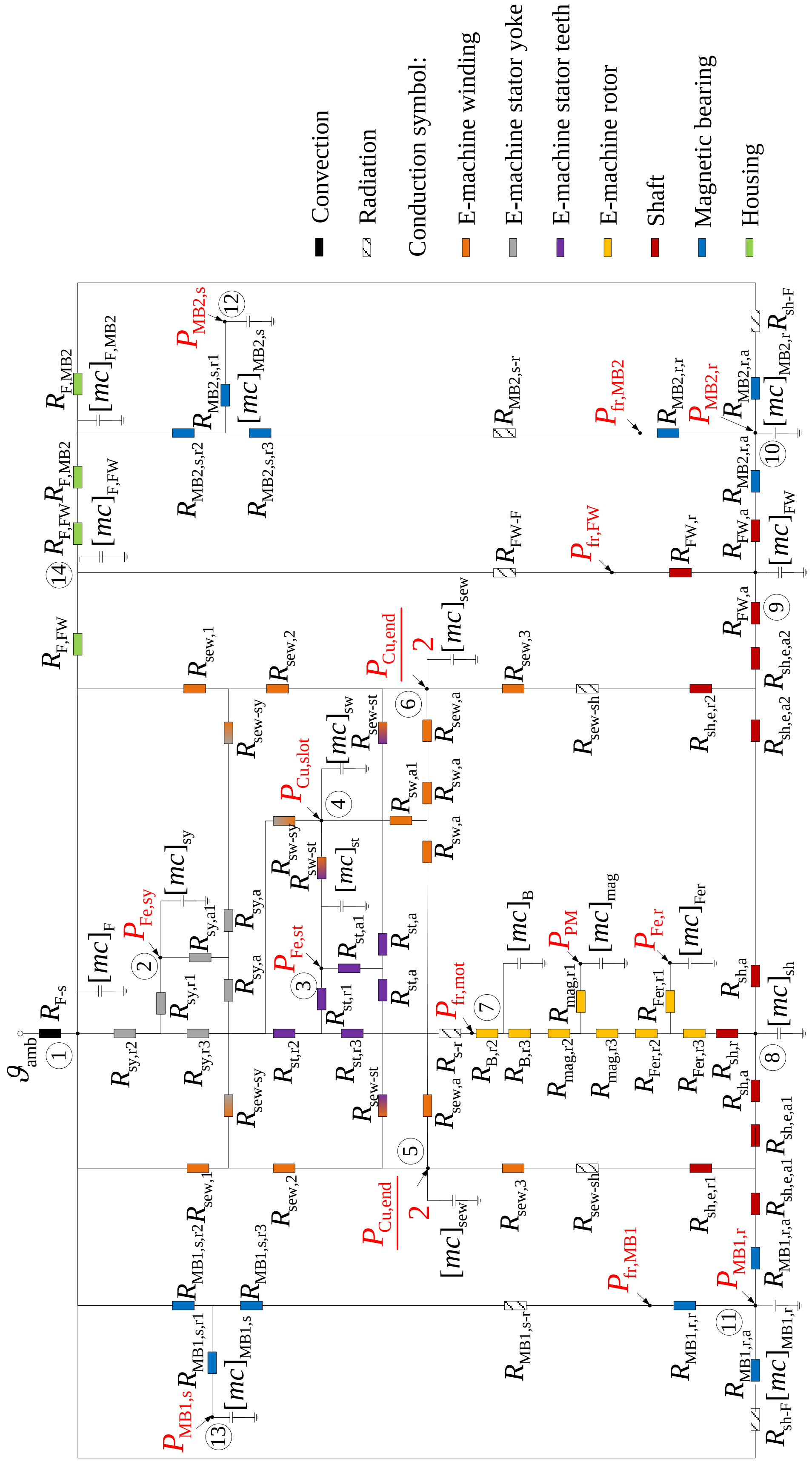

Fig. 9-4 Thermal network of the flywheel system

(ϑ_{amb}: ambient temperature, node: 1-PM machine housing, 2-PM machine stator yoke, 3-PM machine stator teeth, 4-Winding in slot, 5-Winding overhang (top), 6-Winding overhang (bottom), 7-PM machine bandage, 8-PM machine shaft, 9-Flywheel body, 10-Rotor of bottom MB, 11-Rotor of top MB, 12-Stator of bottom MB, 13-Stator of top MB, 14-Flywheel housing)

The heat sources are in accordance with the loss components in Table 9-4. The calculated heat transfer includes:

a) Heat Conduction

Heat conduction is modeled by conductive thermal resistance (colored components in Fig. 9-4) between two direct contact bodies or inside one body with large dimensions, characterized by the thermal conductivity of the medium material and the geometry of the bodies. The parameters of the used material are shown in Table 9-2.

b) Heat Convection

The water cooling on the stator surface is considered to be convective heat transfer. It is also modeled with a thermal resistance $R_{\text{F-s}}$ (black component in Fig. 9-4), depending on the heat transfer coefficient and the cooling surface. An equivalent convection heat transfer coefficient of $\alpha_{\text{eq}} = 4202\ \text{W}/(\text{m}^2 \cdot \text{K})$ (in Chapter 9.5) is calculated depending on our cooling system and applied on the outer surface of the E-machine and top magnetic bearing.

Table 9-2 Material thermal properties of components in the system used for thermal calculation (ρ: mass density, λ: thermal conductivity, c: specific heat capacity, $\parallel$: parallel direction of fibers or in plane of the laminated iron sheets, $\perp$: transversal direction of fibers or in the laminated direction of the iron sheets)

Component	Material	ρ [kg/m^3]	λ [W/(m·K)]	c [J/(kg·K)]
E-machine Winding	Copper [64]	8960	394	385
Winding impregnation	Resin (MC62+W363)	1620	0.9	1150
Laminated iron package	NO20 [64]	7650	0.6 $\perp$ 31 $\parallel$	430
Slot insulation	Nomex [64]	-	0.11	-
E-machine bandage	Carbon fiber (HTS40) +resin (Araldite LY556+Aradur 917)	1540	3.7 $\perp$ 6.4 $\parallel$	877
Magnet	Sm_2Co_{17}	8400	10	400
Flywheel body and shaft	Steel 30CrNiMo8	7760	38	430
Housing	Aluminum AlZnMgCu1.5	2780	145	960

c) Heat Radiation

The radiative heat transfer between the rotor and stator is modelled with *Kirchhoff*'s law of thermal radiation (9-2). The heat transfer depends on the emissivity ε of the emitting and absorbing surfaces. The emissivity on the designed rotor surfaces are measured and shown in Table 9-3. A non-painted steel surface has an emissivity $\varepsilon = 0.65$. Higher emissivity $\varepsilon = 0.95$ can be achieved, if the surface is painted black.

The radiative heat transfer between the rotor and stator is calculated by

$$P_{\mathrm{rad}} = \frac{\sigma \cdot (T_{\mathrm{r}}^4 - T_{\mathrm{s}}^4)}{\frac{1-\varepsilon_{\mathrm{r}}}{\varepsilon_{\mathrm{r}} \cdot A_{\mathrm{r}}} + \frac{1}{A_{\mathrm{r}} \cdot F_{\mathrm{sr}}} + \frac{1-\varepsilon_{\mathrm{s}}}{\varepsilon_{\mathrm{s}} \cdot A_{\mathrm{s}}}}, \tag{9-2}$$

where the subscript *s* denotes the stator inner surface, *r* denotes the rotor outer surface. F_{sr} is the facing factor depending on the position of two surfaces. A is the surface area, T is the absolute temperature (in K) on the surface (The corresponding celsius temperature is denoted by ϑ in °C), σ is *Stefan-Boltzmann* constant, $\sigma = 5.67\times10^{-8}$ W/(m$^2\cdot$ K^4), and ε is the surface emissivity.

In order to evaluate the radiation effect, an equivalent heat transfer coefficient of radiation is defined as (9-3), which gives a better comparison with convectional heat transfer. The equivalent radiative thermal resistance $R_{\mathrm{s\text{-}r}}$ in Fig. 9-4 can be calculated by (9-4).

$$\alpha_{\mathrm{rad,eq}} = \frac{P_{\mathrm{rad}}}{A_{\mathrm{r}} \cdot (T_{\mathrm{r}} - T_{\mathrm{s}})} \tag{9-3}$$

$$R_{\mathrm{s\text{-}r}} = R_{\mathrm{rad,eq}} = \frac{P_{\mathrm{rad}}}{T_{\mathrm{r}} - T_{\mathrm{s}}} = \frac{1}{\alpha_{\mathrm{rad,eq}} \cdot A_{\mathrm{r}}} \tag{9-4}$$

Table 9-3 Measured emissivity on the surfaces of different materials used in thermal calculation

Surface	Emissivity
Laminated iron package	0.25
Carbon fiber bandage surface	0.8
Steel rotor surface	0.65 (non-painted) 0.95 (black-painted)
Aluminum housing inner surface	0.5 (non-painted) 0.95 (black-painted)

9.3 Loss Components for Thermal Calculation

According to the calculations in the previous chapters, the loss components in the flywheel system are summarized in Table 9-4. The losses in the magnetic bearings depend on the control forces or current applied on the rotor and the rotor dynamic behavior, hence it is difficult to calculate precisely. A rough calculation was carried out, assuming the rotor located in a centered position without eccentricity and the maximum current of 8 A is applied as the worst case estimation. The losses in the MB stator include the copper losses and iron losses. The losses in the magnetic bearing rotor are calculated according to the results in Chapter 7.4. The calculation leads to a rotor loss of 26.2 W in the radial MB and 24.7 W in the combined one for the maximum operating speed. All the loss components are used as heat sources in the thermal network.

Table 9-4 Calculated loss components of the designed flywheel system in vacuum (air pressure 0.3 Pa), used for thermal calculation

Parameter	Symbol	Value	
Speed [min^{-1}]	n	12000	24000
E-machine with rated load			
Torque on the shaft [Nm]	M_e	22.2	11.1
Copper losses at 150 °C [W]	$P_{Cu, AC, 150\,°C}$	496.4	486.4
Iron losses in stator teeth [W]	$P_{Fe,st}$	135.8	277.2
Iron losses in stator yoke [W]	$P_{Fe,sy}$	226.3	211.1
Losses in magnets [W]	P_{PM}	26.4	28.4
Losses in rotor iron [W]	$P_{Fe,r}$	4.8	5.4
E-machine at no load			
Torque on the shaft [Nm]	M_e	0	0
Copper losses at 150 °C [W]	$P_{Cu, AC, 150\,°C}$	0	221.8
Iron losses in stator teeth [W]	$P_{Fe,st}$	116.4	277.5
Iron losses in stator yoke [W]	$P_{Fe,sy}$	164.4	219.2
Losses in magnets [W]	P_{PM}	0.4	29.4
Losses in rotor iron [W]	$P_{Fe,r}$	1.0	4.1
Magnetic bearings			
Losses in radial MB stator [W]	$P_{MB1,s}$	96.7	113.0
Losses in radial MB rotor [W]	$P_{MB1,r}$	9.3	26.2
Losses in combined MB stator [W]	$P_{MB2,s}$	94.0	109.7
Losses in combined MB rotor [W]	$P_{MB2,r}$	8.9	24.7
Air friction losses			
On flywheel rotor [W]	$P_{fr, FW}$	1.57	6.28
On E-machine rotor [W]	$P_{fr, mot}$	0.079	0.317
On radial MB rotor [W]	$P_{MB, 1}$	0.0125	0.050
On combined MB rotor [W]	$P_{MB, 2}$	0.014	0.055

9.4 Temperature Rises and Heat Flows

In order to have a better view of the heat sources and heat flow paths among the system components, the thermal model in Fig. 9-4 is simplified and drawn in Fig. 9-5, only used for a better view of the heat flow paths.

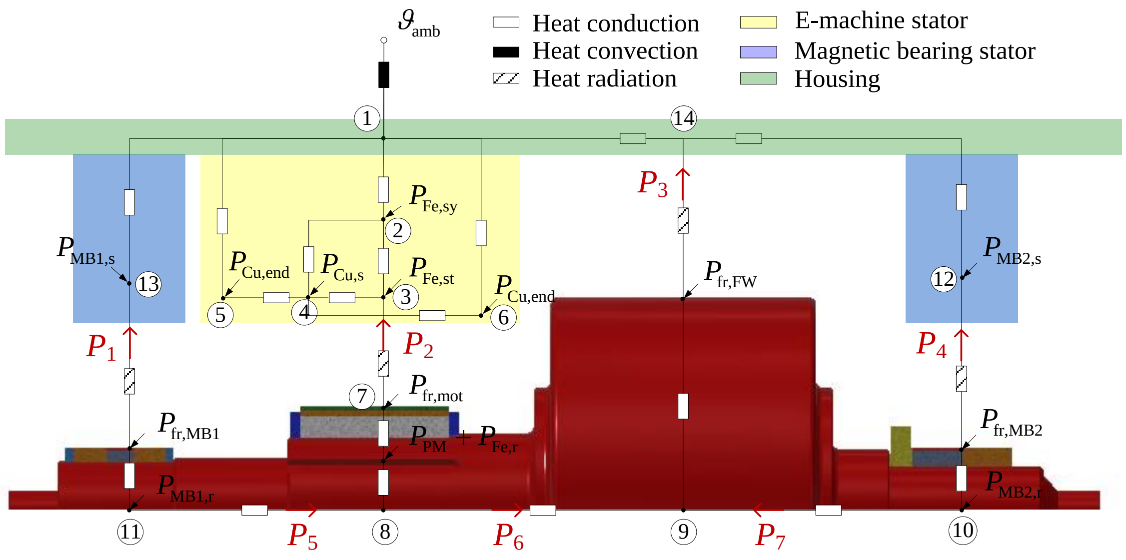

Fig. 9-5 Simplified drawing of the thermal network in Fig. 9-4 with heat flow paths $P_0 \sim P_7$:

(ϑ_{amb}: ambient temperature, node: 1-PM machine housing, 2-PM machine stator yoke, 3-PM machine stator teeth, 4-Winding in slot, 5-Winding overhang (top), 6-Winding overhang (bottom), 7-PM machine bandage, 8-PM machine shaft, 9-Flywheel body, 10-Rotor of bottom MB, 11-Rotor of top MB, 12-Stator of bottom MB, 13-Stator of top MB, 14-Flywheel housing)

9.4.1 Continuous Operation with Full Power

1) Comparison with FEM Calculation

The thermal analysis was firstly performed for the rated power continuous operation at OP_1 ($12000\ \mathrm{min}^{-1}$) and OP_2 ($24000\ \mathrm{min}^{-1}$) respectively, assuming the flywheel is fully utilized and neglecting the varying losses for varying speeds. By applying the calculated losses in Table 9-4 as heat sources into the thermal network, the steady state temperature rises are calculated and shown in Table 9-5. The calculation assumes the flywheel body surface and housing inner surface are painted black with the emissivity of 0.95.

To verify the calculation of the thermal network, a 3D model is built in FEM program *JMAG Designer* (Fig. 9-6). As the E-machine has 72 magnet segments in circumferential direction and 48 slots, a unit model is defined with an angular pitch of 15° which contains 3 magnet segments and 2 slot pitches. The steady state temperatures calculated in FEM model are shown in Table 9-5. The results calculated by two methods have a good agreement.

As can be seen in Table 9-5, the temperature rises in the stator (lower than 30 K) are not critical due to the effective water cooling, while the rotor temperature rise is over

60 K higher than the stator due to the bad rotor cooling condition. Therefore, concerning the rotor temperature, OP_2 is more critical than OP_1. The maximum rotor temperature rise for OP_2 is about 96.3 K, occurring on the rotor of the top magnetic bearing. The minimum temperature rise of the rotor is 68.3 K on the flywheel body, 28 K lower than the hot spot. The bandage of the E-machine has a temperature rise of 87.4 K. Concerning the coolant temperature of 40 °C, a maximum temperature of 127.4 °C will be expected on the bandage. The maximum allowed temperature on the bandage is 141 °C, which is called glass transition temperature. Above this temperature, the gradual and reversible material transition will occur where the material transits from a hard and relatively brittle "glassy" state into a viscous or rubbery state [71]. The worst case temperature of 127.4 °C is 13.6 K lower than the temperature limit.

Table 9-5 Calculated steady state temperature rises [K] in the flywheel system for continuous operation at OP_1 and OP_2, calculated with the modeled thermal network in Fig. 9-4 and the FEM program *JMAG* for an emissivity $\varepsilon_r = 0.95$ on the flywheel body surfaces and $\varepsilon_s = 0.95$ on the housing inner surface. The emissivities on other surfaces are assigned with the values in Table 9-3

Node	Name	OP_1		OP_2	
		Network	FEM	Network	FEM
1	PM machine housing	1.4	2.5	1.6	2.7
2	PM machine stator yoke	7.0	6.6	8.2	7.3
3	PM machine stator teeth	16.5	15.2	20.0	18.4
4	Winding in slot	18.8	18.2	21.2	20.6
5	Winding overhang (top)	22.1	23.6	24.3	25.6
6	Winding overhang (bottom)	22.1	23.8	24.3	26.0
7	PM machine bandage	58.5	54.2	87.4	82.9
8	PM machine shaft	57.0	52.7	86.0	78.8
9	Flywheel body	44.3	40.5	68.3	60.6
10	Rotor of bottom MB	45.9	46.2	73.4	77.8
11	Rotor of top MB	60.0	60.6	96.3	100.5
12	Stator of bottom MB	10.1	17.2	12.5	18.8
13	Stator of top MB	2.4	3.1	2.9	3.2
14	Flywheel housing	5.1	9.0	6.6	10.2

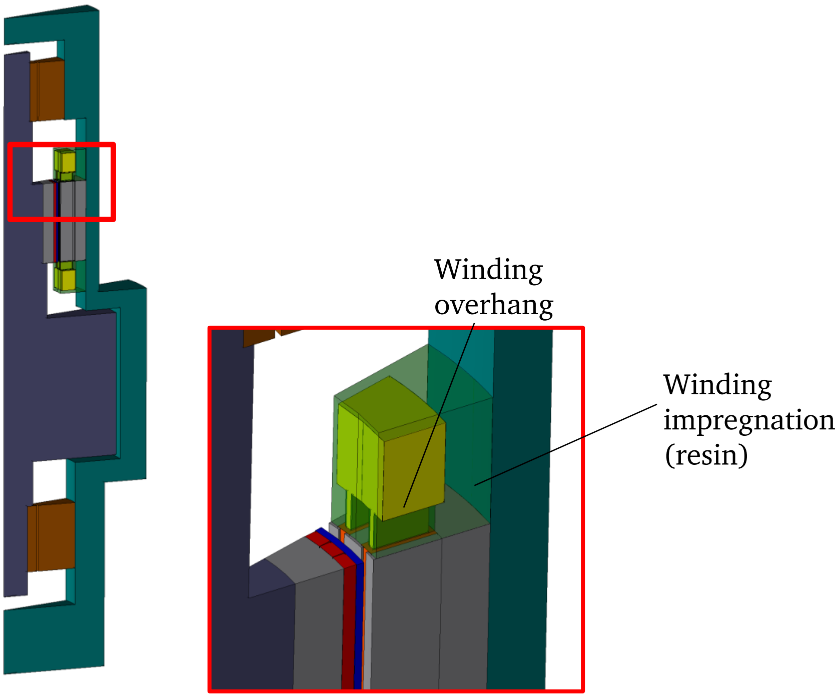

Fig. 9-6 FEM model of the flywheel system for thermal calculation in *JMAG Designer*

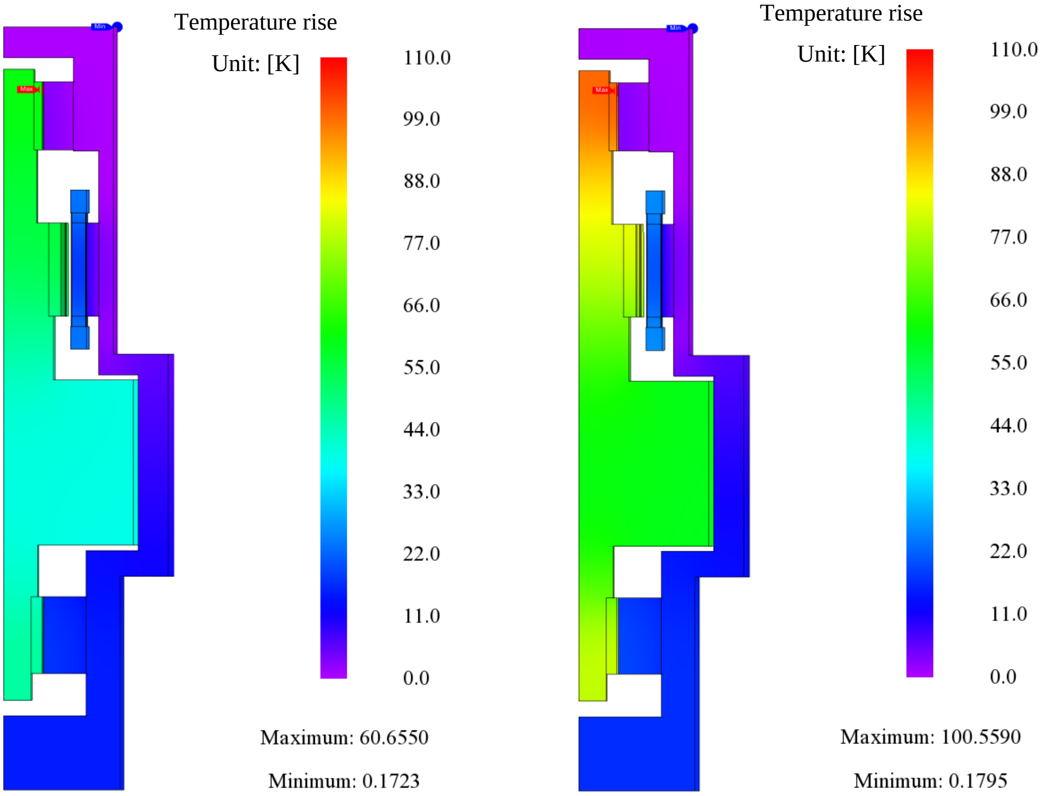

a) b)

Fig. 9-7 Contour plot of the temperature rise in the flywheel system for continuous operation, calculated in *JMAG Designer*: a) OP_1: with rated power at 12000 min^{-1}, b) OP_2: with rated power at 24000 min^{-1}

2) Painted Rotor vs. Non-painted Rotor

To investigate the effect of surface painting, Table 9-6 compares the temperature rises of the system for non-painted and painted rotor and housing inner surfaces for continuous operation at OP_2. Without rotor or stator painting, 37.7 K higher temperature rise on the rotor bandage will be obtained compared to the case with painting on both stator and rotor. Painting only on the stator side will lead to a temperature drop of 21.9 K compared to non-painting case, while painting only on the rotor will lead to 10.8 K temperature drop.

Concerning the heat flows in Table 9-7, most of the heat is dissipated from the flywheel body (heat path P_3) and PM machine rotor (heat path P_2) to the stator side. The equivalent radiative heat transfer coefficient $\alpha_{\mathrm{rad,eq}}$ is calculated for different positions on the rotor in Table 9-8. On the flywheel body surface $\alpha_{\mathrm{rad,eq}} = 4.68\ \mathrm{W/(m^2 \cdot K)}$ for the non-painting case, which is rather low compared to the value in normal static air which is approx. $14\ \mathrm{W/(m^2 \cdot K)}$. If the rotor and stator surfaces are painted black, a higher $\alpha_{\mathrm{rad,eq}} = 8.90\ \mathrm{W/(m^2 \cdot K)}$ can be obtained. The heat dissipation from the flywheel body to the housing (heat path P_3) also increases from 62.9 W to 71.8 W, nearly 14 % higher compared to the non-painted case. Therefore, it is suggested to use black painting for both rotor and stator to obtain higher thermal safety margin.

Table 9-6 Calculated steady state temperature rises [K] of the flywheel system for continuous operation at OP_2 (rated power, 24000 min^{-1}), calculated with the modeled thermal network in Fig. 9-4 for various emissivities on the housing inner surfaces (ε_s) and the rotor surface (ε_r)

Node	Name	$\varepsilon_r = 0.65$	$\varepsilon_r = 0.65$	$\varepsilon_r = 0.95$	$\varepsilon_r = 0.95$
		$\varepsilon_s = 0.5$	$\varepsilon_s = 0.95$	$\varepsilon_s = 0.5$	$\varepsilon_s = 0.95$
1	PM machine housing	1.6	1.6	1.6	1.6
2	PM machine stator yoke	8.2	8.2	8.2	8.2
3	PM machine stator teeth	20.2	20.1	20.2	20.0
4	Winding in slot	21.4	21.3	21.3	21.2
5	Winding overhang (top)	24.5	24.4	24.5	24.3
6	Winding overhang (bottom)	24.5	24.4	24.5	24.3
7	PM machine bandage	125.1	103.2	114.3	87.4
8	PM machine shaft	124.2	102.1	113.3	86.0
9	Flywheel body	109.2	85.3	97.4	68.3
10	Rotor of bottom MB	114.0	90.3	102.3	73.4
11	Rotor of top MB	134.0	112.2	123.2	96.3
12	Stator of bottom MB	12.4	12.5	12.4	12.5
13	Stator of top MB	2.9	2.9	2.9	2.9
14	Flywheel housing	6.4	6.5	6.4	6.6

Table 9-7 Calculated heat flows [W] for steady state continuous operation at OP_2 (rated power, 24000 min^{-1}), calculated with the modeled thermal network in Fig. 9-4 for various emissivities on the housing inner surfaces (ε_s) and the rotor surface (ε_r)

Heat path	$\varepsilon_r = 0.65$	$\varepsilon_r = 0.65$	$\varepsilon_r = 0.95$	$\varepsilon_r = 0.95$
	$\varepsilon_s = 0.5$	$\varepsilon_s = 0.95$	$\varepsilon_s = 0.5$	$\varepsilon_s = 0.95$
P_1	7.1	6.8	6.9	6.7
P_2	15.8	11.4	13.8	8.7
P_3	62.9	68.5	65.6	71.8
P_4	5.5	4.7	5.1	4.2
P_5	19.1	19.4	19.4	19.5
P_6	37.4	42.2	39.7	45.0
P_7	19.2	20.0	19.7	20.5

Table 9-8 Calculated equivalent radiative heat transfer coefficient $\alpha_{rad,eq}$ [$W/(m^2 \cdot K)$] for steady state continuous operation at OP_2 (rated power, 24000 min^{-1}), calculated with the modeled thermal network in Fig. 9-4 for various emissivities on the housing inner surfaces (ε_s) and the rotor surface (ε_r)

Rotor surface	$\varepsilon_r = 0.65$	$\varepsilon_r = 0.65$	$\varepsilon_r = 0.95$	$\varepsilon_r = 0.95$
	$\varepsilon_s = 0.5$	$\varepsilon_s = 0.95$	$\varepsilon_s = 0.5$	$\varepsilon_s = 0.95$
Rotor of top MB	3.32	3.80	3.49	4.39
PM machine bandage	4.18	3.78	4.04	3.55
Flywheel body	4.68	6.65	5.52	8.90
Rotor of bottom MB	3.04	3.42	3.17	3.91

9.4.2 Operation with a Fully-utilized Cycle

The operation of the flywheel at a constant operating point, i.e. constant power at constant speed, is non-realistic, as the speed of the flywheel varies with the power flowing in and out. Assuming the flywheel is continuously charged and discharged, which means fully utilized, a duty cycle in Fig. 9-8 will be expected. The cycle period is 90 s, including one charging period and one discharging period. The charging time t_{ch} = 45 s, when the flywheel is charged from minimum speed 12000 min^{-1} to maximum speed 24000 min^{-1} with a full power. And the discharging time is also t_{dch} = 45 s, when the flywheel is discharged from maximum speed to minimum speed with a full power.

A transient temperature calculation was conducted for both continuous operation at OP_2 and cycling operation. Fig. 9-9 shows the temperature rise versus time for both black-painted rotor and stator. The time constant of the rotor is about 4 hours which is much bigger than the stator due to the big mass. For cycling operation, a steady state temperature rise of 73.0 K is obtained at the E-machine bandage, which is smaller compared to 87.4 K for continuous operation. A comparison of the steady state temperature rises for continuous operation at OP_2 and duty cycle operation is shown in Table 9-9. A temperature drop of 14.1 K can be expected for the operation with a duty cycle.

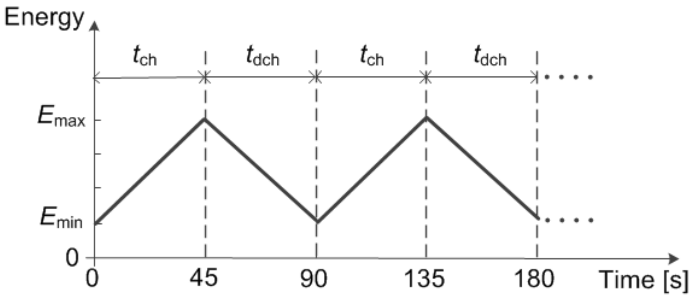

Fig. 9-8 Assumed fully-utilized driving cycle of the flywheel

(t_{ch}: charging time, t_{dch}: discharging time, E: instantaneous energy in the flywheel)

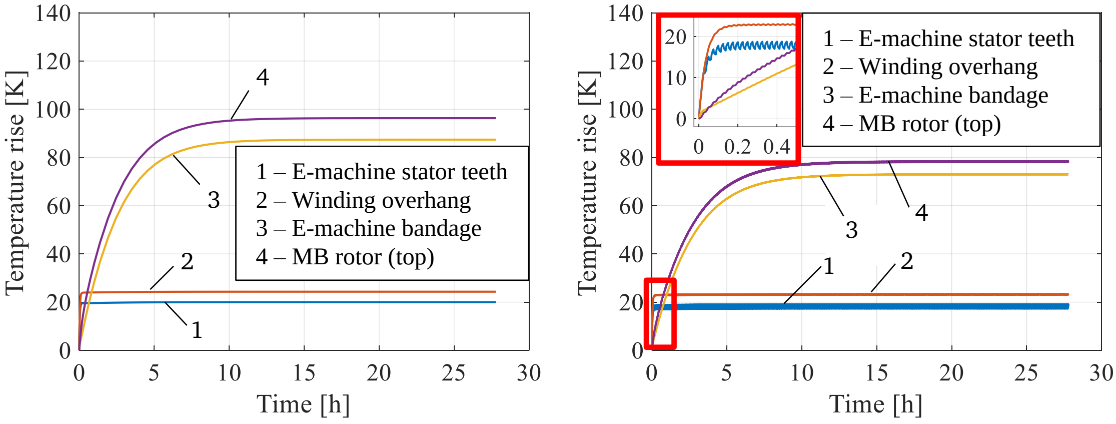

a) b)

Fig. 9-9 Calculated transient temperature rises of the flywheel system with black-painted rotor and black-painted stator: a) continuous operation at OP_2, b) operating with defined duty cycle in Fig. 9-8

Table 9-9 Calculated steady state temperature rises [K] in the flywheel system (model in Fig. 9-4) for continuous operation at OP_2 and duty cycle operation in Fig. 9-8, calculated for both black-painted stator surface ε_s = 0.95 and rotor surface with ε_r = 0.95

Node	Name	Continuous	Duty cycle
1	PM machine housing	1.6	1.5
2	PM machine stator iron	8.2	7.7
3	PM machine stator teeth	20.0	18.2
4	Winding in slot	21.2	20.2
5	Winding overhang (top)	24.3	23.3
6	Winding overhang (bottom)	24.3	23.3
7	PM machine bandage	87.4	73.0
8	PM machine shaft	86.0	71.6
9	Flywheel body	68.3	56.2
10	Rotor of bottom MB	73.4	59.7
11	Rotor of top MB	96.3	78.4
12	Stator of bottom MB	12.5	9.4
13	Stator of top MB	2.9	2.7
14	Flywheel housing	6.6	4.7

9.5 Stator Cooling System

Due to the high current loading in the stator winding (Table 6-3), a water cooling is necessary and realized by a cooling jacket (Fig. 9-10). A spiral cooling duct with 12 turns is designed. The duct has a width of 12 mm and a height of 10 mm with a distance of 4 mm between the two adjacent turns. The coolant is water with the properties shown in Table 9-10.

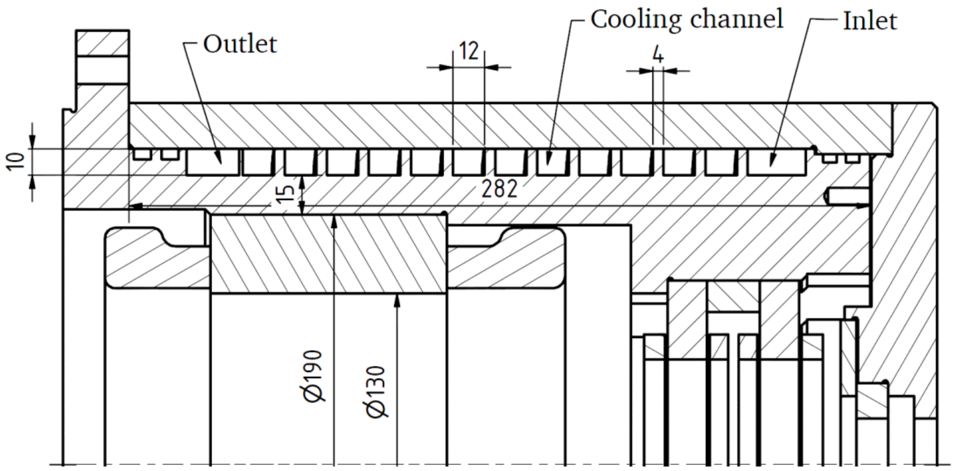

Fig. 9-10 Section view of the cooling channel (dimensions in mm)

Table 9-10 Properties of water at 40 °C, atmosphere pressure

Parameter	Symbol	Value
Density	$\rho_{\mathrm{H_2O}}$	992.2 kg/m^3
Specific heat capacity	$c_{\mathrm{H_2O}}$	4179 J/(kg · K)
Thermal conductivity	$\lambda_{\mathrm{H_2O}}$	0.623 W/(m · K)
Kinematic viscosity	$\nu_{\mathrm{H_2O}}$	0.658×10^{-6} m^2/s

A coolant flow rate $\dot{V} = 2.6$ l/min is designed for the cooling system. Thus the coolant flow speed

$$\upsilon_{\mathrm{H_2O}} = \frac{\dot{V}}{A_{\mathrm{k}}}, \tag{9-5}$$

where A_{k} is the cross section of the cooling channel. $\upsilon_{\mathrm{H_2O}} = 0.361$ m/s is obtained for the designed cooling channel. The heat transfer coefficient at the cooling channel surface can be calculated by

$$\alpha_k = 0.024 \cdot (c_{H_2O} \cdot \rho_{H_2O})^{0.3} \cdot \frac{\lambda_{H_2O}^{0.7}}{d_k^{0.2} \cdot \nu_{H_2O}^{0.5}} \cdot \upsilon_{H_2O}^{0.8}, \tag{9-6}$$

where d_k is the hydraulic diameter of the cooling channel, calculated with the cross section A_k and the circumference U_k of the cooling channel

$$d_k = \frac{4 \cdot A_k}{U_k}. \tag{9-7}$$

For the designed cooling channel, the calculated $d_k = 10.9$ mm. By using the parameters in Table 9-10, the heat transfer coefficient at the cooling channel surface is $\alpha_k = 2244\ \mathrm{W/(m^2 \cdot K)}$. In the thermal network in Fig. 9-4 the housing is assumed to be cylinder without cooling channels. Therefore, an equivalent heat transfer coefficient α_{eq} is calculated by (9-8) and applied on outer surface of the housing.

$$\alpha_{eq} = \frac{l_k \cdot U_k}{A_s}, \tag{9-8}$$

where l_k is the total length of the spiral cooling jacket, A_s is the surface area of the stator housing without cooling channel. For the dimensions in Fig. 9-10, $\alpha_k = 4202\ \mathrm{W/(m^2 \cdot K)}$ is obtained.

As the calculated total losses of the system P_d at 24000 $\mathrm{min^{-1}}$ with rated power is about 1289 W. The temperature rise in the coolant is calculated to be 7.2 °C by

$$\Delta\vartheta_{H_2O} = \frac{P_d}{c_{H_2O} \cdot \rho_{H_2O} \cdot A_k \cdot \upsilon_{H_2O}}. \tag{9-9}$$

The inlet temperature of the coolant ϑ_i is designed to be 37 °C. Thus the outlet temperature of the coolant ϑ_o is 44.2 °C, calculated by

$$\vartheta_o = \vartheta_i + \Delta\vartheta_{H_2O}. \tag{9-10}$$

The average temperature of the coolant

$$\vartheta_{amb} = \frac{\vartheta_i + \vartheta_o}{2} \tag{9-11}$$

is used as the ambient temperature for the thermal calculation, which is 40.6 °C.

10. Conceptual Design of a 150 kW E-machine for an Onboard Flywheel

The flywheel system designed in previous chapters is a preliminary demonstrative prototype aiming at the verification of the theoretical design method and the construction feasibility for the laboratory testing. Therefore, the system specifications and design concept are not specified for the onboard application. In fact, based on the analysis in Chapter 3, a reasonable sizing of an onboard flywheel leads to a storage capacity of 1.5 kWh and the power rating of 450 kW. In order to reduce the construction difficulties and costs, 3 parallel flywheel modules are adopted instead of one large dimensional unit. Thus the energy and power rating of each module are accordingly downsized to 0.5 kWh and 150 kW. However, due to the power limit in the *EW* lab, the power rating has to be further downsized to 35 kVA. Therefore, the aim of the first-step prototyping is to fulfill the energy capacity requirement, regardless of the power rating. For the second step in the future, the full power requirement will also be fulfilled. Meanwhile, special considerations for the onboard devices should also be taken into account, e.g. the high energy and power density, the influence of the gyroscopic effect and the robustness against the potential impacts. As a conception for the follow-up design for the onboard application, a theoretical design of a PM machine with a full power of 150 kW is proposed in this chapter. The basic design approach for a PM machine with similar power rating is proposed in [76].

10.1 Design Specifications and Special Requirements

1) Design specifications and operating characteristics

The specifications of the 150 kW E-machine are shown in Table 10-1 and the operating characteristics are shown in Fig. 10-1. The machine has the same speed range and voltage limitation as the prototype E-machine. But the power requirement is 150 kW instead of 35 kVA. Additionally the inverter frequency is increased to 24 kHz instead of 12 kHz compared to the prototype E-machine. As the inductance of the 150 kW machine is relatively low, higher modulation frequency can reduce the current harmonics, thus avoiding high rotor losses. Field weakening is used between the speed 12000 min^{-1} and 24000 min^{-1} due to the voltage limit.

2) Critical considerations

The critical considerations of the 150 kW E-machine are similar to the prototype machine, including high rotor mechanical strength, low rotor losses and no demagnetization problems, etc.

Table 10-1 150 kW E-machine design specifications

Parameters	Symbol	Value	Unit
Maximum speed	$n_{\max}$	24000	min^{-1}
Minimum speed	$n_{\min}$	12000	min^{-1}
Nominal output voltage (r.m.s.) of inverter	U_{AC}	396	V
Max. phase voltage (r.m.s., Y connection)	$U_{\mathrm{s,\,max}}$	228.6	V
Inverter max. switching frequency	f_{T}	24	kHz
Rated output power (motor)	P_{N}	150	kW
Operation duty type	Continuous duty		

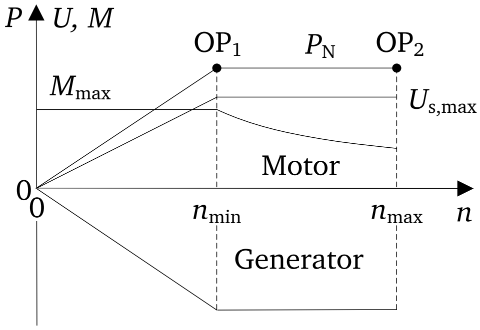

Fig. 10-1 Operating characteristics of the E-machine, P_{N} = 150 kW, $n_{\min}$ = 12000 min^{-1}, $n_{\max}$ = 24000 min^{-1}, $U_{\mathrm{s,\,max}}$: max. terminal voltage, M: torque

10.2 E-machine Preview

The designed 150 kW E-machine is a 4-pole PM machine with surface mounted rotor magnets, shown in Fig. 10-2. The magnets are directly glued on the solid shaft without laminated iron package in order to obtain a higher rotor stiffness. The magnets are segmented to reduce eddy current losses. Each pole has 12 magnet segments in circumferential direction and 11 segments in axial direction. The pole coverage ratio is 1. The stator has 36 slots and three-phase short pitched distributed two-layer winding with q = 3. The dimensions and main parameters of the machine are shown in Table 10-2.

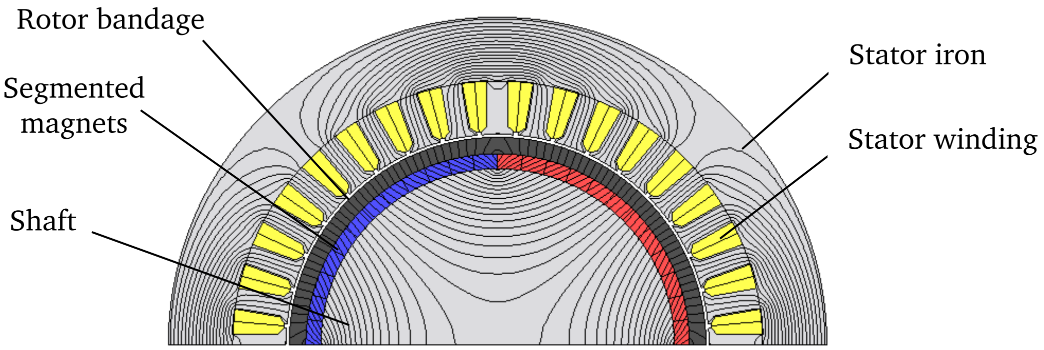

Fig. 10-2 Section view of the 150 kW E-machine geometry (with no-load flux lines), ½ model in *JMAG*

Table 10-2 150 kW E-machine main dimensions and design parameters

Parameter	Symbol	Value
Stator inner diameter	d_{si}	140 mm
Stator outer diameter	d_{so}	210 mm
Shaft diameter	d_{sh}	117 mm
Iron stack length	L_{Fe}	308 mm
Air gap length	δ	1 mm
Bandage thickness	h_{B}	5.5 mm
Magnet dimension	$l_{\mathrm{m}} \cdot b_{\mathrm{m}} \cdot h_{\mathrm{m}}$	28 mm×7.6 mm×5.0 mm
Segmentation per pole	$c_{\mathrm{m}} \cdot z_{\mathrm{m}}$	12 (circumferential)×11 (axial)
Air gap flux density	$B_{\delta,1}$	0.453 T
Thermal loading	$A \cdot J$	4228 A/cm· A/mm^2
Material	Bandage	Carbon fiber HTS5631+epoxy resin
	Magnet	VACOMAX 225 HR (Sm_2Co_{17})
	Iron sheet	NO 20
Cooling	Water cooled with jacket on the stator outer surface	

Concerning the rotor mechanical protection, a prefabricated carbon fiber bandage is used on the outer surface of the magnets. They are assembled by cold shrinking with an undersize of 0.16 mm between the contact surfaces. This shrinking fitting causes a maximum tensile stress of 652 MPa in the bandage for a 20 % over-speed rotation at 28800 min^{-1} at the temperature of 150 °C, which is calculated based on the method introduced in Chapter 6.5. The bandage has a theoretical maximum tensile strength of 2615 MPa. Thus a safety factor of 4.0 is reserved.

The stator iron is laminated with the iron sheet with a thickness of 0.2 mm. The iron sheet type is NO 20. The stacking factor is 0.95. The iron is slotted and wound with a three-phase short pitched distributed two-layer winding with q = 3. Table 10-3 shows the design parameters of the stator. Fig. 10-3 shows the dimensions of the stator iron sheet.

The designed current density in the stator winding is 9.6 A/mm^2 and the current loading is 440.4 A/cm for operation at OP$_1$, leading to a thermal loading of $A \cdot J = 4228$ A/cm $\cdot$ A/mm^2. The thermal loading at OP$_2$ is slightly lower than OP$_1$ due to a slightly lower current (Table 10-4). The machine is water cooled with the cooling jacket on the housing.

Table 10-3 Stator parameters of the designed 150 kW E-machine

Parameter	Symbol	Value	Parameter	Symbol	Value
Pole count	$2p$	4	Nr. of strands per turn	a_i	14
Slot number	Q_s	36	Slot area	A_slot	138.6 mm^2
Short pitching	w/τ_s	8/9	Slot filling factor	k_fill	0.406
Nr. of turns per phase	N_s	12	Current loading at OP$_1$	A	440.4 A/cm
Nr. of turns per coil	N_c	4	Current density at OP$_1$	J	9.6 A/mm^2
Parallel branches	a	4	Resistance (phase)	$R_{\mathrm{s},20\,°\mathrm{C}}$	7.88 mΩ
Diameter of wires	d_Cu	0.8 mm		$R_{\mathrm{s},150\,°\mathrm{C}}$	11.6 mΩ

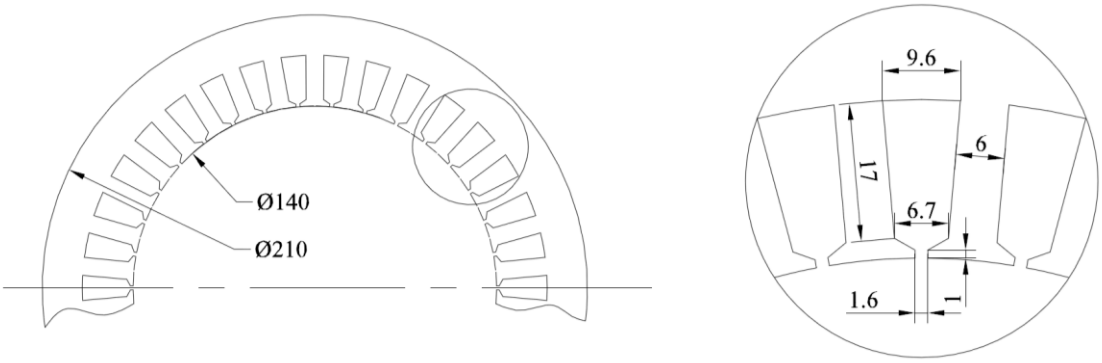

Fig. 10-3 Stator iron design, iron sheet NO 20 (dimensions in mm)

10.3 E-machine Loss Calculation

The losses in the machine are calculated numerically by a 2D-model in *JMAG.* The loss components include iron losses, stator winding losses, losses in the magnets. The overall results are given in Table 10-4 for the operating points OP$_1$ and OP$_2$.

Table 10-4 Calculated 150 kW E-machine electromagnetic performance and loss components, calculated by 2D model in *JMAG* which is fed by a series of current sources representing a superimposition of current fundamental and harmonics in Table 10-5

Parameter	Symbol	Value	
		OP_1	OP_2
Speed [min^{-1}]	n	12000	24000
Base frequency [Hz]	f	400	800
Back EMF [V]	U_p	186.2	370.8
Current [A]	I_s	269	242
	I_d	0	-200
	I_q	269	136
Current angle [°]	β	0	55.8
Phase voltage (r.m.s.) [V]	$U_{s,\,ph}$	227.0	224.5
Power factor	$\cos\varphi$	0.834	0.935
Electromagnetic torque [Nm]	M_e	119.9	59.8
Electromagnetic power [kW]	P_e	150.7	150.3
Copper losses at 150 °C [W]	$P_{Cu,\,DC,\,150\,°C}$	2520.8	2045.3
	$P_{Cu,\,AC,\,150\,°C}$	3016.4	3445.3
Iron losses in stator teeth [W]	$P_{Fe,st}$	459.6	785.7
Iron losses in stator yoke [W]	$P_{Fe,sy}$	745.3	637.9
Losses in magnets [W]	P_{PM}	32.3	48.3
Losses in rotor iron (i.e. shaft) [W]	$P_{Fe,r}$	99.0	83.1
Air friction losses [W]	P_{fr}	0.34	1.36
Total losses [W]	P_d	4352.94	5001.66
Efficiency [%]	η	97.2	96.8

10.3.1 Harmonics due to PWM Voltage Supply

Considering the additional losses caused by the harmonics due to the inverter modulation, the machine is fed by a current source superposed by the fundamental and the harmonics shown in Fig. 10-4. They are obtained from the *Matlab Simulink* model introduced in Chapter 6.4.1.

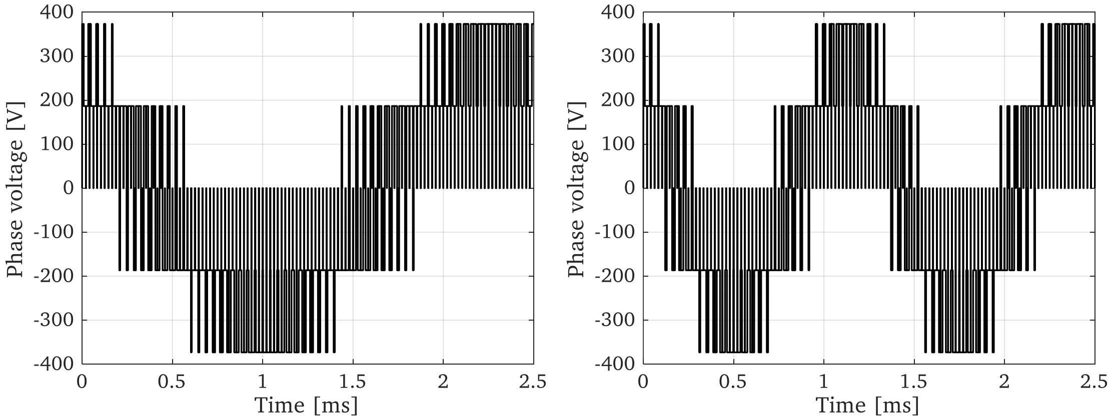

a) 400 Hz 800 Hz

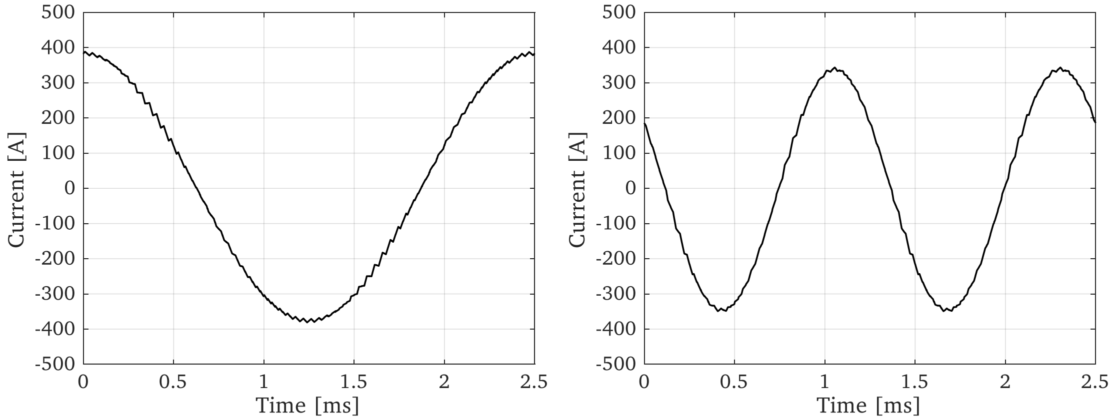

b) 400 Hz 800 Hz

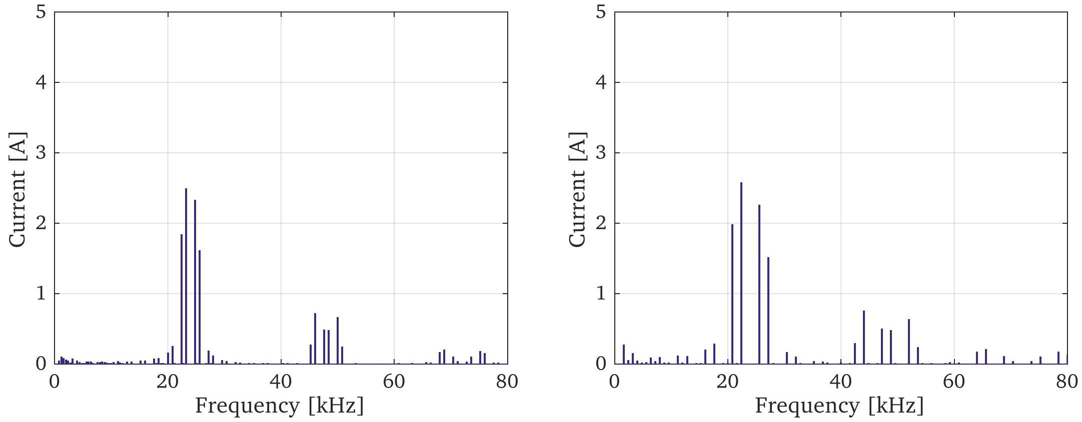

c) 400 Hz 800 Hz

Fig. 10-4 Calculated voltage and current waveforms and current harmonics of phase *U* in the inverter-fed PM machine, switching frequency $f_T = 24$ kHz : a) phase voltage, b) current, c) harmonics of current (fundamental not shown)

Table 10-5 Calculated harmonics of the current used for loss calculation in phase U due to PWM voltage supply, switching frequency $f_T = 24$ kHz

OP$_1$: 12000 min^{-1}				OP$_2$: 24000 min^{-1}		
Frequency [Hz]		Current [A]	Phase angle [°]	Frequency [Hz]	Current [A]	Phase angle [°]
f_s	400	379.98	0.2	800	342.26	56.3
$f_T - 4 \cdot f_s$	22400	1.84	-44.4	20800	1.98	-47.8
$f_T - 2 \cdot f_s$	23200	2.49	-157.4	22400	2.58	-159.1
$f_T + 2 \cdot f_s$	24800	2.33	-23.4	25600	2.26	-21.7
$f_T + 4 \cdot f_s$	25600	1.62	-136.4	27200	1.52	-133.0
$2 \cdot f_T - 5 \cdot f_s$	46000	0.72	-78.5	44000	0.75	-82.2
$2 \cdot f_T - f_s$	47600	0.48	55.7	47200	0.50	54.8
$2 \cdot f_T + f_s$	48400	0.48	122.6	48800	0.48	123.5
$2 \cdot f_T + 5 \cdot f_s$	50000	0.67	-103.3	52000	0.64	-99.6

10.3.2 E-machine Loss Calculation

10.3.2.1 Losses in Stator Winding

The alternating current feeding causes additional copper losses in the winding as discussed in Chapter 6.3.2. The losses depend on the current frequency, wire dimension as well as the wire arrangement and can be calculated following (6-12) … (6-27).

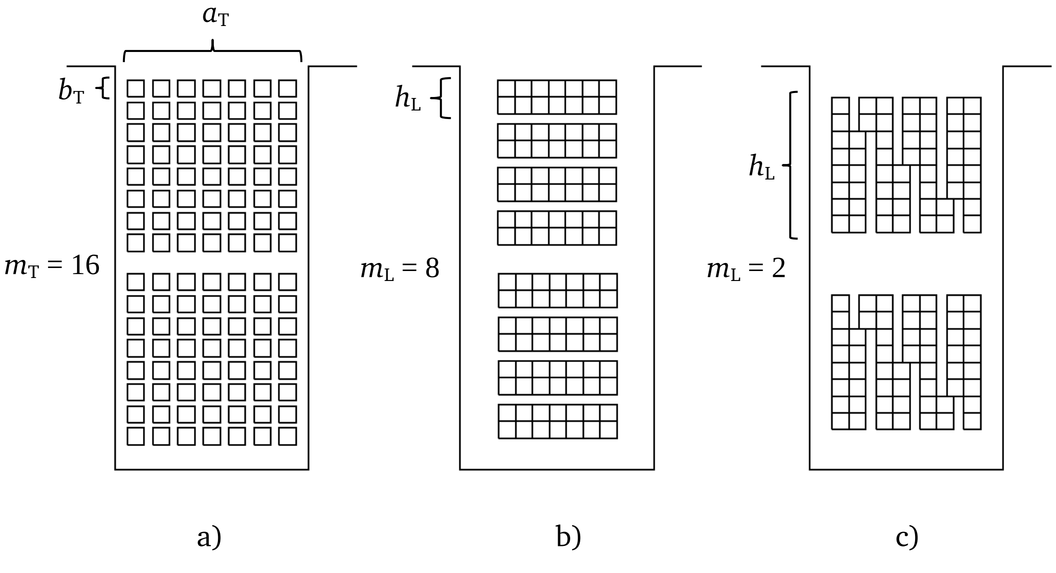

a) b) c)

Fig. 10-5 Wire arrangements for the additional losses calculation: a) due to skin and proximity effect, b) due to circulating current: best case, c) due to circulating current: worst case

The winding of the designed machine has $N_\mathrm{c} = 4$ turns for each coil with $a_\mathrm{i} = 14$ parallel strands for each turn. Thus in each slot, 56 wires should be arranged for both upper and lower layer. The diameter of the round wire is $d_\mathrm{Cu} = 0.8$ mm, thus the equivalent dimension of the assumed square wire, calculated by (6-15), is $b_\mathrm{T} = 0.71$ mm. An average slot width $b_\mathrm{Qm} = 8.15$ mm is obtained from the stator geometry in Fig. 10-3. With the slot filling factor of $k_\mathrm{fill} = 0.406$, a feasible arrangement of the wires in one slot is: $a_\mathrm{T} = 7$ and $m_\mathrm{T} = 16$ as shown in Fig. 10-5 a).

Concerning the arrangement of parallel strands, the best case is shown in Fig. 10-5 b). The equivalent h_L is $2 \cdot b_\mathrm{T}$ and $m_\mathrm{L} = 8$. The worst case is shown in Fig. 10-5 c). The equivalent h_L is $8 \cdot b_\mathrm{T}$ and $m_\mathrm{L} = 2$.

Table 10-6 Calculated copper losses in the winding fed by the current with harmonics in Table 10-5, winding resistance $R_\mathrm{s} = 0.0116\ \Omega$ at temperature $\vartheta = 150$ °C

(f: harmonic frequency, $\hat{I}_{sk}$: current amplitude, $P_{\mathrm{Cu,DC},k}$: DC resistive losses, $P_{\mathrm{Cu,AC},k}$: AC resistive losses, $P_\mathrm{Cu,add,pr}$: additional losses due to skin and proximity effect, $P_\mathrm{Cu,add,circ}$: additional losses due to circulating current in the winding)

OP_1: 12000 min^{-1}								
f [Hz]	$\hat{I}_{sk}$ [A]	$P_\mathrm{Cu,add,pr}/P_{\mathrm{Cu,DC},k}$	$P_\mathrm{Cu,add,circ}/P_{\mathrm{Cu,DC},k}$			$P_{\mathrm{Cu,DC},k}$ [W]	$P_{\mathrm{Cu,AC},k}$ [W]	$P_{\mathrm{Cu,AC},k}/P_{\mathrm{Cu,DC},k}$
			best	worst	average			
400	379.98	1.013	1.023	1.360	1.191	2520.5	2990.3	1.19
10400	1.84	37.84	47.92	19.18	33.55	0.06	3.80	64.3
11200	2.49	40.27	50.08	19.52	34.80	0.11	7.33	67.7
12800	2.33	45.28	54.31	20.19	37.25	0.09	7.06	74.5
13600	1.62	47.86	56.37	20.51	38.44	0.05	3.57	77.9
22000	0.72	122.31	95.38	27.50	61.44	0.01	1.51	166.9
23600	0.48	128.32	97.50	27.98	62.74	0.004	0.70	173.6
24400	0.48	131.31	98.52	28.21	63.37	0.004	0.71	176.9
26000	0.67	137.26	100.50	28.68	64.59	0.008	1.44	183.4
Σ	-	-	-	-	-	2520.8	3016.4	1.20
OP_2: 24000 min^{-1}								
f [Hz]	$\hat{I}_{sk}$ [A]	$P_\mathrm{Cu,add,pr}/P_{\mathrm{Cu,DC},k}$	$P_\mathrm{Cu,add,circ}/P_{\mathrm{Cu,DC},k}$			$P_{\mathrm{Cu,DC},k}$ [W]	$P_{\mathrm{Cu,AC},k}$ [W]	$P_{\mathrm{Cu,AC},k}/P_{\mathrm{Cu,DC},k}$
			best	worst	average			
800	342.26	1.052	1.092	2.277	1.685	2044.9	3419.1	1.67
8800	1.98	33.15	43.50	18.48	30.99	0.07	3.95	57.7
10400	2.58	37.84	47.92	19.18	33.55	0.12	7.48	64.3
13600	2.26	47.86	56.37	20.51	38.44	0.09	6.95	77.9
15200	1.52	53.15	60.37	21.15	40.76	0.04	3.42	84.9
20000	0.75	114.76	92.57	26.90	59.74	0.01	1.56	158.4
23200	0.50	126.82	96.98	27.86	62.42	0.004	0.75	171.9
24800	0.48	132.80	99.03	28.33	63.68	0.004	0.72	178.5
28000	0.64	144.63	102.84	29.24	66.04	0.007	1.37	191.4
Σ	-	-	-	-	-	2045.3	3445.3	1.68

The designed machine adopts a double-layer short pitching winding in 36 slots with $w/\tau_s = 8/9$. The winding arrangement leads to 12 slots filled with different phases. Therefore, the correction factor $k_{s,ph}$ is 0.955.

The copper losses of the designed machine are calculated in Table 10-6 concerning the current harmonics in Table 10-5. The current displacement effect causes 20 % additional losses at the operating speed of 12000 min^{-1} with the rated power. 68 % additional losses will be caused at the operating speed of 24000 min^{-1} with the rated power. Therefore, even though the DC resistive losses at 24000 min^{-1} is lower than 12000 min^{-1}, the AC copper losses are even higher.

10.3.2.2 The Influence of Winding Parameters on Copper Losses

The copper losses depend on the current density J, which is determined by the wire diameter d_{Cu} and the number of parallel wires per turn per coil a_i, as described by

$$J = \frac{I_s}{a \cdot A_{Cu}}, \text{ with } A_{Cu} = \frac{\pi}{4} \cdot d_{Cu}^2 \cdot a_i, \tag{10-1}$$

where I_s is the stator current, a is the number of parallel branches. A_{Cu} is the total section area of copper wires for each turn per coil.

The current density determines the DC resistance for a constant current loading A. Meanwhile, d_{Cu} and a_i determine the slot area (10-2) and slot depth, which influence the slot leakage flux and the additional copper losses.

$$A_{slot} = \frac{2 \cdot N_c \cdot A_{Cu}}{k_{fill}}, \tag{10-2}$$

where N_c is the number of turns per coil and k_{fill} is the effective slot filling factor.

In order to discuss the influence of current density on the copper losses, various combinations of d_{Cu} and a_i are chosen as shown in Table 10-7. a_T and m_T can be calculated by (6-22) and (6-23). The best case to reduce the circulating current within parallel wires is to arrange the parallel wires in parallel with the slot bottom as much as possible, leading to $m_L = 2 \cdot N_c$. Instead the worst case is to arrange the parallel wires in perpendicular to the slot bottom. Thus $m_L = 2$.

Table 10-7 Wire arrangements for various combinations of d_{Cu} and a_i
(winding parameters: Nr. of turns per coil $N_\mathrm{c} = 4$, parallel branches $a = 4$, slot filling factor $k_\mathrm{fill} = 0.4$)

	d_{Cu} = 0.6 mm						d_{Cu} = 0.7 mm					
a_i	a_T	m_T	Best case		Worst case		a_T	m_T	Best case		Worst case	
			m_L	$h_\mathrm{L}/b_\mathrm{T}$	m_L	$h_\mathrm{L}/b_\mathrm{T}$			m_L	$h_\mathrm{L}/b_\mathrm{T}$	m_L	$h_\mathrm{L}/b_\mathrm{T}$
5	8	5	8	1	2	2	7	6	8	1	2	3
10	9	9	8	1	2	5	8	10	8	1	2	5
15	9	13	8	2	2	7	8	15	8	2	2	7
20	9	17	8	2	2	9	8	19	8	2	2	9
25	10	21	8	3	2	10	9	23	8	3	2	11
30	10	24	8	3	2	12	9	26	8	3	2	13
35	10	27	8	3	2	14	9	30	8	4	2	15
40	11	30	8	4	2	15	10	33	8	4	2	17
45	11	33	8	4	2	17	10	36	8	5	2	18
50	11	36	8	5	2	18	10	39	8	5	2	20
	d_{Cu} = 0.8 mm						d_{Cu} = 0.9 mm					
a_i	a_T	m_T	Best case		Worst case		a_T	m_T	Best case		Worst case	
			m_L	$h_\mathrm{L}/b_\mathrm{T}$	m_L	$h_\mathrm{L}/b_\mathrm{T}$			m_L	$h_\mathrm{L}/b_\mathrm{T}$	m_L	$h_\mathrm{L}/b_\mathrm{T}$
5	8	6	8	1	2	3	7	7	8	1	2	3
10	9	12	8	1	2	6	8	13	8	2	2	6
15	9	16	8	2	2	8	8	18	8	2	2	9
20	9	21	8	3	2	10	8	22	8	3	2	11
25	10	25	8	3	2	12	9	26	8	3	2	13
30	10	28	8	4	2	14	9	30	8	4	2	15
35	10	32	8	4	2	16	9	34	8	4	2	17
40	11	35	8	4	2	18	10	37	8	5	2	19
45	11	39	8	5	2	19	10	41	8	5	2	20
50	11	42	8	5	2	21	10	44	8	5	2	22
	d_{Cu} = 1.0 mm											
a_i	a_T	m_T	Best case		Worst case							
			m_L	$h_\mathrm{L}/b_\mathrm{T}$	m_L	$h_\mathrm{L}/b_\mathrm{T}$						
5	8	7	8	1	2	4						
10	9	13	8	2	2	7						
15	9	19	8	2	2	9						
20	9	23	8	3	2	12						
25	10	28	8	3	2	14						
30	10	32	8	4	2	16						
35	10	36	8	4	2	18						
40	11	39	8	5	2	20						
45	11	42	8	5	2	21						
50	11	46	8	6	2	23						

The current density J for various combinations of d_{Cu} and a_i calculated by (10-1) is shown in Fig. 10-6, which decreases for increasing d_{Cu} and a_i. However, the skin and proximity effect and the influence of circulating current also increase as shown in Fig. 10-7, in which the influence of circulating current is more significant. The reason is that the section area of the copper wires is increased for higher d_{Cu} and a_{i}, leading to an increased slot area and depth, which increases the current displacement effect.

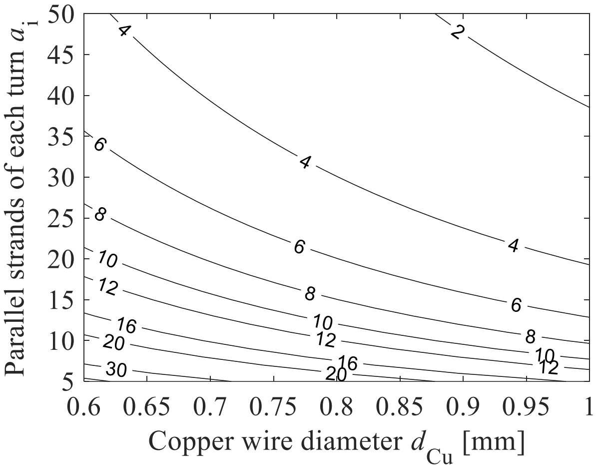

Fig. 10-6 Calculated current density [A/mm^2] in the winding for various combinations of wire diameter d_{Cu} and number of parallel wires a_{i} at OP_2 of the designed machine (electromagnetic power 150 kW, feeding current I_{s} = 242 A at frequency f = 800 Hz)

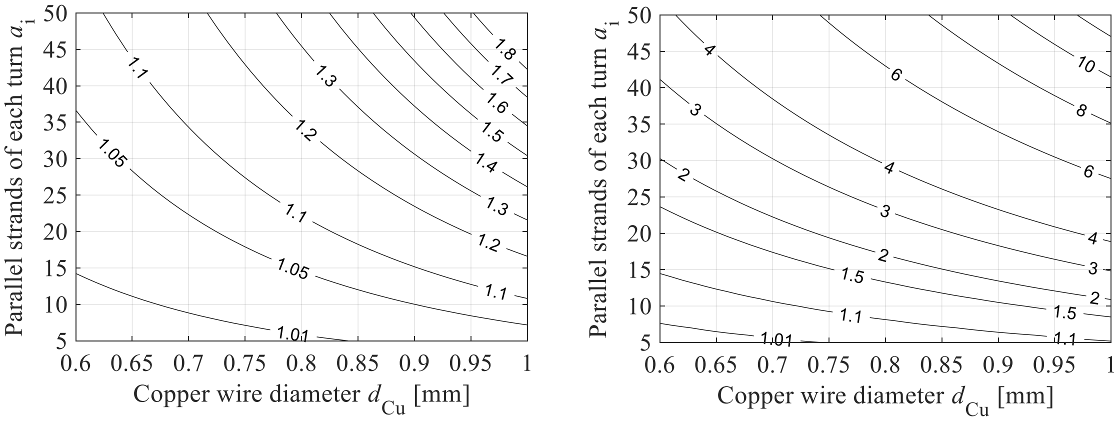

a) b)

Fig. 10-7 Calculated additional loss ratio for fundamental current (k = 1) feeding at OP_2 with I_{s} = 242 A, frequency f = 800 Hz: a) $P_{\mathrm{Cu,\,add,\,pr,\,1}}/P_{\mathrm{Cu,\,DC,\,1}}$ due to skin and proximity effect, b) $P_{\mathrm{Cu,\,add,\,circ,\,1}}/P_{\mathrm{Cu,\,DC,\,1}}$ due to circulating current in parallel wires

The resulting copper losses considering these two effects are shown in Fig. 10-8 b) in comparison to the DC resistive losses shown in Fig. 10-8 a), which neglects the current displacement effect. Even though low DC resistive losses can be obtained for low current density with a combination of high d_{Cu} and a_{i}, considering the additional losses, lower current density may cause even higher AC resistive losses instead. Therefore, minimum AC resistive losses can be obtained by choosing a series of d_{Cu} and a_{i} combinations as shown in Fig. 10-8 b). In the designed machine, d_{Cu} = 0.8 mm and a_{i} = 14 are determined and the resulting copper losses are 3445 W for the feeding current of 242 A with a frequency of 800 Hz.

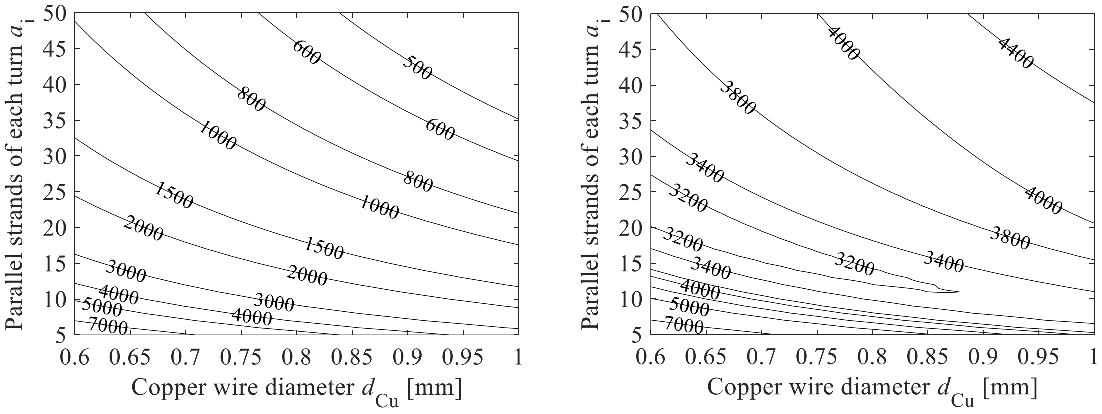

a) b)

Fig. 10-8 Calculated copper losses in the winding for fundamental current (k = 1) at OP$_2$ with I_s = 242 A, frequency f = 800 Hz: a) DC resistive losses $P_{\mathrm{Cu,\,DC,\,1}}$ [W] without current displacement, b) AC resistive losses $P_{\mathrm{Cu,\,AC,\,1}}$ [W] including additional losses due to current displacement

10.3.2.3 Losses in Laminated Iron

The iron losses are calculated numerically in *JMAG*. After getting the numerical results, two correction factors are used considering the bridging effect between the iron sheets due to insulation damage during the laser cutting process. A loss increase factor of k_{Vd} = 1.8 is used for the stator teeth and k_{Vy} = 1.5 is used for the stator yoke. The calculated iron losses are shown in Table 10-4.

10.3.2.4 Losses in the Rotor

The eddy current losses in the rotor which are induced by the m.m.f. of the stator and current harmonics are calculated numerically with a 2D-model in *JMAG*. Each magnet segment is modeled to consider the effect of radial segmentation. To consider the effect of the axial segmentation, the conductivity of the magnets κ_m used in the 2D-model is modified by [53]

$$\kappa_{\mathrm{m,eff}} = \kappa_{\mathrm{m}} / (1 + b_{\mathrm{m}} / l_{\mathrm{m}}) , \tag{10-3}$$

where κ_m is the physical conductivity of the magnet material. b_m and l_m are the width and length of each segment. The total calculated eddy current losses in the magnets are shown in Table 10-4.

The harmonics in the air gap penetrate the magnets and also cause losses in the solid shaft which are also calculated and included in Table 10-4.

10.4 E-machine Thermal Performance

For the thermal performance evaluation, the thermal model in Chapter 9 is used. Fig. 9-5 is shown again in Fig. 10-9 in order to have a better view of the heat sources and heat flow paths. The dimension of the machine in Fig. 10-9 is not the correct dimension for the designed 150 kW machine, but used here only for schematically showing the heat flows.

10.4.1 Continuous Operation

The thermal analysis was carried out for the rated power continuous operation at OP_2 (24000 min^{-1}) as it is the worst case, assuming the flywheel is continuously fully utilized and neglecting the varying losses for varying speeds. The water cooling is used with the cooling channels on the outer surface of the machine stator iron. The equivalent heat transfer coefficient is designed to be 5000 $\text{W}/(\text{m}^2 \cdot \text{K})$.

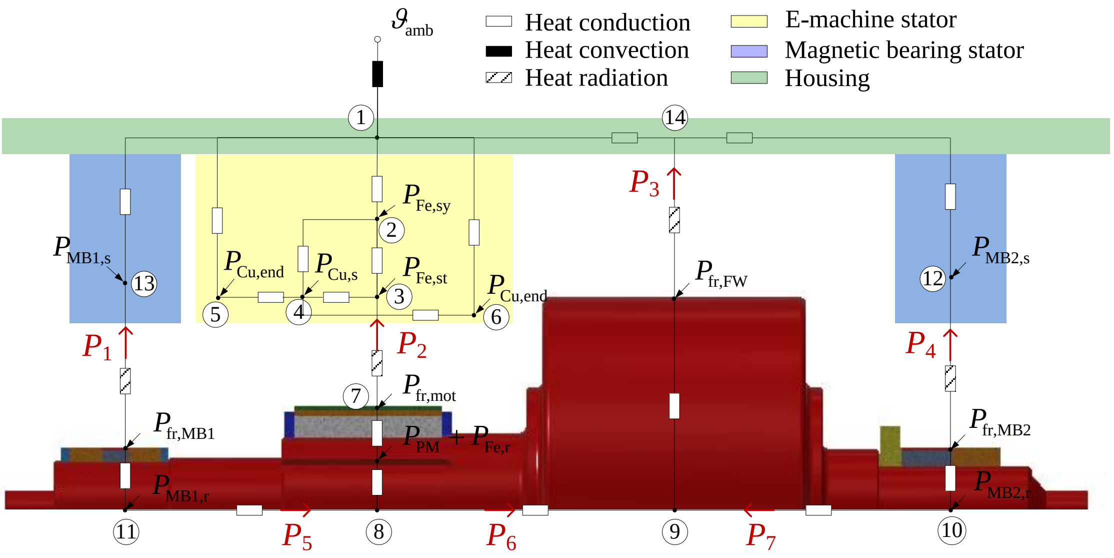

Fig. 10-9 Thermal network of the flywheel system with heat flow paths $P_0 \sim P_7$

(ϑ_{amb}: ambient temperature, node: Node 1: E-machine housing, Node 2: E-machine stator yoke, Node 3: E-machine stator teeth, Node 4: Winding in slot, Node 5: Winding overhang (top), Node 6: Winding overhang (bottom), Node 7: PM machine bandage, Node 8: PM machine shaft, Node 9: Flywheel body, Node 10: Rotor of bottom MB, Node 11: Rotor of top MB, Node 12: Stator of bottom MB, Node 13: Stator of top MB, Node 14: Flywheel housing)

Table 10-8 Calculated steady state temperature rises [K] of the flywheel system with the thermal network (model in Fig. 9-4) for continuous operation at OP_2 (rated power, 24000 min^{-1}), calculated for various emissivities on the stator surfaces (ε_s) and the rotor surface (ε_r)

Node	Name	$\varepsilon_r = 0.65$	$\varepsilon_r = 0.65$	$\varepsilon_r = 0.95$	$\varepsilon_r = 0.95$
		$\varepsilon_s = 0.5$	$\varepsilon_s = 0.95$	$\varepsilon_s = 0.5$	$\varepsilon_s = 0.95$
1	PM machine housing	2.8	2.8	2.8	2.8
2	PM machine stator iron	13.0	13.0	13.0	12.9
3	PM machine stator teeth	33.7	33.5	33.6	33.4
4	Winding in slot	46.4	46.3	46.4	46.2
5	Winding overhang (top)	65.9	65.8	65.9	65.7
6	Winding overhang (bottom)	65.9	65.8	65.9	65.7
7	PM machine bandage	178.5	161.5	170.4	147.6
8	PM machine shaft	178.8	161.3	170.5	147.1
9	Flywheel body	144.0	119.5	132.3	100.5
10	Rotor of bottom MB	149.6	125.3	138.0	106.4
11	Rotor of top MB	191.0	173.3	182.5	158.7
12	Stator of bottom MB	16.3	16.6	16.4	16.8
13	Stator of top MB	4.5	4.5	4.5	4.4
14	Flywheel housing	8.8	9.2	9.0	9.4

Table 10-9 Calculated heat flows [W] for steady state continuous operation at OP_2 (rated power, 24000 min^{-1}) for various emissivities on the stator surfaces (ε_s) and the rotor surface (ε_r) (model in Fig. 9-4)

Heat path	$\varepsilon_r = 0.65$	$\varepsilon_r = 0.65$	$\varepsilon_r = 0.95$	$\varepsilon_r = 0.95$
	$\varepsilon_s = 0.5$	$\varepsilon_s = 0.95$	$\varepsilon_s = 0.5$	$\varepsilon_s = 0.95$
P_1	7.3	6.2	6.8	5.3
P_2	79.3	65.5	72.5	55.3
P_3	96.3	111.5	103.6	122.1
P_4	5.0	3.7	4.3	2.8
P_5	20.7	20.0	20.5	19.1
P_6	67.6	82.1	74.6	92.3
P_7	22.4	23.1	22.7	23.6

Table 10-10 Calculated equivalent radiative heat transfer coefficient $\alpha_{rad,eq}$ [W/($m^2 \cdot K$)] for steady state continuous operation at OP_2 (rated power, 24000 min^{-1}) for various emissivities on the stator surfaces (ε_s) and the rotor surface (ε_r) (model in Fig. 9-4)

Rotor surface	$\varepsilon_r = 0.65$	$\varepsilon_r = 0.65$	$\varepsilon_r = 0.95$	$\varepsilon_r = 0.95$
	$\varepsilon_s = 0.5$	$\varepsilon_s = 0.95$	$\varepsilon_s = 0.5$	$\varepsilon_s = 0.95$
Rotor of top MB	2.40	2.23	2.32	2.10
PM machine bandage	4.10	3.83	3.97	3.62
Flywheel body	5.45	7.73	6.43	10.26
Rotor of bottom MB	2.10	1.90	2.00	1.75

By applying the calculated losses of the machine in Table 10-4 and the losses of other components in Table 9-4 as heat sources into the thermal network, the steady state temperature rises and heat flows are calculated and are shown in Table 10-8 and Table

10-9. Four cases are evaluated for different emissivity of non-painted and painted rotor and stator surfaces.

The hot spot of the stator occurs at winding overhang with temperature rises about 66 K for 4 cases. The rotor painting has very little influence on the stator temperature. For an ambient temperature of 40 °C, the maximum temperature on the winding overhang will reach 106 °C. The machine is designed for the insulation class H with the maximum allowed hot spot temperature of 180 °C for continuous operation. Thus 74 K thermal margin is reserved.

The rotor temperature is more critical. The maximum temperature rise is 191.0 K for the non-painted case, occurring at the position of the top magnetic bearing. The PM machine bandage has a temperature rise of 178.5 K. Considering a coolant temperature of 40 °C, the temperature at bandage is 77.5 K higher than the plastic transition temperature limit of 141 °C of the material. The overheat will cause material failure of the bandage. Even if the rotor and stator are both painted black, the lower temperature rise of 147.6 K is still not acceptable. Therefore, the machine cannot be used for continuous operation due to the high rotor losses.

Compared to the demonstrated machine designed for the flywheel prototype in previous chapter, the rotor losses in these two machines are both accounting for nearly 0.1 % of the rated power. The temperature rise of the rotor compared to the stator side can be roughly calculated by

$$\Delta\vartheta = \frac{P_{\mathrm{d,\,r}}}{\alpha_{\mathrm{rad,\,eq}} \cdot A_{\mathrm{r}}} = \frac{0.001 \cdot P_{\mathrm{N}}}{\alpha_{\mathrm{rad,\,eq}} \cdot A_{\mathrm{r}}}, \tag{10-4}$$

where $P_{\mathrm{d,r}}$ is the rotor losses, P_{N} is the rated power, A_{r} is the rotor surface area, $\alpha_{\mathrm{rad,eq}}$ is the equivalent radiative heat transfer coefficient on the rotor surface.

If we consider only the E-machine, neglecting the flywheel body, as these two machines have similar rotor diameter, the rated power is scaled by axial length. Therefore, $P_{\mathrm{N}} / A_{\mathrm{r}}$ should be also similar. Also, these two machines have similar $\alpha_{\mathrm{rad,eq}}$ as shown in Table 9-8 and Table 10-10. Thus the temperature rise should also be similar. However, if considering the flywheel body, the rotor surface of the flywheel is much bigger than the demonstrated machine (28 kW) in the prototype, which effectively helps the rotor heat dissipation. By comparing the heat dissipation by the E-machine and the flywheel body for these two machines in Table 9-7 and Table 10-9, one can easily find that, for the 150 kW machine, nearly 40 % of the rotor heat is dissipated on the E-machine surface and 60 % on the flywheel body. While for the 28 kW machine, the values are 15 % on the E-machine and 80 % on the flywheel body. Therefore, the rotor heat dissipation problem arises in the big machine. It is recommended to reduce the E-machine rotor losses, for example, by using a filter to reduce the current harmonics.

10.4.2 Operation with a Duty Cycle

A typical driving cycle of a flywheel used for braking energy accumulation of a tram is assumed as shown in Fig. 10-10. The cycle period is 60 s, including charging time t_{ch} = 10 s when the tram decelerates and the flywheel is charged with the braking energy, the high speed idling time t_1 = 10 s when the flywheel is fully charged and the tram stops, the discharging time t_{dch} = 10 s when the tram uses the energy in the flywheel for starting, and the low speed idling time t_0 = 30 s when the flywheel is fully discharged and the tram operates with constant speed.

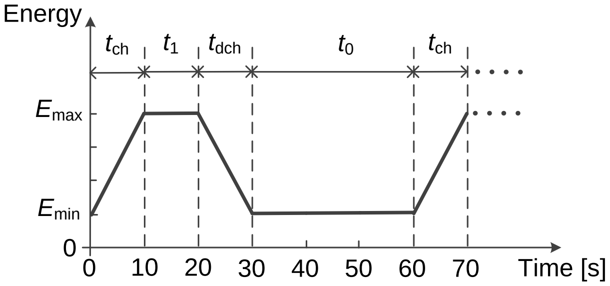

Fig. 10-10 Assumed driving cycle of a flywheel used for a tram

(t_{ch}: charging time, t_1: time for idling at max. speed, t_{dch}: discharging time, t_0: time for idling at min. speed)

A transient temperature calculation was conducted for both continuous operation at OP_2 and cycling operation defined in Fig. 10-10. Fig. 10-11 shows the temperature rise versus time for both painted rotor and stator. The time constant of the rotor is about 4 hours which is much bigger than the stator due to the big rotor mass. For cycling operation, a steady state temperature rise of 95.1 K is obtained at the E-machine bandage, which is smaller compared to 147.6 K for continuous operation. Compared to the temperature limit of 141 °C of the bandage material, a safety thermal margin of 5.9 K is reserved for the coolant temperature of 40 °C, which is rather small. Again, for a safe operation without rotor overheating, it is recommended to reduce the rotor losses. A comparison of the steady state temperature rises for continuous operation at OP_2 and duty cycle operation is shown in Table 10-11.

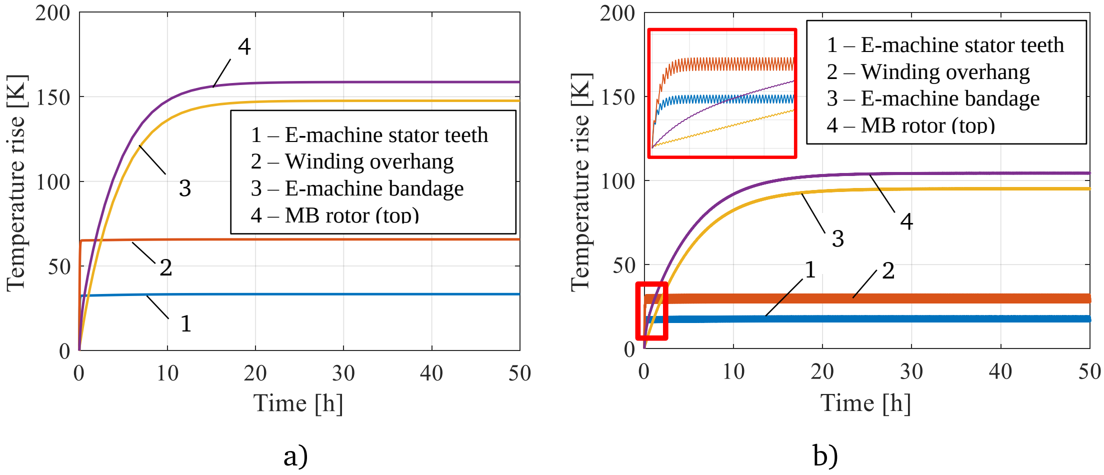

a)

b)

Fig. 10-11 Calculated transient temperature rises of the flywheel, black-painted rotor and black-painted stator: a) continuous operation at OP_2, b) operating with defined duty cycle in Fig. 10-10

Table 10-11 Calculated steady state temperature rises [K] in the flywheel system (model in Fig. 9-4) for continuous operation at OP_2 and duty cycle operation (in Fig. 10-10), calculated for both black-painted stator surface $\varepsilon_s = 0.95$ and rotor surface with $\varepsilon_r = 0.95$

Node	Name	Continuous	Duty cycle
1	PM machine housing	2.8	1.6
2	PM machine stator iron	12.9	7.2
3	PM machine stator teeth	33.4	18.1
4	Winding in slot	46.2	23.8
5	Winding overhang (top)	65.7	30.0
6	Winding overhang (bottom)	65.7	30.0
7	PM machine bandage	147.6	95.1
8	PM machine shaft	147.1	94.9
9	Flywheel body	100.5	68.8
10	Rotor of bottom MB	106.4	73.0
11	Rotor of top MB	158.7	104.4
12	Stator of bottom MB	16.8	13.8
13	Stator of top MB	4.4	3.2
14	Flywheel housing	9.4	6.8

10.5 Short Circuit Performance

The magnet used in this machine is Sm_2Co_{17} with the demagnetizing curve shown in Fig. 6-21. The demagnetizing curve has no obvious “knee” point at the temperature of 150 °C, but almost a linear curve. Assuming 3 % of remanence loss is acceptable, the demagnetizing field strength should be lower than 1177 kA/m.

The three phase short circuit calculation is performed in *JMAG* and the results are shown in Table 10-12. For the initial condition of no load, the peak phase current is 2065 A. The maximum demagnetizing field in magnets is 845.0 kA/m, which is lower than 1177 kA/m. Three phase short circuit leads to no irreversible demagnetization in magnets at 150 °C.

Table 10-12 Calculated demagnetization for three phase sudden short circuit at 24000 min^{-1}, 150 °C, calculated in *JMAG*, initial condition: No load

Parameter	Symbol	No load
Induced voltage	$\hat{U}_\mathrm{p}$	524.4 V
Max. sudden short circuit current	$\hat{I}_\mathrm{sc,\,pk}$	2065 A
Demagnetizing field in magnets	$\lvert H_\mathrm{sc,\,max} \rvert$	845.0 kA/m
Max. sudden short circuit torque	$M_\mathrm{sc,\,max}$	-487.3 Nm

11. Critical Considerations of Light-weight Rotor Design with Composite Material

11.1 Composite Material

As described by (1-2), lighter materials with high strength are preferred for a flywheel rotor to obtain higher specific energy. Widely used materials are fiber reinforced composite materials with their strength and density shown in Table 1-5. In this chapter, two composite materials composed with carbon fiber filament Toray T700 and Toray M46 are chosen and used as examples to introduce the design criteria of the light-weight rotors. The material properties will be introduced first. Based on that, the design criteria will be discussed followed by a few examples. As an outlook for the future, the aim of this chapter is to point out the feasibility and basic design constraints and criteria, instead of obtaining an optimum design.

11.1.1 Orthotropic Property

The fiber reinforced composite materials are composed of fiber filaments and matrix. The material property depend on the portion of fiber volume V_{fiber} in the composite, defined by

$$\varphi = \frac{V_{\text{fiber}}}{V_{\text{composite}}} \,. \tag{11-1}$$

Table 11-1 shows the properties of the used materials. Different from metal materials, the composite material shows anisotropic properties, that the strength, modulus and thermal properties are fiber oriented. The fiber has higher strength and stiffness than the matrix. For the flywheel rotor, where a high tangential stress is critical, the fiber is oriented in the circumferential direction to obtain a high circumferential strength. A small shifting angle may be applied in order to increase the strength in axial direction. The presented material M46 has slightly lower tensile strength than T700, but a higher modulus.

Table 11-1 Properties of the chosen composite materials $\varphi = 0.6$
($\parallel$: parallel direction of fibers, $\perp$: transversal direction of fibers)

		T700+Epoxy resin	M46+Epoxy resin
Mass density	ρ [kg/m^3]	1550	1600
Young's modulus	$E_{\parallel}$ [MPa]	125000	245000
	$E_{\perp}$ [MPa]	7800	6900
Shear modulus	$G_{\perp\parallel}$ [MPa]	4400	3900
	$G_{\perp\perp}$ [MPa]	5330	-
Poisson's ratio	$\nu_{\perp\parallel}$	0.34	0.34
	$\nu_{\parallel\perp}$	0.021	0.021
	$\nu_{\perp\perp}$	0.35	0.35
Tensile strength	$R_{\parallel}^{+}$ [MPa]	2450	2160
	$R_{\perp}^{+}$ [MPa]	70	45
Compressive strength	$R_{\parallel}^{-}$ [MPa]	1570	980
	$R_{\perp}^{-}$ [MPa]	170	135
Shear strength	$R_{\perp\parallel}$ [MPa]	98	59
Thermal expansion coefficient	$\alpha_{\parallel}$ [10^{-6}/K]	0.4	-0.7
	$\alpha_{\perp}$ [10^{-6}/K]	36.1	35.5

11.1.2 Failure Criteria

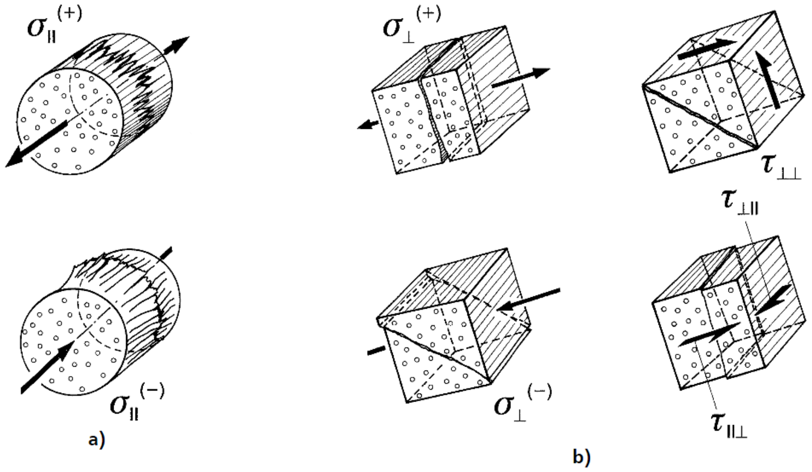

Fig. 11-1 Composite failure: a) fiber fracture due to tensile stress and compressive stress along fiber direction, b) delamination and fiber pull-out due to tensile and compressive stress in the perpendicular direction and due to shear stress [54, 72] (σ: normal stress, τ: shear stress, $\parallel$: parallel direction of fibers, $\perp$: transversal direction of fibers, + denotes tension, - denotes compression)

According to [72], the failure of the composite is distinguished by fiber fracture and matrix fracture, as shown in Fig. 11-1. The fiber fracture occurs if the stress along the fiber $\sigma_{\parallel}^{\pm}$ is higher than the material strength $R_{\parallel}^{\pm}$ for both tensile and compressive conditions, expressed by

$$\begin{cases} \sigma_{\parallel}^{+} / R_{\parallel}^{+} \geq 1, \text{ for tension} \\ \left|\sigma_{\parallel}^{-}\right| / R_{\parallel}^{-} \geq 1, \text{ for compression} \end{cases} . \tag{11-2}$$

The matrix fracture is characterized by delamination and fiber pull-out (Fig. 11-1). Delamination means the separation occurs between fiber layers. If the fiber is separated from the matrix, it is called fiber pull-out. The combination of the nominal stress $\sigma_{\perp}^{\pm}$ and shear stress τ may lead to this fracture. Many failure criterions are proposed by, e.g. *Hashin-Rotem*[73], *Hoffmann* [72], *Puck* [72]. As in our case, the filaments are wound along circumferential direction of the rotor, the composite rim has an axisymmetric structure. The centrifugal load is also axisymmetric. Therefore, theoretically no shear stress will occur at constant speed rotation. Therefore, a more simplified failure criteria can be used, described by

$$\begin{cases} \sigma_{\perp}^{+} / R_{\perp}^{+} \geq 1, \text{ for tension} \\ \left|\sigma_{\perp}^{-}\right| / R_{\perp}^{-} \geq 1, \text{ for compression} \end{cases} . \tag{11-3}$$

This criteria is a simple and direct way to predict the composites failure and is only valid when the shear stress can be neglected.

11.1.3 Stress due to Rotation

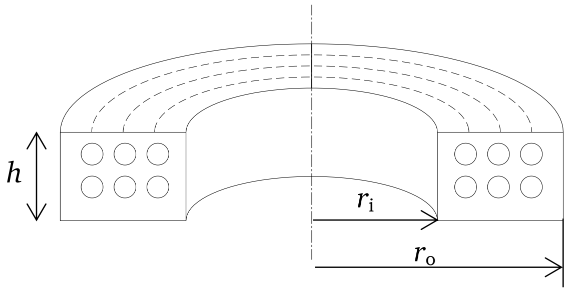

Fig. 11-2 Composite rim dimensions (r_i: inner radius, r_o: outer radius, h: axial length)

Assuming a composite rim with the inner radius r_i and outer radius r_o in Fig. 11-2, the stress caused by rotating centrifugal force σ_t, σ_r and displacement u_r can be calculated by formulas in Table C-4 and can be rewritten as

$$\sigma_{\mathrm{t}} = \rho \cdot (2 \cdot \pi \cdot n)^2 \cdot r_{\mathrm{o}}^2 \cdot \frac{3+\tilde{\nu}_{\parallel\perp}}{9-E_{\mathrm{v}}^2} \cdot \left[E_{\mathrm{v}} \cdot L \cdot \left(\frac{r}{r_{\mathrm{o}}}\right)^{E_{\mathrm{v}}-1} + E_{\mathrm{v}} \cdot (L-1) \cdot \left(\frac{r}{r_{\mathrm{o}}}\right)^{-E_{\mathrm{v}}-1} - \frac{E_{\mathrm{v}}^2 + 3 \cdot \tilde{\nu}_{\parallel\perp}}{3+\tilde{\nu}_{\parallel\perp}} \cdot \left(\frac{r}{r_{\mathrm{o}}}\right)^2 \right], \tag{11-4}$$

$$\sigma_{\mathrm{r}} = \rho \cdot (2 \cdot \pi \cdot n)^2 \cdot r_{\mathrm{o}}^2 \cdot \frac{3+\tilde{\nu}_{\parallel\perp}}{9-E_{\mathrm{v}}^2} \cdot \left[L \cdot \left(\frac{r}{r_{\mathrm{o}}}\right)^{E_{\mathrm{v}}-1} - (L-1) \cdot \left(\frac{r}{r_{\mathrm{o}}}\right)^{-E_{\mathrm{v}}-1} - \left(\frac{r}{r_{\mathrm{o}}}\right)^2 \right], \tag{11-5}$$

$$u_{\mathrm{r}} = \left[\frac{\sigma_{\mathrm{t}}}{\tilde{E}_{\parallel}} - \frac{\tilde{\nu}_{\parallel\perp} \cdot \sigma_{\mathrm{r}}}{\tilde{E}_{\perp}} \right] \cdot r\,, \tag{11-6}$$

where

r: arbitrary radial position on the rim, $r_{\mathrm{i}} \le r \le r_{\mathrm{o}}$.

ρ : material mass density in kg/m^3.

$\tilde{\nu}_{\parallel\perp}$: *Poisson*'s ratio, see Appendix C.

$E_{\mathrm{v}} = \sqrt{\dfrac{\tilde{E}_{\parallel}}{\tilde{E}_{\perp}}}$, $\tilde{E}_{\parallel}$, $\tilde{E}_{\perp}$: *Young*'s modulus in tangential and radial direction, see Appendix C.

$L = \dfrac{\alpha^{-E_{\mathrm{v}}-1} - \alpha^2}{\alpha^{-E_{\mathrm{v}}-1} - \alpha^{E_{\mathrm{v}}-1}}$, α: the ratio of inner radius and outer radius $\alpha = \dfrac{r_{\mathrm{i}}}{r_{\mathrm{o}}}$.

The specific stress is defined by

$$H(\alpha, r/r_{\mathrm{o}}) = \frac{\sigma_{\mathrm{t}}}{\rho \cdot (2 \cdot \pi \cdot n)^2 \cdot r_{\mathrm{o}}^2} = \frac{3+\tilde{\nu}_{\parallel\perp}}{9-E_{\mathrm{v}}^2} \cdot \left[E_{\mathrm{v}} \cdot L \cdot \left(\frac{r}{r_{\mathrm{o}}}\right)^{E_{\mathrm{v}}-1} + E_{\mathrm{v}} \cdot (L-1) \cdot \left(\frac{r}{r_{\mathrm{o}}}\right)^{-E_{\mathrm{v}}-1} - \frac{E_{\mathrm{v}}^2 + 3 \cdot \tilde{\nu}_{\parallel\perp}}{3+\tilde{\nu}_{\parallel\perp}} \cdot \left(\frac{r}{r_{\mathrm{o}}}\right)^2 \right], \tag{11-7}$$

$$R(\alpha, r/r_{\mathrm{o}}) = \frac{\sigma_{\mathrm{r}}}{\rho \cdot (2 \cdot \pi \cdot n)^2 \cdot r_{\mathrm{o}}^2} = \frac{3+\tilde{\nu}_{\parallel\perp}}{9-E_{\mathrm{v}}^2} \cdot \left[L \cdot \left(\frac{r}{r_{\mathrm{o}}}\right)^{E_{\mathrm{v}}-1} - (L-1) \cdot \left(\frac{r}{r_{\mathrm{o}}}\right)^{-E_{\mathrm{v}}-1} - \left(\frac{r}{r_{\mathrm{o}}}\right)^2 \right]. \tag{11-8}$$

By defining the tip velocity (in m/s) at outer radius by

$$v_{\mathrm{R}} = 2 \cdot \pi \cdot n \cdot r_{\mathrm{o}}\,. \tag{11-9}$$

The stress in the rim can be simplified and written by

$$\sigma_{\mathrm{t}} = \rho \cdot v_{\mathrm{R}}^2 \cdot H(\alpha, r/r_{\mathrm{o}}), \tag{11-10}$$

$$\sigma_{\mathrm{r}} = \rho \cdot v_{\mathrm{R}}^2 \cdot R(\alpha, r/r_{\mathrm{o}}). \tag{11-11}$$

Take the composite material with carbon fiber Toray T700 for example, as the specific stress is a function of α and r/r_{o}, the stress distribution in a rim for different α can be plotted in Fig. 11-3. The maximum radial stress occurs in the middle area of the rim. The maximum tangential stress occurs in the middle for a thick rim (small α) and occurs on the inner surface for a thin rim (higher α).

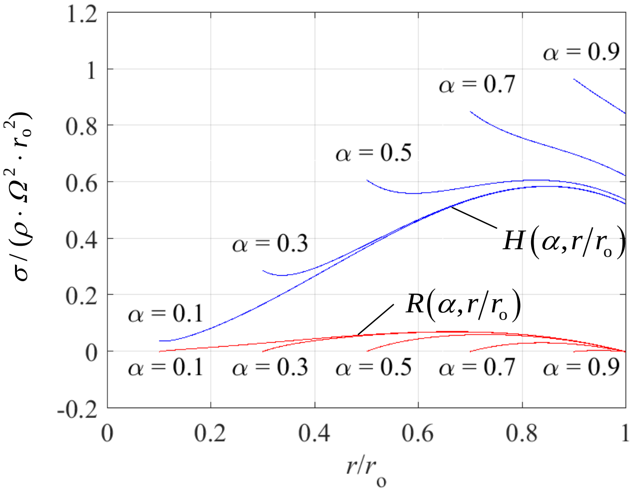

Fig. 11-3 Calculated specific stress distribution in a single rim for material T700 (r_o: outer radius, $\alpha = r_i/r_o$, r_i: inner radius, ρ: density, Ω: angular rotational speed, $\Omega = 2 \cdot \pi \cdot n$)

As can be seen from Fig. 11-3 that the maximum specific stress is a function only depending on α, which is written as $H_{max}(\alpha)$ and $R_{max}(\alpha)$ and are plotted in Fig. 11-4. This diagram can be used to determine the maximum stress in a rotating rim for certain α and certain velocity v_R by using

$$\sigma_{t,max} = \rho \cdot v_R^2 \cdot H_{max}(\alpha), \tag{11-12}$$

$$\sigma_{r,max} = \rho \cdot v_R^2 \cdot R_{max}(\alpha). \tag{11-13}$$

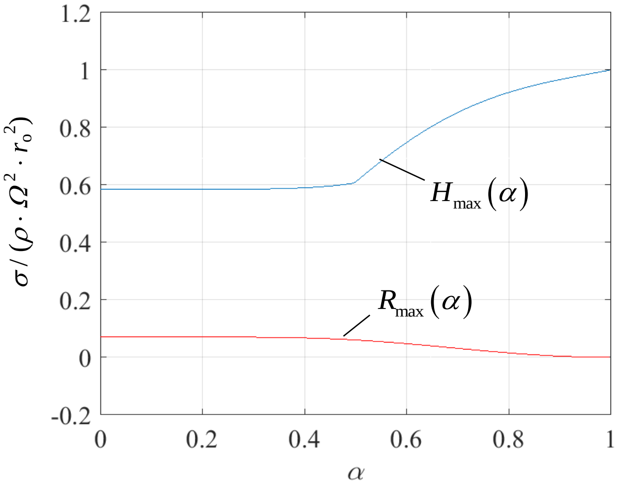

Fig. 11-4 Calculated maximum specific stress $H_{max}(\alpha)$ and $R_{max}(\alpha)$ for material T700

11.2 Single Rim Design

11.2.1 Energy Capacity and Specific Energy per Mass

The energy stored in the assumed rim can be calculated by

$$E=\frac{1}{2}\cdot J\cdot \Omega^2=\frac{1}{4}\cdot m\cdot(1+\alpha^2)\cdot r_o^2\cdot \Omega^2=\frac{1}{4}\cdot m\cdot(1+\alpha^2)\cdot v_R^2. \tag{11-14}$$

Thus, the specific energy per mass can be written by

$$\frac{E}{m}=\frac{1}{4}\cdot(1+\alpha^2)\cdot v_R^2. \tag{11-15}$$

The specific energy depends only on α and tip velocity v_R. In order to obtain high specific energy, a high v_R is always expected. However, high v_R leads to high stress which is limited by the material strength.

11.2.2 Material Strength Constraints and Maximum Tip Velocity

Using the maximum stress failure criteria, the stress constraints are defined by

$$\sigma_{\mathrm{t,max}}\le R_{\parallel}^{+}/k_{\mathrm{sf}}, \tag{11-16}$$

$$\sigma_{\mathrm{r,max}}\le R_{\perp}^{+}/k_{\mathrm{sf}}, \tag{11-17}$$

where k_sf is the safety factor.

Substituting (11-12) and (11-13) into (11-16) and (11-17), one can obtain (11-18) and (11-19), which give the maximum permitted velocity $v_{\mathrm{R,t}}(\alpha)$ limited by the stress in tangential direction and $v_{\mathrm{R,r}}(\alpha)$ limited by the stress in radial direction. The permitted velocity should be lower than both limitations.

$$v_{\mathrm{R,t}}(\alpha)\le\sqrt{\frac{R_{\parallel}^{+}/k_{\mathrm{sf}}}{\rho\cdot H_{\max}(\alpha)}} \tag{11-18}$$

$$v_{\mathrm{R,r}}(\alpha)\le\sqrt{\frac{R_{\perp}^{+}/k_{\mathrm{sf}}}{\rho\cdot R_{\max}(\alpha)}} \tag{11-19}$$

$$v_{\mathrm{R}}(\alpha)\le\min\left\{v_{\mathrm{R,t}}(\alpha),v_{\mathrm{R,r}}(\alpha)\right\} \tag{11-20}$$

For the chosen material T700 and with the maximum specific strength in Fig. 11-4 and a safety factor $k_\mathrm{sf}=2$, the velocity limitations and feasible values are calculated and shown in Fig. 11-5. For a thick rim (small α) the velocity is limited by radial stress and for a thin rim (big α) it is limited by tangential stress. The feasible velocity is the common area under these two boundary lines. The maximum available v_R is the intersection of these two boundary lines which is 947 m/s. At this velocity, the stress reaches the maximum allowed value simultaneously in both tangential and radial direction, indicating a fully utilization of the material strength.

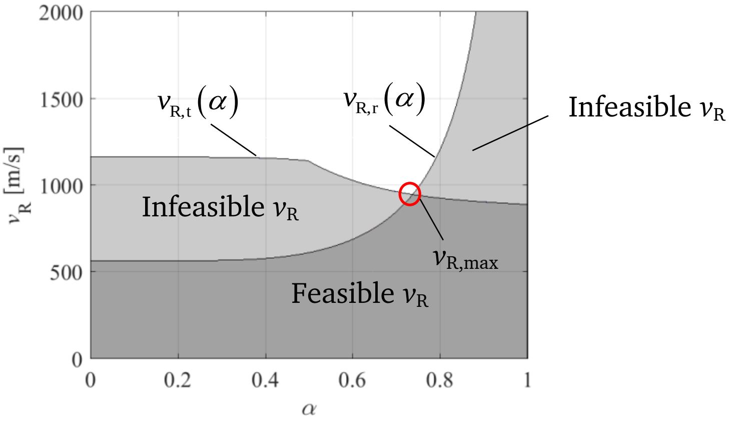

Fig. 11-5 Calculated velocity limitations of material T700 calculated by (11-18) and (11-19)

11.2.3 Specific Energy and Energy Density per Volume

The specific energy is calculated by (11-15). The overall volume of the rim is defined by

$$V_o = \pi \cdot r_o^2 \cdot h. \tag{11-21}$$

The mass is calculated by

$$m = \rho \cdot \pi \cdot (r_o^2 - r_i^2) \cdot h = \rho \cdot \pi \cdot (1-\alpha^2) \cdot r_o^2 \cdot h = \rho \cdot (1-\alpha^2) \cdot V_o. \tag{11-22}$$

By substituting (11-22) into (11-15), one can obtain the energy density per volume

$$\frac{E}{V_o} = \frac{1}{4} \cdot \rho \cdot (1-\alpha^4) \cdot v_R^2. \tag{11-23}$$

The specific energy and energy density are plotted in Fig. 11-6. A high specific energy can be obtained for a thin rim with $\alpha > 0.74$, meeting the tangential strength boundary. However, higher α leads to a decreasing energy density, which means a bigger overall volume. An optimum design point (α_{opt}, $v_{R,opt}$) can be determined to be the intersection of the two velocity boundaries, where the maximum E/V_o and high E/m are obtained.

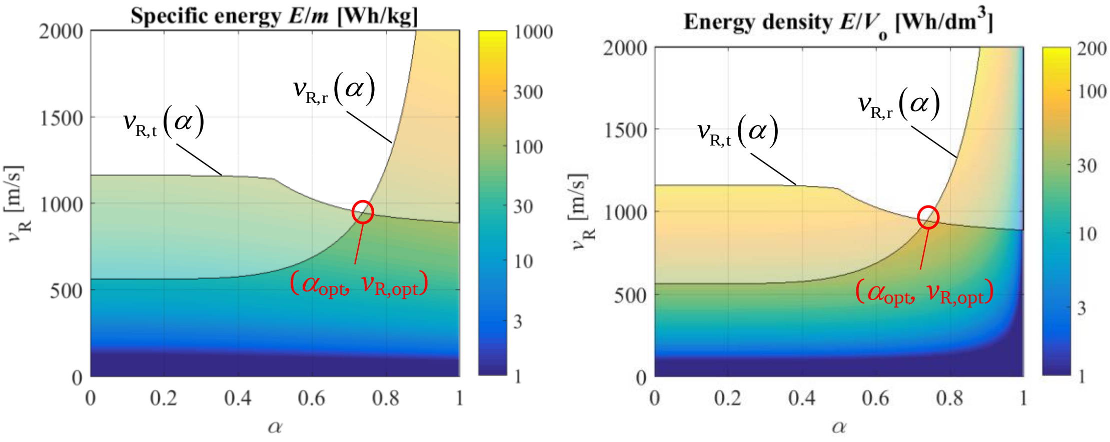

a) b)

Fig. 11-6 Calculated specific energy and energy density of the rim with material T700: a) specific energy in Wh/kg, b) energy density in Wh/dm^3

Table 11-2 Calculated optimum parameters of the chosen materials

	α_{opt}	$v_{\mathrm{R,opt}}$ [m/s]	$(E/m)_{\mathrm{opt}}$ [Wh/kg]	$(E/V_{\mathrm{o}})_{\mathrm{opt}}$ [Wh/dm^3]
T700	0.737	947	95.9	67.9
M46J	0.769	880	85.5	56.0

11.2.4 Single Rim Dimensioning

After obtaining the feasible velocity region, one can choose α and velocity v_{R} from Fig. 11-5 and then a single rim rotor can be dimensioned. For a given energy capacity E, by using Fig. 11-6, the mass m and the overall volume V_{o} can be determined and also can be calculated by

$$m = \frac{E}{\frac{1}{4}\cdot(1+\alpha^2)\cdot v_{\mathrm{R}}^2}, \tag{11-24}$$

$$V_{\mathrm{o}} = \frac{E}{\frac{1}{4}\cdot\rho\cdot(1-\alpha^4)\cdot v_{\mathrm{R}}^2}. \tag{11-25}$$

The outer radius r_{o} can be determined by (11-26) with the chosen velocity v_{R} and the given speed n_{max}. The height h can be determined by (11-27). The inner radius r_{i} can be calculated from the definition of α. Thus the dimensions of the single rim are determined.

$$r_{\mathrm{o}} = \frac{v_{\mathrm{R}}}{2\cdot\pi\cdot n_{\mathrm{max}}} \tag{11-26}$$

$$h = \frac{m}{\rho \cdot \pi \cdot (1-\alpha^2) \cdot r_o^2} = \frac{V_o}{\pi \cdot r_o^2} \tag{11-27}$$

Following the methodology above, a single rim rotor is dimensioned for the energy capacity of 0.5 kWh and maximum rotational speed 24000 min^{-1} and shown in Table 11-3. Different α and velocities are chosen and compared.

Table 11-3 Design of a single rim rotor with composite material T700

	Rim I	Rim II	Rim III	Rim IV
E [kWh]	0.5	0.5	0.5	0.5
n_{max} [min^{-1}]	24000	24000	24000	24000
J [kgm^2]	0.57	0.57	0.57	0.57
α	0.300	0.500	0.738 (optimum)	0.900
v_{R} [m/s]	568	612	947(optimum)	904
r_{o} [mm]	226	243	377	360
r_{i} [mm]	68	122	278	324
h [mm]	90.7	71.1	16.5	40.6
m [kg]	20.5	15.4	5.2	4.9
V_{o} [dm^3]	14.5	13.2	7.4	16.5
E/m [Wh/kg]	24.4	32.5	96.1	102.8
E/V_{o} [$\mathrm{Wh/dm}^3$]	34.4	37.8	67.9	30.3

The axisymmetric cross section of the rotor geometries are drawn in Fig. 11-7. The rim cross section is represented by filled gray color. As can be seen, Rim III has the maximum diameter and minimum volume by using the optimum parameters. Comparing Rim I, II and III, as the outer diameter increases (indicating velocity v_{R} increases) and the rim becomes thinner (α increases), the required axial length becomes smaller in order to obtain a constant inertia. The total mass or volume of the rim decreases from Rim I to Rim III, verifying the plot of the specific energy in Fig. 11-6 a). Comparing Rim III and Rim IV, the velocity and outer diameter are similar. As the value of α is bigger for Rim IV, the axial length should be increased, in order to obtain a constant inertia. Therefore, Rim IV has a lower energy density than Rim III, which also explains the plot of the energy density in Fig. 11-6 b).

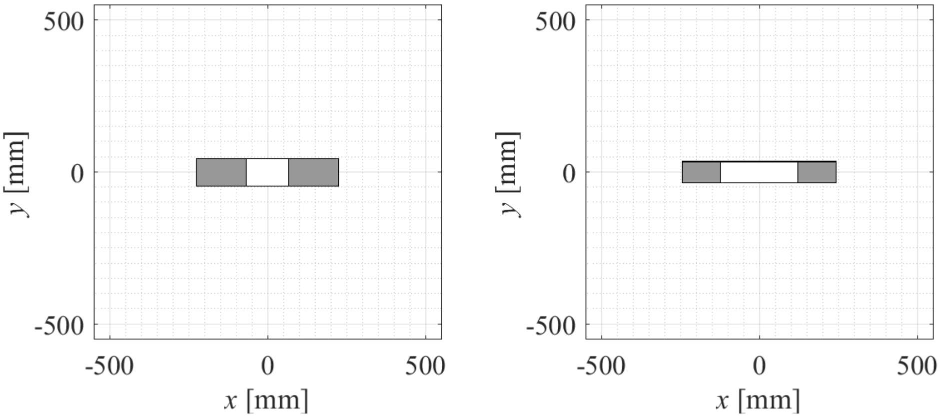

Rim I: $\alpha = 0.3$, $v_R = 568$ m/s   Rim II: $\alpha = 0.5$, $v_R = 612$ m/s

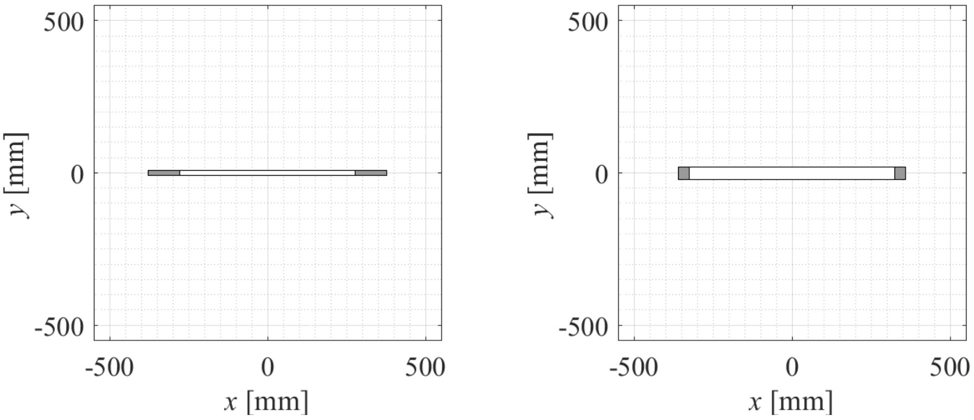

Rim III: $\alpha = 0.738$, $v_R = 947$ m/s   Rim IV: $\alpha = 0.9$, $v_R = 904$ m/s

Fig. 11-7 Rim dimensions shown in *x*-*y* plane for the design in Table 11-3 for the energy capacity of 0.5 kWh and maximum speed 24000 min^{-1} (filled color representing cross section of the rim)

One should also note that, even though Rim III has the optimum combination of velocity and α, the height of rim III is too small due to the small energy capacity. The stiffness in y-direction of this geometry is very low and may suffer from flexural deformation. That is saying, choosing the optimum velocity cannot guarantee an optimum shape. For example, if the energy capacity is increased to 5 kWh instead of 0.5 kWh, the dimensions in Fig. 11-8 will be obtained. Therefore, other constraints (such as rotor eigen-frequency) should also be taken into account to determine the final dimensions.

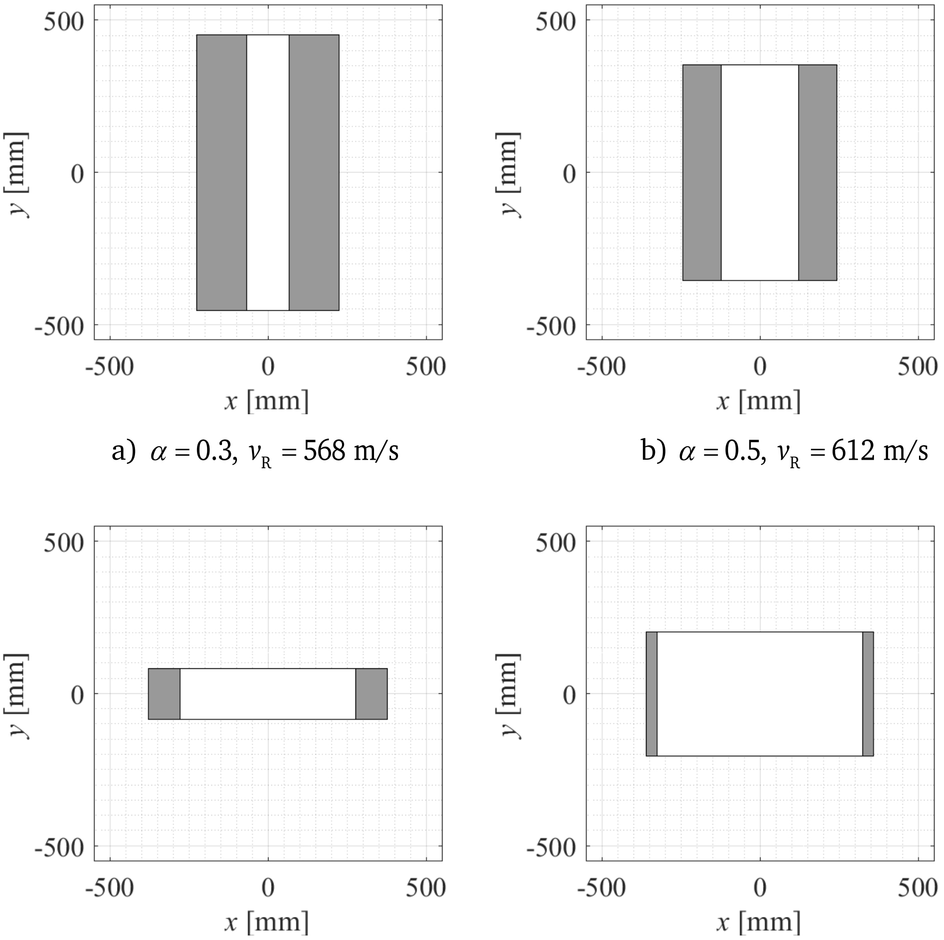

a) $\alpha = 0.3$, $v_\mathrm{R} = 568$ m/s

b) $\alpha = 0.5$, $v_\mathrm{R} = 612$ m/s

c) $\alpha = 0.738$, $v_\mathrm{R} = 947$ m/s

d) $\alpha = 0.9$, $v_\mathrm{R} = 904$ m/s

Fig. 11-8 Rim dimensions shown in *x-y* plane for the design in Table 11-3 for the energy capacity of 5 kWh and maximum speed 24000 min^{-1} (filled color representing cross section of the rim)

11.3 Multi-Rim Design

The *E/m* is limited by the stress in rim as shown in Fig. 11-6. Even though the stress in radial direction is smaller than tangential direction, due to the low material strength in radial direction, the radial stress becomes critical for $\alpha < \alpha_\mathrm{opt}$ (i.e. a thick rim) and limits the rotor velocity as well as the specific energy. One approach to reduce the radial stress is to use multi-rims with smaller thickness instead of one thick single rim. These rims are assembled with interference fittings, thus a radial compressive pressure is acting on each contact surface at standstill, i.e. the rims are pre-loaded with compressive stress. This compressive stress has a counteracting effect against the tensile stress at rotational state, thus the total stress in the rim can be reduced. Fig. 11-9 shows the specific stress distribution in one single rim compared to a two-layer rim at rotational state for $\alpha = 0.6$, $v_R = 689$ m/s. The two-layer rim is assembled with an interference fitting of 0.64 mm, leading to a contact pressure of 34.8 MPa and two rims pre-loaded with compressive stress in radial direction. At rotational state, as expected, the specific radial stress is reduced from 0.047 to 0.015 (by approx. 67.4 %). This means the rotational speed can be further increased from 689 m/s to 1220 m/s (by 77 %) according to (11-19). However, it should be noted that in tangential direction, due to the contact pressure, the maximum specific tensile stress is increased from 0.75 to 0.92 for the two-layer rim, which causes the maximum allowed velocity decreasing from 1026 m/s to 925 m/s according to (11-18). Therefore, the tangential stress becomes critical in the two-layer rim, which determines the maximum velocity. Nevertheless, the two-layer rim can achieve higher maximum velocity up to 925 m/s compared 689 m/s in a single rim. Thus a higher specific energy E/m can be obtained by using a two-layer rim.

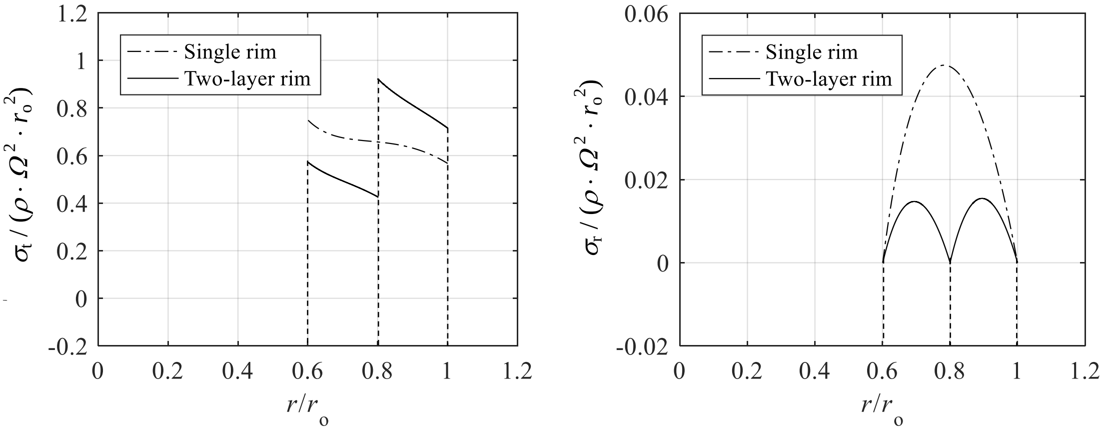

a) b)

Fig. 11-9 Calculated specific stress due to rotation in one single rim and two-layer rim: a) tangential direction, b) radial direction

For a better understanding of the effect by using a two-layer rim, Fig. 11-10 shows the comparison of the specific energy E/m and energy density E/V_o for a single rim and two-layer rim. As stated above, the velocity limitations determine E/m and E/V_o, represented by a feasible region in Fig. 11-6. By using two-layer rim, the velocity limitation due to radial stress is increased, while the limitation due to tangential stress is decreased, as shown in Fig. 11-10. Thus a new feasible region is formed. Compared to single rim, the new feasible region can achieve higher specific energy E/m and energy density E/V_o. Therefore, multi-rim is often used in the flywheel rotor design.

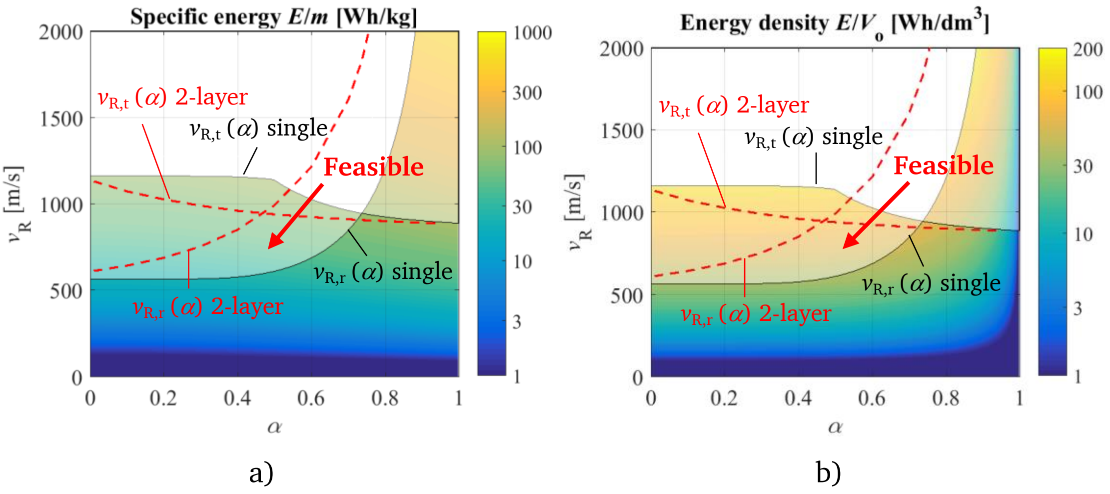

Fig. 11-10 Calculated specific energy and energy density for single rim and two-layer rim with material T700, showing the changed velocity limitations: a) specific energy in Wh/kg, b) energy density in Wh/dm^3

11.4 Rim Connected to Shaft

11.4.1 Assembly with a Flexible Hub

For an outer rotor design such as in [17], where the rim is not connected to a shaft, it can be dimensioned with more degrees of freedom. If the rim is required to be connected to a shaft, more constraints should be taken into account.

A hub is usually used to connect a component with a big diameter to a small-diameter shaft. Due to the low stiffness and big dimension of the composite rim, high speed rotation causes large deformation and displacement on the inner surface. The hub should also be flexible in order to compensate this deformation for a valid connection.

The displacements of the designed rims in Table 11-3 are calculated by (11-6) and shown in Table 11-4. A scheme in Fig. 11-11 shows how the rim and shaft deform due to rotation and thermal expansion. Due to rotation, the radial displacement of the rim and shaft both increase. The rim has larger displacement than the shaft due to the low stiffness. For rim II which is relatively thick, the displacement on the inner surface $\Delta u_{\mathrm{i,rim}}$ is 0.346 mm at the speed 24000 min^{-1} and for a thin rim, e.g. rim III, it is as high as 2.73 mm. For a feasible connection, the hub should be able to compensate this displacement and also endurable to the tensile stress caused by the large strain or deformation. While at standstill, 150 °C, thermal expansion causes an enlarged outer surface of the shaft and a smaller inner surface of the rim. For rim II and rim III, the calculated displacements are -0.152 mm and -0.194 mm, respectively. This means the hub will be compressed and should be able to cope with this compressive stress. Therefore, a flexible hub which is radially elastic is required.

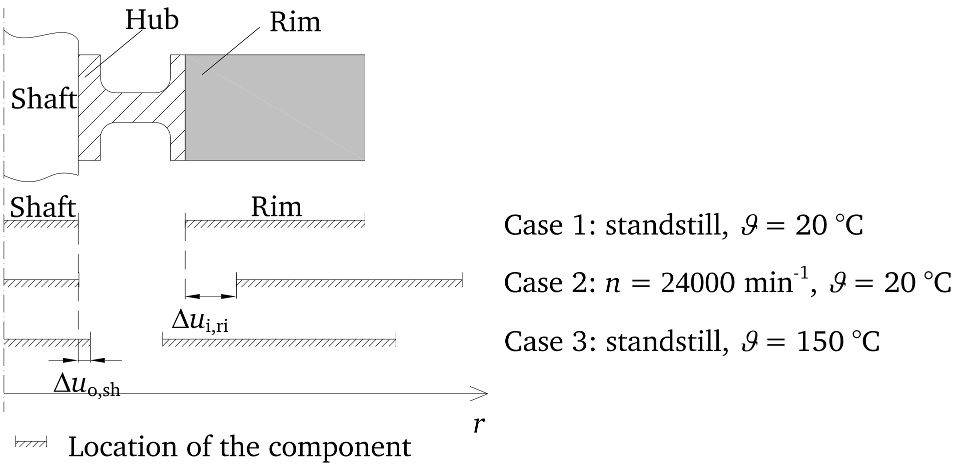

Fig. 11-11 Scheme of rotor showing displacement of the shaft and rim compared to standstill, 20 °C ($\Delta u_{o,sh}$: displacement of shaft outer surface, $\Delta u_{i,rim}$: displacement of rim inner surface)

Table 11-4 Calculated displacement of the designed rim in Table 11-3

<table>
<tr><td colspan="7">Shaft outer radius $r_{o,sh}$ = 50 mm. Material: steel 30CrNiMo8.
Dimension of rims are shown in Table 11-3. Material: T700</td></tr>
<tr><td colspan="2" rowspan="2">Condition</td><td rowspan="2">$\Delta u_{o,sh}$ [mm]</td><td colspan="4">$\Delta u_{i,rim}$ [mm]</td></tr>
<tr><td>Rim I</td><td>Rim II</td><td>Rim III</td><td>Rim IV</td></tr>
<tr><td>Case 1</td><td>Standstill, $\vartheta = 20$ °C</td><td>0</td><td>0</td><td>0</td><td>0</td><td>0</td></tr>
<tr><td>Case 2</td><td>$n = 24000\ \text{min}^{-1}$,
$\vartheta = 20$ °C</td><td>0.0051</td><td>0.0785</td><td>0.346</td><td>2.73</td><td>3.18</td></tr>
<tr><td>Case 3</td><td>Standstill, $\vartheta = 150$ °C</td><td>0.081</td><td>-0.101</td><td>-0.152</td><td>-0.194</td><td>-0.081</td></tr>
</table>

A flexible hub can be constructed into various structures. Here only two examples are given.

Fig. 11-12 shows the flexible hub made of carbon fiber reinforced plastic, which has lower stiffness than metalic materials. The maximum velocity of the inertia rim can reach 800 m/s. The critical aspect for this hub is that the low stiffness lowers the rotor eigen-frequency, which may cause vibration and resonance for bending and torsional loads.

Fig. 11-13 shows a split hub where the hub ring is split into 24 segments and welded to the shaft at the top and bottom joints. As decribed in [74], "*the hub with the leaves is press-fit to the rotor with a minimal amount of interference to be assembled to the rotor, which will minimize the stress concentration between the ring and the rotor. The inner shell* *hub and ring allow a rather flexible deformation of the composite rotor and a split ring that expands and presses against the inner surface of the composite rotor while spinning.*”

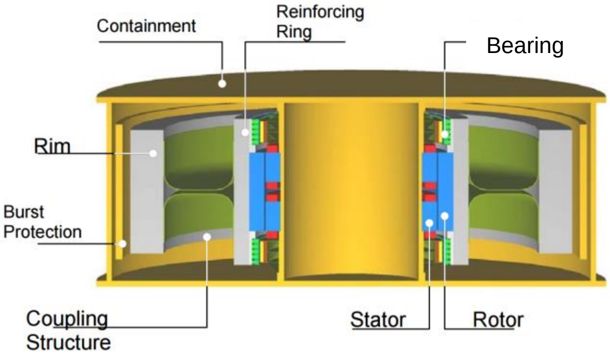

Fig. 11-12 Rotor structure of the 10 kWh flywheel with the power of 2 MW (levitated by a high temperature super-conducting magnetic bearing), entirely made of carbon fiber reinforced plastic except the machine and bearing components, velocity of the reinforcing ring 360 m/s, velocity of the inertia rim 800 m/s [35]

a) b)

Fig. 11-13 Split hub (aluminum 7075-T6) in order to increase the expansion in radial direction for an active contact with the rims (inner rim: E-glass fiber+epoxy, outer rim: graphite fiber T300+epoxy), usable stored energy 0.5 kWh, maximum speed 40000 min^{-1}, rim velocity 712 m/s, outer diameter 340 mm, height 138 mm [74]

11.4.2 Assembly without Hub

Another possibility is to directly mount the rim on the shaft without hub connection. In this case, α is usually small and multi-rims are usually used instead of one thick rim. The determination of the dimensions of such rotor has more degrees of freedom, such as the shaft diameter, the thickness and the material of each rim layer, as well as the number of layers. The critical consideration here is the interference fitting between each rim layer, for which the following aspects should be considered.

1) Rim Separation

Due to the tensile deformation of the rims at high rotational speed, the rim layers tend to separate from each other. The interference fitting should be able to ensure a successful connection of the rims.

As described in [39] for a rotor structure shown in Fig. 11-14, the rotor is built with 7 layer rims assembled on a titanium shaft by press fitting. The designed nominal speed is 40000 min^{-1}. The spin testing was performed and it revealed that (quoted from [39]): *the failure mode was not a hoop fiber burst, but a controllable loss of mass balance. The flywheel maintained excellent mass balance up to and past 36,000 rpm. At about 42,000 rpm, the flywheel began to show slight balance changes, which was expected, since some of the flywheel's internal rings had transitioned from radial compression to radial tension and had begun to physically separate. At about 47,500 rpm (1120 m/s), the flywheel showed a rapidly increasing mass balance shift due to further ring-to-ring and rim-to-metallic hub separation. Driving the test to higher speeds, at this point, would have resulted in increased vibrations leading to failure of the quill shaft that supported the flywheel during the test, thereby dropping the flywheel to the bottom of the spin test pit.*

Fig. 11-14 Flywheel rotor composed of 7-layer composite rim and titanium shaft, developed by *Center for Electromechanics, University of Texas at Austin, USA,* 2015, for onboard storage on a hybrid electric transit bus, with E = 1.93 kWh, v_R = 902 m/s, m = 58.2 kg, n_max = 40000 min^{-1}, r_o = 431 mm, h = 152 mm [39]

2) High Compressive Stress

In order to avoid losing contact, the interference fitting between each layer should be able to compensate the deformation at rotational state. If too many rim layers are assembled, a high compressive stress will occur on the inner layer rim at standstill, especially if the temperature increases.

Take the designed steel rotor for the demonstrator in previous chapters as an example. The steel rotor has an inertia of 0.57 kgm^2 and maximum rotational speed of

24000 min^{-1} with the dimensions shown in Table 11-5. The specific energy E/m is 7.6 Wh/kg. Now additional rims will be assembled on the outer surface of the shaft. The thickness of each rim is 40 mm, which has low manufacturing difficulties. The dimensions here are without any optimizations, just as an example for the illustration of the critical design limitations. As can be seen from Table 11-5, as the rim layer increases, the inertia and stored energy also increase. The tip velocity can be increased to 628.3m/s with 3-layer rims. The fittings between each layer are determined to ensure no separation will occur at the maximum rotational speed. As the outer rim has the largest deformation at high speed rotation, the fittings increases from the inner to outer contact surfaces. High modulus material (Rotor V with M46J) can be used to reduce the deformation, thus the required fittings are smaller.

Table 11-5 Design of different rotor structures

(Δu: interference fitting, shaft material: steel 30CrNiMo8)

Rotor	I	II	III	IV	V
Rim material	-	T700	T700	T700	M46J
	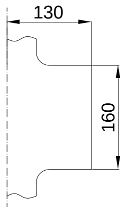	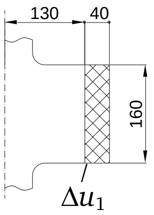	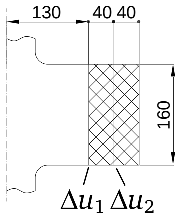	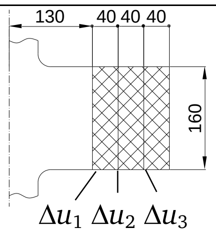	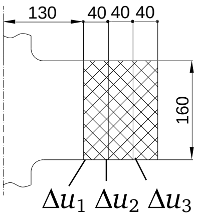
E [kWh]	0.5	0.68	1.06	1.75	1.78
n_{max} [min^{-1}]	24000	24000	24000	24000	24000
J [kgm^2]	0.57	0.77	1.21	1.99	2.02
m [kg]	65.9	75.4	87.6	102.5	103.1
v_{R} [m/s]	327	427	528	628.3	628
E/m [Wh/kg]	7.6	9.0	12.1	17.0	17.2
Δu [mm]	-	$\Delta u_1 = -0.19$	$\Delta u_1 = -0.18$ $\Delta u_2 = -0.295$	$\Delta u_1 = -0.18$ $\Delta u_2 = -0.29$ $\Delta u_3 = -0.46$	$\Delta u_1 = -0.05$ $\Delta u_2 = -0.15$ $\Delta u_3 = -0.23$

For the rotors in Table 11-5, the stresses for different operating conditions are calculated in Table 11-6. The stress distributions of rotor IV are plotted in Fig. 11-15 as an example. Compressive stress is denoted with negative values and tensile stress with positive ones. A positive value of the contact pressure indicates a good contact condition of two surfaces, while negative value indicates losing contact.

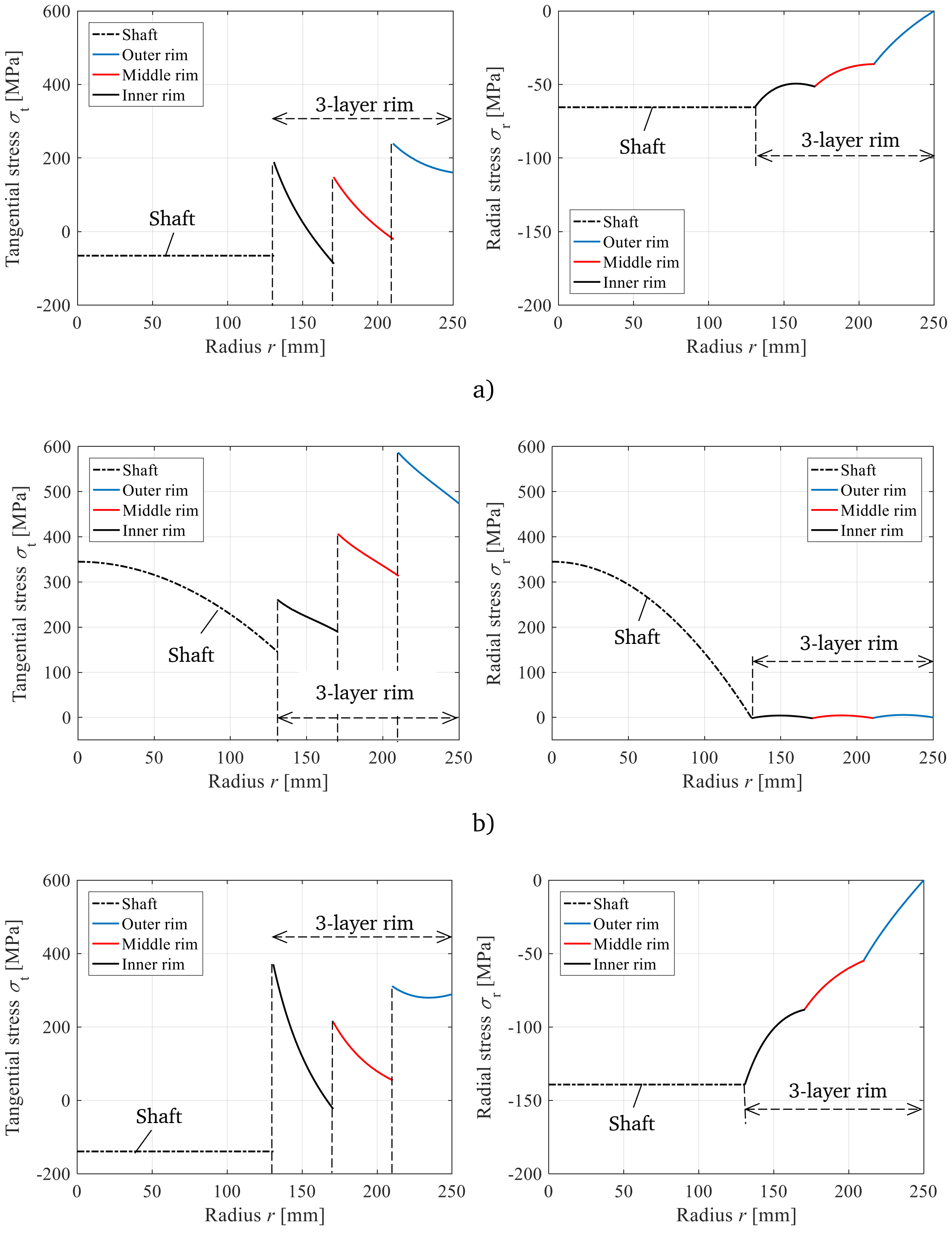

a)

b)

c)

Fig. 11-15 Analytically calculated stress in the designed rotor IV in Table 11-5 for operating conditions: a) Standstill, 20 °C, b) $n = n_{\max}$, 20 °C, c) Standstill, 150 °C

At standstill, 20 °C in Fig. 11-15 a), the stresses are caused by interference fitting. The rims and shaft are compressed with each other, therefore, the radial stress is negative. The tangential stress in the shaft is negative, as the shaft is compressed by the rim. The tangential stress in the rim behaves differently for different locations: for the area close to the inner surface it is tensile, while on the area close to the outer surface, it is compressive. The maximum tensile stress in tangential direction occurs on the outer rim which is $\sigma^{+}_{\mathrm{t,max}} = 239\ \mathrm{MPa}$. This value is far from critical compared to the material tangential strength of $R^{+}_{\parallel} = 2450\ \mathrm{MPa}$. The maximum radial stress occurs on the inner surface of the inner-most rim which is $\sigma^{-}_{\mathrm{r,max}} = -\ 65.1\ \mathrm{MPa}$. Compared to the compressive material strength of $R^{-}_{\perp} = 170\ \mathrm{MPa}$, a safety factor of 2.6 is reserved.

For the condition $n = n_{\max}$, 20 °C in Fig. 11-15 b), due to the centrifugal force, the stresses in tangential direction are all tensile. The maximum value occurs on the inner surface of the outer-most rim. which is $\sigma^{+}_{\mathrm{t,max}} = 586\ \mathrm{MPa}$. Compared to the material tangential strength of $R^{+}_{\parallel} = 2450\ \mathrm{MPa}$, a safety factor of 4.2 is reserved. In radial direction, as described earlier, the rims tend to separate from each other due to the deformation under the centrifugal force. The contact pressure between each layer decrease compared to the standstill and becomes zero if separation occurs. Therefore, the interference fitting should be designed to be larger than the deformation to obtain a valid connection. As seen from Table 11-6, with the designed fittings, the contact pressure at maximum rotational speed is 1.5 MPa, indicating a valid contact.

The condition standstill, 150 °C in Fig. 11-15 c), occurs occasionally e.g. when the rotor is decelerated to standstill and the temperature is still high. In this case, the critical stress is the compressive stress due to the thermal expansion and interference fitting of the rims. Each single rim tends to expand in both inner surface and outer surface, which increases the contact pressure on the two contact surfaces in addition to the interference fitting. The maximum radial stress is as high as $\sigma^{-}_{\mathrm{r,max}} = -138.9\ \mathrm{MPa}$ which is close to the compressive strength of $R^{-}_{\perp} = 170\ \mathrm{MPa}$.

The stress calculations are carried out for all the rotors in Table 11-5 and shown in Table 11-6. The stress distributions are similar to rotor IV. For increasing number of layers, an increasing compressive stress $\sigma^{-}_{\mathrm{r,max}}$ at standstill, 150 °C can be obtained, which may become a limitation for further increasing the number of layers. By using high modulus material (M46J in rotor V), required interference fitting can be reduced due to smaller deformation at rotational state. Therefore, a smaller compressive stress of $\sigma^{-}_{\mathrm{r,max}} = 110.6\ \mathrm{MPa}$ at static state, 150 °C can be obtained. However, compared to the material strength $R^{-}_{\perp} = 135\ \mathrm{MPa}$ for M46, this value is still critical.

Table 11-6 Calculated stress in rims and pressure on the contact surfaces for the rotors in Table 11-5 for different operating conditions

(σ_t: stress in tangential direction, σ_r: stress in radial direction, "+": tensile, "-": compressive, p: contact pressure, the subscripts correspond to the contact surfaces and fittings in Table 11-5)

Rotor		II	III	IV	V
Case 1: standstill, 20 °C	$\sigma_{t,\max}^{+}$ [MPa]	159	181	239	183
	$\sigma_{r,\max}^{+}$ [MPa]	-	-	-	-
	$\sigma_{r,\max}^{-}$ [MPa]	-31.4	-51.4	-65.1	-27.6
	P_1 [MPa]	31.4	51.4	65.1	24.2
	P_2 [MPa]	-	31.2	51.0	27.6
	P_3 [MPa]	-	-	36.0	23.9
Case 2: $n = n_{\max}$, 20 °C	$\sigma_{t,\max}^{+}$ [MPa]	267	407	586	597
	$\sigma_{r,\max}^{+}$ [MPa]	5.0	5.6	5.6	5.6
	$\sigma_{r,\max}^{-}$ [MPa]	-2.5	-1.5	-1.5	-2.1
	P_1 [MPa]	2.5	1.55	1.5	2.1
	P_2 [MPa]	-	1.24	1.5	2.0
	P_3 [MPa]	-	-	1.5	1.2
Case 3: standstill, 150 °C	$\sigma_{t,\max}^{+}$ [MPa]	326	332	370	441
	$\sigma_{r,\max}^{+}$ [MPa]	-	-	-	-
	$\sigma_{r,\max}^{-}$ [MPa]	-79.7	-117.9	-138.9	-110.6
	P_1 [MPa]	79.7	117.9	138.9	110.6
	P_2 [MPa]	-	57.4	87.7	64.4
	P_3 [MPa]	-	-	54.6	44.9

3) Assembly Feasibility

Take rotor IV in Table 11-5 as an example, the required fitting between the outer rim and middle rim is $\Delta u_3 = -0.46$ mm. Press fitting may cause huge stress concentration on the rims and leads to delamination in axial direction. One possibility for the assembly is by shrink fitting, for which the rims should be cooled down in order to reduce the fittings after shrinking. For the orthotropic materials of carbon fiber, when the temperature drops, the inner surface of the composite rim will enlarge while the outer surface will shrink. Therefore, the assembled components should be both cooled down. Assume the temperature of the components after cooling is -170 °C, which can be realized by nitrogen liquid (boiling temperature -195.79 °C) cooling method. The deformation of each individual component of rotor IV at temperature -170 °C before assembly is shown in Table 11-7 and Fig. 11-16. The displacements between each contact surface due to the low temperature are also presented in Fig. 11-16. Comparing these values with the designed fittings in Table 11-5, one can see that the outer rim and the middle rim will perform a press fitting as the deformation of 0.26 mm is smaller than the designed fitting of 0.46 mm (absolute value). For the other contact surfaces, the assembly with a clearance will be possible. If the rotor is composed of more layer rims, an even higher fitting is expected for the outer rims. Therefore, the assembly feasibility would be a limitation and should be taken into account.

Table 11-7 Calculated displacement Δu of the rotor components in rotor IV due to thermal expansion at temperature -170 °C before assembly

	Δu_i at inner surface [mm]	Δu_o at outer surface [mm]
Shaft	-	-0.309
Inner rim	+0.118	-0.13
Middle rim	+0.123	-0.133
Outer rim	+0.127	-0.134

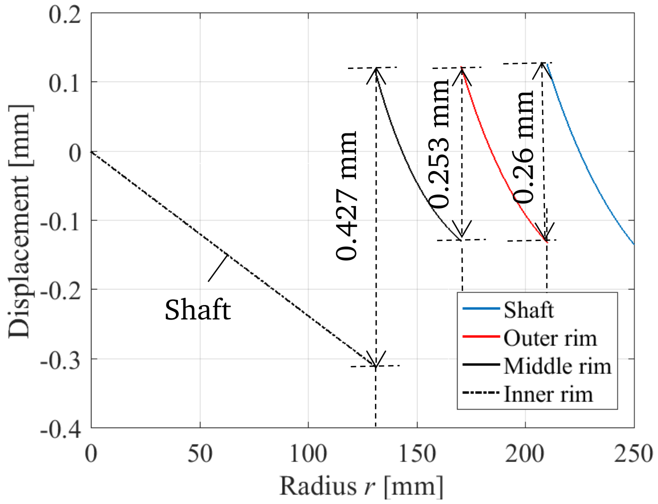

Fig. 11-16 Calculated displacement of the rotor components in rotor IV due to thermal expansion at the temperature of -170 °C before assembly

12. Conclusions and Outlook

This thesis presents the methodology and results for the energetic evaluation and design of a flywheel energy storage system (FESS).

The first purpose is to give a quantitative evaluation of the energetic performance of the systems equipped with flywheels. Two systems are chosen for the analysis: one 5 kWp (kWp: peak power) household PV system and one onboard tramway system. In both systems, the power flow models have been developed, including the loss models of the flywheel. Based on the given load and generation profiles, case studies are carried out and the energy saving potentials of each system are analyzed. The energetic efficiencies of the flywheel are evaluated regarding variable flywheel specifications. The results show that, by using a 3 kWh flywheel in the investigated PV system, 15.1 % extra energy saving can be achieved compared to a household without PV system or storage devices. But the overcall energy efficiency of the flywheel is only 40 % for the investigated one-year operating cycle. The main reason is the high self-discharge due to internal losses (7.7 % of the maximum stored energy per hour) and the long term idling operating cycle (for hours). For the second application in the tramway system, an energy saving potential of 20.9 % can be seen by using a 1.5 kWh onboard FESS with the power rating of 450 kW. Due to the frequent charge/discharge cycling (approx. 1 min), the utilization of the flywheel is much higher that an overall energy efficiency of 75.5 % can be obtained. Therefore, the flywheel is not suitable for long term storage for the used operating strategy in the investigated PV system. It is not comparable to the commercial chemical batteries regarding no matter the energetic performance or the costs. For the application in tramway system, the energy saving potential and energetic efficiency are both comparable to the commercial supercaps. But it still remains an open topic regarding the costs and lifetime. Nevertheless, for the current commercial available technologies, the flywheel gains more benefits in the short-term storage application.

Based on the specifications determined in the power flow analysis, a downsized flywheel demonstrator is designed and constructed for the energy storage capacity of 0.5 kWh and rated power of 28 kW. The design methodology is introduced in this thesis. Firstly, the mechanical design of the flywheel rotor is carried out for the maximum operating speed of 24000 min^{-1}. A method is proposed for the rotor body dimensioning based on the material properties and the inertia requirement. The rotor eigen-frequency is analyzed. The rotor construction issues, such as balancing solutions and rotor hardening process are discussed. The designed rotor has a mass of 90 kg, achieving a specific energy density of 5.6 Wh/kg with respect only to the rotor.

For the energy conversion, a 4-pole permanent magnet machine is designed according to the given design specifications and limits. The machine has a rotor structure with surface mounted magnets. A carbon fiber bandage is assembled on the outer surface of the magnets for protection. The stress in the rotor components is analyzed for the purpose to determine the bandage thickness and fittings. The magnets are segmented to reduce the eddy current losses. The losses in the designed machine are calculated by FEM program. An average efficiency of 96 % is obtained for the two designed operating points. Additionally, the influence of the design parameters (air gap length and magnet thickness) on the machine performances is discussed.

After the component design, the prototype set-up is presented. A valid assemble course is presented considering the complicated system structure and is verified by the prototyping. In addition, due to the safety consideration, two outer housings are designed as burst containments in case of the rotor structural failure.

After obtaining the complete system structure, a lumped parameter thermal network based on the radiative heat transfer is modeled for the system thermal performance analysis. The loss analysis is firstly carried out for the system components, including E-machine, magnetic bearings and the air friction losses of the rotor for the low pressure in vacuum. Two operating conditions are investigated: continuous operation and the operation with a fully-utilized duty cycle with continuous charge and discharge. The critical temperature is on the rotor due to the inefficient heat dissipation in vacuum. The results show that the designed system is sustainable for continuous operation with a thermal margin of 13.6 K, limited by the plastic transition temperature of the E-machine bandage. Black-painted on both rotor and stator is recommended, otherwise 38 K higher temperature rise will be obtained for the non-painted case. For the operation with the defined duty cycle, 14.4 K lower temperature rise can be expected compared to continuous operation, i.e. 28 K thermal margin to the thermal limit.

In the end of the thesis, two outlooks are given for future work:

One is the theoretical design of a PM machine with a full power of 150 kW which is supposed to be used for the onboard application. Due to the high power, high rotor losses are expected. The designed machine is not thermally endurable for continuous operation. The cycling operation is possible with 6 K safety thermal margin. Therefore, an optimized design or other feasible solutions to reduce the rotor losses are recommended.

The second outlook focuses on the discussion of the critical limitations and design criteria of light-weight rotors which are constructed with fiber reinforced composite materials in order to obtain higher specific energy. It is found out that, for the design of a rotor composed with a single rim, there exist an optimum velocity and optimum ratio of the inner radius to outer radius which lead to high specific energy and maximum energy density. Multi-rim design can reduce the radial stress due to rotation, which can further increase the velocity and specific energy compared to a thick rim. However, when considering the connection of the rim to the shaft, the fittings are critical and become a limitation for high velocities. Hub structural optimization and fitting designs should be the focus for an optimum design.

For the future work, the following aspects are proposed for further investigations:

1) Commission of the current prototype

The functioning of the current prototype is to be verified by a series of testing. The commission of the levitation system should be accomplished. The E-machine is supposed to be driven by an inverter in order to test the levitation system at rotational condition, as well as the electromagnetic performance of the E-machine. The insulation test in vacuum condition is also necessary. The component losses will be measured in order to verify the theoretical calculation. The temperature will be measured during the operation. Finally, the prototype is supposed to be driven with the defined operating cycle, in which the thermal performance and the overall energy performance will be investigated.

2) Rotor dynamics and vibration

The dynamic behavior of the rotor, especially with big inertia, is critical for high speed operation. Due to the manufacture and assemble tolerance, inevitable eccentricity occurs in the rotor which cause unbalanced force in the rotor. To compensate the unbalanced force and levitate the rotor successfully within the tolerant orbit, a fast respond magnetic bearing controller is required. The control parameters, such as stiffness and damping, should be properly determined. In addition, the vibrating and acoustic performance of the system should be also investigated.

3) Eddy current loss analysis in the PM machine

As the eddy current loss calculation in the E-machine rotor was performed by a 2D model in *JMAG*, with segmented magnets in circumferential direction. The effect of axial segmentation is considered by an equivalent electric conductivity. This equalization should be verified by a 3D calculation. Future work may focus on the discussion about the influence of the segmentation on the eddy current losses in the magnets as well as rotor back iron (laminated or solid). Preliminary work has been done in [81] by both analytical method and 3D simulation. But the investigation about axial segmentation is not clearly analyzed, for which further investigation is required.

4) Rotor structural optimization

A simple constant thickness steel rotor configuration is used in the prototype, which has low specific energy density. Higher specific energy density can be obtained by using high strength material, such as carbon fiber composite material. Therefore, a proper rotor configuration is required for a light weight rotor design, concerning both the mechanical strength and the assemble procedure. Widely used configuration is multi-rim combined with a flexible hub. Also, outer rotor configuration is attractive due to the high degree of integration. The design criteria and critical limitations are discussed in Chapter 11, but no feasible design is proposed. Future work can be carried out focusing on the structural design and optimization for different rotor configurations.

13. References

Literature

[1] G. Genta, *Kinetic energy storage : theory and practice of advanced flywheel systems* 1st. ed. London, UK & Boston, USA: Butterworths, 1985.

[2] S. M. Mousavi G, F. Faraji, A. Majazi, *et al.*, "A comprehensive review of Flywheel Energy Storage System technology," *Renewable and Sustainable Energy Reviews,* vol. 67, Jan., pp. 477-490, 2017.

[3] ABB, "PowerStore: Renewable microgrid stabilization," Brochure: 9AKK100580A2551 EN A4 12/12, 2012.

[4] H. Darrelmann, "Comparison of high power short time flywheel storage systems," in *Proc. 21st International Telecommunication Energy Conference (INTELEC 1999)*, Copenhagen, Denmark, 1999, Paper ID: 30-2, 8 pages.

[5] B. B. Plater and J. A. Andrews. Advances in Flywheel Energy-Storage Systems. *PowerPulse.Net* Available: http://www.darnell.com/NewsServices/PowerPulse/, 2001.

[6] R. Peña-Alzola, R. Sebastián, J. Quesada, *et al.*, "Review of flywheel based energy storage systems," in *Proc. 2011 International Conference on Power Engineering, Energy and Electrical Drives (POWERENG 2011)*, Malaga, Spain, 2011, pp. 589-594.

[7] S. Sabihuddin, E. A. Kiprakis and M. Mueller, "A Numerical and Graphical Review of Energy Storage Technologies," *Energies,* vol. 8, no. 1, pp. 172-216, 2015.

[8] M. E. Amiryar and K. R. Pullen, "A Review of Flywheel Energy Storage System Technologies and Their Applications," *Applied Sciences,* vol. 7, no. 3, p. 286, 2017.

[9] A. Chatzivasileiadi, E. Ampatzi and I. Knight, "Characteristics of electrical energy storage technologies and their applications in buildings," *Renewable and Sustainable Energy Reviews,* vol. 25, Sep., pp. 814-830, 2013.

[10] US Department of Energy Global Energy Storage Database. [Online]. Available: http://www.energystorageexchange.org/projects.

[11] N. Ghaviha, J. Campillo, M. Bohlin, *et al.*, "Review of Application of Energy Storage Devices in Railway Transportation," *Energy Procedia,* vol. 105, May, pp. 4561-4568, 2017.

[12] T. Ratniyomchai, S. Hillmansen and P. Tricoli, "Recent developments and applications of energy storage devices in electrified railways," *IET Electrical Systems in Transportation,* vol. 4, no. 1, pp. 9-20, 2014.

[13] R. Panek, P. Cahyna, R. Dejarnac, *et al.*, "Status of the COMPASS Tokamak Reinstallation in Institute of Plasma Physics AS CR," in *Proc. 36th European Physical Society Conference on Plasma Physics 2009 (EPS 2009)*, Sofia, Bulgaria, 2009, Europhysics Conference Abstracts (ECA), vol. 33 E, pp. 1403-1406.

[14] V. Babuska, S. M. Beatty, B. J. deBlonk, *et al.*, "A review of technology developments in flywheel attitude control and energy transmission systems," in *Proc. 2004 IEEE Aerospace Conference Proceedings*, Big sky, Montana, USA, 2004, vol. 4, pp. 2784-2800.

[15] T. D. Nguyen, K. Tseng, S. Zhang, *et al.*, "A Novel Axial Flux Permanent-Magnet Machine for Flywheel Energy Storage System: Design and Analysis," *IEEE Transactions on Industrial Electronics,* vol. 58, no. 9, pp. 3784-3794, 2011.

[16] Active Power,"CleanSource XT UPS," 2017, [Online]. Available: http://www.activepower.com/.

[17] L. Quurck, M. Richter, M. Schneider, *et al.*, "Design and practical Realization of an innovative Flywheel Concept for industrial Applications.," *Technische Mechanik,* vol. 37, no. 2-5, pp. 151-160, 2017.

[18] Y. Pei, A. Cavagnino, S. Vaschetto, *et al.*, "Flywheel energy storage systems for power systems application," in *Proc. 2017 6th International Conference on Clean Electrical Power (ICCEP 2017)*, Santa Margherita Ligure, Italy, 2017, pp. 492-501.

[19] M. Schneider, S. Rinderknecht and D. Schaab, "Loss models of a PMSM in an outer rotor flywheel concept," in *Proc. 2017 IEEE International Electric Machines and Drives Conference (IEMDC 2017)*, Miami, Florida, USA 2017, pp. 1400-1405.

[20] M. Strasik, P. E. Johnson, A. C. Day, *et al.*, "Design, Fabrication, and Test of a 5-kWh/100-kW Flywheel Energy Storage Utilizing a High-Temperature Superconducting Bearing," *IEEE Transactions on Applied Superconductivity,* vol. 17, no. 2, pp. 2133-2137, 2007.

[21] E. Severson, R. Nilssen, T. Undeland, *et al.*, "Magnetic Equivalent Circuit Modeling of the AC Homopolar Machine for Flywheel Energy Storage," *IEEE Transactions on Energy Conversion,* vol. 30, no. 4, pp. 1670-1678, 2015.

[22] E. Severson, R. Nilssen, T. Undeland, *et al.*, "Outer-rotor ac homopolar motors for flywheel energy storage," in *Proc. 7th IET International Conference on Power Electronics, Machines and Drives (PEMD 2014)*, Manchester, United Kingdom 2014, pp. 584-589.

[23] W. Li, K. T. Chau, T. W. Ching, *et al.*, "Design of a High-Speed Superconducting Bearingless Machine for Flywheel Energy Storage Systems," *IEEE Transactions on Applied Superconductivity,* vol. 25, no. 3, pp. 1-4, 2015.

[24] T. D. Nguyen and G. Foo, "Sensorless control of a dual-airgap axial flux permanent magnet machine for flywheel energy storage system," *IET Electric Power Applications,* vol. 7, no. 2, pp. 140-149, 2013.

[25] J. L. Strubhar, R. C. Thompson, T. T. Pak, *et al.*, "Lightweight containment for high-energy rotating machines," *IEEE Transactions on Magnetics,* vol. 39, no. 1, pp. 378-383, 2003.

[26] D. Bender, "Recommended Practices for the Safe Design and Operation of Flywheels," Sandia National Laboratories, Albuquerque, New Mexico; Livermore, California, U.S.A, Report: SAND2015-10759, Dec. 2015.

[27] A. R. Millner, "A Flywheel Energy Storage and Conversion System for Solar Photovoltaic Applications," in *Proc. International Gas Turbine Conference and Exhibit and Solar Energy Conference*, San Diego, California, USA, 1979, vol. 2: Solar Energy, V002T03A001, pp. 1-6.

[28] T. L. Dinwoodie, "Flywheel storage for photovoltaics: an economic evaluation of two applications " Energy Laboratory, MIT, Massachusetts, USA, Report: MIT-EL-80-002, 1980.

[29] R. D. Hay, A. R. Millner and P. O. Jarvinen, "Performance testing and economic analysis of a photovoltaic flywheel energy storage and conversion system," in *Proc. 1980 Flywheel technology symposium*, Scottsdale, Arizona, USA, 1980, pp. 259-267.

[30] C. J. Rydh and B. A. Sandén, "Energy analysis of batteries in photovoltaic systems. Part II: Energy return factors and overall battery efficiencies," *Energy Conversion and Management,* vol. 46, no. 11, pp. 1980-2000, 2005.

[31] Variobahn in Heidelberg [Online]. Available: http://www.trampicturebook.de/.

[32] H. Wirth, "Recent Facts about Photovoltaics in Germany," Fraunhofer Institute for Solar Energy Systems ISE, Report: Jan. 2018.

[33] N. Pflugradt. Load profile generator [Online]. Available: https://www.loadprofilegenerator.de/.

[34] SMA Solar Technology AG. Sunny Portal [Online]. Available: https://www.sunnyportal.com.

[35] H. Darrelmann, W.-R. Canders, F. Laube, *et al.*, "Dynastore - A Flywheel EnergyStorage System for Power Quality Applications in the 10 kWh Class," in *Proc. Electric Energy Storage, Application and Technology*, San Francisco, California, USA, 2003, Session: 11, 6 pages.

[36] K.-P. Kairies, D. Magnor and D. U. Sauer, "Scientific Measuring and Evaluation Program for Photovoltaic Battery Systems(WMEP PV-Speicher)," *Energy Procedia,* vol. 73, Jun., pp. 200-207, 2015.

[37] P. W. Parfomak, "Energy Storage for Power Grids and Electric Transportation: A Technology Assessment " Congressional Research Service Report: R42455 Mar. 27, 2012.

[38] P. Arboleya, P. Bidaguren and U. Armendariz, "Energy Is On Board: Energy Storage and Other Alternatives in Modern Light Railways," *IEEE Electrification Magazine,* vol. 4, no. 3, pp. 30-41, 2016.

[39] M. M. Flynn, J. J. Zierer and R. C. Thompson, "Performance Testing of a Vehicular Flywheel Energy System," SAE International, USA, SAE Technical Paper: 2005-01-0809, 2005.

[40] M. Beek and M. Klohr, "RNV und der MITRAC Energy Saver - ein Erfahrungsbericht," (in German), *ZEVrail,* vol. 137, Jul., pp. 202-209, 2013.

[41] B. Buchmayr, *Werkstoff- und Produktionstechnik mit Mathcad: Modellierung und Simulation in Anwendungsbeispielen* (in German), 1. ed. Berlin, Heidelberg: Springer-Verlag Berlin Heidelberg, 2002.

[42] Maxwell Technologies Inc. Datasheet K2 Ultracapacitors - 2.7 V series [Online]. Available: http://www.maxwell.com/.

[43] B. Engel, C. Söffker and F. Hörl, "The innovative traction system with the flywheel of the Lirex$^{\text{TM}}$," in *Proc. World Congress of Railway Research (WCRR)*, Cologne, Germany, 2001, 7 pages.

[44] M. Hedlund, J. Lundin, J. de Santiago*, et al.*, "Flywheel Energy Storage for Automotive Applications," *Energies,* vol. 8, no. 10, p. 10636, 2015.

[45] Thyssenkrupp AG, "Vergütungsstahl Werkstoff-Nr. 1.7225 / 1.7227," 2017.

[46] Böhler Edelstahl, "Böhler V145: Vergütungsstahl heat treatable steel," 2017.

[47] F. K. Schymski, "Elektromechanische Konstruktion eines Schwungradspeichers," Bachelor Thesis, Technische Universität Darmstadt, Darmstadt, Germany, 2017.

[48] AALCO Metall of AMARI Metall GmbH, "Datasheet: ALZnMgCu1,5 (EN AW-7075)," 2017.

[49] VDI e.V., *VDI-Wärmeatlas* (in German), 11. ed. (VDI-Buch). Berlin, Heidelberg: Springer Vieweg, 2013.

[50] Vacuumschmelze, "Rare earth permanent magnets VACODYM&VACOMAX," 2015.

[51] JSOL Corporation, "JMAG User's Manual, Version 16, Volume 2. Solver," 2016.

[52] T. Lu, "Weiterentwicklung von hochtourigen permanenterregten Drehstromantrieben mit Hilfe von Finite-Elemente-Berechnungen und experimentellen Untersuchungen," Ph. D. Thesis, Technische Universität Darmstadt, Darmstadt, Germany, 2004.

[53] A. Binder, "Analytical calculation of eddy-current losses in massive rotor parts of high-speed permanent magnet machines," in *Proc. Symposium on Power Electronics, Electrical Drives, Automation & Motion (SPEEDAM)*, Ischia, Italy, 2000, pp. (C2) 1-6.

[54] G. Bergmann, "Five-Axis Rotor Magnetic Suspension with Bearingless PM Motor Levitation Systems," Ph. D. Thesis, Technische Universität Darmstadt, Darmstadt, Germany, 2013.

[55] Cogent Power Ltd., "Electrical Steel, Thin Non Oriented ", 2017.

[56] Deutsche Edelstahlwerke GmbH, "Cr-Ni-Mo-legierter Vergütungsstahl: 1.6580 (30CrNiMo8)," 2017.

[57] *Mechanical vibration - Balance quality requirements for rotors in a constant (rigid) state - Part 1: Specification and verification of balance tolerances*, ISO 1940-1, 2003.

[58] A. Krings and J. Soulard, "Overview and Comparison of Iron Loss Models for Electrical Machines," *Journal of Electrical Engineering,* vol. 10, no. 3, pp. 162-169, 2010.

[59] A. C. Hagg and G. O. Sankey, "The Containment of Disk Burst Fragments by Cylindrical Shells," *Journal of Engineering for Power,* vol. 96, no. 2, pp. 114-123, 1974.

[60] SCHMOLZ + BICKENBACH, "Steel Tubes," 2017.

[61] ThyssenKrupp Materials International, "Werkstoffdatenblatt: Warmgefertigte Hohlprofile für den Stahlbau gemäß DIN EN 10210 ", 2011.

[62] Pfeiffer Vacuum GmbH. Duo 3 DC [Online]. Available: https://www.pfeiffer-vacuum.com/de/.

[63] H.-P. Liu, M. Werst, J. J. Hahne*, et al.*, "Prediction of Windage Losses of an Enclosed High Speed Composite Rotor in Low Air Pressure Environments," in *Proc. ASME Summer Heat Transfer Conference (SHTC)*, Las Vegas, Nevada, U.S.A, 2003, vol. 1, pp. 15-23.

[64] J. Pyrhonen, T. Jokinen and V. Hrabovcova, *Design of Rotating Electrical Machines* ed. Chichester, West Sussex, UK: Wiley, 2008.

[65] M. Klohr, "Entwicklung und Konstruktion einer umrichtergespeisten magnetgelagerten Permanentmagnet-Synchronmaschine für 40kW, 40000 /min," Ph. D. Thesis, Technische Universität Darmstadt, Darmstadt, Germany, 2008.

[66] H. Bannwarth, "Gas Physics and Vacuum Technology," in *Liquid Ring Vacuum Pumps, Compressors and Systems: Conventional and Hermetic Design.*Weinheim, Germany: Wiley, 2006, pp. 1-109.

[67] R. Wrobel and P. H. Mellor, "A General Cuboidal Element for Three-Dimensional Thermal Modelling," *IEEE Transactions on Magnetics,* vol. 46, no. 8, pp. 3197-3200, 2010.

[68] D. Kuehbacher, A. Kelleter and D. Gerling, "An improved approach for transient thermal modeling using lumped parameter networks," in *Proc. 2013 International Electric Machines & Drives Conference (IEMDC 2013)*, 2013, pp. 824-831.

[69] P. H. Mellor, D. Roberts and D. R. Turner, "Lumped parameter thermal model for electrical machines of TEFC design," *IEE Proceedings B - Electric Power Applications,* vol. 138, no. 5, pp. 205-218, 1991.

[70] Z. Kolondzovski, "Thermal and Mechanical Analyses of High-Speed Permanent-Magnet Electrical Machines," Ph. D. Thesis, Aalto University, Espoo, Finland, 2010.

[71] *Plastics - Differential scanning calorimetry (DSC) - Part 2: Determination of glass transition temperature and glass transition step height*, ISO 11357-2, 2013.

[72] A. Puck, *Festigkeitsanalyse von Faser-Matrix-Laminaten* 1. ed. München Wien: Carl Hanser Verlag, 1996.

[73] Z. Hashin and A. Rotem, "A Fatigue Failure Criterion for Fiber Reinforced Materials," *Journal of Composite Materials,* vol. 7, no. 4, pp. 448-464, 1973.

[74] S. K. Ha, M. H. Kim, S. C. Han, *et al.*, "Design and Spin Test of a Hybrid Composite Flywheel Rotor with a Split Type Hub," *Journal of Composite Materials,* vol. 40, no. 23, pp. 2113-2130, 2006.

Publications of the Author

[75] N. Erd, X. Li and A. Binder, "Power Flow Simulation of Flywheel Energy Storage Systems for Tramways," *Renewable Energy and Power Quality Journal,* vol. 1, no. 15, pp. 149-153, 2017.

[76] X. Li, N. Erd and A. Binder, "Design and calculation of a 130 kW high-speed permanent magnet synchronous machine in flywheel energy storage systems for urban railway application," in *Proc. 2017 6th International Conference on Clean Electrical Power (ICCEP)*, Santa Margherita Ligure, Italy, 2017, pp. 452-459.

[77] X. Li, N. Erd and A. Binder, "Evaluation of flywheel energy storage systems for residential photovoltaic installations," in *Proc. International Symposium on Power Electronics, Electrical Drives, Automation and Motion (SPEEDAM)*, Anacapri, Italy, 2016, pp. 255-260.

[78] X. Li, N. Erd, J. An, *et al.*, "Design of a High-Speed Flywheel Energy Storage Demonstrator," in *Proc. 7th VDE/VDI Symposium on Drive Systems*, Karlsruhe, Germany, 2017, pp. 19-24.

Bachelor and Master Projects of Supervised Students

[79] S. H. Naqvi, "Comparison of High Speed Induction Machine and Permanent Magnet Synchronous Machine for Diurnal Cycle Flywheel Energy Storage System," Master Thesis, Technische Universität Darmstadt, Darmstadt, Germany, 2016.

[80] M. J. Ruß, "Mechanical Design of a Flywheel System," Bachelor Thesis, Technische Universität Darmstadt, Darmstadt, Germany, 2017.

[81] G. Che, "Loss Analysis of High Speed Permanent Magnet Synchromous Machine in Flywheel Energy Storage Systems," Master Thesis, Technische Universität Darmstadt, Darmstadt, Germany, 2017.

Appendix A. Drawing of the Flywheel System (without Burst Containment)

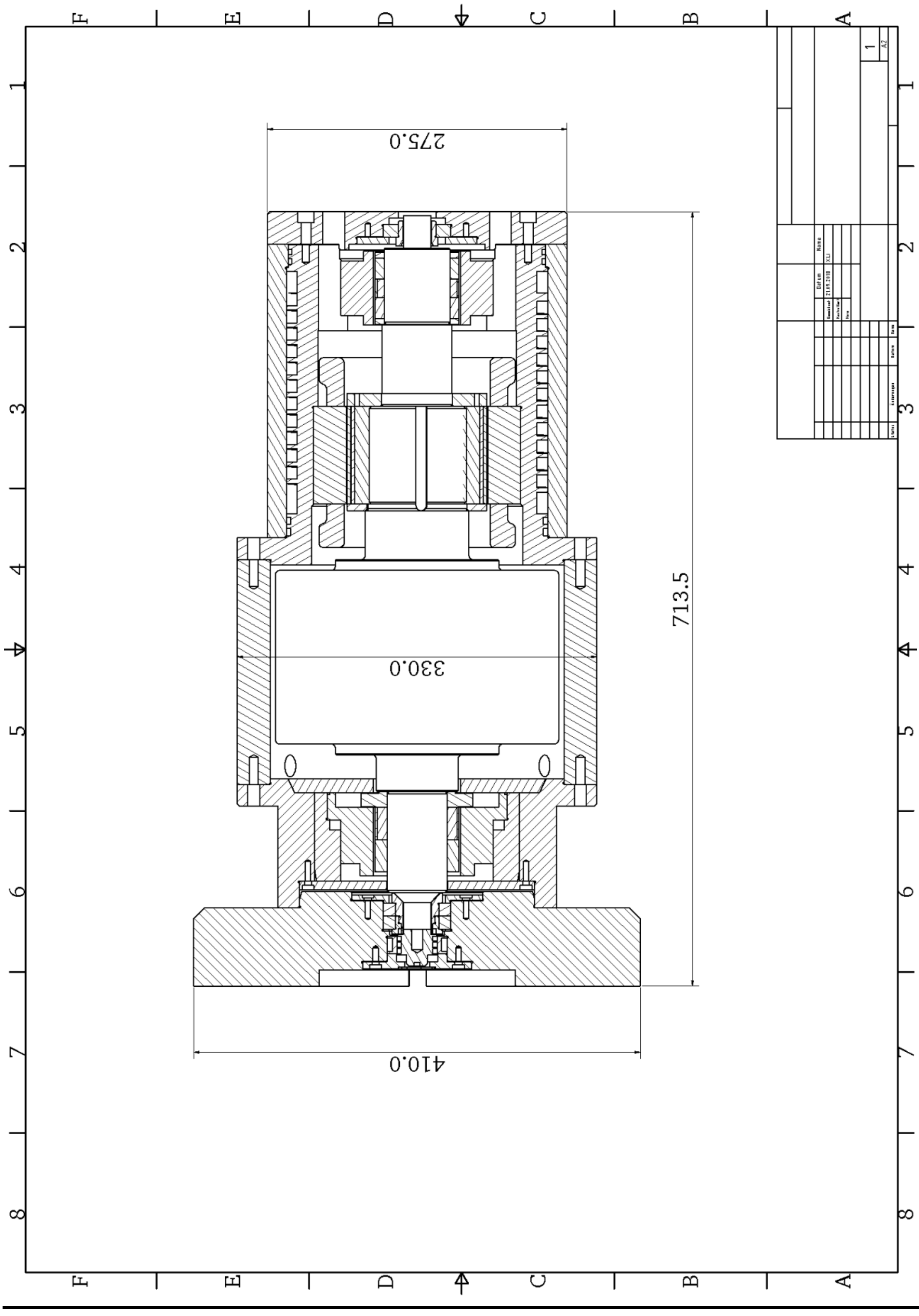

Appendix B. Design Parameters of Prototype E-machine

Parameters	Symbol	Value	Unit
Maximum speed	n_{max}	24000	min^{-1}
Minimum speed	n_{min}	12000	min^{-1}
Inverter DC-link voltage	U_{DC}	560	V
Nominal output voltage (r.m.s.) of inverter	U_{AC}	396	V
Max. phase voltage (r.m.s., Y connection)	$U_{s, max}$	228.6	V
Inverter switching frequency	f_T	12	kHz
Rated output power (motor, at 12000 min^{-1})	P_N	28	kW
Rated torque (motor, at 12000 min^{-1})	M_N	22.28	Nm
Max. current (r.m.s.)	I_{max}	50	A
Operation duty type	Continuous duty		

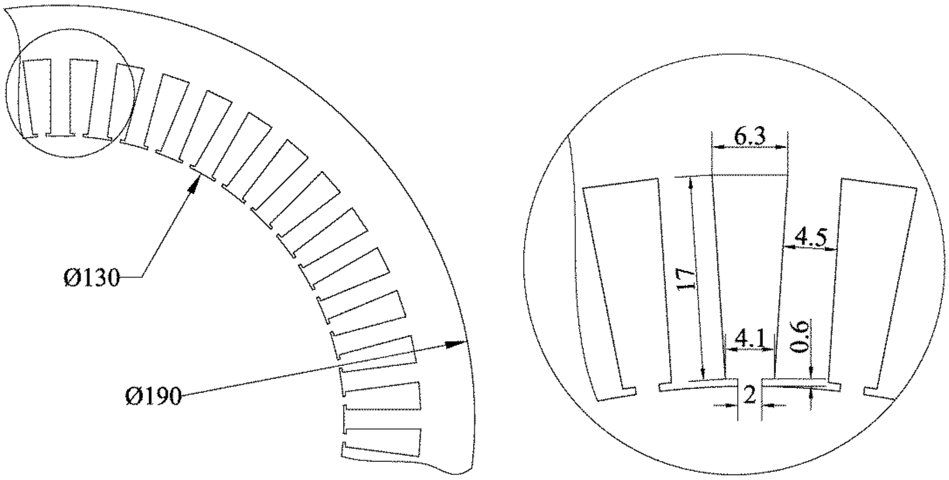

Fig.B-1 Stator iron design, iron sheet NO 20 (dimensions in mm)

Parameter	Symbol	Value
Dimensions		
Stator inner diameter	d_{si}	130 mm
Stator outer diameter	d_{so}	190 mm
Rotor outer diameter	d_{ro}	128 mm
Shaft diameter	d_{sh}	90 mm
Iron stack length	L_{Fe}	90 mm
Air gap length	δ	1 mm
Bandage thickness	h_{B}	3 mm
Undersize of bandage	Δu	0.15 mm
Magnet dimension	$l_{\mathrm{m}} \cdot b_{\mathrm{m}} \cdot h_{\mathrm{m}}$	22.5 mm×4.9 mm×3.2 mm
Segmentation per pole	$c_{\mathrm{m}} \cdot z_{\mathrm{m}}$	18 (circumferential)×4 (axial)
Pole coverage ratio	α_{p}	1
Slot dimension	-	See Fig.B-1
Winding parameters		
Pole count	$2p$	4
Slot number	Q_{s}	48
Nr. of slot per pole per phase	q	4
Short pitching	w/τ_{s}	10/12
Winding factor	$k_{\mathrm{ws,1}}$	0.925
Nr. of turns per phase	N_{s}	44
Nr. of turns per coil	N_{c}	11
Parallel branches	a	4
Nr. of strands per turn	a_{i}	4
Diameter of wires	d_{Cu}	0.75 mm
Slot area	A_{slot}	88.8 mm^2
Slot filling factor	k_{fill}	0.438
Electromagnetic parameters		
Resistance	$R_{\mathrm{s,20\,°C}}$	43.81 mΩ
	$R_{\mathrm{s,150\,°C}}$	66.15 mΩ
Inductance	L_{s}	0.98 mH
Current loading at OP$_1$	A	316.1 A/cm
Current density at OP$_1$	J	6.9 A/mm^2
Thermal loading	$A \cdot J$	2181 A/cm · A/mm^2
Air gap flux density	$B_{\delta,1}$	0.45 T
Flux linkage	Ψ_{p}	0.1077 Vs
Esson's number [kVA·min/m^3]	C_0	1.54 kVA·min/m^3
Max. tip velocity at rotor outer surface [m/s]	v_{tip}	160.8 m/s
Flux density in stator tooth (no load)	B_{ts}	0.68 T
Flux density in stator yoke (no load)	B_{ys}	1.4 T
Flux density in rotor yoke (no load)	B_{yr}	1.2 T

Bandage material: carbon fiber HTS5631+epoxy resin [54]
($\parallel$: parallel direction of fibers, $\perp$: transversal direction of fibers**)**

Parameter	Symbol	Value
Density	ρ	1540 kg/m^3
Tensile modulus	$E_{\parallel}$	145.28 GPa
	$E_{\perp}$	12.02 GPa
Shear modulus	$G_{\parallel\perp} = G_{\perp\parallel}$	5.562 GPa
	$G_{\perp\perp}$	4.329 GPa
Poisson's ratio	$\nu_{\parallel\perp}$	0.278
	$\nu_{\perp\parallel}$	0.023
	$\nu_{\perp\perp}$	0.388
Tensile strength	$R_{\parallel}^{+}$	2615 MPa
	$R_{\perp}^{+}$	90 MPa
Compressive strength	$R_{\perp}^{-}$	205 MPa
Shear strength	S	105 MPa
Coefficient of thermal expansion	$\alpha_{\parallel}$	0.139×10^{-6}/°C
	$\alpha_{\perp}$	34.3×10^{-6}/°C

Magnet material: VACOMAX 225 (Sm_2Co_{17}) [50]

Parameter	Symbol	Value
Remanence	B_{r}	1.03 T
Coercivity	H_{cB}	720 kA/m
Magnetic polarization	H_{cJ}	1590 kA/m
Relative permeability	μ_{M}	1.14
Energy density	$(BH)_{\mathrm{max}}$	190 kJ/m^3
Temperature coefficient of remanence	$TK_{\mathrm{B_r}}$	- 0.035 %/K (20-150 °C)
Temperature coefficient of coercivity	$TK_{H_{\mathrm{cJ}}}$	- 0.19 %/K (20-150 °C)
Max. continuous temperature	T_{max}	350 °C

Winding diagram

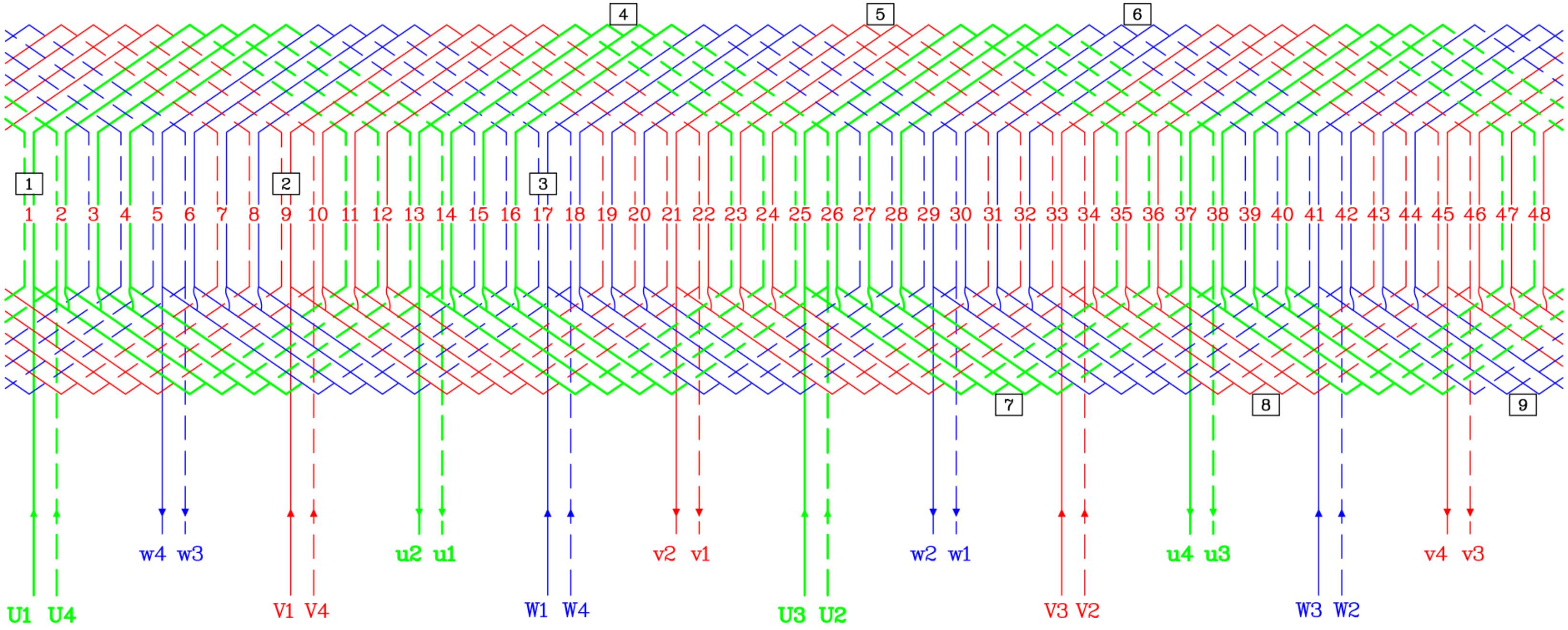

3-phase winding for 4-pole PM machine: Nr. of slots/pole/phase $q = 4$, short pitching 10/12, parallel branches $a = 4$.

(Nr. 1 … 9: positions for temperature sensors PT100)

Iron sheet:

SURA® NO20

1 (2)

			Typical Values			
T	W/kg at 50 Hz	A/m at 50 Hz	W/kg at 400 Hz	W/kg at 2500 Hz	W/kg at 5000 Hz	W/kg at 10000 Hz
0,10	0,02	30	0,17	2,79	9,01	27,0
0,20	0,07	37	0,72	10,6	31,8	95,6
0,30	0,14	42	1,49	24,4	65,6	191
0,40	0,23	46	2,50	40,4	108	315
0,50	0,32	51	3,80	58,4	159	
0,60	0,42	55	5,17	78,4	219	
0,70	0,54	61	6,70	103	290	
0,80	0,66	68	8,36	133	375	
0,90	0,80	78	10,3	166	477	
1,00	0,95	91	12,2	205		
1,10	1,14	111	14,8	253		
1,20	1,36	145	17,9			
1,30	1,65	214	21,4			
1,40	2,00	411	25,3			
1,50	2,40	1082	29,7			
1,60	2,75	2690				
1,70	3,06	5375				
1,80	3,32	9372				

	Guaranteed Values	Typical Values
Loss at 1.0 T , 50 Hz, W/kg	–	0,95
Loss at 1.0 T , 400 Hz, W/kg	15,0	12,2
Loss at 1.0 T , 2500 Hz, W/kg	215	205
Resistivity, μΩcm		52
Density g/cm³		7,65
Yield strength, N/mm²		400
Tensile strength, N/mm²		505
Young's modulus, RD, N/mm²		185 000
Young's modulus, TD, N/mm²		200 000
Hardness HV5 (VPN)		180

RD represents the rolling direction
TD represents the transverse direction
Values for yield strength (0.2 % proof strength)
and tensile strength are given for the rolling direction
Values for the transverse direction are approximately 5% higher

cogent
Surahammars Bruks AB

Jan 2010

SURA® NO20

2 (2)

T	W/kg at 50 Hz	A/m at 50 Hz	A/m at 400 Hz	A/m at 2500 Hz	A/m at 5000 Hz	A/m at 10000 Hz
0,10	0,02	30	29	42	51	75
0,20	0,07	37	40	67	87	128
0,30	0,14	42	48	87	116	166
0,40	0,23	46	55	103	141	202
0,50	0,32	51	61	118	165	
0,60	0,42	55	67	133	189	
0,70	0,54	61	73	148	217	
0,80	0,66	68	80	165	248	
0,90	0,80	78	89	183	284	
1,00	0,95	91	101	204	324	
1,10	1,14	111	121	227		
1,20	1,36	145	155			
1,30	1,65	214	230			
1,40	2,00	411	466			
1,50	2,40	1082	1268			
1,60	2,75	2690				
1,70	3,06	5375				
1,80	3,32	9372				

Typical Values

	Typical Values
Loss at 1.0 T , 50 Hz, W/kg	0,95
Loss at 1.0 T , 400 Hz, W/kg	12,2
Loss at 1.0 T , 2500 Hz, W/kg	205
Resistivity, $\mu\Omega$cm	52
Density g/cm^3	7,65
Yield strength, N/mm^2	400
Tensile strength, N/mm^2	505
Young's modulus, RD, N/mm^2	185 000
Young's modulus, TD, N/mm^2	200 000
Hardness HV5 (VPN)	180

RD represents the rolling direction
TD represents the transverse direction
Values for yield strength (0.2 % proof strength)
and tensile strength are given for the rolling direction
Values for the transverse direction are approximately 5% higher

cogent
Surahammars Bruks AB

Jan 2010

Appendix C. Stress in Multi-layer Rotor Components

The investigated model is a 3-layer planar model as presented in Fig. C-1, including rotor components of shaft, magnets and bandage. The purpose is to calculate the stress distribution and displacement of each component as well as the contact pressure between each layer for the given geometries and interference fittings under rotational and thermal loads. The calculation method and formulas are excerpted from [54] and summarized in this chapter for readers' convenience. For more details, one can refer to [54].

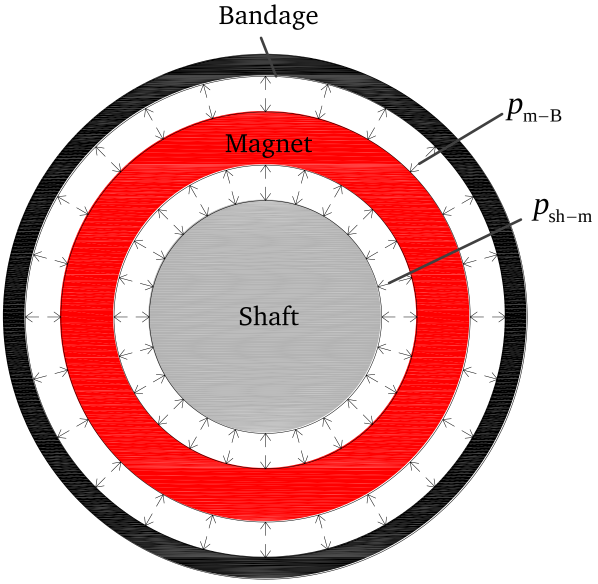

Fig. C-1 3-layer planar model, showing rotor components: shaft, magnet and bandage, $p_{\mathrm{sh\text{-}m}}$ and $p_{\mathrm{m\text{-}B}}$ are contact pressures between two contact layers

Two assumptions are available for a planar model: plane stress and plane strain. The former one assumes the normal stress in z-direction is zero. It is assumed for a very thin disk and is adequate enough if the thickness of the disk is small compared to the diameter. Plane strain assumes the normal stain in z-direction is zero. It is correct for an infinite long cylinder and also can approximate the stress in the mid-plane of a very thick disk. The deviation of these two assumptions is about 3 % for isotropic materials [1]. For different assumptions, the material parameters should be corrected accordingly as shown in Table C-1. For the rotor structure in this thesis, plane strain assumption is more suitable and is adopted for the calculation.

Table C-1 Material parameters under plane stress and plane strain assumptions [54]

Isotropic material	Orthotropic material
$\tilde{E} = \begin{cases} E : \text{plane stress} \\ \dfrac{E}{1-\nu^2} : \text{plane strain} \end{cases}$	$\tilde{E}_{\parallel} = \begin{cases} E_{\parallel} : \text{plane stress} \\ \dfrac{E_{\parallel}}{1-\nu_{\perp\parallel} \cdot \nu_{\parallel\perp}} : \text{plane strain} \end{cases}, \tilde{E}_{\perp} = \begin{cases} E_{\perp} : \text{plane stress} \\ \dfrac{E_{\perp}}{1-\nu_{\perp\perp} \cdot \nu_{\perp\perp}} : \text{plane strain} \end{cases}$
$\tilde{\nu} = \begin{cases} \nu : \text{plane stress} \\ \dfrac{\nu}{1-\nu} : \text{plane strain} \end{cases}$	$\tilde{\nu}_{\perp\parallel} = \begin{cases} \nu_{\perp\parallel} : \text{plane stress} \\ \dfrac{\nu_{\perp\parallel} + \nu_{\perp\perp} \cdot \nu_{\perp\parallel}}{1-\nu_{\parallel\perp} \cdot \nu_{\perp\parallel}} : \text{plane strain} \end{cases}, \tilde{\nu}_{\parallel\perp} = \begin{cases} \nu_{\parallel\perp} : \text{plane stress} \\ \dfrac{\nu_{\parallel\perp} + \nu_{\parallel\perp} \cdot \nu_{\perp\perp}}{1-\nu_{\perp\perp} \cdot \nu_{\perp\perp}} : \text{plane strain} \end{cases}$

The expressions of stress and displacement caused by inner and outer pressure are presented in Table C-2 and Table C-3, respectively, for both isotropic and orthotropic materials and circular and annual cross sections. The stress and displacement due to rotational and thermal loads are presented in Table C-4 and Table C-5, respectively. For the rotor structure shown in Fig. C-1, the shaft has a circular cross section, while the magnet and bandage have annular cross sections. The shaft and magnet have isotropic material properties, while the bandage has orthotropic properties.

The displacement equations of each layer due to the contact pressure, rotational and thermal loads are

$$\begin{cases} u_{\text{r, sh}}(r) = -p_{\text{sh}-\text{m}} \cdot \delta_{\text{o, sh}}(r) + u_{\text{r}\vartheta,\text{ sh}}(r) + u_{\text{r}\omega,\text{ sh}}(r) \\ u_{\text{r, m}}(r) = p_{\text{sh}-\text{m}} \cdot \delta_{\text{i , m}}(r) - p_{\text{m-B}} \cdot \delta_{\text{o, m}}(r) + u_{\text{r}\vartheta,\text{ m}}(r) + u_{\text{r}\omega,\text{ m}}(r) \\ u_{\text{r, B}}(r) = p_{\text{m}-\text{B}} \cdot \delta_{\text{i, B}}(r) + u_{\text{r}\vartheta,\text{ B}}(r) + u_{\text{r}\omega,\text{ B}}(r) \end{cases}, \tag{C-1}$$

where subscript *sh* stands for shaft, *m* stands for magnet, *B* stands for bandage. *p* is the contact pressure, which is to be determined by applying the boundary conditions

$$\begin{cases} u_{\text{r, sh}}(r_{\text{o, sh}}) = u_{\text{r, m}}(r_{\text{i, m}}) \\ u_{\text{r, B}}(r_{\text{i, B}}) - u_{\text{r, m}}(r_{\text{o, m}}) - \Delta u = 0 \end{cases}, \tag{C-2}$$

where Δu is the undersize of the bandage inner surface compared to the magnet outer surface. As the magnets are glued on the shaft (or rotor iron package), the undersize between the shaft and magnet is 0.

By applying the boundary condition (C-2) into (C-1), the contact pressure $p_{\text{sh-m}}$ and $p_{\text{m-B}}$ can be determined.

After obtaining the contact pressure, the stress distribution in each layer can be calculated. (C-3) gives the expressions of tangential stress. The total stress is a sum of the stress caused by contact pressure, rotation and thermal expansion.

$$\begin{cases}\sigma_{\mathrm{t,\,B}}(r)=\sigma_{\mathrm{t}p_{\mathrm{m-B}},\,\mathrm{B}}(r)+\sigma_{\mathrm{t\omega,\,B}}(r)+\sigma_{\mathrm{t}\vartheta,\,\mathrm{B}}(r)\\ \sigma_{\mathrm{t,\,m}}(r)=\sigma_{\mathrm{t}p_{\mathrm{sh-M}},\,\mathrm{m}}(r)+\sigma_{\mathrm{t}p_{\mathrm{m-B}},\,\mathrm{m}}(r)+\sigma_{\mathrm{t\omega,\,m}}(r)+\sigma_{\mathrm{t}\vartheta,\,\mathrm{m}}(r)\\ \sigma_{\mathrm{t,\,sh}}(r)=\sigma_{\mathrm{t}p_{\mathrm{sh-m}},\,\mathrm{sh}}(r)+\sigma_{\mathrm{t\omega,\,sh}}(r)+\sigma_{\mathrm{t}\vartheta,\,\mathrm{sh}}(r)\end{cases} \tag{C-3}$$

Table C-2 Formulas of radial σ_{r} and tangential stress σ_{t} and radial displacement u_{r} of circular and annular cross sections for isotropic and orthotropic materials under inner boundary pressure p_{i} [54] (subscript p: pressure)

Cross section properties	Formulas of radial and tangential stress and radial displacement
▪ annular cross section ▪ thin-walled ▪ iso-and orthotropic	$\delta_{\mathrm{i}}(r)=\dfrac{r^2}{\tilde{E}_{\parallel}\cdot(r_{\mathrm{o}}-r_{\mathrm{i}})}$ $u_{\mathrm{rp}}(r)=\delta_{\mathrm{i}}(r)\cdot p_{\mathrm{i}}$ $\sigma_{\mathrm{tp}}(r)\cong\dfrac{(r_{\mathrm{o}}-r_{\mathrm{i}})/2}{r_{\mathrm{o}}-r_{\mathrm{i}}}\cdot p_{\mathrm{i}}$
▪ annular cross section ▪ thin-walled ▪ isotropic	$\delta_{\mathrm{i}}(r)=\dfrac{r^2\cdot(1-\tilde{\nu})+r_{\mathrm{o}}^2\cdot(1+\tilde{\nu})}{r\cdot\tilde{E}\cdot(r_{\mathrm{o}}^2-r_{\mathrm{i}}^2)}\cdot r_{\mathrm{i}}^2$ $u_{\mathrm{rp}}(r)=\delta_{\mathrm{i}}(r)\cdot p_{\mathrm{i}}$ $\sigma_{\mathrm{rp}}(r)=\dfrac{r_{\mathrm{i}}^2}{r_{\mathrm{o}}^2-r_{\mathrm{i}}^2}\cdot\left(\dfrac{r_{\mathrm{o}}^2}{r^2}-1\right)\cdot(-p_{\mathrm{i}})$ $\sigma_{\mathrm{tp}}(r)=\dfrac{r_{\mathrm{i}}^2}{r_{\mathrm{o}}^2-r_{\mathrm{i}}^2}\cdot\left(\dfrac{r_{\mathrm{o}}^2}{r^2}+1\right)\cdot(p_{\mathrm{i}})$
▪ annular cross section ▪ thin-walled ▪ orthotropic	$\delta_{\mathrm{i}}(r)=\dfrac{r^{E_{\mathrm{v}}}\cdot r_{\mathrm{o}}^{-2E_{\mathrm{v}}}\cdot(\tilde{\nu}_{\parallel\perp}/E_{\mathrm{v}}-1)-r^{-E_{\mathrm{v}}}\cdot(1+\tilde{\nu}_{\parallel\perp}/E_{\mathrm{v}})}{E_{\mathrm{v}}\cdot\tilde{E}_{\perp}\cdot(r_{\mathrm{o}}^{-2E_{\mathrm{v}}}-r_{\mathrm{i}}^{2E_{\mathrm{v}}}-1)}\cdot r_{\mathrm{i}}^{1+E_{\mathrm{v}}},$ $u_{\mathrm{rp}}(r)=\delta_{\mathrm{i}}(r)\cdot p_{\mathrm{i}}$ $\sigma_{\mathrm{tp}}(r)=\left(\dfrac{r_{\mathrm{i}}^{1+\mathrm{E_v}}}{r_{\mathrm{i}}^{2\mathrm{E_v}}-r_{\mathrm{o}}^{2\mathrm{E_v}}}\cdot r^{\mathrm{E_v}\text{-}1}+\dfrac{r_{\mathrm{i}}^{1-\mathrm{E_v}}}{r_{\mathrm{i}}^{\text{-}2\mathrm{E_v}}-r_{\mathrm{o}}^{\text{-}2\mathrm{E_v}}}\cdot r^{-\mathrm{E_v}-1}\right)\cdot(-p_{\mathrm{i}}),$ $\sigma_{\mathrm{tp}}(r)=E_{\mathrm{v}}\cdot\left(\dfrac{r_{\mathrm{i}}^{1+\mathrm{E_v}}}{r_{\mathrm{i}}^{2\mathrm{E_v}}-r_{\mathrm{o}}^{2\mathrm{E_v}}}\cdot r^{\mathrm{E_v}-1}-\dfrac{r_{\mathrm{i}}^{1-\mathrm{E_v}}}{r_{\mathrm{i}}^{-2\mathrm{E_v}}-r_{\mathrm{o}}^{-2\mathrm{E_v}}}\cdot r^{-\mathrm{E_v}-1}\right)\cdot(-p_{\mathrm{i}})$ Where $E_{\mathrm{v}}=\sqrt{\dfrac{\tilde{E}_{\parallel}}{\tilde{E}_{\perp}}}$

Table C-3 Formulas of radial σ_r and tangential stress σ_t and radial displacement u_r of circular and annular cross sections for isotropic and orthotropic materials under outer boundary pressure p_o [54] (subscript p: pressure)

Cross section properties	Formulas of radial and tangential stress and radial displacement
▪ circular cross section ▪ isotropic	$\delta_\mathrm{o}(r) = r \cdot \frac{1-\tilde{v}}{\tilde{E}}$ $u_\mathrm{rp}(r) = \delta_\mathrm{o}(r) \cdot \left(-p_\mathrm{o}\right)$ $\sigma_\mathrm{rp}(r) = -p_\mathrm{o}$ $\sigma_\mathrm{tp}(r) = -p_\mathrm{o}$
▪ annular cross section ▪ thin-walled ▪ iso-and orthotropic	$\delta_\mathrm{o}(r) = \frac{r^2}{\tilde{E}_{\parallel} \cdot (r_\mathrm{o} - r_\mathrm{i})}$ $u_\mathrm{rp}(r) = \delta_\mathrm{o}(r) \cdot \left(-p_\mathrm{o}\right)$ $\sigma_\mathrm{tp}(r) \cong \frac{(r_\mathrm{o} + r_\mathrm{i})/2}{r_\mathrm{o} - r_\mathrm{i}} \cdot (-p_\mathrm{o})$
▪ annular cross section ▪ thin-walled ▪ isotropic	$\delta_\mathrm{o}(r) = \frac{r^2 \cdot (1-\tilde{v}) + r_\mathrm{i}^2 \cdot (1+\tilde{v})}{r \cdot \tilde{E} \cdot (r_\mathrm{o}^2 - r_\mathrm{i}^2)} r_\mathrm{o}^2$ $u_\mathrm{rp}(r) = \delta_\mathrm{o}(r) \cdot \left(-p_\mathrm{o}\right)$ $\sigma_\mathrm{rp}(r) = \frac{r_\mathrm{o}^2}{r_\mathrm{o}^2 - r_\mathrm{i}^2} \cdot (1 - \frac{r_\mathrm{i}^2}{r^2}) \cdot (-p_\mathrm{o})$ $\sigma_\mathrm{rp}(r) = \frac{r_\mathrm{o}^2}{r_\mathrm{o}^2 - r_\mathrm{i}^2} \cdot (1 + \frac{r_\mathrm{i}^2}{r^2}) \cdot (-p_\mathrm{o})$
▪ annular cross section ▪ thin-walled ▪ orthotropic	$\delta_\mathrm{o}(r) = \frac{r^{E_\mathrm{v}} \cdot (1 - \tilde{v}_{\parallel\perp}/E_\mathrm{v}) + r^{-E_\mathrm{v}} \cdot r_\mathrm{i}^{2E_\mathrm{v}} (1 + \tilde{v}_{\parallel\perp}/E_\mathrm{v})}{E_\mathrm{v} \cdot \tilde{E}_\perp \cdot (r_\mathrm{o}^{2\mathrm{E_V}} - r_\mathrm{i}^{2E_\mathrm{v}})} \cdot r_\mathrm{o}^{1+E_\mathrm{v}}$ $u_\mathrm{rp}(r) = \delta_\mathrm{o}(r) \cdot \left(-p_\mathrm{o}\right)$ $\sigma_\mathrm{rp}(r) = (\frac{-r_\mathrm{o}^{1+E_\mathrm{v}}}{r_\mathrm{i}^{2E_\mathrm{v}} - r_\mathrm{o}^{2E_\mathrm{v}}} \cdot r^{E_\mathrm{v}-1} + \frac{r_\mathrm{o}^{1+E_\mathrm{v}} \cdot r_i^{2E_\mathrm{v}}}{r_\mathrm{i}^{2E_\mathrm{v}} - r_\mathrm{o}^{2E_\mathrm{v}}} \cdot r^{-E_\mathrm{v}-1}) \cdot (-p_\mathrm{o})$ $\sigma_\mathrm{tp}(r) = E_\mathrm{v} \cdot (\frac{-r_\mathrm{o}^{1+E_\mathrm{v}}}{r_\mathrm{i}^{2E_\mathrm{v}} - r_\mathrm{o}^{2E_\mathrm{v}}} \cdot r^{E_\mathrm{v}-1} - \frac{r_\mathrm{o}^{E_\mathrm{v}+1} \cdot r_\mathrm{i}^{2E_\mathrm{v}}}{r_\mathrm{i}^{2E_\mathrm{v}} - r_\mathrm{o}^{2E_\mathrm{v}}} \cdot r^{-\mathrm{E_V}-1}) \cdot (-p_\mathrm{o})$ Where $E_\mathrm{v} = \sqrt{\frac{\tilde{E}_{\parallel}}{\tilde{E}_\perp}}$

Table C-4 Formulas of radial σ_{r} and tangential stress σ_{t} and radial displacement u_{r} of circular and annular cross sections for isotropic and orthotropic materials due to rotation at the speed n (s^{-1}) [54] (subscript ω: rotation)

Cross section properties	Formulas of radial stress, tangential stress and radial displacement
▪ circular cross section ▪ isotropic	$\sigma_{\mathrm{r}\omega}(r,n)=\frac{3+\tilde{\nu}}{8}\cdot\rho\cdot(2\cdot\pi\cdot n)^2\cdot r_{\mathrm{o}}^2\cdot\left(1-\frac{r^2}{r_{\mathrm{o}}^2}\right)$ $\sigma_{\mathrm{t}\omega}(r,n)=\frac{3+\tilde{\nu}}{8}\cdot\rho\cdot(2\cdot\pi\cdot n)^2\cdot r_{\mathrm{o}}^2\left(1-\frac{1+3\cdot\tilde{\nu}}{3+\tilde{\nu}}\cdot\frac{r^2}{r_{\mathrm{o}}^2}\right)$ $u_{\mathrm{r}\omega}(r,n)=\frac{-\rho\cdot\pi^2\cdot n^2\cdot r^3\cdot\left\lfloor r_{\mathrm{o}}^2\cdot\left(\tilde{\nu}^2+2\cdot\tilde{\nu}-3\right)+r^2\cdot\left(1-\tilde{\nu}^2\right)\right\rfloor}{2\cdot r_{\mathrm{o}}^2\cdot\tilde{E}}$
▪ annular cross section ▪ thin-walled ▪ isotropic and orthotropic	$\sigma_{\mathrm{t}\omega}(r,n)=\rho\cdot(2\cdot\pi\cdot n)^2\cdot r^2$ $u_{\mathrm{r}\omega}(r,n)=\frac{4\cdot\rho\cdot\pi^2\cdot n^2\cdot r^3}{\tilde{E}_{\parallel}}$
▪ annular cross section ▪ thin-walled ▪ isotropic	$\sigma_{\mathrm{r}\omega}(r,n)=\frac{3+\tilde{\nu}}{8}\cdot\rho\cdot(2\cdot\pi\cdot n)^2\cdot r_{\mathrm{o}}^2\cdot\left(1+\frac{r_{\mathrm{i}}^2}{r_{\mathrm{o}}^2}-\frac{r_{\mathrm{i}}^2}{r^2}-\frac{r^2}{r_{\mathrm{o}}^2}\right)$ $\sigma_{\mathrm{t}\omega}(r,n)=\frac{3+\tilde{\nu}}{8}\cdot\rho\cdot(2\cdot\pi\cdot n)^2\cdot r_{\mathrm{o}}^2\cdot\left(1+\frac{r_{\mathrm{i}}^2}{r_{\mathrm{o}}^2}+\frac{r_{\mathrm{i}}^2}{r^2}-\frac{1+3\cdot\tilde{\nu}}{3+\tilde{\nu}}\cdot\frac{r^2}{r_{\mathrm{o}}^2}\right)$ $u_{\mathrm{r}\omega}(r,n)=\frac{-\rho\cdot\pi^2\cdot n^2\cdot\left\lfloor r_{\mathrm{o}}^2\cdot r_{\mathrm{i}}^2\left(-\tilde{\nu}^2-3-4\cdot\tilde{\nu}\right)+r_{\mathrm{o}}^2\cdot r^2\cdot\left(\tilde{\nu}^2-3+2\cdot\tilde{\nu}\right)\right\rfloor}{2r\tilde{E}}+$ $+\frac{-\rho\cdot\pi^2\cdot n^2\left\lfloor r^2\cdot r_{\mathrm{i}}^2\cdot\left(\tilde{\nu}^2-3+2\cdot\tilde{\nu}\right)+r^4\cdot\left(1-\tilde{\nu}^2\right)\right\rfloor}{2\cdot r\cdot\tilde{E}}$
▪ annular cross section ▪ thin-walled ▪ orthotropic	$\sigma_{\mathrm{r}\omega}(r,n)=\rho\cdot(2\cdot\pi\cdot n)^2\cdot r_{\mathrm{o}}^2\cdot\frac{3+\tilde{\nu}_{\parallel\perp}}{9-E_{\mathrm{v}}^2}\cdot f_1(c_{\mathrm{k}},r)$ $\sigma_{\mathrm{t}\omega}(r,n)=\frac{\rho\cdot(2\cdot\pi\cdot n)^2\cdot r_{\mathrm{o}}^2}{9-E_{\mathrm{v}}^2}\cdot\left[(3+\tilde{\nu}_{\parallel\perp})\cdot E_{\mathrm{v}}\cdot f_2(c_{\mathrm{k}},r)-\left(E_{\mathrm{v}}^2+3\cdot\tilde{\nu}_{\parallel\perp}\right)\cdot\left(\frac{r}{r_{\mathrm{o}}}\right)^2\right]$ $u_{\mathrm{r}\omega}(r,n)=\left[\frac{\sigma_{\mathrm{t}\omega}(r,n)}{\tilde{E}_{\parallel}}-\frac{\tilde{\nu}_{\parallel\perp}\cdot\sigma_{\mathrm{r}\omega}(r,n)}{\tilde{E}_{\perp}}\right]\cdot r$ Where: $f_1(c_{\mathrm{k}},r)=\frac{1-c_{\mathrm{k}}^{E_{\mathrm{v}}+3}}{1-c_{\mathrm{k}}^{2E_{\mathrm{v}}}}\cdot\left(\frac{r}{r_{\mathrm{o}}}\right)^{E_{\mathrm{v}}-1}+\frac{1-c_{\mathrm{k}}^{E_{\mathrm{v}}-3}}{1-c_{\mathrm{k}}^{2E_{\mathrm{v}}}}\cdot c_{\mathrm{k}}^{E_{\mathrm{v}}+3}\cdot\left(\frac{r_{\mathrm{o}}}{r}\right)^{E_{\mathrm{v}}+1}-\left(\frac{r}{r_{\mathrm{o}}}\right)^2$ $f_2(c_{\mathrm{k}},r)=\frac{1-c_{\mathrm{k}}^{E_{\mathrm{v}}+3}}{1-c_{\mathrm{k}}^{2E_{\mathrm{v}}}}\cdot\left(\frac{r}{r_{\mathrm{o}}}\right)^{E_{\mathrm{v}}-1}-\frac{1-c_{\mathrm{k}}^{E_{\mathrm{v}}-3}}{1-c_{\mathrm{k}}^{2E_{\mathrm{v}}}}\cdot c_{\mathrm{k}}^{E_{\mathrm{v}}+3}\cdot\left(\frac{r_{\mathrm{o}}}{r}\right)^{E_{\mathrm{v}}+1}$, $c_k=\frac{r_{\mathrm{i}}}{r_{\mathrm{o}}}$

Table C-5 Formulas of radial σ_r and tangential stress σ_t and radial displacement u_r of circular and annular cross sections for isotropic and orthotropic materials due to thermal expansion for temperature rise of $\Delta\vartheta$ [54]

Cross section properties	Formulas of radial stress，tangential stress and radial displacement
▪ circular cross section ▪ isotropic	$\sigma_{\mathrm{r}\vartheta}(r)=0$ $\sigma_{\mathrm{t}\vartheta}(r)=0$ $u_{\mathrm{r}\vartheta}(r)=\tilde{\alpha}\cdot\Delta\vartheta\cdot r$, with $\tilde{\alpha}=(1+v)\cdot\alpha$
▪ annular cross section ▪ thin-walled ▪ Isotropic and orthotropic	$\sigma_{\mathrm{t}\vartheta}(r)=0$ $u_{\mathrm{r}\vartheta}(r)=\tilde{\alpha}_{\parallel}\cdot\Delta\vartheta\cdot r$
▪ annular cross section ▪ thick-walled ▪ isotropic	$\sigma_{\mathrm{r}\vartheta}(r)=0$ $\sigma_{\mathrm{t}\vartheta}(r)=0$ $u_{\mathrm{r}\vartheta}(r)=\tilde{\alpha}\cdot\Delta\vartheta\cdot r$, with $\tilde{\alpha}=(1+v)\cdot\alpha$
▪ annular cross section ▪ thick-walled ▪ orthotropic	$\sigma_{\mathrm{r}\vartheta}(r)=\dfrac{\tilde{E}_{\parallel}\cdot(\tilde{\alpha}_{\parallel}-\tilde{\alpha}_{\perp})\cdot\Delta\vartheta}{1-E_\mathrm{v}^2}\cdot\left[f_{1\vartheta}(r)+f_{2\vartheta}(r)-1\right]$ $\sigma_{\mathrm{t}\vartheta}(r)=\dfrac{\tilde{E}_{\parallel}\cdot(\tilde{\alpha}_{\parallel}-\tilde{\alpha}_{\perp})\cdot\Delta\vartheta\cdot E_\mathrm{v}}{1-E_\mathrm{v}^2}\cdot\left(f_{1\vartheta}(r)-f_{2\vartheta}(r)-\dfrac{1}{E_\mathrm{v}}\right)$ $u_{\mathrm{r}\vartheta}(r)=\left[\dfrac{\sigma_{\mathrm{t}\vartheta}(r)}{\tilde{E}_{\parallel}}-\dfrac{\tilde{v}_{\parallel\perp}\cdot\sigma_{\mathrm{r}\vartheta}(r)}{\tilde{E}_{\perp}}\right]\cdot r$ Where: $f_{1\vartheta}(r)=\dfrac{\left(r_\mathrm{i}^{1+E_\mathrm{v}}-r_\mathrm{o}^{1+E_\mathrm{v}}\right)\cdot r^{E_\mathrm{v}-1}}{r_\mathrm{i}^{2E_\mathrm{v}}-r_\mathrm{o}^{2E_\mathrm{v}}}$, $f_{2\vartheta}(r)=\dfrac{\left(r_\mathrm{i}^{2E_\mathrm{v}}\cdot r_\mathrm{o}^{1+E_\mathrm{v}}-r_\mathrm{i}^{1+E_\mathrm{v}}\cdot r_\mathrm{o}^{2E_\mathrm{v}}\right)\cdot r^{-E_\mathrm{v}-1}}{r_\mathrm{i}^{2E_\mathrm{v}}-r_\mathrm{o}^{2E_\mathrm{v}}}$ With: $\tilde{\alpha}_{\parallel}=\left(1+\dfrac{v_{\parallel\perp}\cdot\alpha_{\perp}}{\alpha_{\parallel}}\right)\cdot\alpha_{\parallel}$, $\tilde{\alpha}_{\perp}=\left(1+\dfrac{v_{\perp\perp}\cdot\alpha_{\perp}}{\alpha_{\perp}}\right)\cdot\alpha_{\perp}$

Appendix D. T-equivalent Thermal Network

Considering a single rod with an axial length of L and a constant cross section A (Fig. D-1), which has a constant internal loss density q_i and constant thermal conductivity λ, the applied boundary conditions are constant temperature ϑ_a and ϑ_b on each end surface.

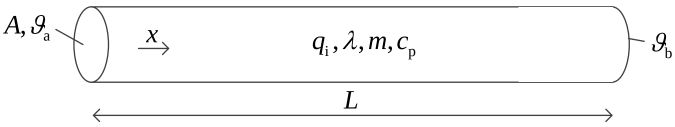

Fig. D-1 One dimensional heat conduction in a rod with internal loss density q_i, axial length L, section area A, mass m, thermal conductivity λ, specific heat capacity c, constant temperatures ϑ_a, ϑ_b at the end surfaces of the rod

The heat equation for steady state heat conduction is

$$\lambda \cdot \frac{\partial^2 \vartheta}{\partial x^2} + q_\mathrm{i} = 0 . \tag{D-1}$$

1) $q_\mathrm{i} = 0$

The analytical solution for $q_\mathrm{i} = 0$ is

$$\vartheta(x) = \frac{\vartheta_\mathrm{b} - \vartheta_\mathrm{a}}{L} \cdot x + \vartheta_\mathrm{a} . \tag{D-2}$$

The conductive heat flux is

$$q_\mathrm{x} = -\lambda \cdot A \cdot \frac{\mathrm{d}\vartheta}{\mathrm{d}x} = \frac{\lambda \cdot A}{L} \cdot (\vartheta_\mathrm{a} - \vartheta_\mathrm{b}) . \tag{D-3}$$

Thus the equivalent thermal resistance and average temperature are calculated by

$$R_\mathrm{x} = \frac{\vartheta_\mathrm{a} - \vartheta_\mathrm{b}}{q_\mathrm{x}} = \frac{L}{\lambda \cdot A} , \tag{D-4}$$

$$\bar{\vartheta} = \frac{1}{L} \cdot \int_0^L \vartheta(x)\ \mathrm{d}x = \frac{\vartheta_\mathrm{a} + \vartheta_\mathrm{b}}{2}. \tag{D-5}$$

Splitting the thermal resistance into two identical parts, the conventional equivalent thermal network is obtained in Fig. D-2 a), with a middle node which gives the average temperature. If there is internal heat generation, the heat source P_i ($P_\mathrm{i} = \int q_\mathrm{i} \mathrm{d}_\mathrm{V} = q_\mathrm{i} \cdot A \cdot L$) will be also connected to the middle node, as well as the thermal capacitance C ($C = m \cdot c$, m: mass of the rod, c: material specific heat capacity) of the rod.

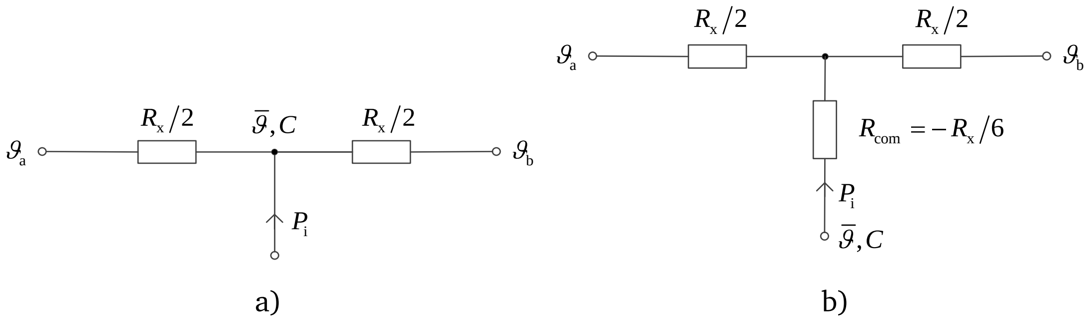

Fig. D-2 Equivalent thermal network for steady state heat conduction in a single rod, internal heat source $P_\mathrm{i} = \int q_\mathrm{i} \mathrm{d}_\mathrm{V} = q_\mathrm{i} \cdot A \cdot L$, thermal capacitance $C = m \cdot c$: a) conventional equivalent network, b) T-equivalent network

2) $q_\mathrm{i} > 0$

If the internal loss density q_i is taken into account, the analytical solution of (D-1) is

$$\vartheta(x) = -\frac{q_\mathrm{i}}{2 \cdot \lambda} \cdot x^2 + \left(\frac{\vartheta_\mathrm{b} - \vartheta_\mathrm{a}}{L} + \frac{q_\mathrm{i} \cdot L}{2 \cdot \lambda} \right) \cdot x + \vartheta_\mathrm{a}. \tag{D-6}$$

The average temperature is

$$\bar{\vartheta} = \frac{1}{L} \cdot \int_0^L \vartheta(x)\ \mathrm{d}x = \frac{q_\mathrm{i}}{12 \cdot \lambda} \cdot L^2 + \frac{\vartheta_\mathrm{a} + \vartheta_\mathrm{b}}{2}. \tag{D-7}$$

The temperature distribution $\vartheta(x)$ is non-linear with x due to the internal loss density q_i, thus a T-equivalent network is used with a negative compensation thermal resistance $R_\mathrm{com} = -R_\mathrm{x}/6$, which is derived by *Kirchhoff*'s circuit law. The internal heat source and heat capacitance are connected to this compensation resistance instead of middle node as shown in Fig. D-2 b). Regarding multi-directional heat flow, a 3-dimentinal equivalent network can be used by connecting 3 T-equivalent resistances as shown in Fig. D-3.

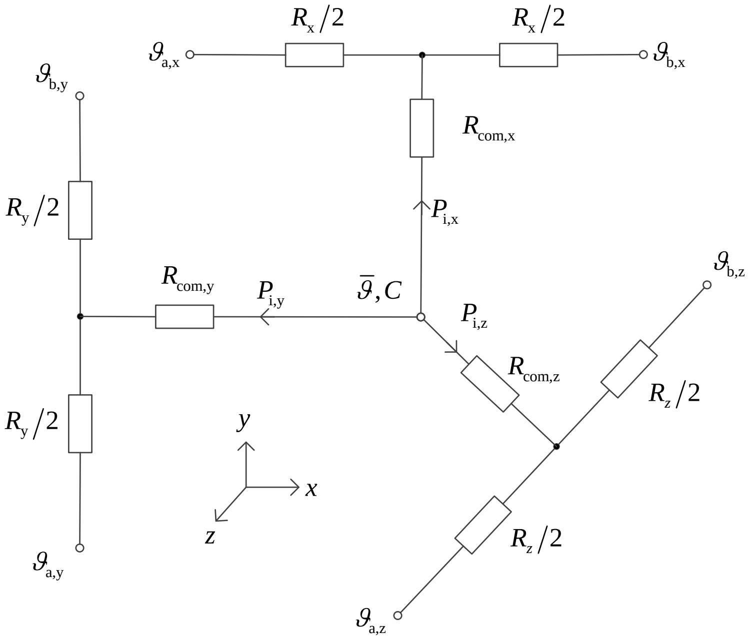

Fig. D-3 3-dimensional T-equivalent thermal network

A comparative study of the above one-dimensional networks are carried out based on three cases with different boundary conditions, the same as in [68]. An internal heat source is considered in Case 1 and Case 2, with fixed temperatures at two end surfaces. In case 3, an external heat flows in end surface *a* is taken into account without internal heat generation. The temperature at end surface *b* is fixed.

Table D-1 Study cases for the comparison of different one-dimensional thermal networks, initial condition: $\vartheta_{x,t=0} = 0$, P_a: external heat flows in at end surface *a*

	ϑ_a [°C]	ϑ_b [°C]	P_a [W]	P_i [W]
Case 1	0	0	0	10
Case 2	0	70	0	10
Case 3	-	0	10	0

Fig. D-4 and Fig. D-5 show the results calculated by different networks compared to the results calculated by finite element method (FEM). The two-node network is composed by a series connection of double one-node network in Fig. D-2 a) with halved parameters, representing a discrete model. For steady state calculation in Fig. D-4, the T-equivalent network shows a very good agreement with the FEM results, while one-node network gives an overestimation of the temperature due to the influence of the distributed losses. Two-node network gives a better estimation than one-node network due to the discretization. However, for the transient calculation for Case 1, which considers the internal heat source without external heat flows in, both conventional networks show large deviations, while T-equivalent network leads to a relatively accurate result. In terms of transient calculation for Case 3, where external heat flows in is considered without internal heat source, the calculation with two-node model coincides well with the FEM result. T-equivalent network shows the worst agreement due to the effect of the negative compensation resistance.

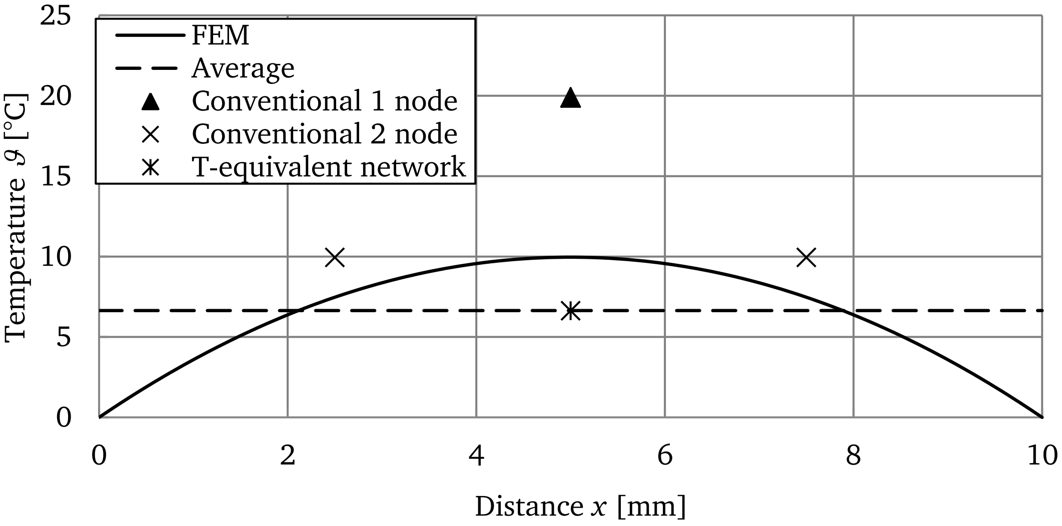

a)

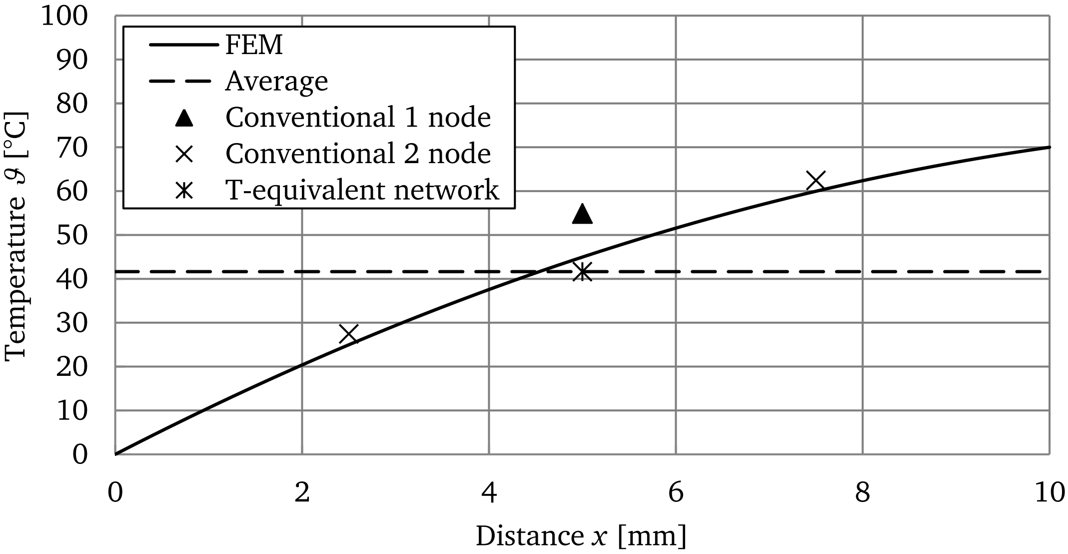

b)

Fig. D-4 Calculation of steady state temperature distribution in the rod, according to [68]: a) Case 1, b) Case 2

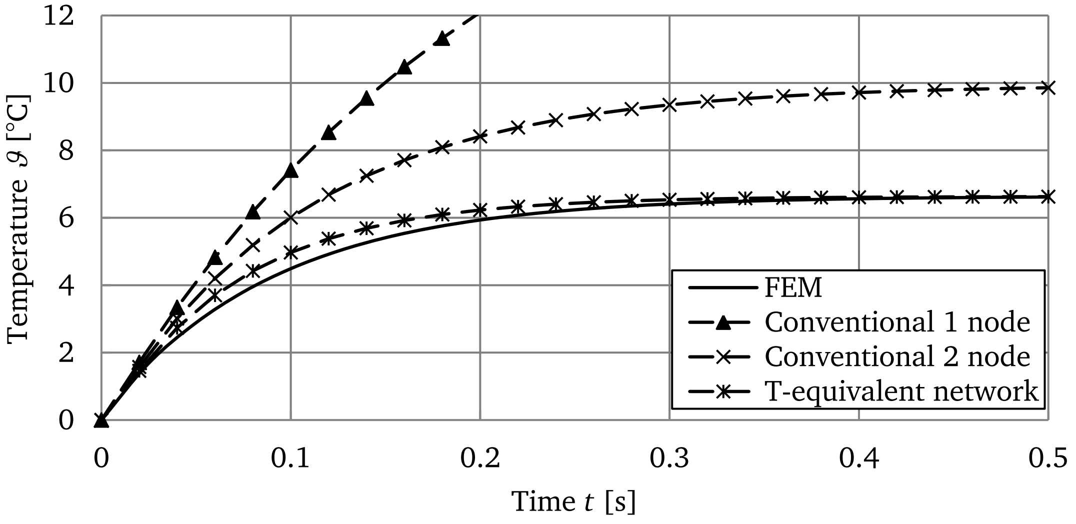

a)

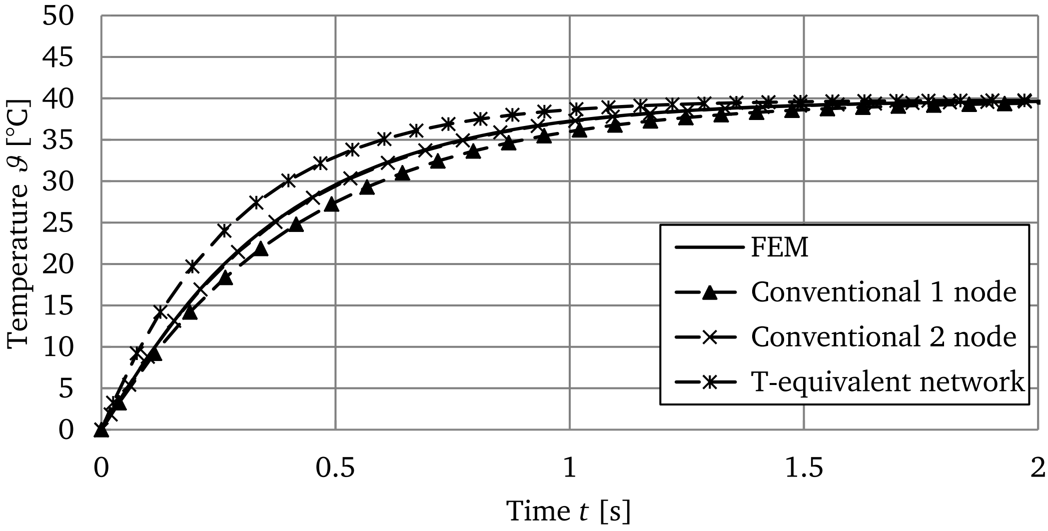

b)

Fig. D-5 Calculation of the transient temperature of the rod, according to [68]:

a) Case 1, b) Case 3

Appendix E. Modeling of the Flywheel Thermal Network

Table E-1 Formulas for the modeling of the flywheel system in Fig. E-1

Convection
$R_{\text{F-s}} = \frac{1}{\alpha_{\text{eq}} \cdot A_{\text{s}}}$
Radiation
The radiative thermal resistance depends on the temperatures of the radiative body and absorptive body, calculated by $P_{\text{rad}} = \frac{\sigma \cdot (T_1^4 - T_2^4)}{\frac{1-\varepsilon_1}{\varepsilon_1 \cdot A_1} + \frac{1}{A_1 \cdot F_{12}} + \frac{1-\varepsilon_2}{\varepsilon_2 \cdot A_2}}$ where the subscript 1 denotes the radiative surface, 2 denotes the absorptive surface. F_{12} is the facing factor depending on the position of the two surfaces. A is the surface area, T is the absolute temperature (in K) on the surface (The corresponding celsius temperature is denoted by ϑ in °C), ε is the surface emissivity, and σ is *Stefan-Boltzmann* constant, $\sigma = 5.67 \times 10^{-8}$ W/(m$^2 \cdot$ K^4).
Conduction
E-machine stator yoke: $R_{\text{sy,r1}} = -\frac{1}{8 \cdot \pi \cdot \lambda_{\text{Fe,r}} \cdot L_{\text{Fe}} \cdot k_{\text{Fe}} \cdot \left(r_{\text{so}}^2 - r_{\text{sb}}^2\right)} \cdot \left[r_{\text{so}}^2 + r_{\text{sb}}^2 - \frac{4 \cdot r_{\text{so}}^2 \cdot r_{\text{sb}}^2 \cdot \ln\left(r_{\text{so}}/r_{\text{sb}}\right)}{r_{\text{so}}^2 - r_{\text{sb}}^2} \right],$ $R_{\text{sy,r2}} = \frac{1}{4 \cdot \pi \cdot \lambda_{\text{Fe,r}} \cdot L_{\text{Fe}} \cdot k_{\text{Fe}}} \cdot \left[1 - \frac{2 \cdot r_{\text{sb}}^2 \cdot \ln\left(r_{\text{so}}/r_{\text{sb}}\right)}{r_{\text{so}}^2 - r_{\text{sb}}^2} \right],$ $R_{\text{sy,r3}} = \frac{1}{4 \cdot \pi \cdot \lambda_{\text{Fe,r}} \cdot L_{\text{Fe}} \cdot k_{\text{Fe}}} \cdot \left[\frac{2 \cdot r_{\text{so}}^2 \cdot \ln\left(r_{\text{so}}/r_{\text{sb}}\right)}{r_{\text{so}}^2 - r_{\text{sb}}^2} - 1 \right];$ $R_{\text{sy,a}} = \frac{L_{\text{Fe}}}{2 \cdot \pi \cdot \lambda_{\text{Fe,a}} \cdot \left(r_{\text{so}}^2 - r_{\text{sb}}^2\right)}, \ R_{\text{sy,a1}} = -\frac{R_{\text{sy,a}}}{3}.$ $[mc]_{\text{sy}} = \rho_{\text{Fe}} \cdot c_{\text{Fe}} \cdot \pi \cdot L_{\text{Fe}} \cdot k_{\text{Fe}} \cdot \left(r_{\text{so}}^2 - r_{\text{sb}}^2\right).$

E-machine stator teeth: $R_{\mathrm{st,r1}} = -\frac{R_{\mathrm{st,r2}}}{3}$, $R_{\mathrm{st,r2}} = R_{\mathrm{st,r3}} = \frac{r_{\mathrm{sb}} - r_{\mathrm{si}}}{2 \cdot \lambda_{\mathrm{Fe,r}} \cdot L_{\mathrm{Fe}} \cdot k_{\mathrm{Fe}} \cdot b_{\mathrm{ts}} \cdot Q_{\mathrm{s}}}$; $R_{\mathrm{st,a}} = \frac{L_{\mathrm{Fe}}}{2 \cdot \lambda_{\mathrm{Fe,a}} \cdot b_{\mathrm{ts}} \cdot h_{\mathrm{s}} \cdot Q_{\mathrm{s}}}$, $R_{\mathrm{st,a1}} = -\frac{R_{\mathrm{st,a}}}{3}$. $[mc]_{\mathrm{st}} = \rho_{\mathrm{Fe}} \cdot c_{\mathrm{Fe}} \cdot b_{\mathrm{ts}} \cdot h_{\mathrm{s}} \cdot Q_{\mathrm{s}}$.
E-machine stator winding in slots: $R_{\mathrm{sw,a1}} = -\frac{R_{\mathrm{sw,a}}}{3}$, $R_{\mathrm{sw,a}} = \frac{L_{\mathrm{Fe}}}{2 \cdot \lambda_{\mathrm{Cu}} \cdot A_{\mathrm{Cu}}}$, $A_{\mathrm{Cu}} = k_{\mathrm{fill}} \cdot A_{\mathrm{slot}}$, $A_{\mathrm{slot}} = \left(b_{\mathrm{s1}} + b_{\mathrm{s2}}\right) \cdot h_{\mathrm{s}} / 2$; $R_{\mathrm{sw\text{-}sy}} = \frac{h_{\mathrm{in}}}{2 \cdot \lambda_{\mathrm{in}} \cdot L_{\mathrm{Fe}} \cdot h_{\mathrm{s}} \cdot Q_{\mathrm{s}}}$; $R_{\mathrm{sw\text{-}sy}} = \frac{h_{\mathrm{in}}}{\lambda_{\mathrm{in}} \cdot L_{\mathrm{Fe}} \cdot b_{\mathrm{s2}} \cdot Q_{\mathrm{s}}}$; $[mc]_{\mathrm{sw}} = \rho_{\mathrm{Cu}} \cdot c_{\mathrm{Cu}} \cdot L_{\mathrm{Fe}} \cdot A_{\mathrm{Cu}} \cdot Q_{\mathrm{s}}$.
E-machine stator winding overhang: $R_{\mathrm{sew,a}} = \frac{L_{\mathrm{d}}}{\lambda_{\mathrm{Cu}} \cdot A_{\mathrm{Cu}} \cdot Q_{\mathrm{s}}}$; $R_{\mathrm{sew\text{-}st}} = \frac{L_{\mathrm{d}}}{\lambda_{\mathrm{resin}} \cdot \left[\pi \cdot \left(r_{\mathrm{sb}}^2 - r_{\mathrm{sew2}}^2\right) - A_{\mathrm{Cu}} \cdot Q_{\mathrm{s}}\right]}$, $R_{\mathrm{sew\text{-}sy}} = \frac{L_{\mathrm{d}}}{\lambda_{\mathrm{resin}} \cdot \pi \cdot \left(r_{\mathrm{so}}^2 - r_{\mathrm{sb}}^2\right)}$; $R_{\mathrm{sew,1}} = \frac{1}{2 \cdot \pi \cdot \lambda_{\mathrm{resin}} \cdot L_{\mathrm{end}}} \cdot \ln\left(\frac{2 \cdot r_{\mathrm{so}}}{r_{\mathrm{so}} + r_{\mathrm{sew1}}}\right)$, $R_{\mathrm{sew,2}} = \frac{1}{2 \cdot \pi \cdot \lambda_{\mathrm{resin}} \cdot L_{\mathrm{end}}} \cdot \ln\left(\frac{r_{\mathrm{so}} + r_{\mathrm{sew1}}}{2 \cdot r_{\mathrm{sew1}}}\right)$, $R_{\mathrm{sew,3}} = \frac{1}{2 \cdot \pi \cdot \lambda_{\mathrm{resin}} \cdot L_{\mathrm{end}}} \cdot \left(r_{\mathrm{sw2}} - r_{\mathrm{sew2}}\right)$; $[mc]_{\mathrm{sew}} = \rho_{\mathrm{Cu}} \cdot c_{\mathrm{Cu}} \cdot V_{\mathrm{Cu,sew}} + \rho_{\mathrm{resin}} \cdot c_{\mathrm{resin}} \cdot V_{\mathrm{resin,sew}}$.
E-machine rotor bandage: $R_{\mathrm{B,r2}} = \frac{1}{2 \cdot \pi \cdot \lambda_{\mathrm{CF}} \cdot L_{\mathrm{rot}}} \cdot \ln\left(\frac{2 \cdot r_{\mathrm{ro}}}{r_{\mathrm{ro}} + r_{\mathrm{mo}}}\right)$, $R_{\mathrm{B,r3}} = \frac{1}{2 \cdot \pi \cdot \lambda_{\mathrm{CF}} \cdot L_{\mathrm{rot}}} \cdot \ln\left(\frac{r_{\mathrm{ro}} + r_{\mathrm{mo}}}{2 \cdot r_{\mathrm{mo}}}\right)$; $[mc]_{\mathrm{B}} = \rho_{\mathrm{CF}} \cdot c_{\mathrm{CF}} \cdot \pi \cdot L_{\mathrm{rot}} \cdot \left(r_{\mathrm{ro}}^2 - r_{\mathrm{mo}}^2\right)$.
E-machine rotor magnet: $R_{\mathrm{mag,r1}} = -\frac{1}{8 \cdot \pi \cdot \lambda_{\mathrm{mag}} \cdot L_{\mathrm{rot}} \cdot \left(r_{\mathrm{mo}}^2 - r_{\mathrm{mi}}^2\right)} \cdot \left[r_{\mathrm{mo}}^2 + r_{\mathrm{mi}}^2 - \frac{4 \cdot r_{\mathrm{mo}}^2 \cdot r_{\mathrm{mi}}^2 \cdot \ln\left(r_{\mathrm{mo}} / r_{\mathrm{mi}}\right)}{r_{\mathrm{mo}}^2 - r_{\mathrm{mi}}^2}\right]$, $R_{\mathrm{mag,r2}} = \frac{1}{4 \cdot \pi \cdot \lambda_{\mathrm{mag}} \cdot L_{\mathrm{rot}}} \cdot \left[1 - \frac{2 \cdot r_{\mathrm{mi}}^2 \cdot \ln\left(r_{\mathrm{mo}} / r_{\mathrm{mi}}\right)}{r_{\mathrm{mo}}^2 - r_{\mathrm{mi}}^2}\right]$,

$$R_{\mathrm{mag,r3}} = \frac{1}{4 \cdot \pi \cdot \lambda_{\mathrm{mag}} \cdot L_{\mathrm{rot}}} \cdot \left[\frac{2 \cdot r_{\mathrm{mo}}^2 \cdot \ln\left(r_{\mathrm{mo}} / r_{\mathrm{mi}}\right)}{r_{\mathrm{mo}}^2 - r_{\mathrm{mi}}^2} - 1 \right];$$

$$[mc]_{\mathrm{mag}} = \rho_{\mathrm{mag}} \cdot c_{\mathrm{mag}} \cdot \pi \cdot L_{\mathrm{rot}} \cdot \left(r_{\mathrm{mo}}^2 - r_{\mathrm{mi}}^2 \right).$$

E-machine rotor iron:

$$R_{\mathrm{Fer,r1}} = -\frac{1}{8 \cdot \pi \cdot \lambda_{\mathrm{Fe,r}} \cdot L_{\mathrm{rot}} \cdot k_{\mathrm{Fe}} \cdot \left(r_{\mathrm{mi}}^2 - r_{\mathrm{sh}}^2 \right)} \cdot \left[r_{\mathrm{mi}}^2 + r_{\mathrm{sh}}^2 - \frac{4 \cdot r_{\mathrm{mi}}^2 \cdot r_{\mathrm{sh}}^2 \cdot \ln\left(r_{\mathrm{mi}} / r_{\mathrm{sh}}\right)}{r_{\mathrm{mi}}^2 - r_{\mathrm{sh}}^2} \right],$$

$$R_{\mathrm{Fer,r2}} = \frac{1}{4 \cdot \pi \cdot \lambda_{\mathrm{Fe,r}} \cdot L_{\mathrm{rot}} \cdot k_{\mathrm{Fe}}} \cdot \left[1 - \frac{2 \cdot r_{\mathrm{sh}}^2 \cdot \ln\left(r_{\mathrm{mi}} / r_{\mathrm{sh}}\right)}{r_{\mathrm{mi}}^2 - r_{\mathrm{sh}}^2} \right],$$

$$R_{\mathrm{Fer,r3}} = \frac{1}{4 \cdot \pi \cdot \lambda_{\mathrm{Fe,r}} \cdot L_{\mathrm{rot}} \cdot k_{\mathrm{Fe}}} \cdot \left[\frac{2 \cdot r_{\mathrm{mi}}^2 \cdot \ln\left(r_{\mathrm{mi}} / r_{\mathrm{sh}}\right)}{r_{\mathrm{mi}}^2 - r_{\mathrm{sh}}^2} - 1 \right];$$

$$[mc]_{\mathrm{Fer}} = \rho_{\mathrm{Fe}} \cdot c_{\mathrm{Fe}} \cdot \pi \cdot L_{\mathrm{rot}} \cdot k_{\mathrm{Fe}} \cdot \left(r_{\mathrm{mi}}^2 - r_{\mathrm{sh}}^2 \right).$$

Shaft:

$$R_{\mathrm{sh,r}} = \frac{1}{2 \cdot \pi \cdot \lambda_{\mathrm{sh}} \cdot L_{\mathrm{rot}}}, \; R_{\mathrm{sh,a}} = \frac{1}{2 \cdot \pi \cdot \lambda_{\mathrm{sh}} \cdot r_{\mathrm{sh}}^2};$$

$$R_{\mathrm{sh,e,r1}} = \frac{1}{2 \cdot \pi \cdot \lambda_{\mathrm{sh}} \cdot L_{\mathrm{sh,e1}}}, R_{\mathrm{sh,e,r2}} = \frac{1}{2 \cdot \pi \cdot \lambda_{\mathrm{sh}} \cdot L_{\mathrm{sh,e2}}}; \; R_{\mathrm{sh,e,a1}} = \frac{L_{\mathrm{sh,e1}}}{2 \cdot \pi \cdot \lambda_{\mathrm{sh}} \cdot r_{\mathrm{sh,e1}}^2}, \; R_{\mathrm{sh,e,a2}} = \frac{L_{\mathrm{sh,e2}}}{2 \cdot \pi \cdot \lambda_{\mathrm{sh}} \cdot r_{\mathrm{sh,e2}}^2};$$

$$[mc]_{\mathrm{sh}} = \rho_{\mathrm{sh}} \cdot c_{\mathrm{sh}} \cdot \pi \cdot \left[r_{\mathrm{sh}}^2 \cdot L_{\mathrm{rot}} + r_{\mathrm{sh,e1}}^2 \cdot L_{\mathrm{sh,e1}} + r_{\mathrm{sh,e2}}^2 \cdot L_{\mathrm{sh,e2}} \right].$$

Flywheel body:

$$R_{\mathrm{FW,r}} = \frac{1}{2 \cdot \pi \cdot \lambda_{\mathrm{sh}} \cdot L_{\mathrm{FW}}}, \; R_{\mathrm{FW,a}} = \frac{L_{\mathrm{FW}}}{2 \cdot \pi \cdot \lambda_{\mathrm{sh}} \cdot r_{\mathrm{FW}}^2};$$

$$[mc]_{\mathrm{FW}} = \rho_{\mathrm{sh}} \cdot c_{\mathrm{sh}} \cdot \pi \cdot r_{\mathrm{FW}}^2 \cdot L_{\mathrm{FW}}.$$

Magnetic bearing rotor:

$$R_{\mathrm{MB1,r,r}} = \frac{1}{2 \cdot \pi \cdot \lambda_{\mathrm{sh}} \cdot L_{\mathrm{MB1,r}}}, \; R_{\mathrm{MB1,r,a}} = \frac{L_{\mathrm{MB1,r}}}{2 \cdot \pi \cdot \lambda_{\mathrm{sh}} \cdot r_{\mathrm{MB1,ro}}^2};$$

$$[mc]_{\mathrm{MB1,r}} = \rho_{\mathrm{sh}} \cdot c_{\mathrm{sh}} \cdot \pi \cdot r_{\mathrm{MB1,ro}}^2 \cdot L_{\mathrm{MB1,r}}.$$

$$R_{\mathrm{MB2,r,r}} = \frac{1}{2 \cdot \pi \cdot \lambda_{\mathrm{sh}} \cdot L_{\mathrm{MB2,r}}}, \; R_{\mathrm{MB2,r,a}} = \frac{L_{\mathrm{MB2,r}}}{2 \cdot \pi \cdot \lambda_{\mathrm{sh}} \cdot r_{\mathrm{MB2,ro}}^2};$$

$$[mc]_{\mathrm{MB2,r}} = \rho_{\mathrm{sh}} \cdot c_{\mathrm{sh}} \cdot \pi \cdot r_{\mathrm{MB2,ro}}^2 \cdot L_{\mathrm{MB2,r}}.$$

Magnetic bearing stator:

$$R_{\mathrm{MB1,s,r1}} = -\frac{\left[r_{\mathrm{MB1,so}}^2 + r_{\mathrm{MB1,si}}^2 - \frac{4 \cdot r_{\mathrm{MB1,so}}^2 \cdot r_{\mathrm{MB1,si}}^2 \cdot \ln\left(r_{\mathrm{MB1,so}} / r_{\mathrm{MB1,si}}\right)}{r_{\mathrm{MB1,so}}^2 - r_{\mathrm{MB1,si}}^2} \right]}{8 \cdot \pi \cdot \lambda_{\mathrm{Fe,r}} \cdot L_{\mathrm{MB1,s}} \cdot k_{\mathrm{Fe}} \cdot \left(r_{\mathrm{MB1,so}}^2 - r_{\mathrm{MB1,si}}^2 \right)},$$

$$R_{\mathrm{MB1,s,r2}} = \frac{1}{4\cdot\pi\cdot\lambda_{\mathrm{Fe,r}}\cdot L_{\mathrm{MB1,s}}\cdot k_{\mathrm{Fe}}}\cdot\left[1-\frac{2\cdot r_{\mathrm{MB1,si}}^2\cdot\ln\left(r_{\mathrm{MB1,so}}/r_{\mathrm{MB1,si}}\right)}{r_{\mathrm{MB1,so}}^2-r_{\mathrm{MB1,si}}^2}\right],$$

$$R_{\mathrm{MB1,s,r3}} = \frac{1}{4\cdot\pi\cdot\lambda_{\mathrm{Fe,r}}\cdot L_{\mathrm{MB1,s}}\cdot k_{\mathrm{Fe}}}\cdot\left[\frac{2\cdot r_{\mathrm{MB1,so}}^2\cdot\ln\left(r_{\mathrm{MB1,so}}/r_{\mathrm{MB1,si}}\right)}{r_{\mathrm{MB1,so}}^2-r_{\mathrm{MB1,si}}^2}-1\right];$$

$$[mc]_{\mathrm{MB1,s}} = \rho_{\mathrm{Fe}}\cdot c_{\mathrm{Fe}}\cdot\pi\cdot L_{\mathrm{MB1,s}}\cdot k_{\mathrm{Fe}}\cdot\left(r_{\mathrm{MB1,so}}^2-r_{\mathrm{MB1,si}}^2\right).$$

$$R_{\mathrm{MB2,s,r1}} = -\frac{\left[r_{\mathrm{MB2,so}}^2+r_{\mathrm{MB2,si}}^2-\dfrac{4\cdot r_{\mathrm{MB2,so}}^2\cdot r_{\mathrm{MB2,si}}^2\cdot\ln\left(r_{\mathrm{MB2,so}}/r_{\mathrm{MB2,si}}\right)}{r_{\mathrm{MB2,so}}^2-r_{\mathrm{MB2,si}}^2}\right]}{8\cdot\pi\cdot\lambda_{\mathrm{Fe,r}}\cdot L_{\mathrm{MB2,s}}\cdot k_{\mathrm{Fe}}\cdot\left(r_{\mathrm{MB2,so}}^2-r_{\mathrm{MB2,si}}^2\right)},$$

$$R_{\mathrm{MB2,s,r2}} = \frac{1}{4\cdot\pi\cdot\lambda_{\mathrm{Fe,r}}\cdot L_{\mathrm{MB2,s}}\cdot k_{\mathrm{Fe}}}\cdot\left[1-\frac{2\cdot r_{\mathrm{MB2,si}}^2\cdot\ln\left(r_{\mathrm{MB2,so}}/r_{\mathrm{MB2,si}}\right)}{r_{\mathrm{MB2,so}}^2-r_{\mathrm{MB2,si}}^2}\right],$$

$$R_{\mathrm{MB2,s,r3}} = \frac{1}{4\cdot\pi\cdot\lambda_{\mathrm{Fe,r}}\cdot L_{\mathrm{MB2,s}}\cdot k_{\mathrm{Fe}}}\cdot\left[\frac{2\cdot r_{\mathrm{MB2,so}}^2\cdot\ln\left(r_{\mathrm{MB2,so}}/r_{\mathrm{MB2,si}}\right)}{r_{\mathrm{MB2,so}}^2-r_{\mathrm{MB2,si}}^2}-1\right];$$

$$[mc]_{\mathrm{MB2,s}} = \rho_{\mathrm{Fe}}\cdot c_{\mathrm{Fe}}\cdot\pi\cdot L_{\mathrm{MB2,s}}\cdot k_{\mathrm{Fe}}\cdot\left(r_{\mathrm{MB2,so}}^2-r_{\mathrm{MB2,si}}^2\right).$$

Housing:

$$R_{\mathrm{F,FW}} = \frac{L_{\mathrm{FW}}}{2\cdot\pi\cdot\lambda_{\mathrm{F}}\cdot\left(r_{\mathrm{Fo,FW}}^2-r_{\mathrm{Fi,FW}}^2\right)},$$

$$[mc]_{\mathrm{F,FW}} = \rho_{\mathrm{F}}\cdot c_{\mathrm{F}}\cdot\pi\cdot L_{\mathrm{FW}}\cdot\left(r_{\mathrm{Fo,FW}}^2-r_{\mathrm{Fi,FW}}^2\right).$$

$$R_{\mathrm{F,MB2}} = \frac{L_{\mathrm{MB2,s}}}{2\cdot\pi\cdot\lambda_{\mathrm{F}}\cdot\left(r_{\mathrm{Fo,MB2}}^2-r_{\mathrm{MB2,so}}^2\right)};$$

$$[mc]_{\mathrm{F,MB2}} = \rho_{\mathrm{F}}\cdot c_{\mathrm{F}}\cdot\pi\cdot L_{\mathrm{MB2,s}}\cdot\left(r_{\mathrm{Fo,MB2}}^2-r_{\mathrm{MB2,so}}^2\right).$$

$$[mc]_{\mathrm{F}} = \rho_{\mathrm{F}}\cdot c_{\mathrm{F}}\cdot\pi\cdot\left(r_{\mathrm{Fo}}^2-r_{\mathrm{so}}^2\right)\cdot\left(L_{\mathrm{Fe}}+2\cdot L_{\mathrm{end}}+L_{\mathrm{MB1,s}}\right).$$

Table E-2 Variables and subscripts in the formulas in Table E-1

<table>
<tr><th colspan="4">Variables</th></tr>
<tr><td>ρ</td><td colspan="3">Mass density</td></tr>
<tr><td>c</td><td colspan="3">Specific heat capacity</td></tr>
<tr><td>λ</td><td colspan="3">Thermal conductivity</td></tr>
<tr><td>A_s</td><td colspan="3">Equivalent cooling surface area</td></tr>
<tr><td>α_{eq}</td><td colspan="3">Equivalent heat transfer coefficient of stator water cooling</td></tr>
<tr><td>$\lambda_{\mathrm{Fe,r}}$, $\lambda_{\mathrm{Fe,a}}$</td><td colspan="3">Thermal conductivity of E-machine stator iron package; r: radial direction, a: axial direction</td></tr>
<tr><td>k_{fill}</td><td colspan="3">E-machine stator slot filling factor</td></tr>
<tr><td>Q_s</td><td colspan="3">Nr. of E-machine stator slots</td></tr>
<tr><td>$V_{\mathrm{Cu,sew}}$</td><td colspan="3">Volume of copper material in impregnated E-machine stator winding over-hang</td></tr>
<tr><td>$V_{\mathrm{resin,sew}}$</td><td colspan="3">Volume of resin material in impregnated E-machine stator winding over-hang</td></tr>
<tr><th colspan="4">Subscript:</th></tr>
<tr><td>Fe</td><td>Laminated iron package</td><td>CF</td><td>Carbon fiber material</td></tr>
<tr><td>Cu</td><td>Copper</td><td>mag</td><td>Magnets</td></tr>
<tr><td>in</td><td>Insulation material in slots</td><td>sh</td><td>Shaft</td></tr>
<tr><td>resin</td><td>Winding impregnation material</td><td>F</td><td>Housing</td></tr>
</table>

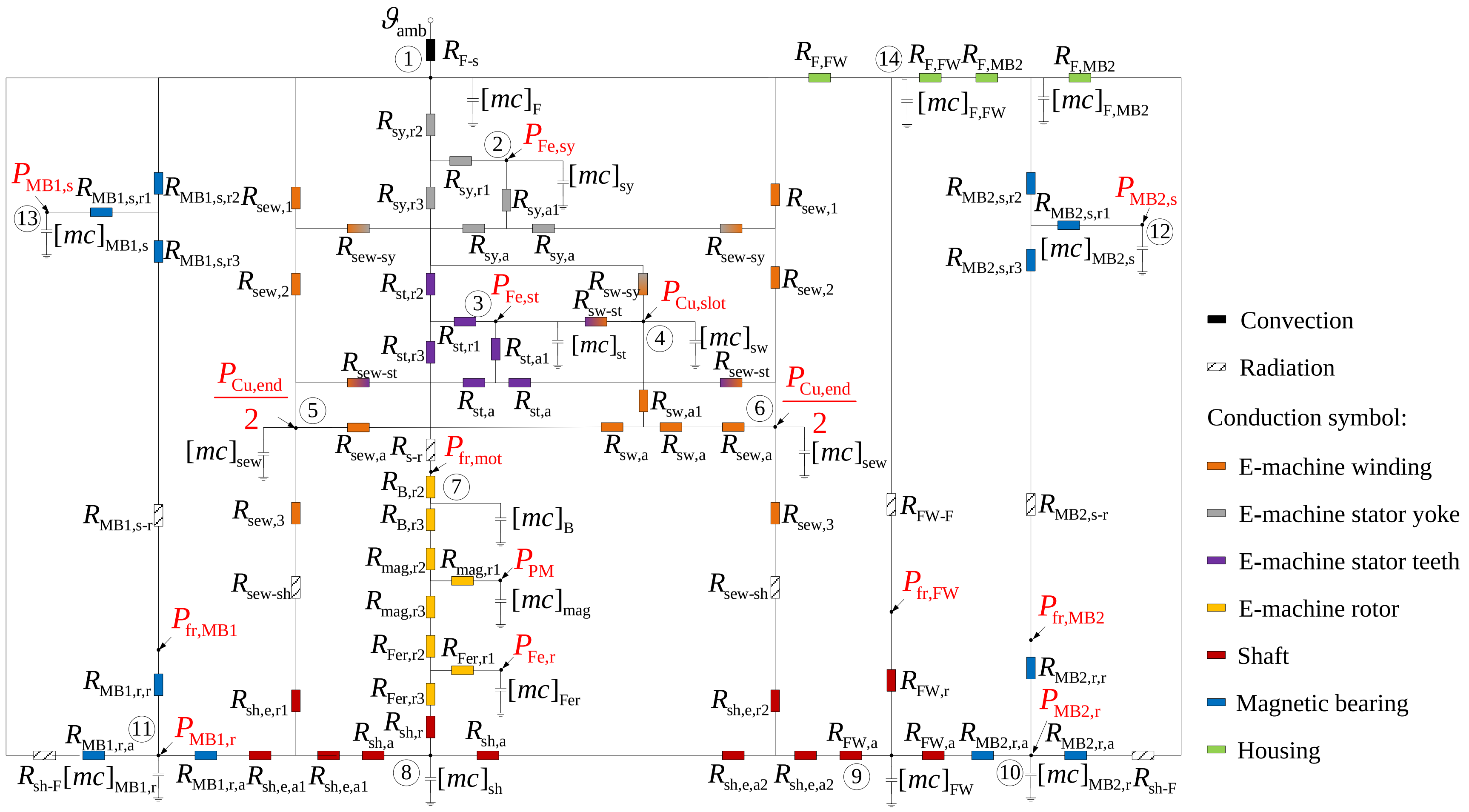

Fig. E-1 Thermal network of the flywheel system

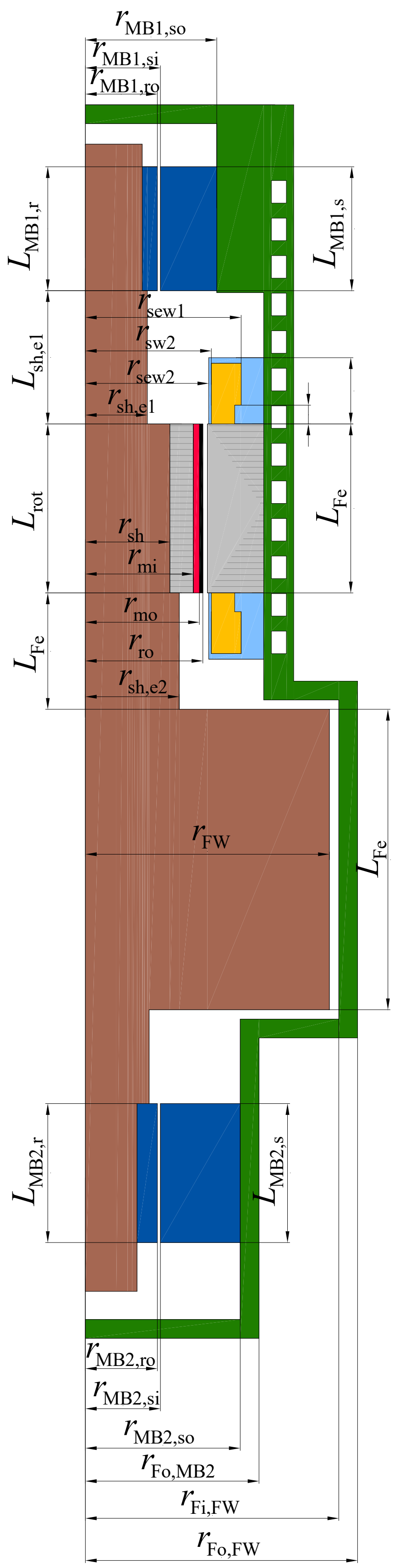

Fig. E-2 Dimensions of the modeled system

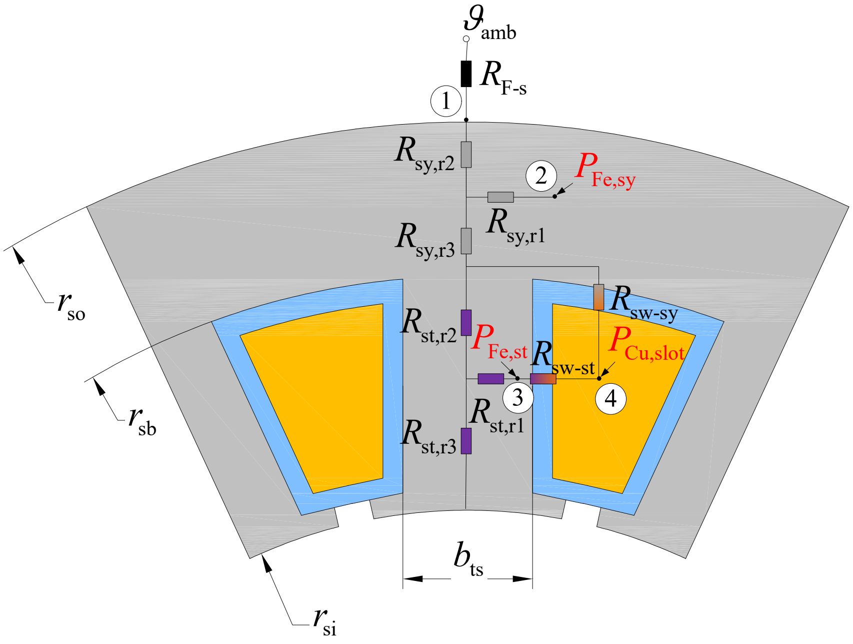

Fig. E-3 Thermal network of the E-machine stator, showing radial heat transfer paths

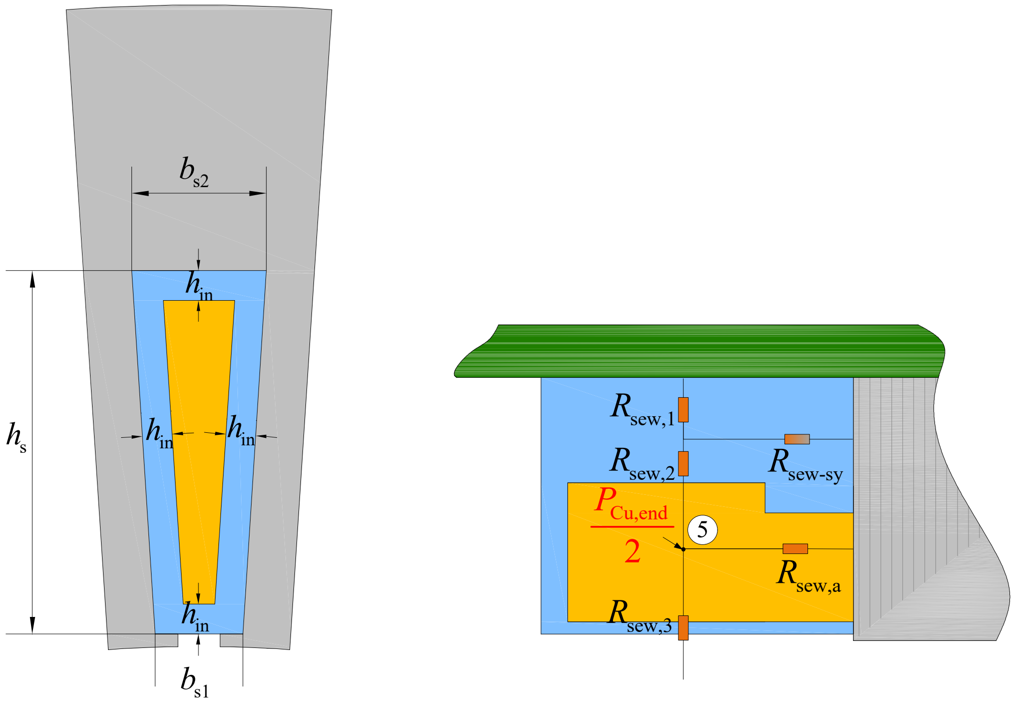

a) b)

Fig. E-4 Modeling of the E-machine winding with impregnated material (in blue color): a) dimensions of winding in slots, b) thermal network of the winding overhang

List of Figures

List of Tables